Influence of the murine transcription factor SRF on mural cell regulated retinal angiogenesis

Dissertation

der Mathematisch-Naturwissenschaftlichen Fakultät
der Eberhard Karls Universität Tübingen
zur Erlangung des Grades eines
Doktors der Naturwissenschaften
(Dr. rer. nat.)

vorgelegt von
Michael Martin Orlich, M.Sc. Molekulare Biomedizin
aus Menden (Sauerland)

Tübingen
2020

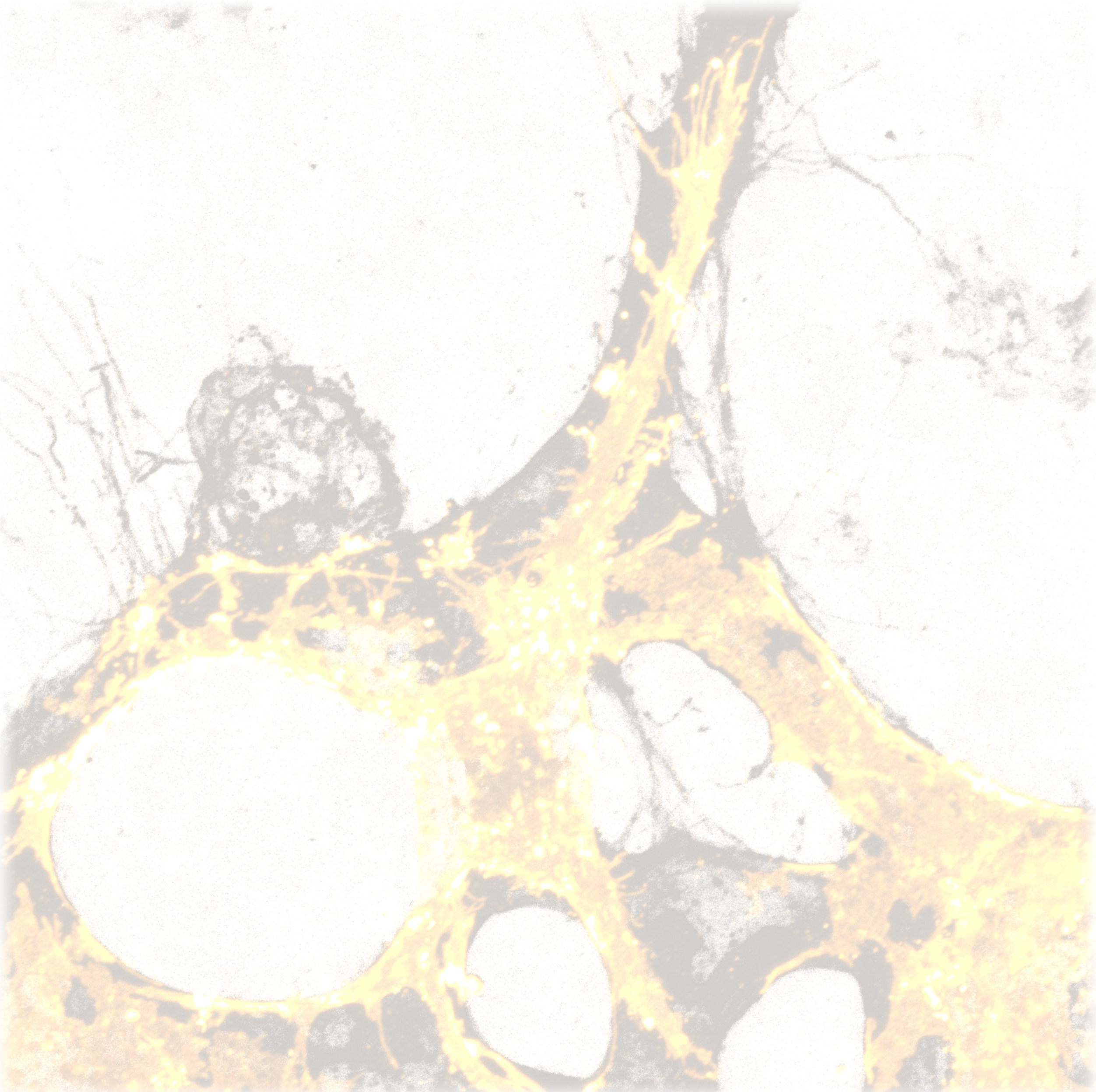

Gedruckt mit Genehmigung der Mathematisch-Naturwissenschaftlichen Fakultät der Eberhard Karls Universität Tübingen.

Tag der mündlichen Qualifikation: 17.11.2020

Stellvertreter Dekan: Prof. Dr. József Fortágh

1. Berichterstatter: Prof. Dr. Alfred Nordheim

2. Berichterstatter: Prof. Dr. Patrick Müller

Declaration

All work presented here was performed by Michael Martin Orlich, unless stated otherwise. Colleagues´s contributions are listed in detail in **Appendix B: Contributions**. The thesis itself was written by Michael Martin Orlich. Most of the data presented in this thesis are part of the manuscript by Orlich et al. (in preparation), which was also written by Michael Martin Orlich. The work was performed under the supervision of Prof. Alfred Nordheim during the period September 2016 - July 2020 at the Interfaculty Institute of Cell Biology, Department of Molecular Biology, University of Tuebingen.

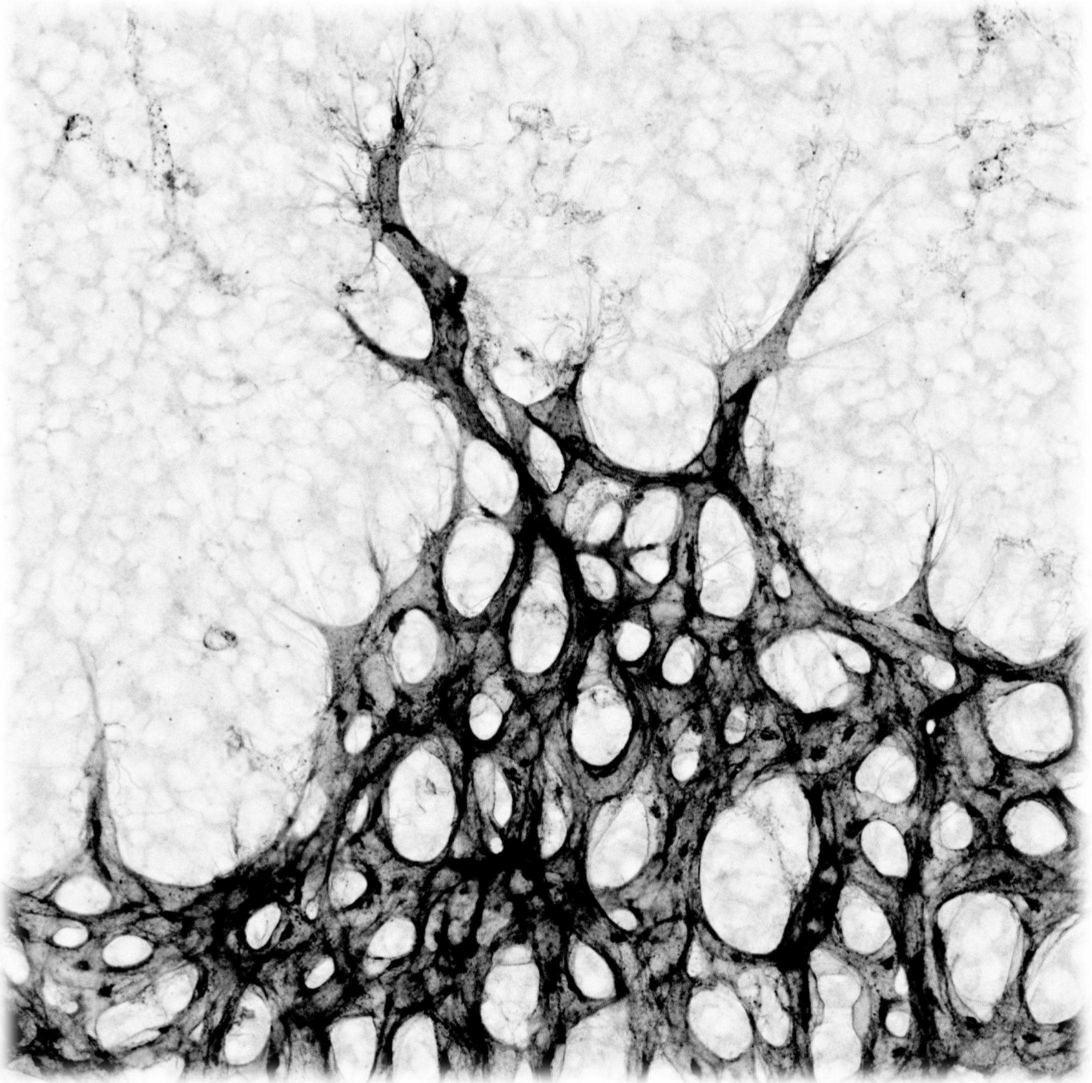

Abstract

Serum Response Factor (SRF) is a ubiquitously expressed transcription factor that regulates the transcription of about 1000 target genes. Endothelial cell (EC)-specific depletion of SRF was previously shown to cause the formation of hemorrhages in the neonatal murine brain and microaneurysms in the retina. However, the physiological role of SRF in mural cells (MCs) remains unknown. MCs wrap around blood vessels and play important roles in angiogenesis, vessel stabilization and homeostasis of the vasculature. They are essential to maintain the integrity of the blood brain barrier and play significant roles in numerous diseases.

To investigate the role of SRF in MCs, *Srf-flex1::Pdgfbr-CreER*^{T2} mice were established, which allow tamoxifen inducible, MC-specific *Srf* deletion (namely *Srf*^{iMCKO}) and the consequences of this *Srf* deletion were investigated in the postnatal mouse retina. Strikingly, by postnatal day 6 (P6), MCs lacking SRF adopt an abnormal morphology, lose the expression of smooth muscle actin and fail to properly co-migrate with angiogenic vascular sprouts. Blood vessels at the sprouting front remain deprived of MCs, become dilated and appear to lose their barrier properties, as red blood cells extravasate into the surrounding tissue. *In vitro* experiments with cultured primary brain MCs (pBMCs) isolated from this mouse *Srf*-knockout model provided first mechanistic insights into the observed phenotype and showed that the lack of SRF leads to cytoskeletal deficiencies which results in reduced MC migration and disruption of MC ability to react to PDGFB stimulation. In contrast, PDGFB stimulation of *Srf* wild type (WT) cells induced the translocation of the SRF cofactor MRTFA into the nucleus, where it activated expression of SRF target genes stimulating cell migration. These observations can explain the reduced MC coverage of the retinal sprouting front at P6 and suggest a mechanistic model of SRF-regulated migration in MCs.

At P12, *Srf*^{iMCKO} mice have developed arterio-venous malformations (AVMs), which become increasingly severe with age. SRF-ablated MCs accumulate in large numbers around the malformed vessels, while the overall MC coverage in the adjacent unaffected vasculature becomes reduced. RNA-Seq, immunohistology and live imaging angiography analyses of *Srf*^{iMCKO} mice suggested that MCs lose their contractile abilities. These data indicate that MCs in *Srf*^{iMCKO} mice cannot maintain the vascular tone, resulting in the compensatory formation of AVMs to channel the blood pressure from arteries to venules.

In contrast, in a pathologic model of ischemic retinopathy, which is characterized by excessive and uncontrolled neovascularization of retinal vessels, MCs acquire pathological functions and promote the retinopathy phenotype. This study identified SRF as an essential factor in pathologic MC activation, likely

through overactivation of SRF via MRTFs. Deletion of mural SRF mitigated ischemic retinopathy and therefore poses SRF as an attractive target for therapy of ischemic retinopathies.

In conclusion, this work revealed new aspects of SRF-mediated MC biology, contrasting their pivotal physiologic functions during developmental angiogenesis and their disease-promoting properties in pathologic angiogenesis.

Zusammenfassung

Der *Serum Response Factor* (SRF) ist ein ubiquitär exprimierter Transkriptionsfaktor, der etwa 1000 Zielgene reguliert. Die Endothel-spezifische Deletion des SRF Gens führt zu Hämorrhagien in neonatalen, murinen Gehirnen, sowie zu Mikroaneurysmen in Retinae. Die physiologische Rolle in muralen Zellen (MZ) ist jedoch noch nicht erforscht worden. MZ bedecken Blutgefäße und spielen eine wichtige Rolle in der Angiogenese, der Homöostase und der Stabilisierung von Blutgefäßen. MZ sind essentiell an der Erhaltung der Integrität der Bluthirnschranke und daher auch an diversen Krankheiten beteiligt.

Zur Erforschung von SRF in MZ wurde die *Srf-flex1::Pdgfbr-CreER*^{T2} Mauslinie etabliert, in der die Applikation von Tamoxifen eine *Srf*-spezifische Deletion in MZ verursachte (im Folgenden Srf^{iMCKO} genannt). Die Konsequenzen dieser Deletion wurden unter Verwendung des postnatalen Mausretina Modells untersucht. Am postnatalen Tag 6 (P6) zeigten *Srf*-deletierte MZ eine abnormale Morphologie und verloren die Fähigkeit zur Expression des Glattmuskelproteins αSMA. Des Weiteren konnten die Zellen nicht ordnungsgemäß mit Endothelzellen komigrieren, was zu einer Reduktion der vaskulären Bedeckung mit MZ speziell an der angiogenen Front führte. Eine direkte Folge hiervon war die Dilatation der Gefäße, sowie der partielle Verlust der Blutretinaschranke, erkenntlich durch Extravasation von Erythrozyten in das umliegende Gewebe. Weitere *in vitro* Experimente unter Verwendung von kultivierten MZ, isoliert aus murinem Hirngewebe (pHMZ), ermöglichte erste mechanistische Einblicke. pHMZ ohne *Srf* besaßen ein kompromittiertes Zytoskelett, wodurch die Fähigkeit zur Migration limitiert war. Des Weiteren konnten diese Zellen nicht mehr auf eine Stimulation mit dem Wachstumsfaktor PDGFB reagieren. Im Gegensatz dazu führte PDGFB Stimulation in *Srf*-Wildtyp Zellen zur Translokation des SRF-Kofaktors MRTFA in den Zellkern. Folglich kam es zu einer erhöhten Expression von SRF kontrollierten Genen mit gesteigerter Migration. Anhand der *in vitro* Ergebnisse konnte die zuvor beobachtete Reduktion der Bedeckung mit vaskulären MZ bei P6 Retinae erklärt werden. Dies erlaubte die Entwicklung eines mechanistischen Modells der SRF regulierten MZ Migration.

Am postnatalen Tag 12 (P12) entwickelten sich in *Srf*^{iMCKO} Tieren arteriovenöse Zusammenführungen (AV-Shunts), die eine direkte Verbindung von Arterien und Venen, unter Umgehung der Kapillargefäße, darstellen. Obwohl insgesamt die MZ Bedeckung der Gefäße im Vergleich zur Kontrolle verringert war, zeigten sich in *Srf*-deletierten MZ eine große Anzahl an AV-Shunts. Unter Verwendung der RNA-Sequenzierungs-, Immunhistologie- und der Angiographie-Analytik konnte gezeigt werden, dass *Srf*^{iMCKO} MZ die Fähigkeit zur Kontraktion verloren hatten. Dies legt nahe, dass die Gefäße dem arteriellen Blutdruck nicht mehr standhalten konnten, was zu einer Druckverringerung durch AV-Shunt Bildung führte.

In einem publizierten pathologischen Modell der ischämischen Retinopathie, das sich durch exzessive und unkontrollierte Gefäßneubildung auszeichnet, werden MZ pathologisch aktiviert. Diese Aktivierung führt hierbei zu einer Verstärkung des pathologischen Phänotyps. Diese Studie identifizierte SRF als einen essentiellen Faktor der pathologischen Aktivierung der MZ. Diese geschieht vermutlich über eine Überaktivierung von SRF. Eine spezifische Deletion von *Srf* in MZ konnte daher den pathologischen Phänotyp der ischämischen Retinopathie abmildern. Aus diesem Grund stellt die Inhibition von SRF eine attraktive Strategie zur Therapie der ischämischen Retinopathie dar.

Zusammenfassend zeigt diese Studie neue Aspekte SRF vermittelter MZ Biologie, indem sie die gegensätzlichen Funktionen von MZ in physiologischer und pathologischer Angiogenese kontrastiert.

Acknowledgements

I would like to thank Prof. Dr. Alfred Nordheim for accepting me as a PhD student, and providing me the opportunity to work on this exciting and challenging project. His supervision and guidance in the course of this project strengthened my interest in vascular biology and laid the foundation for my further research endeavours. Furthermore, I thank Prof. Dr. Patrick Müller for all his support and valuable comments as a great second supervisor and TAC member. I would also like to thank Dr. Frank Chan for his insightful comments and valuable input as my TAC member.

I thank the International Max Planck Research School (IMPRS) “From Molecules to Organisms” for accepting me to the PhD program. I am especially grateful to Dr. Sarah Danes and Sybille Patheiger, who provided continuous support in many aspects. I would like to thank the Karl-Kuhn foundation, who partially funded this project and helped me in making great progress. I would also thank the EMBO society, who supported me with a short-term fellowship.

I would like to express my sincere gratitude to all the collaborators who contributed significantly to the project. I would like to thank Prof. Dr. Ralf Adams for providing the *Pdgfrb(BAC)-CreER*^{T2} mouse line and strongly supporting this project with his tremendous knowledge. I also thank Dr. Rodrigo Diéguez-Hurtado for being a great collaborator and providing excellent input during this project.

I would like to thank Prof. Dr. Mathias Seeliger, Dr. Regine Muehlfriedel and Dr. Vithiyanjali Sothilingam, for their fantastic collaboration and support even beyond this project. Their methodical support greatly pushed this project in the right direction.

Furthermore, I would like to thank Dr. Hartwig Wolburg for transmission electron microscopy (TEM) of retina samples and providing inputs for the interpretation of TEM images. This valuable help greatly enhanced my understanding of EM microscopy. Manny thanks also to Gabi Frommer-Kaestle for competent preparation of EM samples.

I thank Christian Feldhaus, Aurora Panzera and Vanessa Carlos, for giving me the opportunity to use the microscopes of the imaging facility at the MPI for Developmental Biology, Tuebingen. I would also thank them for teaching me the technicalities and enhancing my skills in microscopy.

An indispensable partner during my PhD was Dr. Konstatin Gaengel, who gave me important inputs and shared his immense knowledge of vascular biology with me. Konstantin, thanks a lot for your initial trust and your support. I am sure we will work together excellently in the near future.

Furthermore, I would like to thank the animal caretakers of the IFIZ, who took care of my mouse lines and always provided me excellent support. I would especially like to mention Carmen, Suzanna, Nicole and Gabi. Thanks for your support.

I would like to thank the entire Nordheim group, that has been an indispensable source of support and motivation during every stage of my PhD. Great thanks to Siggi, who significantly enhanced my knowledge of working with mice and played a major role in helping me write the proposals for animal experimentations. Many thanks to Anke for all her support, especially in animal breeding. I am sure that without her help and positive attitude, I wouldn’t be able to handle this enormous amount of work. Thank you so much Catrin for all the scientific and nonscientific discussions; and your help in proofreading basically everything I wrote. Your help was extremely valuable to me. Mohan, thank you for being a great company during the whole time we’ve been through. Also great thanks to Ivana, for all the valuable scientific discussions and your support when I needed it. Great thanks to Heidemie. Thanks that I could ask you for help irrespective of the situation. Your help was always valuable to me. Many thanks to Elena who always gave me excellent technical support.

I would also like to thank the students that I supervised and who put a lot of efforts in my projects. I was able to learn a lot as to how to guide students. I would like to especially mention Cansu, who was my first student whom I supervised through all the stages of a master thesis. It was a good experience and your efforts helped the progress of my project. Another great and diligent student was Stella. Thanks, that you chose to work with me as your supervisor for the second time. I would also like to thank Pascal who worked with great effort during the final stage of my project, and provided his extremely valuable contributions to the project.

I thank Caner and Nils for being great friends from the first day of my work towards a PhD. I always enjoyed the time we spent together and I hope that this will not change in the future. Caner, I also thank you for your great bioinformatical support. Thanks for always being patient with me.

An dieser Stelle möchte ich mich auch an diejenigen richten, die mich schon seit einer sehr langen Zeit begleiten. Danke an all meine Freunde aus meiner Heimat, die mich immer unterstützt haben, egal in welcher Phase meines bisherigen Lebens. Es ist ein großes Glück so viele verlässliche Menschen hinter sich zu haben.

Ein riesen Dank geht an meine Familie und speziell an meine Eltern. Ohne euch hätte ich nicht studieren können. Danke, dass Ihr in jeder Situation an mich geglaubt habt und mich bedingungslos unterstützt habt. Ich hoffe ich kann eure Tugenden in der Zukunft weitergeben.

Zuletzt möchte ich mich bei meiner Partnerin bedanken, die mich fast die ganze Zeit in Tübingen begleitet. Durch dich ist dieser Ort ein neues zu Hause geworden. Ich danke dir vor allem für all die Geduld, die du mir entgegengebracht hast.

Contents

Chapter 1

1 Introduction

1.1 The vascular system

To sustain physiological functions, vertebrates need an efficient system to transport gases, nutrients, signaling molecules and cells between different tissues of the body. This task is fulfilled by the cardiovascular system, which consists of two hierarchical and highly tree-like branched tubular networks, the blood and the lymphatic system (**Figure 1.1**). The heart pumps blood, rich in O_2 and nutrients via efferent arteries and arterioles into the capillaries, where most exchange with the tissue occurs. Afferent venules and veins carry deoxygenated and CO_2-rich blood back to the heart and lungs for oxygenation [1]. This process requires a high cardiac pressure to drain interstitial liquid out of the vessels into the adjacent tissues. The majority of the liquid is reabsorbed by the venous blood vessels due to osmotic pressure inside the vessels. The remaining interstitial liquid is absorbed by the lymphatic system [2]. In contrast to the blood circuit, the lymphatic system is blind-ended and organized in capillaries and ducts. Moreover, lymphatic vessels also facilitate trafficking of immune cells through the body to lymph nodes and lymphoid organs to sustain immune functions of the body. Both systems are strictly separated and only connect in one unique contact point, the subclavian vein [3]. Maintenance of physiological functions of the body requires both vessel systems and their dysfunction contributes strongly to the pathogenesis of many diseases such as arteriosclerosis, hemorrhaging and ischemic stroke, diabetes and metastatic cancer [4,5]. In addition, numerous genetic disorders are linked to vascular diseases. Examples are hereditary hemorrhagic telangiectasia (HHT) and the cavernous malformations (CCMs).

1.1.1 Architecture and functions of the vascular system

The vascular system is organized into a hierarchical network of arteries, veins and capillaries. Arteries and veins consist of three layers. The inner layer, named *tunica intima*, is formed by endothelial cells (ECs) and a surrounding basement membrane (BM). The *tunica intima* is enveloped by the *tunica media*, which consists of vascular smooth muscle cells (SMCs) and elastic fibers responsible for vascular stability, tone and blood pressure regulation [1]. ECs and SMCs share a common BM, which consists of extracellular matrix proteins such as laminins and collagens, and which provides mechanical support and also contributes to signaling [6]. The outer layer is built by the *tunica adventitia*, a layer of connective tissue [7]. Depending on the caliber and the pressure to which the vessels are exposed, the exact composition of the three layers can differ. Arteries are exposed to high cardiac pressure and therefore harbor a stronger developed *tunica media* and *tunica adventitia*. Veins instead are exposed to low cardiac pressure and are primary points of immune cell extravasation, which justifies thinner layers in comparison to arteries. Arteries drain the blood via arterioles into small caliber capillaries, which themselves are comprised of a single EC layer covered by BM and therein embedded pericytes (PCs), which are in direct contact to ECs [8]. Dependent on the organ function, the PC coverage of the capillaries differs greatly between 1:1 to 1:3 (PC:ECs) in the central nervous system, and 1:100 in the skeletal muscle [9]. However, not only the PC coverage on capillaries can differ, but also the EC morphology itself is strongly dependent on the specific needs of the organ [7]. EC morphology within the central nervous system (CNS) is characterized by a continuous EC morphology. In addition, ECs of the CNS express high numbers of tight and adherence junctions to build a selective permeable barrier, referred to as the blood brain/retina barrier (BBB, BRB), which restricts the passage of solutes from the blood stream to the tissue of the CNS [10]. In contrast, EC morphology can also be fenestrated or even discontinuous, as found in organs where primary filtration and exocrine functions are performed, such as the kidney or liver. Taken together, the vascular system is a highly specialized organ of ECs, supporting SMCs and PCs which are respectively adapted to the individual needs of the organ [7].

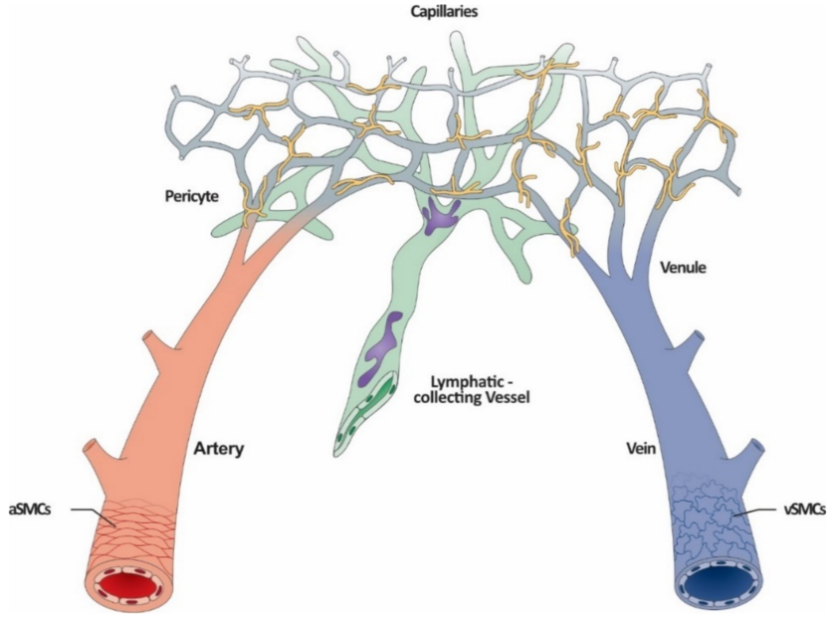

Figure 1.1 | Architecture of the mammalian vascular system. The vascular system is tubular and tree-like in structure, separated into large diameter arteries carrying O_2-rich blood from the heart and funnel into smaller arterioles which drain into the capillaries. Here, exchange of gases and nutrients with the tissue is facilitated. Deoxygenated and metabolite-enriched blood is transported back via afferent venules, draining into large caliber veins. Arteries and veins are covered by contractile SMCs, conferring resistance of vessels to the blood pressure. Capillaries instead are covered by PCs, which stabilize vessels, but most likely do not fulfill contractile functions. Lymphatic vessels collect fluid which drains out of the arterial system. Modified from Adams and Alitalo, 2007 [1].

1.1.2 Development and maintenance of the vascular system

1.1.2.1 Angiogenesis is the main driver of vascular growth

During embryonic development, the vascular system is the first organ to develop, emphasizing the importance to supply tissues with gases and nutrients at early embryonic stages to ensure further development. The primitive embryonic vascular system is generated through vasculogenesis, the *de novo* process in which endothelial progenitor cells of mesenchymal origin, also named angioblasts, start to aggregate and form so called blood islands. These islands start to fuse and build a honeycomb-shaped primitive plexus, which gives rise to the dorsal aorta and the cardinal vein [1,11,12,13]. Another mechanism of vessel establishment is intussusception, where an already established vessel starts to divide in two by insertion of tissue pillars within the vessel to expand the vasculature [1,14,15].

Besides vasculogenesis and intussusception, the vast majority of blood vessels are established through angiogenesis, i.e. the sprouting of new blood vessels from preexisting ones (**Figure 1.2**) [12]. Angiogenesis is usually initiated when a tissue experiences to hypoxia. This leads to the stabilization of the hypoxia inducible factor 1α (HIF1α), which activates the transcription of proangiogenic factors. One of the most potent and best characterized proangiogenic factors is the vascular endothelial growth factor A (VEGFA) [16]. Secreted VEGFA forms a gradient originating from the hypoxic area and binds to its receptors, the vascular endothelial growth factor receptor 1 and 2 (VEGFR1 and VEGFR2), which are mainly expressed on ECs. VEGFRs are receptor tyrosine kinases, which dimerize upon binding of VEGFs. This causes the autophosphorylation of the intracellular receptor domains and activates multiple downstream signal cascades involved in angiogenesis. VEGFR1 has a high affinity to VEGFA, but functions as a decoy, leading to inhibition of angiogenesis and thus making it an important regulatory substance [17,18]. In contrast, VEGFR2 is the major inducer of angiogenesis and activates the EC upon binding to its ligand [19]. Activation of an EC leads to its specialization into a so called tip cell. Tip cells are characterized by being highly invasive and motile. Phenotypically, a tip cell forms long filopodia in order to sense the VEGFA gradient [20]. Furthermore, tip cells express high levels of Delta-like-4 (DLL4), the ligand of the Notch1 receptor. Binding of DLL4 to the Notch1 receptor on a neighboring EC restricts VEGFR2 signaling and leads to a specialization of such a neighboring EC into a stalk cell [21]. In comparison to tip cells, stalk cells show low levels of VEGFR2 signaling and are characterized by high proliferative and low motile behavior. In this selection process, Dll4-Notch1 signaling plays a pivotal role. Several studies have shown that compromising Dll4-Notch1 signaling leads to excessive tip cell formation and thus to aberrant sprouting, branching and fusion of vascular tubes [21–23]. Furthermore, fascinating live imaging studies on the vascular development in zebrafish showed that tip cell selection is a highly dynamic process rather than static and deterministic. Tip cell and stalk cell fate can vary and cells are even competing for tip cell position [24].

Tip cells are acting as pioneering cells, capable of sensing VEGFA to migrate towards the gradient. Matrix metalloproteinases (MMPs) are secreted by tip cells in order to degrade extracellular matrix and further support invasive migration towards hypoxic tissue areas [1]. Stalk cells instead follow behind mainly by proliferation. They express BM and junctional proteins to build a luminal structure giving rise to a new nascent vessel. Nevertheless, after the immature vessel is established it needs to be stabilized quickly. Therefore, tip cells secrete platelet derived growth factor B (PDGFB) to attract PCs, which settle on the newly lumenized vessel, wrap around the ECs and integrate into the BM [25].

A growing vessel can also encounter a second growing vessel and these two parts can fuse, thereby generating a new vessel in a process called anastomosis. If the nascent vessel gets perfused by the blood stream, the vessel develops junctions between ECs and matures further [26]. A non-perfused vessel however is dispensable and therefore destabilizes and retracts, leaving a trace of BM behind, which is commonly referred to as empty sleeve [27]. Vessel selection by blood flow is therefore a further important mechanism to orchestrate the organized development of blood vessels.

1.1.2.2 Regulatory factors in guidance of angiogenesis

Angiogenesis is a multicellular and complex process that is tightly regulated. Disturbances within its regulation often lead to diseases, thus making its tight regulation essential. Many pro- and anti-angiogenic factors regulate proper and guided vessel growth. As previously mentioned, VEGFA is one of the best studied chemo-attractants in vessel growth that is crucial for angiogenesis. Early studies have shown that already a heterozygous deletion of one copy of the *Vegfa* gene in mice during embryonic development is incompatible with live [28]. Binding of VEGFA to the VEGFR2 activates a plethora of downstream signaling pathways. Here to mention are the mitogen activated protein kinase (MAPK) and the Rho/actin signaling pathway involved in the control of proliferation and migration, respectively.

Seminal work has highlighted that VEGFR2-mediated activation of the Rho/actin signaling pathway plays an essential role in EC activation. Rho-GTPase-mediated remodeling of the actin cytoskeleton leads to the activation of the serum response factor (SRF) transcription factor via its co-transcriptional activators myocardin-related transcription factors A and B (MRTFA/B) [29]. Tip cells lacking *Srf* or *Mrtfa/b* were unable to modulate the actin cytoskeleton properly, which resulted in stunted filopodia and disrupted migration [29,30]. Ablation of the Rho-GTPase CDC42 caused a similar phenotype, emphasizing the importance of proper cytoskeletal modulation via the Rho-GTPase/actin pathway [31].

Besides angiogenesis-promoting factors, also angiogenesis-inhibiting factors are necessary in order to precisely regulate and fine tune vessel growth. Deletion of the VEGFR1 gene *Flt1* results in embryonal lethality and ECs showed increased proliferation and disorganization [32]. Ablation of the intracellular tyrosine kinase domain of VERGFR1 instead lead to a fully developed and functional vascular system, which suggests it functions as a decoy regulating VEGFR2 signaling[33].

The mammalian VEGF family consist, besides VEGFA, of four further growth factor members, VEGFB, VEGFC, VEGFD, and the placental growth factor (PLGF), a protein mainly active during embryonic development [34]. The binding affinity of VEGFs varies depending on the receptor, thereby leading to phosphorylation of different intracellular tyrosine residues, which enables further fine tuning of downstream signaling [35]. VEGFC and VEGFD can also bind VEGFR3, one of the main regulators of lymphangiogenesis [3].

In addition to VEGFs and VEGFRs, a plethora of pro- and anti-angiogenic factors exist, that additionally fine tune angiogenesis. Neuropilins (NRP1 and NRP2) were originally described in the regulation of axonal growth in neurons. In angiogenesis, they act as pro-angiogenic co-receptors in VEGFR signaling and are capable of binding the specific VEGF isoform $VEGF_{165}$ to promote tip cell guidance and migration behavior [36]. Furthermore, NRP1 is required for arterial specification of vessels [37].

An anti-angiogenic factor is sphingosine-1 phosphate (S1P), which is produced by ECs and red blood cells (RBCs). S1P is distributed through the blood stream and binds to the S1PR1 receptor on ECs. This prevents the internalization of VEGFR2, which usually promotes downstream activation of VEGFR2 signaling [38].

The VEGFA-VEGFR2 signaling axis also induces expression of DLL4, the ligand of Notch1. DLL4 activates Notch1 in neighboring cells via juxtracrine signaling. Notch1 activation results in lower VEGFR2 and higher VEGFR1 expression, thereby shifting the balance of the neighboring cell towards a stalk cell. Deletion of *Notch1* or *Dll4* lead to the induction of tip cell fate and thus to aberrant sprouting [21]. Another Notch ligand, Jagged1 (JAG1), is mainly expressed on stalk cells but has only weak Notch activating abilities. JAG1 is therefore thought to compete with DLL4 for Notch binding, raising the idea of tip cell-stalk cell competition [19,39]. The highly dynamic character of tip cell and stalk cell commitment was shown not only in mice, but also in the zebrafish model and in *in silico* models [24]. Both cell types are not trapped in one or the other cell fate but can actually change their phenotype repeatedly. Further investigations showed that synchronization of Notch signaling leads to impairment of vascular morphogenesis and therefore demonstrates the need of tip cell-stalk cell competition for optimal angiogenesis [40]. However, recent studies carried out in zebrafish and mouse model systems challenged the current understanding of DLL4-

Notch1 regulated competition [41,42]. They showed that Notch1 levels rather that DDL4 levels are more important in tip cell – stalk cell competition. Strikingly, Notch1 endothelial knockout (KO) cells indeed tend to develop a tip cell phenotype. However, specific deletion of *Dll4* in tip cells, which were thought to lose competition abilities, were able to sustain at the leading edge [42].

Taken together, the angiogenesis-based expansion of the vascular system needs to be tightly regulated in order to generate healthy blood vessels. Many pro-, but also anti-angiogenic pathways are active to guide the vasculature directionally and to prevent hyper-sprouting. After initiation of vessel sprouting by tip cell and stalk cell signaling, the newly formed vessel needs to mature.

1.1.2.3 Maturation and remodeling of the primitive vasculature

Maturation of a newly formed vessel is an essential event in advanced vascular development. Without maturation, a vessel cannot be sustained and needs to retract. As in sprouting, countless pathways are also involved in vessel maturation. One crucial and early step of maturation is the recruitment of PCs and SMCs, collectively known as mural cells (MCs), to the developing endothelium (**Figure 1.2**).

PDGFB-PDGFRβ signaling builds the basis for MC recruitment. Early work on PDGFB-deficient mouse embryos found capillaries deprived of PCs, leading to micro-aneurisms [43]. It was further shown, that a lack of PCs leads to enlargement of vessels through hyperplasia and edema, emphasizing the importance of PC coverage in normal vessel maturation [44]. Newer studies confirmed these observations using the mouse retina vascular model system [45,46]. During sprouting angiogenesis, PDGFB is mainly secreted by tip cells and forms a gradient sensed by MCs, which express PDGFRβ and thus leads to co-migration of MCs behind tip cells [47]. The PDGFB gradient is tightly regulated to ensure directional MC migration. Secreted PDGFB is bound to the heparin sulfate proteo-glycans at the extracellular matrix due to its C-terminal retention motive [48]. This enables PDGFB binding in close vicinity to the EC and limits the range of action, which is important for MC guidance and the close contact between MCs and ECs.

A further player in MC attraction is Notch3, another member of the Notch family, which is mainly expressed on MCs. Deletion of *Notch3* impairs MC recruitment and differentiation of SMCs in zebrafish as well as in mice [49,50]. However, the mechanisms behind how Notch3 regulates the MC-EC contact are only poorly understood.

MCs are thought to stabilize vessels by establishing contacts and signaling pathways to ECs. One important MC-derived paracrine ligand is angiopoietin-1 (ANG1). The binding of ANG1 to its receptor TIE2 expressed on ECs induces vascular quiescence and shows that ANG1 is a critical factor in the maintenance of vascular integrity [51]. Indeed, genetic ablation of either ANG1 or TIE2 leads to vascular abnormalities and embryonal lethality [52,53]. ANG1 prevents hypervascularization in wound healing and mitigates VEGFA-driven leakage [54,55]. Activation of TIE2 is known to act via the PI3K-AKT signaling pathway to induce endothelial quiescence. TIE2 can also be bound by ANG2, a second member of the ANG family. ANG1 and ANG2 compete for the TIE2 binding site. However, ANG2 mainly suppresses TIE2 signaling and is therefore a pro-angiogenic factor [56]. High expression levels of ANG2 are usually found in ischemic tissues such as the tumor microenvironment but also in tip cells, where it acts in an autocrine manner to promote angiogenesis [57,58]. Furthermore, recent studies found that TIE2 signaling suppresses the activation of the proangiogenic transcription factor FOXO1 [45,59]. FOXO1 leads *inter alia* to the expression of MMPs and VEGFR2. Interestingly, it was shown that pharmacological inhibition of MC recruitment attenuates ANG1-TIE2 signaling, leading to the expression of VEGFR2 and ANG2. This increases susceptibility of ECs to VEGFA and further increases FOXO1 activation in a positive feedback loop. The consequences are severe disintegration of ECs and inflammation of the surrounding tissue. However, application of ANG1 or blockade of ANG2 was able to attenuate the observed phenotype [45,60]. Furthermore, a recent study revealed a so far unknown metabolic function of FOXO1 as a metabolic checkpoint during proliferation and growth of ECs [61].

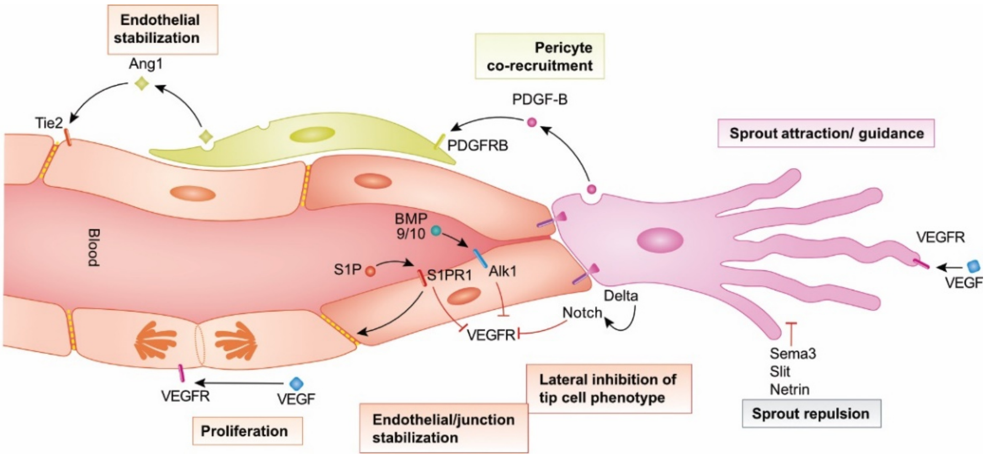

Figure 1.2 | Angiogenic sprouting and stabilization. ECs express VEGFR2 and are activated upon binding of VEGF. Endothelial tip cells (magenta) are motile, invasive and can sense the VEGF gradient by possessing long filopodia. Tip cells express high levels of DLL4 which induces Notch signaling in stalk cells (red) and inhibits VEGFR signaling. In addition, tip cells secrete PDGFB to attract PDGFRβ positive MCs (green), which in turn stabilize the immature sprouting vessel via ANG1/TIE2 signaling. Further BMP9/10-ALK1 and SP1-S1PR1 signaling of stalk cells inhibits their tip cell potential and thereby promotes establishment of EC-junctions between stalk cells. VEGF signaling in stalk cells increases their proliferation to follow between migratory tip cells. Modified from Betsholtz, 2018 [62].

If a new vessel is perfused by the blood stream, further maturation is initiated. Conversely, a lack of perfusion makes vessels obsolete and initiates their retraction, which leaves an empty ColIV^{+} sleeve behind [63]. A previous report identified DLL4-Notch signaling as a regulator in vessel regression. In this study, vessel regression was induced in a mouse model by hyperoxia [64]. Interestingly, pharmacological inhibition of Dll4-Notch signaling attenuated vessel regression. Apparently, Dll4-Notch signaling induces vasoconstrictors and leads to non-perfused vessels and thus to their regression. However, the mechanism of how retraction is organized remains poorly understood. Based on observations on murine hyaloid vessels, EC death has been proposed as the major mechanism of retraction but this mechanism could not be confirmed in retinal vasculature during remodeling [65,66]. A recent publication suggested a model of reverse anastamosis to explain vessel retraction [27]. Perfused vessels are exposed to shear stress leading to the polarization of ECs against the flow. In turn, a lack of shear stress in non-perfused vessels abrogates these polarization signals and causes backwards migration of ECs in a reverse process of anastomosis.

Another important part of vascular development is the specification into arteries and veins in order to define a directional blood flow. Indeed, arterial ECs express several proteins such as transcription factors, extracellular matrix (ECM) and signaling molecules, which are largely absent in venous ECs [1]. One well-known membrane protein involved in angiogenesis with a largely specific expression on arteries is ephrin (Eph)-b2. In contrast, its ligand Eph-B4 is highly abundant on veins [67].

Interestingly, the Notch pathway was shown to control arterial specification of ECs. Although components of the Notch pathway are crucial in sprouting angiogenesis, KO models of *Notch1/4*, *Jag1* and *Dll4* also show defects in arteriovenous specification [1,68,69]. More recent studies identified venous derived tip cells as contributors to arterial vessel formation [41,42]. The level of endothelial Notch signaling is important to activate expression of the chemokine receptor CXCR4, thereby guiding migration of tip cells towards arteries [41,42,70]. As Notch is activated via VEGFR2 signaling and NRP1 assisted signaling, VEGFA rather supports the arterial EC fate. In contrast, venous cell fate was shown to be guided at least in part by the transcription factor COUP-TFII by suppressing Notch activation [71].

1.1.2.4 Maintenance of the vasculature – definition and impact of mural cells

As previously mentioned, MC coverage is an essential step in maturation of newly formed vessels. MCs are a collective term to describe both PCs and SMC (**Figure 1.3**). PCs share the BM together with capillary ECs. They are connected through tight junctions and adherence junctions via selective and restricted contact points known as "peg-socket" arrangements [9]. PCs usually lie on top of microvessels and surround capillaries with long protrusions. Traditionally, they were thought to mainly take part in vessel maturation. However, a recent study revealed their regulatory function during sprouting angiogenesis. PCs express the soluble form of VEGFR1 (sFlt1) in close vicinity to endothelial tip cells, enabling fine tuning of the VEGFA gradient by restricting over-activation VEGFR2 signaling [72]. PCs were also shown to take part in maintenance of the BBB/BRB during development [45,59,73]. Interestingly, a recent study showed that PCs seem to be dispensable for the BRB during adulthood, proved by a specific, diphtheria toxin mediated PC ablation [45]. Nevertheless, these vessels were susceptible to external VEGFA treatment. In addition, this study only observed PC deprived vessels after a short time period. Long-term effects of PC ablation in adulthood were not studied so far. A further report analyzed the expression profile of PCs of the CNS and observed high expression of ATP-binding cassette (ABC)-transporters and soluble carrier proteins which are highly important for BBB/BRB homeostasis, reinforcing the importance of PCs for vessel maintenance [74].

In contrast to PCs, SMC are localized on arteries, arterioles, venules and veins [9]. SMCs are solenoid in structure and possess finger-like protrusions surrounding the vessels. In addition, SMCs express several smooth muscle genes (SMG), which are mainly needed to generate contraction force around the vessel. This force is crucial to keep vessels in shape. Moreover, the permanent basal contraction known as vascular tone is necessary to maintain resistance of vessels against the blood pressure. Depending on the extent of pressure the vessel is exposed to, the SMC coverage and degree of SMG expression can differ. Arterial vessels are exposed to the highest pressure, therefore arterial SMCs (aSMC) are more abundant and express higher SMG levels compared to venous SMCs (vSMCs) [74]. However, the reduced SMC amount and SMG expression levels on veins are still pivotal to prevent venous diseases [75].

PCs were also described to possess contractile abilities to regulate microvascular flow together with SMCs. However, these abilities of PCs are controversially debated in literature, as some studies confirm the contractile ability of PCs and others strictly deny it [76,77]. Strikingly, detailed comparisons of these reports revealed a different definition of PCs. The studies which identified contractile abilities of PC more likely characterized aSMCs, which do indeed regulate microvascular blood flow through contraction. This example emphasizes the difficulty in identifying the MC subclasses of PCs, aSMCs and vSMCs correctly. The confusion between these two cell types likely originates from their high similarity. A previously mentioned RNA profiling study using murine brain cells employed single cell RNA-sequencing (RNA-Seq) to differentiate various brain tissue cell types based on their expression profile [74]. Vanlandewijck et al. (2018) showed a high similarity of PCs to vSMCs, which further obscures the previously discussed strict separation between these cell types. The existence of transitional cell types between SMCs with high SMG expression and PCs with almost no SMG expression are likely (**Figure 1.3**) [78].

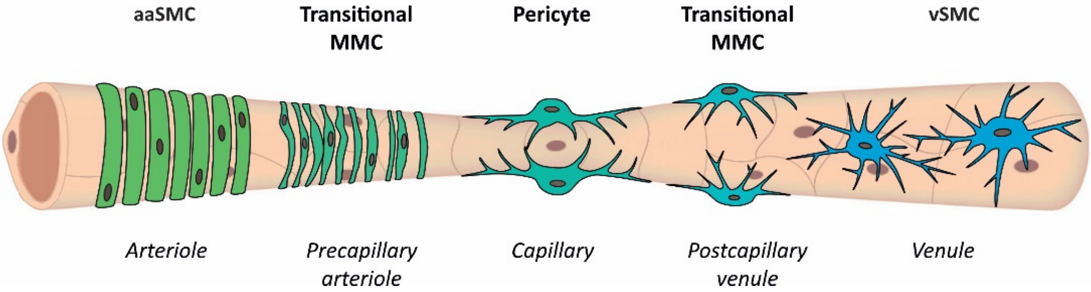

Figure 1.3 | The continuum of MCs. Illustration of MC morphology depending on the position along the vascular tree from arteriole to venule. MCs can be subgrouped into SMCs and PCs. Arteriolar SMCs (aaSMCs) possess a finger-like morphology and express high levels of SMGs, leading to a contractile phenotype able to regulate the vascular tone. PCs are located on capillaries, which they surround with their long protrusions. PCs are negative for smooth muscle markers such as αSMA and SM22α. Venous SMCs (vSMC) can be found on venules and possess a stellate shaped morphology. In comparison to aaSMCs, SMG expression is low in vSMCs. Transitional microvascular MCs (MMCs) occupy pre- and post-capillary vessels and present a hybrid subgroup between the respective extremes. Modified from Holm et al., 2018 [78].

Especially the characterization of PCs remains a challenging task due to the lack of unique markers. So far, no molecular marker is known which exclusively distinguishes PCs from SMCs. Furthermore, PCs are highly adapted to the specific needs of the organotypic vasculature, which additionally complicates a general molecular definition [78]. For example, PCs in the CNS maintain the BBB/BRB and are therefore tightly connected to ECs. In contrast, PCs of the liver, namely stellate cells, are more loosely distributed in the perisinusoidal space and fulfill important tasks in retinol metabolism [79]. Established markers for a comprehensive detection of MCs of the CNS are PDGFRβ and the chondroitin sulfate transmembrane proteoglycan NG2, a marker for the MC plasma membrane. In addition, the type 3 cytoskeletal protein Desmin (DES) reliably marks intracellular parts of the MC cytoskeleton [9]. In order to differentiate between PCs and SMCs, the smooth muscle markers αSMA or SM22α can be used in addition to positional and morphological criteria [9].

In conclusion, a more comprehensive analysis comprising multiple criteria such as (i) several markers, (ii) position on the vasculature and (iii) cell morphology are needed for the robust differentiation between PCs and SMCs.

A well-designed study on MCs relies on laborious *in vivo* work on established marker-based conditional knockout models. However, there also exist a lot of *in vitro* studies claiming functions that so far could not be proven *in vivo*. Such cell culture approaches lack the comprehensive molecular verification of *in vivo* models, which makes the results difficult to interpret [80]. Due to the reasons mentioned above, our knowledge about MCs is limited and studies using animal models are therefore indispensable. Chen et al. (2016) generated a murine PDGFRβ driven CreER^{T2} line, capable of reliably targeting MCs [81].

1.1.2.5 Regulation of the vascular tone by contraction of SMCs

The main function of SMCs is to control blood flow and pressure by precise regulation of the vessel diameter. To achieve this, they are able to sustain or alter the vascular tone by means of their contractility. Failure in this regulation results in cardiovascular diseases such as arterial hypertension [82]. SMC contraction is a multistep mechanism regulated by an interplay between cytoskeletal and signaling components. Especially the interaction between actin and myosin filaments generates tensional force [83]. A large amount of these cytoskeletal proteins can be found in SMCs. For example, the actin content in aortic SMCs can make up roughly to 40 % of total protein content [84]. However, not only the content but also the organization is crucial. In contrast to striated muscle, where actin and myosin filaments are organized in a superordinate system, actin filaments of SM are attached to membrane-anchored dense bodies [85]. This decentralized structure allows greater elastic properties of the cell. Additional proteins, such as SM22α, bundle actin filaments and likely enhance force generation [86].

SMC contraction is initiated by an increase of the intracellular Ca^{2+} concentration. This increase can be regulated through different processes. Incoming action potentials originating from neurons or stretch-dependent ion channels in the SMC plasma membrane trigger a depolarization [83]. Usually, Ca^{2+} influx is assisted by L-type ion channels abundant on the plasma membrane. The incoming Ca^{2+} stream leads to additional ion influx by activation of ryanodine receptors (RYR) embedded in the sarcoplasmic reticulum (SR) of the SMC [87]. The SR is known as a Ca^{2+} storage within the cell and is needed for reinforcement of the ion signal. In addition, paracrine or endocrine signals are also able to trigger Ca^{2+} influx by respective receptor binding. Potent peptides are e.g. endothelin-1 (Edn1) and angiotensin-2 (AT2) [88,89]. Their binding induces phospholipase C activation, leading to the generation of inositol trisphosphate (IP_3). This diffusible second messenger then binds the IP receptor Ca^{2+} channel (InsP3R) located at the SR, stimulating further Ca^{2+} influx [82].

Once the intracellular Ca^{2+} concentration rises above a certain threshold, the regulatory protein Calmodulin (CaM) is activated upon binding of Ca^{2+} ions [90]. CaM activation leads to activation of the myosin light chain kinase (MLCK), which is a regulatory kinase able to phosphorylate the regulatory chain on myosin. This phosphorylation initiates a conformational change in the myosin head, thereby switching on the ATPase activity of myosin and thus stimulating the interaction of the myosin head with actin. This interaction is known as *cross bridge cycling* and generates the tensional force [91]. Interestingly, the amount of generated tension is relative to the concentration of intracellular Ca^{2+}. The interaction between myosin and actin can be reversed by the myosin light chain phosphatase (MLCP), ultimately leading to relaxation.

Additionally, Ca^{2+} is transported out of the cytoplasm by Ca^{2+}/Na^{+} as well as Mg^{2+}/Ca^{2+}-ATPases located in the plasma membranes of the cell and the SR [82]. By utilization of the described pathway, the SMC is able to influence the diameter of blood vessels and is therefore capable of blood pressure regulation.

1.1.3 Vascular diseases

The vasculature fulfills numerous and pivotal functions throughout the body. Therefore, it is not surprising that pathological changes are frequently severe and life threatening. There exist numerous genetic disorders, triggered by mutations in key genes affecting cardiovascular development. Some of these disorders, as well as some gene unrelated diseases, are briefly introduced in this chapter.

Arteriovenous malformations (AVMs) are severe vascular pathologies in which arteries form direct connections to veins, thereby circumventing the capillary system. These formations are unstable due to the relatively high blood pressure in the affected veins. AVMs are prominent in the hereditary hemorrhagic telangiectasia (HHT) disease also known as morbus Ossler-Weber-Rendu syndrome. The origin of this disorder lies in mutations of the *Eng* or the *Alk1* gene, which are parts of the transforming growth factor beta (TGFβ) signaling pathway [92]. HHT causes micro-aneurysms (telangiectasias), which can be frequently found in mucosal tissues, leading to conspicuous nose bleedings in patients. Of note, AVMs can also arise in every other organ. Rupture of AVMs in brain, lung or liver results in serious consequences [93]. Jin et al. (2017) studied the molecular fundamentals of the endothelial *Eng* gene using murine loss and gain of function models [94]. Interestingly, ENG seems to regulate endothelial migration. Loss of function mutation of *Eng* caused defective migration of ECs during remodeling and thus lead to failure of arteriole establishment. In turn, gain of function mutation promoted the tip cell potential of ECs [94]. Recently, the compound thalidomide was used in pre-clinical and clinical trials where it showed a phenotypic mitigation of HHT [95]. Thalidomide stimulated *Pdgfb* expression in ECs, which leads to the attraction of MCs and improved stabilization of malformed vessels, bringing MCs into focus for HHT treatment.

Malformations of capillaries of the brain are formed in Cerebral Cavernous Malformations (CCMs). CCM is a rare vascular disease mostly triggered by mutations in CCM genes [96]. These vascular lesions are prone to leak due to thin-walled vessels. In addition, blood tends to clot within the lesions, thus leading to severe hemorrhagic strokes. CCMs were shown to be triggered by defective EC migration and the small GTPase CDC42 seems to interact with CCM proteins guiding the development of malformations [31,97]. So far, PCs were thought to be exclusively supportive in their function. However, a recent study revealed that PCs are indeed able to acquire disease promoting characteristics. MC specific deletion of the transcription factor *Rbpj* in mice activates MCs pathologically and promotes vascular lesions resembling CCMs [98].

Cerebral autosomal dominant arteriopathy with subcortical infarcts and leukoencephalopathy (CADASIL) is a further MC-related vascular disease linked to mutations in the *Notch3* gene [50]. Notch3 is involved in the recruitment and differentiation of MCs. A mouse model has shown that simultaneous *Notch1* and *Notch3* deletion recapitulates CADASIL phenotype in retinas [99]. It was shown that MCs seemingly do not differentiate properly, but the molecular mechanisms behind this phenotype remains elusive.

A disease promoting ability of PCs was also previously observed in a mouse model of retinopathy of prematurity (ROP), a pathology prominent in infants. A premature birth exposes the infants to relatively high oxygen concentrations too early, suppressing further growth of immature retinal blood vessels. Nevertheless, progressing maturation of retinal tissue causes severe hypoxia, promoting an uncontrolled angiogenic response and ultimately the formation of leaky clustered capillary loops, namely neovascular tufts (NVTs) [100]. PCs were shown to be pathologically activated during NVT formation, which further aggravates the formation of NVTs. Genetically, inhibition of PDGFB-driven PC migration Mitigation of this phenotype [46].

Even though not a primarily vascular disease, solid malign tumors highjack the cardiovascular system by secretion of proangiogenic factors to attract vessels. Tumors need to acquire a vascular network for further growth and thus engage in tumor neoangiogenesis. Antiangiogenic therapies therefore aim to inhibit this step to starve the tumor to death. After an initial success, this strategy unfortunately leads to resistance and increased aggressiveness of malign cells. Furthermore, the vasculature of tumors is often tortuous and leaky, providing entrance of metastasizing cells to the circulatory system [101]. New therapeutic approaches aim to normalize the vasculature in order to lower aggressiveness and metastatic behavior [102].

1.1.4 The murine retina as tool to study vascular development in health and disease

The developing mouse retina is one of the most investigated angiogenesis models. This has multiple reasons. First, mouse models are generally widespread animal model systems. Therefore, a wide range of genetic tools such as reporters, loss and gain of function models are available. In addition, the mouse retina is easily accessible and can be used for pharmacological treatments by intra-vitreous injections [103]. Moreover, it facilitates microscopic imaging due to its flat nature. Minimal working steps are needed for whole mount preparations. However, the most relevant reason for the use of retinas in angionesis research is that the retinal vasculature grows in a stereotypic fashion, simplifying the analysis and interpretation of vascular changes. The hallmarks of angiogenesis (sprouting, maturation and remodeling) are well recapitulated by this model.

Mice are born without a retinal vasculature. Blood supply of the inner eye and the lens is ensured by a temporal structure, namely the hyaloid vessels, which start to regress immediately after birth [65,104]. Retinal vessels arise by angiogenesis from the optic disc in the center of the retina and grow from there radially towards the edge of the retina guided by an astrocyte-originating VEGFA gradient. This results in the formation of the superficial plexus, comprised of a single vascular layer with alternating arteries and veins, connected by a capillary network (**Figure 1.4**) [105]. Completion of the superficial plexus takes place until postnatal day (P) 7-10. Afterwards at P10, ECs start to sprout vertically towards the outer retina and anastomose to a planar deep plexus, completed at around P17. This process is followed by backwards sprouting in order to form an intermediate plexus. During this time, the superficial plexus undergoes extensive remodeling and pruning of excessive vessels. Until the third postnatal week (P21), the development of the retinal vasculature is completed and consists of three planar vascular layers [106]. All these developmental steps are tightly controlled, making it a reliable and sensitive system which is well suited for imaging analyses.

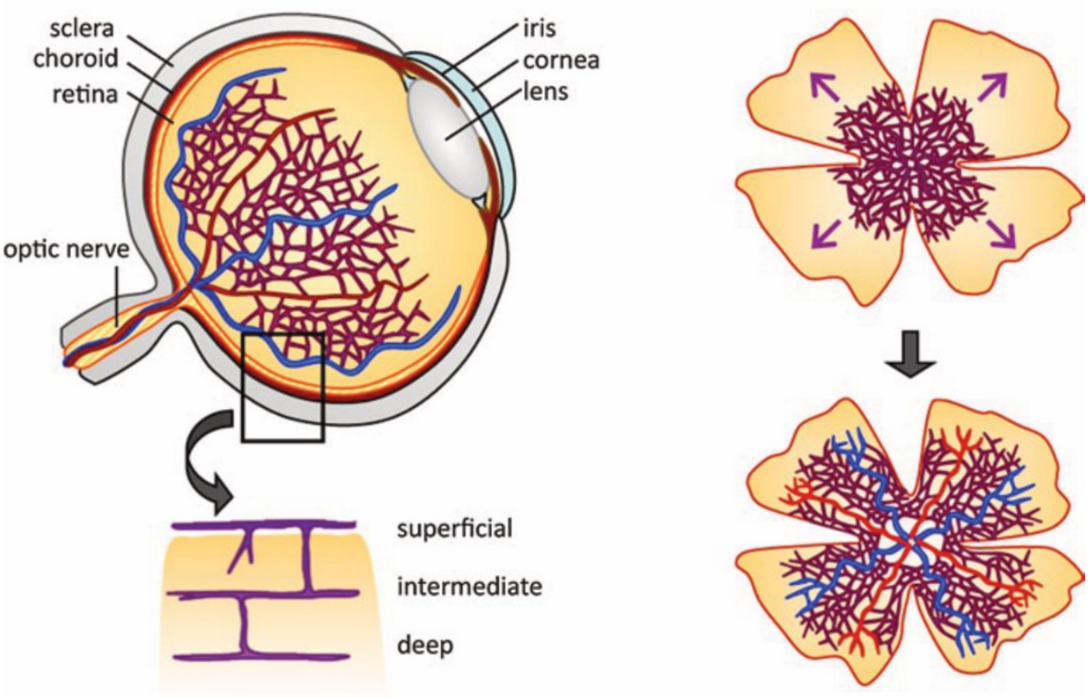

Figure 1.4 | Development of the murine retina. Left sagittal view on the postnatal eye and magnification on retinal vascular layers (left). Arterial and venous vessels are marked in red and blue, respectively. Vessels start to originate from the optic nerve and grow radially towards the lens. During the first 7-10 days of postnatal development, a superficial layer establishes consisting of alternating arteries, veins and capillaries in between (superficial plexus). Afterwards, superficial vessels grow vertically into deeper layers of the retinal tissue to form the deep plexus. Subsequently, the intermediate plexus is formed by backwards sprouting. The mature retina finally consists of three plexi, which can be analyzed upon preparation (right). Four incisions enable preparation of flat whole mounts which greatly facilitate microscopic analysis. Reprinted from Ruhrberg and Bautch, 2013 [107].

The mouse retina is also an excellent model for ischemic pathologies such as ROP. Especially the oxygen induced retinopathy (OIR) mouse model is frequently used. In this model, neonates at P7 are kept under hyperoxic conditions (75 % O_2) for 5 days, which leads to vessel regression due to the lack of hypoxia. After this initial high oxygen phase, neonates are transferred back to normoxic conditions (21 % O_2), leading to strong hypoxia caused by the lack in vessel infrastructure and finally causes an angiogenic response [108]. However, neovascularization at this stage is uncontrolled and results in the pathologic formation of NVTs. After 5 days back in normoxia, the NVT development reaches its peak at P17 and afterwards starts to resolve until approximately P25. The OIR model is therefore a powerful tool to study ischemic pathological vessel development and regression [109].

1.2 Serum response factor (SRF)

1.2.1 Cellular functions of SRF

The serum response factor (SRF) is a conserved, ubiquitously expressed transcription factor regulating a wide range of biological processes. It was identified to drive *c-fos* gene expression upon stimulation of cultured mouse fibroblasts with serum [110]. Since its discovery, a wide range of biological functions of SRF has been uncovered. *In vitro* studies mostly performed in fibroblasts identified the MAPK pathway as upstream activator of SRF, regulating immediate early gene response upon mitogen stimuli [111].

Initial *in vivo* studies found that SRF is activated early in development since its ablation leads to embryonal lethality due to a failure in mesoderm formation [112]. Later, a wealth of studies suggested functions of SRF in development and regeneration of the liver, in T- and B-cell activities of the immune system, in neurons of the developing brain and especially in the cardiovascular circuit [113]. Schratt et al. (2002) uncovered the essential role of SRF in the regulation of the actin skeleton assembly by the use of SRF-deficient embryonic stem cells (ES) and thereby showed the mediation of cell motility and migration by SRF [114]. Observed abnormalities such as defects in ES cell spreading, adhesion and migration were accompanied by defects in the actin cytoskeleton. The expression of essential parts of the cytoskeleton such as actin was dramatically reduced. Many previously observed phenotypes *in vivo* and *in vitro* could be at least partially explained by the SRF-mediated cytoskeletal impairments. It became increasingly clear that SRF is a master regulator of the cytoskeleton. More recent studies used chromatin immunoprecipitation in combination with sequencing (ChIP-Seq) and identified considerably more than 1000 SRF target genes, of which many belong to the cytoskeleton or are cytoskeletal regulators [115,116].

SRF belongs to the MADS box proteins, which bind to a consensus sequence *CC(A/T)*$_6$*GG* also known as CArG box. Interestingly, most SM specific genes, but also many cardiac and skeletal muscle specific genes, are under control of CArG-box elements. This makes SRF an important determinant of muscle gene expression. Indeed, postnatal *Srf* deletion in SMCs led to impaired contraction of intestinal SMCs which was apparent by defective peristalsis [117]. Cardiomyocyte-specific deletion of *Srf* leads to embryonal lethality due to cardiac defects, whereas its deletion in adult cardiac tissue results in a dilated cardiomyopathy, ultimately leading to death [118,119]. Dysfunctions in SRF-ablated skeletal tissue were also observed, as muscle cells failed in hyperthrophical growth after birth, resulting in perinatal death [120]. All of the here mentioned studies could partially be explained by a lack of muscle genes which mediate contractile behavior of muscle cells. Taken together, SRF is a critical determinant in the regulation of the immediate early response to convert mitogen stimuli to growth behavior. In addition, SRF drives expression of essential muscle genes important in differentiation and function of different classes of myocytes.

1.2.2 Regulation of SRF activation by ternary complex factors and the myocardin family

SRF target genes can be distinguished into two classes. Class I gene products belong to the immediate early response gene family and consist of proteins promoting cell cycle transition from G_0 to G_1. Prominent examples are c-FOS and EGR-1. In contrast, Class II genes consist of at least three groups. One group consists of muscle-specific and contractile gene products (e.g. αSMA, SM22α and MYL9). A second group encodes actin microfilament components (e.g. β-actin and Vinculin) and the third group encompasses genes responsible for motility (e.g. Rho GTPases) [113].

Due to the fact that SRF controls the expression of such a tremendous number of genes, one may ask the question how SRF enables the expression of specific functional gene sets in different cell types. Previous reports demonstrated that SRF is permanently bound to DNA but, surprisingly, cannot drive expression itself. Instead, SRF is dependent on different cofactors for activation [121]. Initially, the ternary complex factors (TCFs) were described as capable to associate with SRF in order to initiate expression [121]. Three TCF cofactors are known: Elk-1, Elk-3 and Elk-4 ,which belong to the large ETS family [122]. Interestingly, the additional DNA binding motif GGA(A/T), namely Ets motif, adjoining the CArG box is necessary for TCFs to establish a ternary complex with SRF [123]. Elk proteins are under control of MAPK signaling. Therefore, growth factors are in principle able to activate TCFs via ERK phosphorylation leading to expression of Class I genes [111].

Another report uncovered a TCF-independent activation of SRF by Rho-GTPases but could not identify a novel SRF partner protein [124]. Nevertheless, a bioinformatical screen identified the new cofactor myocardin, whose expression is restricted to the cardiovascular system [125]. Expression of a dominant negative version of myocardin or its downregulation in *Xenopus* embryos results in downregulation of cardiac-specific genes. Conversely, forced myocardin expression leads to ectopic expression of muscle genes [125,126]. Moreover, myocardin knockout mutant murine embryos die at embryonic day (E) 10.5 due to absent SMC development [127]. This reliably proved the importance of myocardin for muscle development. In order to drive CArG-box dependent muscle specific genes, myocardin forms a stable ternary complex with SRF. In *Srf* knockout mutant cells, myocardin has no transcriptional activity, proving its inability to act independently of SRF [128]. Interestingly, myocardin has been shown to compete with Elk-1 for SRF binding in order to modulate the cellular phenotype [129]. *In vitro* stimulation of SMC cultures with PDGFB activates Elk-1 phosphorylation via the MAPK pathway and consequently leads to repression of myocardin, favoring Class I gene set transcription. This mechanism allows a switch from a contractile SMC phenotype to a proliferative one.

Lastly, two more factors which belong to the myocardin family where identified, namely myocardin related transcription factor A and B (MRTFA/B) [128]. In contrast to myocardin, expression of MRTFA/B is not restricted to the cardiovascular system and at least low expression levels can be found in almost all tissues [128]. MRTFs share a large similarity to myocardin and can also bind SRF in order to establish a complex which initiates transcriptional activation of SRF targets [130]. Nevertheless, although they are able to initiate smooth muscle gene expression, they cannot fully compensate a loss of myocardin. This could potentially be explained by a relatively weak binding of MRTFs to SRF compared to myocardin [128]. Despite the high similarity between MRTFs, null mouse mutants display different phenotypes. MRTFA knockouts are viable and fertile. However, females fail to develop functional myoepithelial cells, which provide contractile force essential for milk secretion by the mammary glands. As a result, mothers fail to feed their offspring [131]. In contrast, MRTFB loss of function mutants, generated by expression of a dominant negative MRTFB version, display differentiation defects of SMCs derived from the neural crest and these mutants die perinatally. This genetic loss of function model however did not reach full penetrance [132]. MRTFB null mice display a similar but more dramatic phenotype of embryonal lethality at E13.5 with a striking reduction of the contractile protein αSMA [133]. These results suggest that MRTFA and MRTFB are only partially redundant in function. Therefore, all three members of the myocardin family are indeed unique in function. Overall, MRTFs seems to initiate SRF-guided expression of genes needed for the cytoskeletal apparatus as well as for the development of muscle cells.

In contrast to Myocardin, which is exclusively present in the nucleus of cells, MRTFs seem to shuttle between cytoplasm and nucleus. The finding that SRF can be regulated independent of TCFs by MRTFs provides the link between Rho-GTPase signaling and SRF [124]. MRTFs possess a RPEL motive that facilitates binding of globular actin (G-actin) which is ubiquitously available in the cytoplasm of a cell. Interestingly, the binding between both proteins leads to the retention of MRTFs in the cytoplasm. As Rho-GTPases are able to manipulate actin dynamics by setting an equilibrium between G-actin and filamentous actin (F-actin), the missing link between the Rho regulated SRF activation was identified [134]. Once F-actin is formed, the concentration of G-actin reduces, resulting in liberation of MRTFs. This leads to nuclear import of MRTFs and to subsequent association with SRF in order to drive expression of Class II genes.

Moreover, recent evidence suggested that actin structures are also formed in the nucleus, deciding about nuclear persistence of MRTFs and their association to SRF [135]. In addition, formin-dependent F-actin formation is able to lower nuclear G-actin concentrations, which likely favors nuclear persistence of MRTFs [136]. More recent reports supported this paradigm and described the nuclear envelope proteins lamins A/C as well as the atypical actin-binding protein MICAL-2 as regulators of nuclear actin [137,138]. Taken together, the mentioned reports provide evidence that the Rho-actin-MRTF-SRF signaling cascade is, in addition to muscle gene regulation, capable to act as mechanosensitive pathway, which enables the cell to reliably react to environmental changes.

Of note, competition between TCFs and MRTFs was recently observed [116,129]. Using mouse embryonic fibroblasts (MEFs), it was shown that deletion of TCFs progressively promoted a hypercontractile and pro-invasive phenotype accompanied by antagonization of a proliferative phenotype [116]. This suggests that an equilibrium between TCFs and MRTFs is maintained by extracellular stimuli in order to sustain physiological cell functions (**Figure 1.5**).

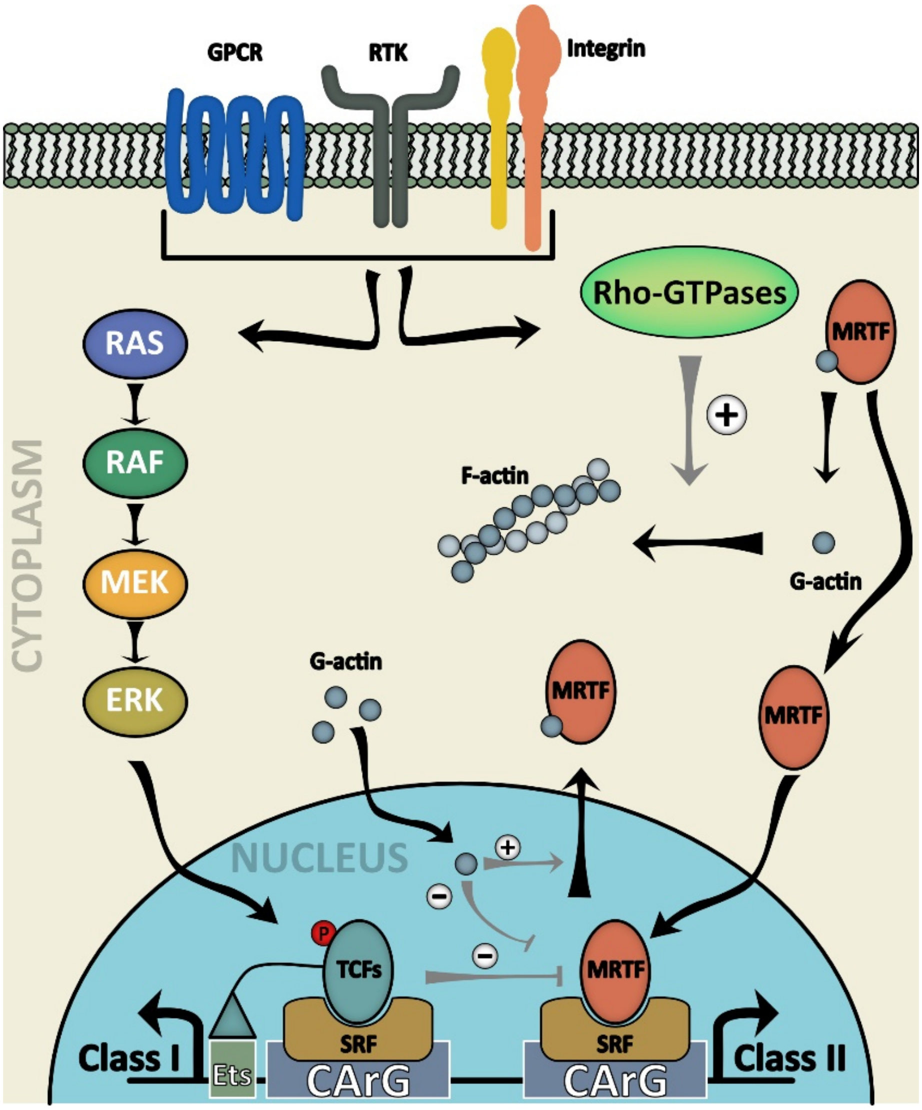

Figure 1.5 | Regulation of SRF activation via MAPK and Rho/actin signaling. SRF can be activated by a multitude of upstream signaling pathways, e.g. through G-protein coupled receptors (GPCR), receptor tyrosin kinases (RTKs) and integrins. Activation of RTKs usually activate MAPK-signaling leading to ERK activation and finally to activation of the ternary complex factors (TCFs, ELK- 1, or ELK -3 or ELK-4) via a phosphorylation cascade (left). TCFs induce expression of Class I genes involved in proliferation. RTKs can also activate Rho-GTPases which polymerize G-actin units into F-actin fibers (right). MRTFs bind G-actin, which leads to masking of the nuclear import sequence, thereby holding them in the cytoplasm. Upon G-actin to F-actin polymerization the intracellular G-actin concentration decreases, leading to unmasking of MRTFs and nuclear translocation. In the nucleus, MRTFs activate Class II gene expression. Class II gene products are usually involved in cytoskeletal and motile functions. Nuclear actin additionally fine-tunes MRTF activation. Moreover, TCFs compete with MRTFs about SRF binding to switch the expression equilibrium towards Class I gene expression.

1.2.3 The MRTF-SRF pathway controls sprouting angiogenesis

Cumulative evidence also suggests an essential role of SRF in angiogenesis. First indications have been observed by stimulation of EC cultures with VEGF. VEGF stimulation remarkably led to stress fiber formation and activated *Srf* expression, which led to initiation of *in vitro* angiogenesis [139]. Moreover, reduction of stress fiber formation by knockdown of SRF or by pharmacological intervention of Rho-GTPases blocked VEGF-induced *in vitro* angiogenesis. Interestingly, VEGF-activated *in vitro* angiogenesis led, besides Rho-actin activation, also to MAPK activation. This study therefore suggested that SRF is a downstream target of VEGF-mediated angiogenesis. Another study investigated the role of SRF in angiogenesis by the generation of murine EC-specific *Srf*-null mutants and found a dramatic effect on the vascular circuit [140]. Knockout of endothelial *Srf* resulted in hemorrhages that started to arise at E9.5 and ended in embryonal lethality at E14.5. This study also revealed that SRF is highly expressed by both, endothelial tip cells and stalk cells. However, SRF appeared to be dispensable for tip cell or stalk cell induction, as the ratio of tip cells to stalk cells was unaffected in the absence of SRF. Whereas the induction of tip cell and stalk cell behavior was not unaffected, a strong morphologic change of tip cells was observed, which was explained by a disruption of cytoskeletal dynamics. Of note, retinal angiogenesis was also highly affected by ablation of endothelial *Srf* [29,30]. Endothelial *Srf*-null mutants displayed drastic hypo-vascularization, apparent by incomplete formation of the primary plexus as well as the absence of the intermediate and deep plexus. Moreover, filopodia formation of tip cells was strongly reduced and those which formed were morphologically stunned. Inability of sprouting was additionally apparent by the formation of microaneurisms and by the downregulation of vascular integrity genes such as VE-Cadherin [29]. Interestingly, the endothelial *Srf*-null phenotype was phenocopied by endothelial knockout of both MRTFs, but not by simultaneous knockout of the TCF factors *Elk1* and *Elk4* [29]. An additional study ablated endothelial *Elk3* and found an only mild and transient angiogenic phenotype [141]. This strongly suggested that VEGF-mediated angiogenesis is regulated by the MRTF-SRF signaling axis, which is essential for remodeling the endothelial actin cytoskeleton needed for tip cell formation and migration. Lastly, the endothelial MRTFA-SRF axis was also shown to induce expression of *Ccn1* and *Ccn2*, which encode regulators of endothelial migration and attraction of MCs during angiogenesis [142].

1.2.4 SRF in disease

As SRF compiles a multitude of external signaling cues and translates them into altered gene expression responses, it is not surprising that dysfunctionality regularly results in disease. During pathologic remodeling of the heart, dysregulation of SRF target genes was observed. Expression profiling in human dilated cardiomyopathy revealed increased myocardin levels [143]. Moreover, elevated levels of myocardin were shown to aggravate cardiomyocyte hypertrophy, whereas blockade of myocardin attenuated this phenotype [144]. In contrast to the mentioned observations, a dominant negative version of SRF (SRF-N) was detected in human heart-failure samples [145]. SRF-N was identified as a product of sequential Caspase-3 cleavage. The lack of functional SRF led to reduced levels of cardiac-specific genes and therefore favored heart-failure. These studies showed that both, increased and decreased SRF activity, can result in pathologic changes of the heart.

Alterations of SRF signaling were also observed in other diseases. Aortic vessel stiffness is a fundamental manifestation of hypertension and SMCs are thought to be involved in this process. Zhou et al. (2017) used a rat hypertension model and revealed that stiffening of SMCs was accompanied by upregulation of SRF and myocardin [146]. Of note, pharmacological inhibition of myocardin in this hypertension rat model system reduced SMC stiffness.

Pathologic alterations were also observed in the brain tissue upon postnatal, endothelial *Srf* deletion in mice [147]. Mutant mice suffered from disintegration of the BBB, apparent by cerebral microbleeds and larger hemorrhages. The observed phenotype was linked with downregulation of genes which encode vital structural parts of the BBB such as tight and adherence junctions as well as BM proteins. As the risk of intracerebral hemorrhages dramatically rises with age, it would be attractive to study the age-depend effect of endothelial and mural SRF on stability of the BBB [148].

As SRF is downstream of MAPK and Rho/actin signaling, SRF was also suggested to take part in neoplastic processes. In fact, infant acute megakaryoblastic leukemia (AMKL) was shown to correlate with a chromosomal modification of the MRTFA gene (*Mkl1,* also called *MAL*). In this case, *MAL* is genomically fused with the *OTT* (also known as RBM15) gene, leading to expression of the OTT-MAL fusion protein, which is constitutively located in the nucleus and not controlled by G-actin levels anymore [149]. OTT-MAL is able to activate the transcription factor RBP-Jκ downstream of Notch signaling, and thus causes megakaryopoiesis [150]. Furthermore, elevated Rho/actin signaling associated with nuclear localization of MRTFs was previously observed in hepatocellular carcinoma (HCC), leading to the idea that SRF activation could drive neoplasia [151]. A recent study used a murine HCC model expressing a constitutively active version of SRF, namely SRF-VP16, in hepatocytes. Stochastic activation of SRF-VP16 was found to give rise to hyperproliferative nodules in the liver, which ultimately resulted in the development of HCC [152]. The mentioned studies underline the importance of understanding SRF signaling in disease.

1.3 Aims

MCs, comprised of PCs and SMCs, were shown to contribute to a multitude of physiological but also pathological processes. MCs are thought to maintain the morphologic shape of the vasculature and dysfunctionality of MCs is often associated with cardiovascular pathologies. Despite the physiological importance of MCs, our knowledge about this cell type is limited. This likely rests in the fact that vascular research was so far strongly focused on ECs. However, it has become clear that MCs play a much more active role in vessel maintenance than previously thought. In addition, the definition of MCs, especially the separation into PCs and SMCs, is very challenging and is seriously debated in the field.

In contrast, the transcription factor SRF was studied extensively in the last decades, leading to description of SRF as master regulator of cytoskeletal functions. Nevertheless, many SRF studies were exclusively performed *in vitro*, and therefore neglected the crosstalk between different cell types *in vivo*. Yet, the function of SRF in MCs of the CNS has so far not been investigated. Since SRF controls SMC identity and also motile functions in other cell types, it is important to understand how SRF influences SMCs in the CNS. Moreover, it is also crucial to investigate, which role SRF plays in the classification of SMCs and PCs and whether SRF executes distinct functions in either cell type.

Therefore, this study aims to investigate the function of SRF in MCs to unravel potential new physiological and pathological roles of MCs in angiogenesis and vascular quiescence. To do so, the novel CreER^{T2} mouse line named Pdgfrb(BAC)-CreER^{T2} was bred with the *Srf*-floxed (Srf-flex1) mouse line to induce postnatal *Srf* deletion specifically in MCs. As a model system to investigate the effects of the *Srf*-knockout in MCs of the CNS, the murine retina angiogenesis model was chosen. Due to its stereotypic vascular growth, it enables the classifications of both, PCs and SMCs. The impact of mural *Srf* deletion was studied at different developmental stages. In early phase angiogenesis, PCs on immature vessels can be studied as main MC type, whereas in later developmental stages SMCs and PCs can be studied simultaneously.

Furthermore, complementary *in vitro* analyses were carried out on primary cultured brain MCs (pBMCs) to support the animal studies. The use of pBMCs allowed additional investigation of isolated processes such as migration and reaction to external stimuli.

Taken together, this study aims to investigate SRF functions in PCs and SMCs of the CNS in order to broaden our knowledge of vascular biology. This study therefore aims at a better understanding of the molecular processes underlying cardiovascular pathologies.

Chapter 2

2 Material and Methods

2.1 Materials

2.1.1 Animal models

2.1.1.1 Pdgfrb-driven Cre/loxP ablation of Srf in mural cells

For efficient deletion of the *Srf* allele in mural cells, the Cre/loxP-system was used. The Cre protein is a bacteriophage P1 based recombinase, which specifically recognizes so called loxP sites, which consist of two 13 bp recognition sites and an 8 bp linker in between [153,154]. If a sequence is flanked by two loxP sites (floxed), recombination of this sequence is catalyzed by Cre [154]. Depending on the loxP site orientation, Cre induce an excision, inversion or translocation of the flanked sequences. Fusion of Cre with the estrogen receptor containing a mutated ligand binding domain, enables a time controlled Cre recombination upon administration of tamoxifen [155].

In this study, *Pdgfrb(BAC)-CreER*^{T2} mice were used [81]. They express CreER^{T2} recombinase under the control of a large murine *Pdgfrb* genomic BAC clone [81,156]. *Pdgfrb* is mainly expressed by mural cells, thus allowing tissue specific gene targeting specifically in mural cells [74]. *Pdgfrb(BAC)-CreER*^{T2} mice were generated and kindly provided by Ralf Adams (Max-Planck Institute for molecular biomedicine, Münster, Germany).

Pdgfrb(BAC)-CreERT2 mice were bred with *Srf-flex1* micecarrying a floxed exon 1 (*flex1*) of the *Srf* gene to obtain *Pdgfrb-CreERT2::Srf-flex1* mice [157]. Postnatal administration of tamoxifen in these mice lead to excision of exon 1 and thus to disruption of the *Srf* gene in mural cells. For some experiments, the *Rosa*^{mTmG} reporter gene was crossed into *Pdgfrb-CreERT2::Srf-flex1* lines [158]. The *Rosa*^{mTmG} reporter expresses the fluorogenic and membrane targeted tdTomato protein under the chicken β-actin core with a CMV enhancer promotor (pCA). Downstream of tdTomato a stop cassette followed by an *eGFP* cassette is located. tdTomato and the stop cassette are flanked by loxP sites, causing a switch from tdTomato to eGFP expression upon Cre mediated recombination. This allows for specific fluorescent labeling of *Srf*-recombined cells.

2.1.2 Mouse lines

Table 1 | List of mouse lines used, comprising official name and generator.

Mouse line	**Symbol**	**Information**	**Source**
C57BL/6N	*Genetic background of all used mice (Jacksons laboratory)*		
Srf-flex1	$\text{Srf}^{\text{tm2.1Nor}}$	*Srf*-floxed exon 1	Alfred Nordheim [157]
Pdgfrβ(BAC)-CreER^{T2}	Tg(Pdgfrb-cre/ERT2)6096Rha	MC specific CreER^{T2} line	Ralf H. Adams [81]
Rosa^{mTmG}	$\text{Gt(ROSA)26Sor}^{\text{tm4(ACTB-tdTomato,-EGFP)Luo}}$	Cre-driven GFP reporter line	Liqun Luo [158]

2.1.3 Primary cells and Cell lines

Table 2 | List of primary cells and cell lines used.

Name	**Mouse line**	**Additional information**
pBMCs	*C57BL/6N*	Wild-type primary brain mural cells (pBMCs)
Srf-flex1 pBMCs	*Srf-flex1*	Homozygous floxed exon 1
Srf-flex1/mTmG pBMCs	*Srf-flex1::Rosa*^{mTmG}	pBMCs with homozygous *Srf*- floxed exon 1 and hemizygous *Rosa*^{mTmG} reporter allele
NIH 3T3	NIH/Swiss	Mouse embryo fibroblast (ATCC CRL-1658)
NIH 3T3-Mal-GFP	NIH/Swiss	Express MRTFA-GFP fusion protein. Gifted from Richard Treisman (The Francis Crick Institute, London, UK)[135]

2.1.4 Antibodies

Table 3 | List of Antibodies/staining reagents used, their source and dilutions used.

Antigen/staining reagent	Source, clone/number	Company	Dilution
NG2	Rabbit, AB5320	Millipore	1:100
CD13	Rat, MCA2183EL	Bio-Rad	1:200
CD140a-FITC	Rat, APA5, 11-1401-82	Invitrogen by Thermo Fisher Scientific	1:100
CD140b-APC	Rat, APB5, 17-1402-82	Invitrogen by Thermo Fisher Scientific	1:25
CD144	Rat, 11D4.1 ,555289	BD Biosciences	1:100
CD31	Goat,AF3628	R&D Systems	1:400
CD31-PE	Rat, 390, 102408	Biolegend	1:50
CD45-PB	Rat, 30F-11, 103126	Biolegend	1:200
ColIV	Rabbit, 2150-1470	Bio-Rad	1:200
Desmin	Rabbit, ab15200	Abcam	1:200
ERG1	Rabbit, ab110639	Abcam	1:100
GFP-Alexa Fluor 488	Rabbit, A21311	Invitrogen by Thermo Fisher Scientific	1:200
ICAM-2	Rat,553326	BD Pharmigen	1:200
Isolectin B4	Bandeiraea simplicifolia	Sigma-Aldrich	1:25
PDGFRβ	Goat, AF1042,	R&D Systems	1:100
SiR-actin	SC001	Spirochrome	1:1000-1:3000
SMA-Cy3	Mouse,C6198, 1A4	Sigma-Aldrich	1:300
SRF	Rabbit, D71A9,5147S	Cell Signaling Technology	1:500
SRF	Rat, 2C5.11	Alfred Nordheim	1:10
Streptavidin Alexa Fluor-400	S32351	Invitrogen by Thermo Fisher Scientific	1:100
Streptavidin Alexa Fluor-488	S11223	Invitrogen by Thermo Fisher Scientific	1:100
Ter119	Rat,TER-199,553671	BD Biosciences	1:200
Ter119-PB	Rat, TER-119, 116232	Biolegend	1:200

α rat Alexa Fluor-488	Donkey, A21208	Invitrogen by Thermo Fisher Scientific	1:500-1:1000
α-goat Alexa Fluor-488	Donkey, A32814	Invitrogen by Thermo Fisher Scientific	1:500-1:1000
α-goat Alexa Fluor-647	Donkey, A21447	Invitrogen by Thermo Fisher Scientific	1:500-1:1000
α-rab Alexa Fluor-488	Donkey, A21206	Invitrogen by Thermo Fisher Scientific	1:500-1:1000
α-rab Alexa Fluor-568	Donkey, A10042	Invitrogen by Thermo Fisher Scientific	1:500-1:1000
α-rab Alexa Fluor-647	Goat, A21244	Invitrogen by Thermo Fisher Scientific	1:500-1:1000
α-rat Alexa Fluor-647	Chicken, A21472	Invitrogen by Thermo Fisher Scientific	1:500-1:1000

2.1.5 Primers

Table 4 | List of primers used and their sequences. All primers were obtained from Sigma-Aldrich.

Primer	Name	Sequence (5’ → 3’)
Actin forward	Actb_fw	CGCGAGCACAGCTTCTTT
Actin reverse	Actb_rev	TCCTTCTGACCCATTCCCAC
Cspg4 forward	NG2_fw	TCCAGTTCTCCACATCCCAG
Cspg4 reverse	NG2_rev	TTAGCTCCTTCTGTCCCAGG
Egr1 forward	Egr1_fw	GAGCACCTGACCACAGAGTC
Egr1 reverse	Egr1_rev	GAGTCGTTTGGCTGGGATAAC
Fos forward	Fos_fw	GCTTTCCCCAAACTTCGACC
Fos reverse	Fos_rev	TTGGCACTAGAGACGGACAG
Gusb forward	Gusb-f	GATGCTGTTCCCGAAGGAGAG
Gusb reverse	Gusb-r	ATTGCTTCCCGTTCATACCACA
Myh11 forward	Myh11_fw	CTGAGGGAGCGATACTTCTCA
Myh11 reverse	Myh11_re	ATGCTTCTGTAGGCTGTGTC
Pdgfrb-Cre genotyping	Pdgfrb_Cre1	GAACTGTCACCGGGAGGA
Pdgfrb-Cre	Pdgfrb_Cre2	AGGCAAATTTTGGTGTACGG
Pdgfrb-Cre genotyping	Pdgfrb_Cre3	CAAATGTTGCTTGTCTGGTG
Pdgfrb-Cre genotyping	Pdgfrb_Cre4	GTCAGTCGAGTGCACAGTTT
Pdgfrβ forward	Pdgfrb_fw	ACAACAACTCACTAGGGCCG
Pdgfrβ reverse	Pdgfrb_rev	GTCACTCGGCACGGAATTG
Rosa26^{mTmG} genotyping	7318	CTCTGCTGCCTCCTGGCTTCT
Rosa26^{mTmG} genotyping	7319	CGAGGCGGATCACAAGCAATA
Rosa26^{mTmG} genotyping	7320	TCAATGGGCGGGGGTCGTT
Sm22a forward	Tagln	CCAGACACCGAAGCTACTCT
Sm22a forward	Tagln	ATTCTTCAGCCACACCTGGA
Srf forward	Tm_SRF1_fw	CACGACCTTCAGCAAGAGGAA
Srf reverse	Tm_SRF2_bw	CAAAGCCAGTGGCACTCATTC
Srf-flex1 genotyping	AW-mads	AGTTCATCGACAACAAGCTGCGG
Srf-flex1 genotyping	BW-3pri	GAGATTTCCACAGAAAGCAACGG
Tbp forward	TBP_f	TTCATGGTGTGTGAAGATAACCC
Tbp reverse	TBP_r	AGAGAGACTGTTGGTGTTCTGA
αSma forward	SMA_fw	GAGCGTGAGATTGTCCGTG
αSma reverse	SMA_rev	TAGGTGGTTTCGTGGATGCC

2.1.6 Vectors

Table 5 | List of vectors used, their sources and experiments in which they were used.

Vector	Generator/Source	Experiment
pTat-Cre	Steven Dowdy	Tat-Cre isolation [159]
(TSM)$_2$	Alfred Nordheim	SRF luciferase reporter-assay [29]
(TMM)$_2$	Alfred Nordheim	SRF luciferase reporter-assay [29]
(MSM)$_2$	Alfred Nordheim	SRF luciferase reporter-assay [29]

2.1.7 Chemicals

Table 6 | List of used chemicals and their sources.

Chemical	**Company**
2-(N-morpholine)-ethane sulfonic acid (MES)	AppliChem
5-Ethynyl-2´-deoxyuridine	Sigma-Aldrich
Acrylamide solution (40 %)	AppliChem PanReac
Albumin Fraction V (BSA)	AppliChem PanReac
Ammonium persulfate (APS)	AppliChem
Bromodeoxyuridine	Sigma-Aldrich
Bromophenol Blue	BIO-RAD
CCG-203971	Sigma-Aldrich
Chloramphenicol	AppliChem
Chloroform (RNase-free)	Honeywell
cOmplete Mini Protease Inhibitor Cocktail	Sigma-Aldrich
Coomassie Brilliant Blue G-250	AppliChem
Diamidino-2-phenylindole (DAPI)	unknown
Dimethyl Sulfoxide (DMSO)	AppliChem PanReac
Ethanol	Sigma-Aldrich
Ethanol (RNase-free)	Sigma-Aldrich
Fluoromount-G	SouthernBiotech
Gelatin (from porcine skin)	Sigma-Aldrich
Glycerol anhydrous	AppliChem PanReac
HEPES	AppliChem PanReac
Hydrochloric acid (2 M HCl)	AppliChem
Imidazole	Merck
Indocyanine green	PULSION Medical Systems AG
Isopropanol	Merck
Isopropanol (RNase-free)	Fisher Chemical
Isopropyl β-D-1-thiogalactopyranoside (IPTG)	AppliChem
Kanamycin Sulfate	AppliChem
Ketamine	Pfizer
LB Agar (Lennox)	Roth
LB Medium, Powder	SERVA
Methanol	Sigma-Aldrich
Milk powder (nonfat dried)	AppliChem PanReac
Mydriaticum Stulln (Tropicamide)	Pharma Stulln
Paraformaldehyde (PFA)	AppliChem
PD-0325901	Sigma-Aldrich
Peanut oil	Sigma-Aldrich
Sodium chloride (NaCl)	Sigma-Aldrich
Sodium dodecyl sulfate (SDS ultrapure)	AppliChem PanReac
Sodium hydroxide (NaOH)	Merck
Sulfuric acid (H_2SO_4)	AppliChem
Tamoxifen	Sigma-Aldrich
Technical Oxygene	Westfalen Gas
TEMED	AppliChem
Trichloroacetic acid (TCA)	AppliChem
TritonX-100	AppliChem

Trizma base (Tris)	Sigma-Aldrich
Trizma hydrochloride (Tris-HCl)	Sigma-Aldrich
Trypan Blue	Fluka AG
Tween 20	AppliChem PanReac
Xylazine	Sigma-Aldrich
β-Mercaptoethanol	AppliChem PanReac

2.1.8 Buffers

Table 7 | Buffers used, their compositions and the methods in which they were used.

Buffer	Composition	Method
Binding buffer	500 mM NaCl, 20 mM Tris, 5 mM imidazole in H_2O, pH 7.4	TAT-Cre purification
Blocking buffer	1 % BSA, 0.3 % TritonX-100 in PBS, pH 7.4	Immunostaining Retina
Blocking buffer	1 % BSA, 10 % donkey serum, 0.1 % TritonX-100 in PBS	Immunostaining cryo sections
Blocking buffer	2 % BSA in PBS, pH 7.4	Immunostaining of cell cultures
Blocking buffer	5 % nonfat died milk in TBST, pH 7.4	Western blot
Cacodylate buffer	0.1 M $Na(CH_3)_2AsO_2*3H_2O$, in H_2O, pH 7.2	Electron microscopy
Dialysis buffer	1.36 M glycerol, 250 mM HEPES, 500 mM NaCl in H_2O pH 7.4	TAT-Cre purification
Dissection media	10 % FCS, 1 % penicillin/streptomycin, 25 mM HEPES in DMEM, pH 7.4	FACS
Elution buffer	500 mM NaCl, 20 mM Tris, 250 mM imidazole in H_2O pH 7.4	TAT-Cre purification
FACS buffer	2 % FCS (heat inactivated), 2 mM EDTA pH 8.0, 25 mM HEPES in phenol free DMEM	FACS
Homogenization buffer	300 mM NaCl, 20 mM Tris, 10 mM imidazole in H_2O, pH 7.4	TAT-Cre purification
Lower Tris buffer	1.5 M Tris-HCl, 0.4 % SDS in H_2O, pH 8.8	SDS-PAGE
MES buffer	20 mM MES, 100 mM NaCl in H_2O pH 5.0	TAT-Cre purification
Pblec	$MgCl_2$, $CaCl_2$, $MnCl_2$, 0.5 % TritonX-100 in PBS , pH 7.4	Immunostaining
PBST	0.1 % TritonX-100 in PBS , pH 7.4	Immunostaining
PCR buffer (10x)	500 mM KCl, 15 mM $MgCl_2$, 0.1 % Tween-20, 100 mM Tris, pH 8.8	Genotyping
Phosphate buffered saline (PBS)	137 mM NaCl, 2.7 mM KCl, 10 mM Na_2HPO_4, 1.8 mM KH_2PO_4 in H_2O, pH 7.4	Universal
Phosphate buffer (PB)	75.4 mM Na_2HPO_4 , 24.6 mM NaH_2PO_4 in H_2O, pH 7.4	Universal
Radioimmunoprecipitation assay buffer (RIPA)	50 mM Tris-HCl, 150 mM NaCl, 1 % TritonX-100, 0.5 % Sodium deoxycholate, 0.1 % SDS, 1 mM EDTA, pH 8.0	Western blot
Sample buffer (6x)	263 mM Tris-HCl, 5.76 M glycerol, 300 mM SDS, 600 mM β-mercaptoethanol, 1.4 µM bromophenol blue in H_2O, pH 6.3	SDS-PAGE
SDS running buffer	192 mM glycin, 25 mM Tris, 0.1 % SDS in H_2O, pH 8.3	SDS-PAGE
Tail lysis buffer	0.1 M Tris-HCl, 5 mM EDTA, 0.2% SDS, 200 mM NaCl, pH 8.3	Genotyping
TBS (10x)	1.38 M NaCl, 200 mM Tris in H_2O, pH 7.6	Western blot

TBST	1x TBS, 0.1 % Tween-20, pH 7.4	Western blot
Towbin	192 mM glycin, 25 mM Tris, 0.04% SDS, 20 % methanol , pH 7.4	Western blot
Upper Tris buffer	500 mM Tris-HCl, 0.4 % SDS, pH 6.3	SDS-PAGE
Wash buffer	300 mM NaCl, 20 mM Tris, 20 mM imidazole, pH 7.4	TAT-Cre purification

2.1.9 Microbiological media

Table 8 | Used microbiological media and their compositions.

Media	Composition
Luria Bertani Broth (LB)	10 g/L tryptone, 5 g/L yeast extract, 5 g/L NaCl, (for plates + 20 g/L Agar)
Terrific Broth (TB)	23.6 g/L Yeast Extract, 11.8 g/L Tryptone, 9.4 g/L K_2HPO_4, 2.2 g/L KH_2PO_4, 4 ml/L Glycerol

2.1.10 Reagents

Table 9 | Used reagents, their sources and the methods in which they were used.

Reagent	Company	Method
Color Prestained Protein Standard (Broad Range)	New England Biolabs	SDS-PAGE
dNTPs 100mM	GENAXXON bioscience	Genotyping
Donkey Serum	Sigma-Aldrich	Immunostaining
FastStart Universal SYBR Green Master (ROX) (2x conc.)	Roche	qPCR
Glycogen (RNA grade, 20 mg/ml)	Thermo Scientific	RNA isolation
HisPur™ Cobalt Resin	Thermo Scientific	TAT-Cre purification
Midori Green	Nippon Genetics Europe	Gel-electrophorese
miScript Nucleics Mix (10x)	QIAGEN	Reverse transcription
M-MLV RT (H–), Point Mutant (along with 5x Reaction Buffer)	Promega	Reverse transcription
Prestained Protein Ladder (PageRuler)	Thermo Scientific	SDS-PAGE
Proteinase K	GENAXXON bioscience	Genotyping
Random Hexamer Primer N6	GENAXXON bioscience	Reverse transcription
RiboLock RNase Inhibitor (40 U/µL)	Thermo Scientific	Reverse transcription
Roti-Quant (Bradford reagent)	Roth	Bradford assay
TaqMan fast advanced master mix	Applied Biosystems	qPCR
TRIzol Reagent	life technologies	Retina RNA isolation

2.1.11 Cell culture reagents

Table 10 | List of used cell culture reagents, their details and source.

Reagent	Details	Company
Collagen Type 1	Rat Tail High Concentration, 9.41 mg/ml	Corning
DMEM	Dulbecco's Modified Eagle Medium supplements: 10 % FCS and 1 % Pen/Strep	Gibco
EBM-2	Endothelial Cell Basal Medium-2	Lonza
FCS	Fetal Calf/Bovine Serum	Gibco
Gelatine	0.4 % in ddH$_2$O	Sigma-Aldrich
MEM	Minimum Essential Medium Eagle	Sigma-Aldrich
Opti-MEM™ I	Opti-MEM™ I Reduced Serum Media	Gibco
PBS	Dulbecco's Phosphate Buffered Saline	Sigma-Aldrich
PDGFBB	Platelet-Derived Growth Factor-BB human	Sigma-Aldrich
Pen/Strep	Penicillin Streptomycin	Gibco
PM	Pericyte Medium, supplements: 2 % FBS, 1x pericyte growth supplement, 1x Pen Strep	ScienCell
Trypsin-EDTA	0.05 % Trypsin-EDTA	Sigma-Aldrich

2.1.12 Kits

Table 11 | List of used kits, their source and the method in which they were used.

Kit	Company	Method
Click-iT EdU Cell Proliferation Kit	invitrogen (Thermo Scientific)	*In vivo* proliferation
DNA-free™ DNA Removal Kit	invitrogen (Thermo Scientific)	Retina RNA purification
Immobilon Western HRP Substrate	Merck Millipore	Western blot
Single Cell/Low Input RNA Library Prep Kit	New England Biolabs	RNA-Seq
TransIT-LT1	Mirus Bio	Transfection
Dual-Luciferase Reporter Assay	Promega	Luciferase assay
Papain Dissociation System	Worthington Biochemical Corporation	Cell dissociation in pBPCs isolation
Qubit™ RNA BR (Broad-Range) Assay Kit	life technologies (Thermo Scientific)	RNA concentration
RNeasy Micro Kit	QIAGEN	RNA isolation of pBPCs

2.1.13 Technical equipment

Table 12 | List of used instruments, their sources and further details.

Instrument	Company	Details/Equipment
Axiozoom	Zeiss	
BD FACS Aria lllu sorter	BD Biosciences	Light source: violet laser 402 nm, blue laser at 488 nm, yellow/green laser at 561 nm, red laser at 640 nm Nozzle: 100 µm
Biospherix OIR chamber A	Biospherix	ProOx P110 O_2 detector
Espion V6	Diagnosys LLC	N/A
EM10A electron microscope	Zeiss	N/A
Gel Documentation Systems	Axigen	Exication WL: 302 nm and 365 nm
HM525 NX	Thermo Scientific	N/A
Illumina E6420L sequencer	New England Biolabs	N/A
LSM800 (confocal microscope)	Zeiss	Objectives: PApo 10x/0.45; Plan-Neofluar 20x/0.5; C-Apochromat 40x/ 1.2 water FCS; Plan-Apochromat 63x/1.4 oil DIC Light-source/detector: Lasermodule LM URGB, GaAsp-PMT detectors, Airyscan module
OCT Spectralis	Heidelberg Engineering	Light source: Superluminescent diode at 870 nm
Olympus (confocal microscope)	Olympus	Objectives: UPlanSApo 10x/ 0.4; UPlanSApo 20x/ 0.75; : UPlanSApo 40x/ 0.95; UPlanSApo 60x/ 1.2 water Light-source (laser)/detector: DPSS (405 nm), Argon (488 nm/515 nm), DPSS (635 nm), GaAsp-PMT detectors
OPTIMA FluoroSTAR	BMG LABTECH	N/A
PolyTron tissue homogenizator	Kinematica AG	Model: PolyTron PT-MR-2100
Quantstudio 7 flex	Applied Biosystems	N/A
Ultracut ultramicrotome	Leica	N/A

2.1.14 Software

Table 13 | List of Software used, their versions and developer/source.

Program	Version	Developer/Source
Affinity suite	1.8.4	Serif Europe Ltd.
Arivis Vision4D	3.3	arivis AG
Axiozoom	V16	Zeiss
Eye Explorer	5.3.3.0	Heidelberg Engineering
Fusion FX	V.070	Vilber
GraphPad Prism	8.0.2	Graphpad
GSEA	4.0.3	The Broad Institute
ImageJ (Fiji)	1.52p	Schindelin et al. 2012 [160]
Microsoft Office	2016	Microsoft
OPTIMA	2.20	BMG LABTECH
Quant Studio	1.3	Applied Biosystems
R	4.0.0	The R foundation for statistical computing

2.2 Methods

2.2.1 Mouse techniques

2.2.1.1 Breeding

Mice were kept in the animal facilities of the Interfaculty Institute for Cell Biology (IFIZ) of the University of Tuebingen under the national guidelines for research animal housing GV-SOLAS. Mice were held in type 2 long polycarbonate cages in groups of 2-5 animals per cage. Conditions were a 12 h day/night cycle, a relative humidity of 60 % and a temperature of 21 °C. New litters were weaned 3 weeks after birth and separated into new cages.

All animal experiments carried out in this work were performed in compliance with the with the relevant laws and guide lines of that apply to the University of Tuebingen. Conducted animal experiments were approved by the local animal ethics committee and conducted with the permission by the regional authorities in Tuebingen (Regierungspraesidium Tuebingen), Germany (IM05/18G and IM02/19G).

2.2.1.2 Genotyping

To genotype new litters of breeding couples, ear marks were taken after weaning. Ear marks were lysed in 100 µl of tail lysis supplemented with 0.2 mg/ml proteinase K buffer over night at 55 °C in an Eppendorf thermomixer at 400 rpm. To inactivate remaining proteinase K activity, samples were incubated at 99 °C for 10 min. Samples were subsequently cooled down and stored at -20 °C until genotyping. Before genotyping, lysates were vortexed for 10 seconds followed by centrifugation for 1 min at maximum speed. The clear supernatant containing genetic material was used for PCR reactions. The PCR reaction was pipetted on ice. Composition and PCR-program of the reaction differed depending on the tested genes as listed in tables **Table 14** and **Table 15**.

Table 14 | Composition of the PCR mixes for genotyping.

Ingredient	**Volume [µl] Srf-flex1 PCR**	**Vol. [µl] Rosa^{mTmG} PCR**	**Vol. [µl] PdgfrbCreER^{T2} PCR**
H_2O	36.75	38.9	36.5
10x PCR-buffer	5	5	5
DMSO	2.5	N/A	N/A
dNTPs (10 mM)	1.5	1	1
Primer 1 (10 mM)	1.5 (AW)	1.2 (7318)	1.5 (Pdgfrb_Cre1)
Primer 2 (10 mM)	1.5 (BW)	0.8 (7319)	1.5 (Pdgfrb_Cre2)
Primer 3 (10 mM)	N/A	7320 1.6	1.5 (Pdgfrb_Cre3)
Primer 4 (10 mM)	N/A	N/A	1.5 (Pdgfrb_Cre4)
RedTaq	0.75	0.75	0.75

Table 15 | List of PCR programs used for genotyping.

Step		**Srf-flex1 PCR**		**Rosa^{mTmG} PCR**		**PdgfrbCreER^{T2} PCR**	
Initial denaturation		94 °C	2 min	94 °C	3 min	94 °C	2 min
35x cycles	Denaturation	94 °C	30 s	94 °C	30 s	94 °C	45 s
	Primer annealing	53 °C	30 s	61 °C	1 min	60 °C	45 s
	Elongation	72 °C	30 s	72 °C	1 min	72 °C	1 min
Final elongation		72 °C	7 min	72 °C	2 min	72 °C	5 min
Hold		4 °C	∞	4 °C	∞	4 °C	∞

After the PCR reaction, amplified DNA-fragments were separated on a 1.5 % electrophoresis agarose gel containing 5 µl Midori Green /120 ml, using 0.4 V/cm^2 for 45 min. Gels were visualized and documented on a gel documentation system.

2.2.1.3 *Tamoxifen treatment*

To induce Cre-mediated recombination of the Srf-flex1 allele or the mTmG allele, mice were treated with tamoxifen. To prepare a 10 mg/ml tamoxifen stock solution, 10 mg tamoxifen was dissolved in 250 µl absolute ethanol by vortexing. After dissolving, the solution was dispersed in 750 µl of peanut oil by vortexing thoroughly. This stock solution was stored at 4 °C for up to 3 days.

To induce Cre-mediated recombination of the *Srf-flex1*-, or the *Rosa*^{mTmG}-allele in newborn pups, pups were treated daily with tamoxifen from postnatal day (P) 1 to P3. For this, a final solution of 2 mg/ml was prepared by dilution of the stock solution 1:5 in peanut oil. Finally, 25 µl (50 µg) of the tamoxifen working solution was injected intraperitoneally (i.p.) into the milk spot (stomach) of the pup. Weight and health status of the pups were monitored over the period of the experiment.

In OIR experiments, animals were injected i.p. with 100 µl of tamoxifen (2 mg/ml) solution on 3 consecutive days between P12 and P14.

To induce Cre-mediated recombination in adult animals (8 weeks old), 100 µl of tamoxifen solution (5 mg/ml) was injected i.p. on 5 consecutive days.

2.2.1.4 *Isolation and preparation of postnatal mouse retinas*

Retinas from postnatal mice were isolated for subsequent staining procedures. Animals were weighed and sacrificed by decapitation (P6-P12) or by exposure to CO_2 followed by cervical dislocation (>P12). Eye balls were subsequently removed and washed in phosphate buffered saline (PBS). Depending on the purpose of staining, eye balls were fixed using 4 % PFA (solved in PBS) for 2 h either on ice (mild fixation for AB staining) or at room temperature (strong fixation for IB4 staining). After fixation, eye balls were washed in PBS before dissection. Dissection was carried out using fine dissection tools and a stereomicroscope. Fixed and washed eye balls were placed in a petri dish and submerged in PBS. Surrounding fatty tissue around the eye and remains of the optic nerve were removed. Then, the cornea was gently dissected to enable access to the inner parts of the eye, followed by removal of the iris. Next, the outer retinal layer, sclera and choroid were gently dissected into small increments to avoid any damage of the retinal layer beneath. Then, the vitreous humor and hyaloid vessels were removed, which provide prenatal blood supply to the issue, but start to regress instantly after birth of the animal. Finally, by making 4 radially incisions into the retinal tissue, the retina was divided into quadrants necessary for later tissue flat mounting. The retina was then ready for subsequent whole mount immunostaining.

2.2.1.5 Whole mount immunostaining of retinas

During the entire immunostaining procedure both retinas of one animal were treated together in one 2 ml reaction tube. All incubation steps were carried out using mild agitation on a shaking platform. Freshly prepared retinas were blocked in blocking solution overnight at 4 °C or at room temperature for 2 h. After incubation, the blocking buffer was removed and samples were incubated with 100 µl primary antibody solution (blocking buffer with 2 % donkey serum; used dilutions see **Table 7**) over night at 4 °C. The next day, the primary antibody solution was removed and retina samples were washed 5 times for at least 20 min with retina washing buffer. Next, samples were incubated with immunofluorescent Alexa-fluorophore coupled secondary antibodies (used dilutions see **Table 3**) for 2 h at room temperature protected from light. The incubation was followed by washing 4 times for at least 20 min with retina washing buffer at room temperature. Finally, samples were washed twice for 5 min using PBS at room temperature to remove any detergent residues. Samples were stored at 4 °C until mounting procedure (max. one day).

If an isolectin-B4 (IB4) staining was performed, blocked Retina samples were incubated thrice in Pblec buffer. Afterwards the tissues were incubated in 100 µL IB4 (1:25) overnight at 4 °C. If a co-staining was necessary, primary antibodies were additionally added. The next day, IB4 stained tissues were washed 5 times for 20 min with retina washing buffer and subsequently incubated in 100 µl of Streptavidin-Alexa-400 or 488 (1:100) together with additional secondary antibodies in retina blocking buffer for 2 h at room temperature. Subsequent washing procedure was carried out as mentioned above.

After completion of the staining procedure, retina samples were mounted on a glass slide for microscopy. For this, 2 retina tissue samples of one animal were transferred to one microscope glass slide using a plastic Pasteur pipette (with cut pipette tip, to prevent any shear force). The retina samples were positioned on the center of the slide with the inner side containing the vessels facing up. Afterwards, the samples were flattened and any dirt was removed using forceps. Furthermore, all excess PBS was removed. 60 µl of Fluoromount-G was added to a microscope cover glass (24x40 mm). The cover glass was inverted and carefully placed over the retina samples. All mounted retinas were kept for 2 h at room temperature protected from light and were afterwards stored at 4 °C until used.

2.2.1.6 Preparation and staining of cryo-sectioned retinas

Cryo-sections of retinas were prepared to enable transversal sectional views on retina tissues. Freshly extracted eye balls were fixed in 4 % PFA in 0.1 M phosphate buffer (PB)-buffer for 5 min at room temperature. Afterwards, eye balls were washed with PB-buffer and retinas were isolated as described above (2.2.1.4). Prepared retinas were post-fixed in 4 % PFA solution for 1 h at room temperature and then washed once in PB-buffer. Retinas were then dehydrated in 30 % sucrose solved in 0.1 M PB-buffer overnight at 4 °C. The next day, retinas were transferred to optimal cutting compound (OCT) and shock frozen in dry ice to minimize freezing artifacts. Frozen samples were stored at -80 °C until used. Histological cryo-sections were cut on a cryostat at -20 °C chamber temperature into transversal 14 µm sections. The cut sections were immobilized on a super-frost microscopy slide. Samples were stored at -20 °C until further processed.

To immunolabel retinal cryo-sections, slides carrying cryo-sections were dried at 37 °C for 30 min. The following staining procedure was carried out in a wet chamber to prevent evaporation of staining solutions. After drying, samples were blocked in blocking solution for 1 h at room temperature. Then, the blocking buffer was replaced with primary AB cocktail in blocking solution. Incubation took place over night at 4 °C. The next day, primary AB cocktail was removed and sections were washed 3 times for 10 min using PBST. Sections were then incubated in secondary AB cocktail in blocking solution and incubated at room temperature for 1 h. Afterwards, samples were again washed 3 times with PBST for 10 min. Finally, samples were mounted in Fluoromount-G and allowed to dry at room temperature in the dark for 2 h before storage at 4 °C until use.

2.2.1.7 Preparation of retinas for transmission electron microscopy (TEM)

(The EM study was performed in collaboration with Dr. Hartwig Wolburg, Institute for Pathology, University of Tuebingen, Medical School. Preparation of TEM samples was performed by Gabi Frommer-Kaestle. TEM Microscopy and interpretation was performed by Dr. Hartwig Wolburg.)

Eye balls were freshly removed and retinas was gently dissected as described above (2.2.1.4) without any fixation. After dissection, the retinas were fixed in Karnowsky’s fixative (2 % PFA, 2 % glutaraldehyde solved in 0.1 M cacodylate buffer). Retinas were then washed in cacodylate buffer and post-fixed in 1 % osmium tetroxide (OsO_4) for 1 h at room temperature and afterwards dehydrated in ascending series of ethanol series (50, 70, 96, 100 %). In the 70 % step, ethanol was saturated with uranyl acetate for contrast enhancement. Final dehydration was completed in propylene oxide. The specimens were embedded in Araldite adhesive. semithin sections (1 µm) and ultrathin sections (50 nm) were generated on a FCR

Reichert Ultracut ultramicrotome. semithin sections were stained by using toluidine blue. Ultrathin sections were mounted on pioloform-coated copper grids, contrasted with lead citrate and analyzed and documented using an EM10A electron microscope.

2.2.1.8 In vivo proliferation assay

To determine proliferation behavior of MCs and ECs in retinas, pups were treated with the thymidine analogue 5-Ethynyl-2´-deoxyuridine (EdU). Injected EdU gets distributed through the blood stream and incorporated into the DNA of proliferating cells. After an incubation time of 2-5 h, proliferating cells contain detectable amounts of incorporated EdU. Retina samples can be stained using a specific click-reaction kit to fluorescently label EdU-containing nuclei. A cell specific co-staining of the cell type of interest allows the detection and ultimately the calculation of proliferating cells.

EdU labeling was performed on mouse pups at the age of P6 and P12. An EdU working solution (5 mg/ml) was prepared by weighing 5 mg EdU into a 2 ml reaction tube and solving it in 100 µl of DMSO by vortexing. After solvation, 900 µl of PBS buffer was added and the tube was vortexed again. 10 µl/g body weight (50 µg/g body weight) EdU working solution was injected i.p. 3 h or 5 h prior organ harvest for detection of EC proliferation or PC proliferation, respectively. Retinas were prepared and stained as previously described (2.2.1.4). After secondary antibody staining, retinas were stained using the Click-iT EdU Cell Proliferation Kit according to the manufacturers instructions with slight modifications. All incubation and washing steps were carried out using mild agitation on a shaking platform at room temperature. Retinas were washed twice for 5 min with 3 % BSA/PBS solution. In the meantime, the Click-iT reaction cocktail was prepared according to the following table (**Table 16**).

Table 16 | Components of the Click-iT reaction cocktail for up to 10 samples. All ingredients were added in the order listed in the table.

Reaction components	**Vol [µl]**
1x Click-iT reaction buffer	860
$CuSO_4$ 1M	40
Alexa Fluor-azide	2.5
Reaction buffer additive	100
Total volume	1000

After washing, the wash solution was carefully removed and the samples were incubated in 100 µl Click-iT reaction cocktail for 2 h at RT protected from light. Then, the reaction mix was removed and the tissues were washed once with 3 % BSA/PBS solution and then washed twice with PBS for 10 min each. Finally, the samples were mounted as described previously (2.2.1.5).

2.2.1.9 Oxygen Induced Retinopathy (OIR)

The OIR disease model was performed in principle according to Connor et al. (2009), with slight modifications [108]. In short, neonatal pups and their mothers were kept at normoxic conditions (room air) from birth to P7 to allow normal vascular development. For 5 days from P7 to P12, the mice were transferred to hyperoxic conditions of 75 % O_2, which represses further vessel development and induces capillary vessel retraction. Finally, the animals were kept for another 5 days from P12 to P17 under normoxic conditions to induce the pathologic neovascular response.

Hyperoxic conditions were realized by transferring the mice to a Biospherix A-Chamber equipped with a ProOx 110 oxygen controller connected to technical oxygen (99.99 % O_2). As CO_2 concentration is regularly elevated in OIR chambers, 100 g of soda lime was kept at the bottom of the chamber as quencher. Over the course of the experiment, oxygen concentration in the chamber was controlled twice a day, while health status of the animals was controlled daily. To discharge the animals from the oxygen chamber, the oxygen concentration was decreased stepwise over a time course of 4 h (1 h of each 60 %, 50 %, 40 %, 30 % O_2).

Tamoxifen injections to induce Cre-mediated recombination took place from P12 to P14 by 3 consecutive i.p. injections (see 2.2.1.3). Health status and weight were controlled daily. At P17, pups were sacrificed by exposure to CO_2 followed by cervical dislocation. Eye balls were removed and prepared as described in [161].

2.2.1.10 Evans blue extravasation assay

Evans blue (EB) assay was performed to determine extravasation of albumin and therefore vessel leakiness. For this, 100 µl of a 1 % EB solution solved in PBS buffer was injected i.p. into animals at P25. After 24 h, animals were sacrificed by exposure to CO_2 followed by cervical dislocation. Subsequently, animals were perfused with 5 ml cold PBS buffer through the left ventricle to wash remains of blood from main vessels, thereby reduced background signals were achieved during later procedures.

Lung and brain tissues were harvested, weighed and transferred to a 2 ml reaction tube. The tissues were homogenized in 1 ml formamide using a homogenizer and incubated for 24 h in an Eppendorf thermomixer at 55 °C and 400 rpm to extract EB dye. After incubation, samples were centrifuged for 10 min at maximum speed in a table centrifuge. The supernatant comprised the EB azo-dye which was measured using a photometer at the maximum absorption of 620 nm. By preparing standards (range between 0 and 500 µg/ml) in formamide, the amount of extravasated EB/mg of tissue was determined.

2.2.1.11 Preparation of single cell suspensions from retinas and fluorescence-activated cell sorting (FACS) for RNA sequencing

(FAC sorting was performed in collaboration with the group of Dr. Stella Autenrieth, University Hospital Tuebingen. FACS was performed by Dr. Kristin Bieber).

In this work, RNA-sequencing (RNA-Seq) of retinal MCs and ECs of P12 *Srf*^{iMCKO} mice and control pups was performed to profile distinct cellular transcriptomes. In short, to isolate MCs and ECs from retinas, retinal tissues were first digested enzymatically with papain to obtain single cell suspensions. Afterwards, MCs and ECs in the single cell suspensions were stained with fluorescently labeled ABs for FACS sorting. Finally, cells were FACS sorted into RLT plus lysis buffer for isolation of the RNA required for RNA-Seq.

Prior to the cell isolation procedure, all required enzyme solutions, media and buffers were prepared. For this, 500 µl of EBSS was added to *Vial 2* of the papain dissociation kit (Worthington). Afterwards 250 µl of the solution of *Vial 2* was transferred to *Vial 1.* Subsequently 5 ml of EBSS was additionally added to *Vial 1*. Solutions in *Vial 1* and *Vial 2* were aliquoted (Tube 1: 250 µl aliquots of *Vial 1*; Tube 2: 15 µl aliquots of *Vial 2*) and stored at -20 °C until required.

Tube 1 (1x per animal) was incubated at 37 °C and 5 % CO_2 (with open lid) for 30 min to ensure physiological pH and optimal performance of papain enzyme reaction. Pups (P12) were sacrificed by decapitation. Eye balls were harvested and kept in dissection media for subsequent retina preparation on ice as described in chapter 2.2.1.4. Prepared retinas were transferred to Tube 1 and incubated for 10 min at 37 °C and 5 % CO_2 followed by a mild up and down pipetting for 10 times using a 1 ml pipette to homogenize the tissue. The incubation and homogenization procedure was repeated once. In the meantime, Tube 2 was incubated at 37 °C and 5 % CO_2 to enable equilibration. After homogenization, the suspension was transferred to Tube 2 and mixed by pipetting up and down. To remove any existing undigested tissue residues, 400 µl of prewarmed EBSS media was added to the suspension, mixed and filtered through a 40 µm cell strainer into a 2 ml reaction tube. Hereafter, the filtered cell suspension was centrifuged for 5 min at 300 x g at 4 °C. All further steps were performed on ice. After centrifugation, the supernatant was carefully removed by pipetting and the remaining cell pellet was resuspended in 120 µl of FACS buffer. 100 µl of the suspension was transferred to a 5 ml FACS tube containing 100 µl of AB master mix (Ter119-PB, CD45-PB, CD140a-FITC, CD140b-APC and CD31-PE in FACS-buffer; dilutions see **Table 7**), followed by mixing and incubation for 30 min on ice.

Meanwhile, 350 µl RLT plus lysis buffer supplemented with β-mercaptoethanol (10 µl/ml) was added to the remaining 20 µl cell suspension, the mixture was vortexed thoroughly and stored at -80 °C as input control for RNA-Seq. After AB incubation, 1 ml of FACS buffer was added to the cell suspension to wash out unbound ABs, followed by centrifugation for 5 min at 300 x g at 4 °C to pellet the cells. Finally, the supernatant was carefully removed and the remaining cell pellet was resuspended in 500 µl FACS buffer containing 50 ng/ml DAPI to label dead cells. The single cell suspension labeled with ABs and DAPI was now ready for FACS procedure.

In FACS, MCs and ECs were separately sorted out of the prepared single cell suspensions. Cell sorting was performed on a FACS Aria-Illu II cell sorter (BD Biosciences) using a 100 µm nozzle. The gating strategy involved the forward and side scatter to exclude cell debris and doublets. DAPI+, Ter-119+, CD45+ and CD140a+ cells were actively excluded in order to remove dead cells, red blood cells, hematopoietic cell lineages and mesenchymal cell lineages, respectively. Samples were positively selected for CD140b+ (MCs) and CD31+ (ECs) into two separate tubes filled with 500 µl RLT plus buffer supplemented with β-mercaptoethanol (10 µl/ml). After sorting, lysates were vortexed thoroughly and stored at -80 °C until RNA isolation for RNA-Seq.

2.2.1.12 Scanning-Laser Ophthalmoscopy (SLO) and optical coherence tomography (OCT)

(The SLO and OCT study was performed in collaboration with the group of Prof. Dr. Mathias Seeliger, Institute for Ophthalmic Research, Tuebingen. SLO and OCT was performed by Dr. Regine Mühlfriedel).

The *in vivo* analysis of retinal layer structure was performed as published previously [162,163]. In short, mice were anesthetized with ketamine (66.7 mg/kg) and xylazine (11.7 mg/kg) and pupils dilated with tropicamide (Mydriaticum Stulln). OCT imaging was performed together with SLO on a commercially available system (Heidelberg Engineering Spectralis, Eye Explorer version 5.3.3.0). This device features a superluminescent diode at 870 nm as low coherence light source. OCT scans are acquired at a speed of 40.000 scans per second and each two-dimensional B-scan (set to 30° field of view) contains up to 1536 A-scans. We use black on white mode, i.e. high reflectivity is shown as dark and low reflectivity as white. For angiography, indocyanine green dye (ICG) was used as published previously in combination with an infrared laser (795 nm; barrier filter 800 nm) [164].

2.2.1.13 Electroretinography (ERG)

(The ERG study was performed in collaboration with the group of Prof. Dr. Mathias Seeliger, Institute for Ophthalmic Research, Tuebingen. ERG was performed by Dr. Vithiyanjali Sothilingam.)

ERGs were obtained according to previously described procedures [165,166]. Mice were dark-adapted overnight before the experiments and their pupils were dilated. Anesthesia was induced by subcutaneous injection of ketamine (66.7 mg/kg), xylazine (11.7 mg/kg) and atropine (1 mg/kg). The Espion V6 equipment (Diagnosys LLC) was used for the ERG measurements. Single flash recordings were obtained both under scotopic (dark-adapted) and photopic (light-adapted)) conditions. Light adaptation was accomplished with a background illumination of 30 cd/m^2 for 10 min., which stayed on during the course of the photopic recordings. Stimuli were presented with increasing intensities, reaching from 10^{-3} cd*s/m^2 to 30 cd*s/m^2, divided into 10 steps of 0.5 and 1 log cd*s/m^2. Ten responses were averaged with an inter-stimulus interval (ISI) of 5 s or 17 s (for 1, 3, 10 and 25 cd*s/m^2).

2.2.2 Microbiological techniques

2.2.2.1 Transformation and storage of bacterial cultures

Chemically competent, frozen *E. coli* cells were thawed on ice for 15 min. 10 ng plasmid DNA (pDNA) was added to the cells followed by another incubation of 15 min on ice. To enable pDNA uptake, cells were heat shocked for 90 s at 42 °C. Subsequently, cells were allowed to recover by addition of 500 µl LB media and incubation at 37 °C for 1 h at 150 rpm. Finally, 100 µl suspension was plated on a LB agar plate containing antibiotics to enable selection of transformed cells. The plate was incubated overnight at 37 °C.

To prepare stocks for long-term storage of bacterial cells, one colony was picked from the plate and further cultivated in 5 ml LB media containing selection reagent (e.g. chloramphenicol or kanamycin) for 16 h. 500 µl bacterial culture was mixed with another 500 µl of a 50 % glycerol stock. The suspension was stored at -80 °C for long-term storage.

2.2.2.2 Cultivation of bacterial cultures for protein expression

BL21 Rosetta^{TM} 2(DE3) pLysS bacterial cells carrying chloramphenicol resistance and previously transformed with the pTat-Cre plasmid carrying kanamycin resistance were cultured in large scale amounts for expression of the Cre recombinase Tat-Cre.

A pre-culture was prepared by inoculation of 100 ml terrific broth (TB) medium with bacterial glycerol stock. The bacterial culture was incubated overnight at 37 °C and 150 rpm. Then, 4.5 l TB media containing selection markers was distributed to six baffled Erlenmeyer flasks. Each flask was inoculated with 10 ml pre-culture. The cultures were incubated at 37 °C and 150 rpm until the optical density at 600 nm (OD_{600}) reached 1.5. Then, expression of Tat-Cre was induced by addition of 1 M IPTG to reach 0.5 mM final concentration. To reduce formation of inclusion bodies (aggregates of expressed protein, provoked by fast expression), cultures were incubated at 19 °C and 150 rpm overnight before Tat-Cre purification.

2.2.3 Biochemical techniques

2.2.3.1 Tat-Cre purification

The Tat-Cre protein expressed from pTat-Cre plasmid contains six His-tag domains, which bind with high affinity to cobalt ions. This allows purification of Tat-Cre protein through cobalt-based affinity chromatography, which is compatible with eukaryotic cell culture conditions.

Overnight *E. coli* expression cultures were pelleted at 6,500 x g for 10 min at 4 °C. The resulting pellet (approx. 30 - 40 g) was resuspended in 5 ml/g pellet of ice-cold homogenization buffer containing complete ultra-protease inhibitor cocktail (1 tablet/50 ml homogenization buffer). Afterwards, the suspension was evenly distributed into 50 ml tubes (30 ml/tube) and lysed by sonification on ice. To remove cell debris, the lysates were centrifuged at 20,000 x g for 30 min at 4 °C. The supernatant was carefully transferred to 3 ml of equilibrated HisPur™ cobalt resin. The suspension was incubated for 1 h at 4 °C and mild agitation to ensure binding of His-tagged Tat-Cre protein to the cobalt resin. All further steps were carried out at 4 °C. After incubation, the suspension was loaded onto a gravity flow column and from each fraction within the following procedure samples were taken (approx. 100 µl) for later analytical purposes. The resin was washed with 10 ml of binding buffer to reduce unspecific binding to the cobalt resin. The column was then washed with 100 ml of washing buffer, containing 20 mM of Imidazole, allowing removal of bound proteins with medium affinity to the resin, caused by natural His-residues. Tat-Cre elution was induced by addition of 15 ml of elution buffer containing high concentration of imidazole (250 mM). The eluted protein was collected in 2 ml fractions. All collected samples were subjected to SDS-PAGE analysis to evaluate purity and yield of the isolation procedure (2.2.3.2).

As the eluted Tat-Cre protein is unstable in high imidazole concentrations, a subsequent dialysis was done to adjust buffer composition. All Tat-Cre-containing elution fractions (containing high concentrations of

Tat-Cre) were pooled in a Pur-A-Lyzer Mega Dialysis Kit and dialyzed in 3 l of dialysis buffer overnight. The next day, protein solution was sterile filtered using a 0.22 µl syringe filter, protein concentration was measured and portioned into 300 µl aliquots. Finally, samples were stored at -20 °C.

2.2.3.2 Sodium dodecyl sulfate -polyacrylamide gel electrophoresis (SDS-PAGE)

SDS-PAGE was performed to assess protein yield and purity of fractions obtained by the Tat-Cre purification procedure (2.2.3.1) and to separate proteins obtained from pBMC cultures. First, a separation gel was prepared (see **Table 17**) and filled into a BIO-RAD Mini-PROTEAN form (approx. ¾ of the form) and covered with isopropanol. After polymerization of the gel, the isopropanol was removed and the stacking gel was prepared and added along with a 10-well comb. During polymerization of the gel, the protein samples were mixed with sample buffer and boiled at 99 °C for 5 min. After heating, samples were cooled down on ice for 5 min and centrifuged for 1 min at maximum speed. 30 µl sample was loaded on the SDS gel. 5 µl protein marker was used as a standard. The SDS-PAGE was performed in a BIO-Rad Mini-PROTEIN chamber filled with SDS running buffer at 120 V for 2 h.

Table 17 | Composition of stacking gel and separation gel for SDS-PAGE. Amounts are calculated for two gels.

	Separating gel		**Stacking gel**
	10 %	**12 %**	**5 %**
ddH_2O	10 ml	9 ml	6,4
40 % Acrylamide	5 ml	6 ml	1 ml
Lower Tris buffer	5 ml	5 ml	-
Upper Tris buffer	-	-	2.5 ml
10 % APS	100 µl	100 µl	50 µl
TEMED	33 µl	33 µl	20 µl

2.2.3.3 Coomassie Brilliant Blue staining

Coomassie Brilliant Blue staining is used for detection of proteins separated by SDS-PAGE. The procedure was carried out to assess the quality of isolated Tat-Cre (2.2.3.1). Gels were covered in ddH_2O and heated for 30 s at 800 W in a microwave. The ddH_2O was exchanged with Coomassie Brilliant Blue solution and the gels were heated again for 30 s in the microwave. Afterwards, gels were incubated for 1-2 h at room temperature with mild agitation. Then, Coomassie Brilliant Blue was discarded and the gels were washed in ddH_2O to remove unbound stain.

2.2.3.4 *Bradford assay*

The Bradford assay was used to determine protein concentrations of dialyzed Tat-Cre isolates or pBMC protein lysates. At the beginning, defined standards (0-10 µg/ml) of bovine serum albumin (BSA) were prepared in 1 ml 1x Bradford reagent in cuvettes. 1-5 µl Tat-Cre sample was added to 1 ml 1x Bradford reagent also in a cuvette. Finally, standards and samples were measured using a photometer at absorbance of 595 nm. The standards were used to plot a standard curve and to calculate sample concentrations.

2.2.3.5 *Western Blot*

Western blot was performed to verify SRF ablation in cultured pBMCs at protein levels. pBMC cultures (control and *Srf-KO*) were grown to 70 % confluence on 6-well cell culture plates. Cells were trypsinized, pelleted and resuspended in ice cold RIPA buffer, followed by agitation for 30 min at 4 °C. Subsequent to agitation, resuspended cells were centrifuged for 30 min at 10,000 x g at 4 °C. The supernatant containing proteins was then transferred into a fresh tube and the protein concentration was determined by the Bradford assay (2.2.3.4). Protein lysates were stored at -20 °C until used.

20 mg of protein was separated by SDS-PAGE and subsequently transferred onto a 0.22 µm polyvinylidene difluoride transfer membrane using a Bio-Rad transfer system for 50 min (2 mA /cm^2 of membrane). Following the transfer, membranes were washed in TBST once and subsequently blocked in blocking buffer for 1 h at room temperature. After blocking, membranes were incubated with the primary AB (see **Table 3**) diluted in blocking buffer overnight at 4 °C. The next day, the membranes were washed three times with TBST and subsequently incubated with corresponding secondary AB (HRP-coupled) diluted in blocking buffer for 1 h. Finally, membranes were washed three times with TBST followed by a washing step with TBS to remove detergents from the membrane. Imaging of membranes was performed by addition of chemiluminescent HRP substrate. Documentation was performed on a Fusion SL documentation system.

2.2.3.6 *Luciferase assay*

The luciferase assay was used to assess transcriptional activity of SRF upon PDGFB stimulation in 3T3 cells. SRF-reporter transfected 3T3 cells ((TSM)$_2$, (TMM)$_2$ and (MSM)$_2$) were starved in starvation media (DMEM+0.3 % FCS), or in starvation media containing MAPK/MRTF inhibitor (PD-0325901 1 µM/CCG-203971 50 µM). The following day, cells were stimulated (excluding control conditions) by addition of PDGFB (25 ng/µl) for 7 h. Afterwards, media was removed and lysates for luciferase assay were prepared according to the manufacturer's instructions. Luciferase activity was measured using an OPTIMA FluoroSTAR.

2.2.4 Cell culture techniques

2.2.4.1 Establishment of primary brain mural cell (pBMC) culture from murine brains

Brain mural cells were isolated from 6 to 8 weeks old C57BL/6N mice which harbor the homozygous *Srf-flex1* allele and a heterozygous *Rosa26*^{mTmG} allele. The isolation procedure was performed as previously described by Tigges et al. (2012) with minor changes [167]. To isolate pBMCs, 3 mice were sacrificed by exposure to CO_2 followed by cervical dislocation. The following isolation procedure took place using sterilized preparation tools and a sterile fume hood. Mice were sprayed with 70 % EtOH and brains were dissected and placed in ice cold MEM media containing 1 % pen/strep. Using a razor blade, the olfactory bulb, cerebellum and medulla were removed. The remaining cortical tissues were pooled and rigorously minced using a razor blade. Minced brains were washed by adding 15 ml MEM and transferring them to a 15 ml tube and the suspension was centrifuged for 5 min at 300 x g at room temperature. Meanwhile, the papain dissociation solution (Worthington) containing Earl's Balanced Salt Solution (EBSS), papain and DNase was prepared according to the manufactures protocol. After centrifugation of the cell suspension, the supernatant was aspirated and the pellet resuspended in 2 ml papain solution, followed by incubation at 37 °C for 70 min. To ensure efficient tissue dissociation, the tube was gently flicked several times every 10 min during incubation. After incubation, the digested tissue was homogenized by slow trituration, passing it 10 times through a 18G needle, followed by passing it 5 times through a 21G needle. The homogenate was then resuspended in 5 ml of 22 % BSA/PBS solution and centrifuged at 1,300 x g for 10 min to separate the cell content in the pellet from the myelin in the upper phase. The supernatant was removed completely by aspiration and the cell pellet was then washed in 10 ml EBM-2 media followed by centrifugation at 300 x g for 5 min. After aspiration of the supernatant, the pellet containing single cells and vascular micro vessels was resuspended in 6 ml EBM2-medium and seeded equally on 3 wells of a 6-well plate coated with 2 % collagen type I (ColI). Plated cells were incubated at 37 °C and 5 % CO_2 for 20 h in a humidified incubator to ensure attachment of viable cells to the plate. After incubation, the plates were carefully washed 3 times with 3 ml PBS. Finally, 3 ml of fresh EMB-2 media was added to each well and the cells were cultured as previously mentioned. The media was replaced with fresh EBM-2 medium every second day until the culture reached confluence after 5 to 9 days. Cultures were then trypsinized, pooled and further cultured in a T25 cell culture flask (2.2.4.2).

The thus established cell culture contained endothelial cells, fibroblasts and mural cells (MCs) and was cultured in EBM-2 medium until the second passage. pBMC culture, was established by culture the cells in pericyte (PC) medium from the third passage onwards, which especially promotes mural cell growth. From passage 5 onwards, pMC cultures were judged to have reached high purity [167]. Expression of mural cell markers was determined by qPCR.

2.2.4.2 Cultivation of pBMCs

Cultivation of pBMCs was performed under standard cell culture conditions at 37 °C in humidified atmosphere with 5 % CO_2. pBMCs were grown in PC medium containing 2 % FCS, pericyte growth supplement and 1 % pen/strep. Cells were cultured on T25 or T75 cell culture flasks coated with 0.2 % CollI for passages <10 or with 0.4 % gelatin for late passages >10 until reaching a confluence of approximately 80 %.

For passaging, culture medium was aspirated followed by washing of the cells using PBS. After washing, the cells were detached by addition of trypsin and incubation for 5 min at 37 °C and 5 % CO_2. Trypsin was inhibited by addition of PC-medium. To remove any trypsin residues in the media, the cell suspension was pelleted at 300 x g for 5 min. The cell pellet was resuspended in PC-medium and seeded in a 1:5 ratio into a new coated cell culture flask.

If determination of the cell concentration was required, a small aliquot was taken from the cell suspension and mixed in a 1:2 ratio (dilution factor) with 0.4 % trypan blue, which only stains dead cells and thus allows determination of living cell counts. Cells were counted using a Neubauer counting chamber with 0.1 mm depth. The cell concentration was calculated as follows:

$$Cell\ concentraion\ \left[\frac{cells}{ml}\right] = \frac{counted\ cells}{counted\ squares} * 10^4 (chamber\ factor) * 2\ (dilution\ factor)$$

To freeze cells for long term storage, the centrifuged cell pellet was resuspended in freezing medium (PC-medium supplemented with 10 % DMSO and 10 % FCS) and transferred into 1 ml cryovials. The vials were transferred into a freezing container filled with isopropanol which enables a gradual freezing of -1 °C/min at -80 °C. Cells were stored up to 2 months at -80 °C. For long term storage, cells were stored in liquid nitrogen. To bring frozen pBMCs back to culture, cryovials were thawed at 37 °C in a water bath and immediately transferred into a cell culture flask containing PC-medium. On the next day the medium was changed and cells were further cultivated as described above.

2.2.4.3 Transfection of 3T3 cells

3T3 cell cultures were transfected using lipofection to introduce vector DNA. For lipofection, 3T3 cells were seeded in a density of 5 x 10^4 cells/well to a 24-well plate and cultured overnight. The following day, 1 µg of vector DNA was mixed with 50 µl of OptiMEM and 3 µl of LT1 lipofectamin reagent was prepared per well of the 24-well plate. After 30 min of incubation at room temperature, the entire solution was added dropwise to the well and incubated for 7 h. Afterwards the medium was replaced with fresh growth medium or starvation medium (depending on the purpose).

2.2.4.4 Tat-Cre transduction of pBMCs

As the cultured pBMCs harbored *Srf-flex1* and *Rosa26*^{mTmG} loci, treatment with the membrane permeable recombinase Tat-Cre induced excision of loxP flanked alleles and led to genetic ablation of *Srf* and a switch from tdTomato to eGFP expression (see chapter 2.1.1.1).

For Tat-Cre transduction, 5 x 10^4 cells/6-well or 2 x 10^4 cells/24-well pBMCs were seeded on 0.2 % Col-I coated plates and cultured overnight. The next day, cells were washed with PBS, before OptiMEM™ reduced serum medium was added (1 ml/6-well or 0.5 ml/24-well). Then, Tat-Cre was added to the wells (360 µg/6-well or 80 µg/24-well) and incubated with the cells for 20 h. The next day, the cells were carefully washed with PBS and recovered in PC-medium for 2 days. After recovery time, cells were directly used for experiments. The recombination efficiency could be estimated by counting of eGFP positive cells compared to total cell count.

2.2.4.5 Stimulation of pBMCs and 3T3 cells

To study how pBMCs react to extracellular stimuli and how SRF signaling is involved, pBMCs and 3T3 cells were stimulated with FCS or PDGFB.

Cells were trypsinized and counted as previously mentioned (2.2.4.2). To analyze gene expression, 5x10^4 cells were seeded on 0.2 % Coll coated 6-well plates and incubated overnight in PC-medium. The next day, the cells were washed with PBS and starved overnight by addition of starvation medium (PC-basal medium supplemented with 0.3 % FCS). The next day mouse PDGFB or FCS was added to the starvation media to a final concentration of 25 ng/ml PDGFB or 10 % FCS. Finally, cells were harvested and RNA was subsequently isolated using trypsin and the Qiagen RNeasy micro kit, resepectively.

For life cell imaging, pBMCs or 3T3 cells (*Srf-KO* or respective control cells) cells were seeded on 0.2 % Coll coated 35 mm µ-Dish (Ibidi) suitable for confocal live imaging and incubated overnight in PC-medium (pBMCs) or DMEM+10 % FCS. The following day, cells were washed with PBS and starved overnight using starvation medium. The next day, 1 µM of the fluorogenic SiR-probes SiR-Actin and SiR-DNA700 were added to visualize respective intracellular structures *in vivo*. Additionally, 1 µM of the efflux pump inhibitor verapamil was added to improve signal intensity of the SiR-probes. pBMCs were imaged at 37 °C for a total of 8 h using a LSM800 (Zeiss) microscope at 40x (NA 1.2) magnification with 1 image cycle/5 min to observe the cytoskeleton dynamics in spatial and temporal resolution. 3T3 cells were at 37 °C for a total of 2 h using a LSM800 (Zeiss) microscope at 20x (NA 0.5) magnification with 1 image cycle/1 min.

2.2.4.6 *Wound closure migration assay*

To observe migration speed of control and *Srf-KO* pBMCs, a wound closure assay was performed. Cells were trypsinized and counted as previously mentioned (2.2.4.2). 10 x 10^4 cells were seeded to 4-well plates of a 0.2 % Coll-coated 35 mm µ-Dish (Ibidi), which harbor a silicone culture insert. Cells were cultured overnight in PC-medium and on the next day, the culture insert was removed to generate wound-like gaps. The dish was washed with PBS and PC-medium containing 20 ng/ml mPDGFB, 750 nM SiR-Actin, 750 nM SiR-DNA700 as well as 1 µM verapamil was added. The stained cells were imaged for 20 h at 37 °C using a LSM800 (Zeiss) microscope at 10x magnification with 1 image cycle/10 min to compare wound closure migration of control and *Srf-KO* pMCs.

2.2.4.7 *Trans-well migration assay*

The Trans-well migration assay is a useful tool to study cell migration, where the cells are seeded in a cylindrical cell culture insert (Boyden chamber) containing a membrane with defined pore size. The insert is nested in a standard cell culture well containing a chemoattractant, so that cells migrate along the generated gradient to the other side of the membrane. The migrated cells can then be stained and counted.

To perform the trans-well assay, *Srf-KO* and pBMCs were trypsinized and counted as previously mentioned (2.2.4.2). Afterwards, the cells were resuspended in starvation media (basal PC-medium supplemented with 0.3 % FCS) and 4 x 10^4 cells were seeded into a Boyden chamber insert with 8 µm pore size placed in a 24-well cell culture plate. Cells were incubated for 2 h at 37 °C and to let cells adhere. Then, the inserts were transferred to a new well containing 600 µl starvation medium supplemented with 20 ng/ml mPdgfbb. Plates were incubated for 6 h at 37 °C to allow cells to migrate towards the gradient. Migration was stopped by replacement of the medium. Cells were fixed on the membranes using 4 % PFA for 10 min at room temperature and subsequently washed with PBS. Afterwards cells were incubated in DAPI (3 µg/ml) to stain the nucleus of migrated cells, followed by washing with PBS, trice. To remove not migrated cells, the inner part of the membrane was cleaned by a cotton swab. Finally, the membrane was cut out of the Boyden chamber and mounted on a microscope slide. Samples were stored at 4 °C till imaged by fluorescence microscopy.

2.2.4.8 Immunostaining of pBMCs

For immunostaining, pBMCs were seeded on 0.2 % CollI-coated glass cover slips and cultured overnight. All following steps were performed at room temperature. The cells were washed once with PBS and subsequently fixed using 4 % PFA for 10 min, followed by washing with PBS. To make intracellular structures accessible for AB penetration, cells were treated with 0.5 % triton in PBS for 5 min and were subsequently washed 3 times with PBS. Afterwards, the cells were blocked in blocking buffer for 1 h to reduce unspecific AB binding in following steps. The cells were then incubated with the primary antibodies in blocking solution for 1 h. Afterwards, the cells were washed 3 times with PBS for at least 5 min. Then, the immunofluorescent Alexa-fluorophore-coupled secondary antibodies (used dilutions see **Table 3**) were added and the cells were incubated for 1 h. After incubation, the cell nuclei were counter stained with DAPI in in PBS for 5 min. Finally, samples were washed 3 times with PBS and mounted on microscope slides using Fluoromount-G. Mounted slides were dried for 30 min and stored at 4 °C until used.

2.2.5 Molecular biological techniques

2.2.5.1 Isolation of RNA

During this study, RNA was isolated from pBMC cultures, from sorted ECs and MCs as well as from brain and retina tissues.

To isolate RNA from pBMC cultures, cells were trypsinized and pelleted by centrifugation. Then, the RNA was isolated from the cell pellet using the RNeasy Micro Kit (Qiagen) by following the manufacturer's instructions.

Isolation of RNA from FAC-sorted MCs and ECs in RLT buffer^{plus} was performed by Rodrigo Diéguez-Hurtado (MPI for Molecular Biomedicine, Muenster, Germany) using the RNeasy Micro Plus Kit (Qiagen) following the manufacturer's protocol.

RNA of brain and retinal tissue was isolated using TRIzol Reagent (life technologies) in accordance with the manufacturer's protocol. As RNA isolation using TRIzol reagent does not include DNase treatment, removal of DNA impurities was performed by applying the DNA-free DNA Removal Kit (Invitrogen) according to the manufacturer's protocol.

Finally, RNA concentrations were determined using the Qubit RNA broad-range (BR) assay kit (life technologies) in agreement with the manufacturer's instructions.

2.2.5.2 Reverse transcription of RNA to cDNA

Total RNA was reverse transcribed to complementary DNA (cDNA) using the reverse transcriptase (RT) M-MLV. RT reactions were prepared as described below.

Table 18 | Components of the reverse transcriptase reaction.

Reagents	Vol [µl]
5x Reaction Buffer	5
5x Random Hexamer Primers	5
10x miScript Nucleics Mix	2.5
M-MLV RT	1
RiboLock RNAse Inhibitor	0.25
Sample RNA	up to 800 ng
RNase-free ddH$_2$O (final volume)	up to 25

The thermocycler program included an initial incubation at 25 °C for 10 min followed by an enzyme specific incubation at 40 °C for 50 min and an inactivation phase at 70 °C for 15 min. After the reaction, samples were diluted 1:50 in ddH$_2$O and stored at -20 °C until used in the quantitative PCR approach.

2.2.5.3 Quantitative polymerase chain reaction (qPCR)

Quantitative PCR (qPCR) was performed to precisely quantify specific target gene expression levels. Transcription levels can be determined using the fluorescent dye SYBR Green, which binds specifically to double stranded DNA. As the increase in fluorescence signal correlates with the copy number of targeted cDNA, precise quantification is enabled.

qPCR reactions were performed in a 386-well plate format as described in **Table 19**. All reactions were performed in triplicates.

Table 19 | Components of the qPCR reaction.

Reagents	Vol
2x SYBR Green PCR Master Mix	5 µl
2 µM Forward and Reverse Primer	1 µl
cDNA 1:50	0.5 µl
ddH$_2$O	up to 10 µl

The reactions were carried out in a QuantStudio 7 Flex Real-Time PCR-System (Thermo Fisher Scientific) with the following cycling conditions (**Table 20**).

Table 20 | qPCR temperature program for the QuantStudio 7 Flex Real-Time PCR-System.

Step	Temp.	Time	
Initial denaturation	95 °C	10 min	
Denaturation	95 °C	15 sec	40 Cycles
Primer annealing and elongation	60 °C	1 min	
Final elongation	98 °C	10 min	

Assays were analyzed with the QuantStudio Real-Time PCR Software. Specificity of qPCR was determined for each reaction by examination of the amplicon melting curve. If a melting curve consisted of only one peak, it was judged as specific. Samples with unspecific melting curves were excluded from analysis. All experiments were evaluated by the delta-CT method ($2^{-\Delta\Delta Ct}$) according to the Formula:

$$Fold\ change = 2^{-(\Delta 1 - \Delta 2)}$$

$$\Delta_1 = Sample\ A\ (C_T\ of\ target\ gene\ (Ctrl) - C_T\ of\ house\ keeping\ gene(Ctrl))$$

$$\Delta_2 = Sample\ B\ (C_T\ of\ target\ gene\ (KO) - C_T\ of\ house\ keeping\ gene\ (KO))$$

For normalization of samples, the β-*glucuronidase* (*Gusb*) or the *TATA-box binding protein* (*Tbp*) served as endogenous controls for determination of fold change levels.

2.2.5.4 RNA-Seq analysis

(The RNA-Seq study was performed in collaboration with the group of Prof. Dr. Ralf Adams at the Max Planck Institute for Molecular Biomedicine, Muenster. Library preparation and sequencing was performed by Dr. Rodrigo Diéguez-Hurtado. Data analysis was performed by Dr. Hyun-Woo Jeong.)

RNA-Seq analysis was carried out to determine transcript levels of retinal MCs and ECs and was performed as previously described [98]. RNA was isolated using the RNeasy Micro kit according to the manufacturer's instructions. RNA-Seq libraries were generated with the Single Cell/Low Input RNA Library Prep Kit and sequenced at the Max Planck Institute for Molecular Biomedicine (Muenster) on an Illumina E6420L device.

The raw sequencing files were obtained in FASTQ format and quality controls were assessed by using FASTQC (https://www. bioinformatics.babraham.ac.uk/projects/fastqc/). Obtained reads were aligned to the mouse genome assembly (GRCm38.p6 Ensembl release 92) using TopHat2 (version 2.1.1), following by generation of gene expression counts by using HTSeq-count (version 0.6.1) with the option -m intersection-nonempty. Final gene expression analysis across the measured samples was performed by using DESeq2 package on protein-coding genes. A principal component analysis (PCA) was used to assess the overall similarity between the samples and performed based on transformed read counts. Differentially expressed genes (DEGs) were selected by using a false discovery rate p-value cut-off <0.05 as well as an absolute $\log_2$ fold change of >0.5.

Gene enrichment analysis (GSEA) of DEGs was performed by me using the GSEA-tool (version 4.0.3) and a cut-off p-value of <0.05.

2.2.6 Morphometric analysis of retinal vasculature

Retinal vasculature microscopy images were analyzed using the ImageJ software tool Fiji. In all quantifications, the control group was set as reference and the mutant group was calculated accordingly. All images for quantifications were obtained from two retinas out of one animal and were averaged and expressed as one value (n=1). In general, 8 (but at least 4) comparable fields of view were imaged per animal and averaged. Images for quantification were taken at high magnification (40x) and with a field of view covering 317 µmx317 µm. The number of utilized animals in each group is indicated in the respective figures.

Vascularized area was measured as ICAM2$^+$, CD31$^+$ or IB4$^+$ area divided by total area. Radial outgrowth was measured as distance from the optic nerve to the periphery of the vascular front for each wedge of the retina. Endothelial filopodia at the angiogenic front were manually counted and normalized to a length of 1000 µm. Branching points were manually counted and divided by the vascularized area. Mural cell coverage was determined by manually counting NG2$^+$ or PDGFRB$^+$ cells at the capillary plexus and the angiogenic front, normalized to the vascularized area. Mural cell coverage determined by DES staining was measured by DES$^+$ area divided by the total vascularized area. Empty sleeve area was measured as Col-IV$^+$ area subtracted by the IB4$^+$ vessel area, leaving only retracted vessels. This retracted vessel area was divided by IB4$^+$ vessel area. SMA signal intensity was measured by SMA intensity on arteries normalized to ICAM2 signal intensity. The background intensity of each assessed channel was subtracted from the respective channel intensity. SMA intensity was assessed by measurement of SMA signal intensity, subtracted by the background intensity. Extravasation of red blood cells was determined by subtraction of the vascularized area from the Ter119$^+$ erythrocyte area to detect extravasated red blood cells. Arteriovenous nicking (crossings of arterioles and venules) was counted manually on whole retina samples. EC density was determined by manually counting ERG$^+$ nuclei to specifically detect ECs and was normalized by dividing by the ICAM2$^+$ vessel area. Levels of proliferating ECs were determined by counting of ERG$^+$/EdU double-positive cells, normalized to ERG$^+$ cells. To measure pericyte proliferation, NG2$^+$ and EdU$^+$ cells were normalized to total amount of NG2$^+$ cells. Arterial and venous diameter was measured on three independent positions within a distance of up to 1000 µm and the individual diameter values were averaged. Smooth muscle cell (SMC) coverage was measured by manually counting eGFP$^+$ cells or measurement of NG2$^+$ or DES$^+$ area on arteries and veins, normalized to the vascularized area. Avascular area of retinas in OIR experiments was measured by using the “polygon selection” tool and normalized to the vascularized area. NVT area was determined by manual selection of NVT areas using the affinity software (expressed in pixel values) normalized to the total area. Pericyte and SMA coverage on NVTs was determined by measurement of the NG2$^+$ or DES$^+$ area normalized to the vascularized area.

Chapter 3

3 Results

3.1 Analyses of MC function during early postnatal angiogenesis

3.1.1 *Srf* is ubiquitously expressed in mural cells

SRF is a ubiquitously expressed transcription factor. However, transcriptional activity of *Srf* has just shown so far in smooth muscle cells (SMCs) but not in pericytes (PCs) of the retinal vascular unit [30]. An existing single cell transcriptomic dataset of the murine brain, published by Vanlandewijck et al. (2018), detected *Srf* expression in SMCs and PCs [74]. In the brain, highest average *Srf* transcription levels were measured in arteriolar smooth muscle cells (aaSMCs) and in arterial SMCs (aSMCs). Venous SMCs (vSMCs) and PCs expressed approximately one third of that of aSMCs (Vanlandewijck et al. (2018)). To verify expression of *Srf* in the murine retinal vasculature, SRF immunohistological-staining (staining) of whole mount retina explants at postnatal day 6 (P6) was performed (**Figure 3.1**). ICAM2, an intracellular adhesion molecule specifically expressed by endothelial cells (ECs) of the central nerve system (CNS), served as EC marker [74]. Furthermore, the chondroitin sulfate proteoglycan NG2 was used as a surface marker for both SMC and PCs. As SMC and PCs are collectively known as mural cells (MCs), the following chapters will refer to MCs, in case both subtypes are simultaneously addressed.

SRF staining showed a ubiquitous signal in MCs in all regions of the retinal vasculature (**Figure 3.1**). To enable comparison of signal intensity between regions of the retinal vasculature, the mean intensity gray value of individual cells was determined. Signal intensity was strongest in aSMCs in comparison to vSMCs and PCs of the capillary plexus (CP) and the angiogenic front (AF), which is in accordance with the results of Vanlandewijck et al. (2018). vSMC and PCs of the AF showed a slightly stronger SRF signal in comparison to PCs of the CP. In addition, SRF signal was also observed in unidentified cells, demonstrating the omnipresence of SRF.

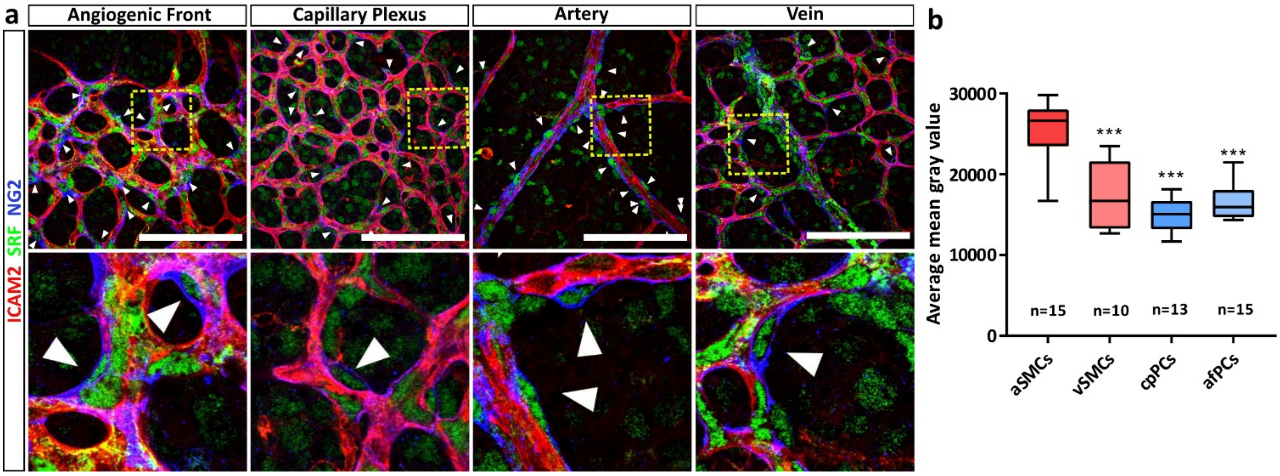

Figure 3.1| SRF expression in murine retinal MCs. (a) Confocal images of P6 murine retina showing endothelial vasculature (ICAM2, red), MCs (NG2, blue) and SRF (green). Representative regions of the retinal vasculature are shown. Yellow, dashed boxes indicate magnified regions (lower row). White arrowheads indicate representative MCs. Note, MCs at the angiogenic front and the capillary plexus are per definition PCs, whereas MCs on arteries and veins are SMCs. Scale bar, 100 µm. **(b)** Quantification of measured SRF signal mean gray value of arterial SMCs (vSMC), venous SMC (vSMC) capillary PCs (cpPCs) and angiogenic front PCs (afPCs). Data are compared to aSMCs and represented as box and whiskers. Number of evaluated cells (n) are indicated. One way anova tukeys test. ***$p<0.0001$.

3.1.2 MC specific tamoxifen-induced conditional knockout of *Srf*

In order to study SRF function in MCs of the CNS, a mouse model was generated in which *Srf* could be conditionally deleted (**Figure 3.2, a**). To do so, the MC specific *Pdgfrb(BAC)-CreER*^{T2} (*Pdgfrb-CreER*^{T2}) mouse line (kindly provided by Prof. Dr. Ralf Adams, MPI Muenster) was crossed with the *Srf*$^{flox/flox}$ (*Srf-flex1*, standing for floxed exon 1) line [81,156,157]. Induction of *Srf* deletion by Cre activity was enabled via tamoxifen administration (i.p. injection into stomach); hereafter the mice are referred to as *Srf*^{iMCKO}, standing for **i**nduced **m**ural **c**ell **k**nock**o**ut (**Figure 3.2**, **b**). This study compares whole litters of *Srf-flex1::Pdgfrb-CreER*^{T2} line matings, thereby comparing littermates harboring the *CreER*^{T2} transgene, which enables targeted *Srf* deletion, with those that harbor no *CreERT*^{2} transgene (littermate controls).

To verify Cre recombination efficiency in cells of the retinal vasculature, the global double fluorescent reporter line *Rosa26*^{mTmG} was crossed into the *Srf-flex1::Pdgfrb-CreER*^{T2} line, leading to specific highlighting of recombined MCs by membrane targeted GFP expression (**Figure 3.3, a**) [158]. In this case, homozygous (*Srf-flex1/Srf-flex1*) animals were compared to hemizygous (*Srf-flex1/Srf- wild type*) animals, leading - upon CreER^{T2} mediated recombination - either to full (*Srf*^{iMCKO}) or partial deletion (littermate control) of the *Srf* gene. This approach excludes potential bias provoked by expression of the CreER^{T2} protein.

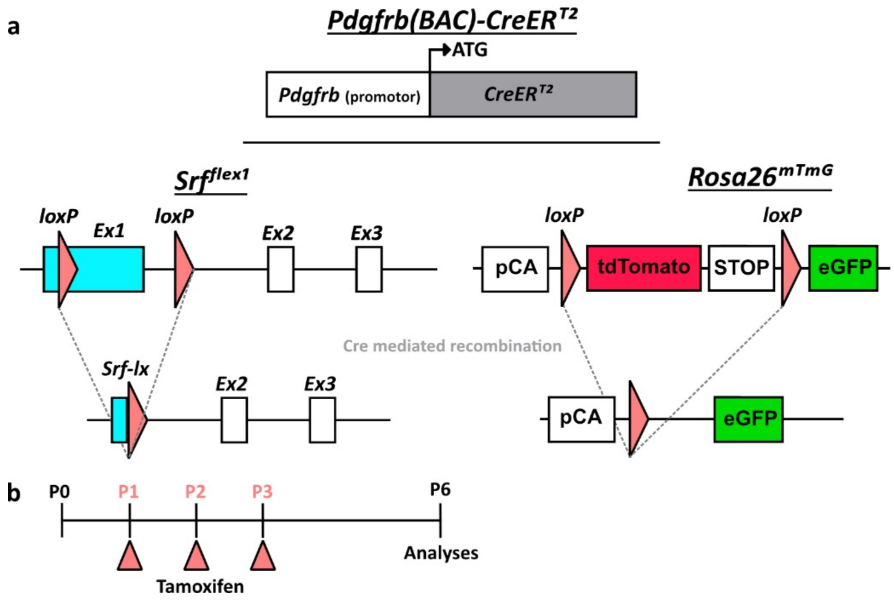

Figure 3.2| The *Srf-flex1::Pdgfrb-CreER*^{T2} mouse model. (a) *Pdgfrb(BAC)-CreER*^{T2} mice, which express CreER^{T2} in a mural cell specific manner were crossed with *Srf-flex1* mice to generate a tamoxifen inducible mural cell knockout of *Srf* (*Srf*^{iMCKO}). LoxP sites are flanking the exon 1 of *Srf*, leading to the generation of a shortened exon 1 (*Srf-lx*) allele upon Cre mediated excision. In some experiments the *Rosa26*^{mTmG} marker transgene was crossed into the *Srf-flex1::Pdgfrb-CreER*^{T2} line to enable labeling of recombined cells, allowing approximate calculation of recombination rate and high resolution visualization. (b) Tamoxifen administration protocol. Pups received 50 µg tamoxifen solved in oil by i.p. injection into the stomach on P1-3. Analysis took place at P6.

A whole mount staining of the retinal vasculature for GFP in P6 *Srf*^{iMCKO} and littermate control animals, co-stained with the MC specific marker PDGFRβ, revealed a recombination efficiency of about 80 % (**Figure 3.3, b and c**). Furthermore, a generic PCR which specifically amplifies the *Srf*-exon1 allele was performed using whole retina lysates (**Figure 3.3, d**). Unrecombined *Srf-flex1* allele resulted in a 1.34 kbp (kilo base pair) product, which was observed in all tested samples. Tamoxifen-induced exon 1 excision instead lead to an additional shortened PCR product of 380 bp, which was only observed in animals carrying the PDGFRβ driven CreER^{T2} allele, thus qualitatively confirming successful recombination. Finally, qPCR analysis of *Srf* expression in fluorescence activated cell sorted (FACS) MCs showed almost completely abolished *Srf* expression in PDGFRβ-positive cells.

Moreover, in this project, primary brain MCs (pBMCs) were isolated, cultured and used for *in vitro* studies in complementation to *in vivo* experiments. These cells were isolated from 6-8 weeks old mice harboring a hemizygous *Srf-flex1* allele, enabling genetic ablation of *Srf* upon treatment with the membrane permeable fusion protein Tat-Cre [168]. *Srf-flex1* cells express normal levels of SRF whereas Tat-Cre treated cells harbor a mutated *Srf* allele, similar to the above mentioned *Srf-flex1::Pdgfrb-CreER*^{T2} tamoxifen inducible mouse model. Treatment of *Srf-flex1* pBMCs with Tat-Cre lead to downregulation of *Srf* as verified by qPCR analysis (**Figure 3.3, f**). In addition, a reduction of SRF protein levels was shown by western blot analysis (**Figure 3.3, g**). Taken together, these results indicate an efficient deletion of the *Srf* allele and thus a strong *Srf* downregulation in retinal MCs as well as in pBMCs in this mouse model.

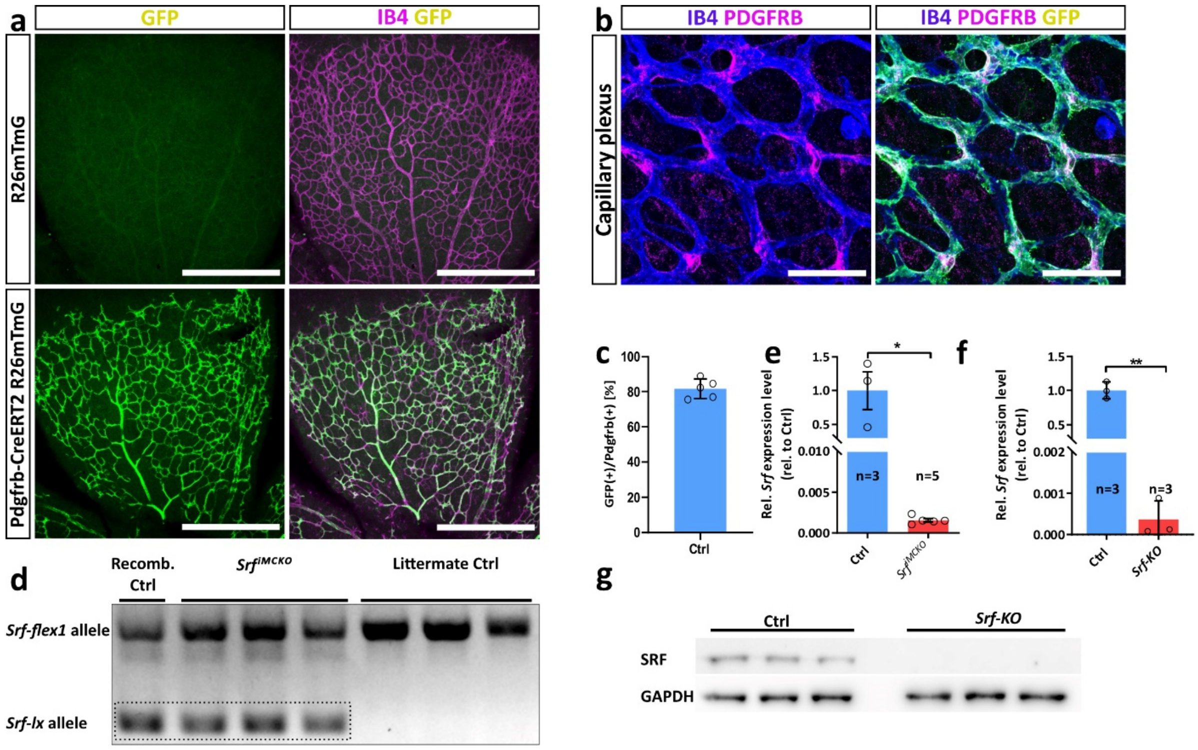

Figure 3.3| Verification of specific *Srf* deletion in retinal MCs and pBMC cultures. (a) Confocal images of stained retinas of tamoxifen induced hemizygote *Srf-flex1* animals with crossed-in $\mathit{Rosa26}^{mTmG}$ reporter allele. Control animals harbor no $\mathit{Pdgfrb\text{-}CreER}^{T2}$ allele, showing no recombination event (upper panels). In contrast, combination of $\mathit{Rosa26}^{mTmG}$ with $\mathit{Pdgfrb\text{-}CreER}^{T2}$ drives GFP expression (lower panels). Retinas were co-stained with EC specific marker IB4. **(b)** High resolution confocal images of retinas stained for IB4 (EC-marker), PDGFRB and GFP (recombined cell) showing specific recombination of mural cells. **(c)** Quantification of recombination rate of MCs. **(d)** Generic PCR of whole retina lysates, showing amplification of *Srf*-Exon1 leading to specific *flex1*-allele band and the recombined *Srf-lx* allele (exon 1 deletion) in Srf^{iMCKO} animals. **(e,f)** qPCR quantification of *Srf* expression levels of sorted retinal MCs (e) and pBMC cultures (f). **(g)** Western blot analysis of Tat-Cre treated (*Srf-KO*) and respective control (Ctrl) pBMC cultures, verifying abolishment of wildtype SRF protein in *Srf-KO* cells. Error bars indicate s.d. of the mean. Statistical comparison by unpaired t-test with Welch's correction. Number of analyzed animals or independent repetitions (n) are indicated. ns= not significant, *p≤0.05, **p≤0.01, ***p≤0.001.

3.1.3 SRF-deficient PCs cause disturbed early vascular morphogenesis

During early angiogenesis at P6, SMCs are immature and most MC coverage of the retinal vasculature is comprised of PCs. Therefore, this developmental stage is optimal to study PC function in angiogenesis. So far, it was shown in various studies that PCs directly influence early angiogenesis. Abnormal PC involvement is linked with leakage in the brain and in the retinal vasculature [45,73]. Furthermore, loss of PCs on the retinal vasculature is one of the hallmarks of diabetic retinopathy [45,59]. To investigate any potential influence of SRF in PCs on early vascular morphogenesis, *Srf*^{iMCKO} retinal explants, in form of flat-mounts, were analyzed at P6.

Staining of retinal flat-mounts with ICAM2 revealed a delay in vascular outgrowth in *Srf*^{iMCKO} retinas (**Figure 3.4, a and b**), causing *Srf*^{iMCKO} retinas to be less vascularized in comparison to control (25.6 ±15.5 %, p=0.0004). Likewise, a reduced number of branches within the capillary plexus, accompanied by increased avascular area, was observed in *Srf*^{iMCKO} retinas (23.2 ±7.8 %, p<0.0001), demonstrating remodeling defects (**Figure 3.4, c and d**). Moreover, the retinal vasculature normally grows radially in an arterial-venous alternating fashion. However, in rare cases arterial vessels can intersect venous vessels. This kind of vessel crossings can lead to disrupted venous perfusion and is known as arterio-venous nicking (AVN). AVN correlates with hypertension and is so far an insufficiently understood pathological formation in humans. Interestingly, *Srf*^{iMCKO} arterial vessels frequently changed growth direction and formed AVNs (**Figure 3.4, a**).

To further determine remodeling defects, retinas were stained for collagen IV (ColIV). ColIV is a vital part of the extracellular matrix (ECM) and is secreted by MCs and ECs early after establishment of a new vessel [8]. In the process of remodeling, lack of perfusion can cause the retraction of newly formed vessels. In such a case, a trace of ColIV is left behind, which can be detected afterwards [27]. *Srf*^{iMCKO} retinas display large areas of ColIV traces (so-called “empty sleeves”) rather than single retraction events. Such “empty sleeves“ could not be observed in the control group (**Figure 3.5**). These data strongly suggest defective remodeling and instability of newly formed vessels in the absence of SRF.

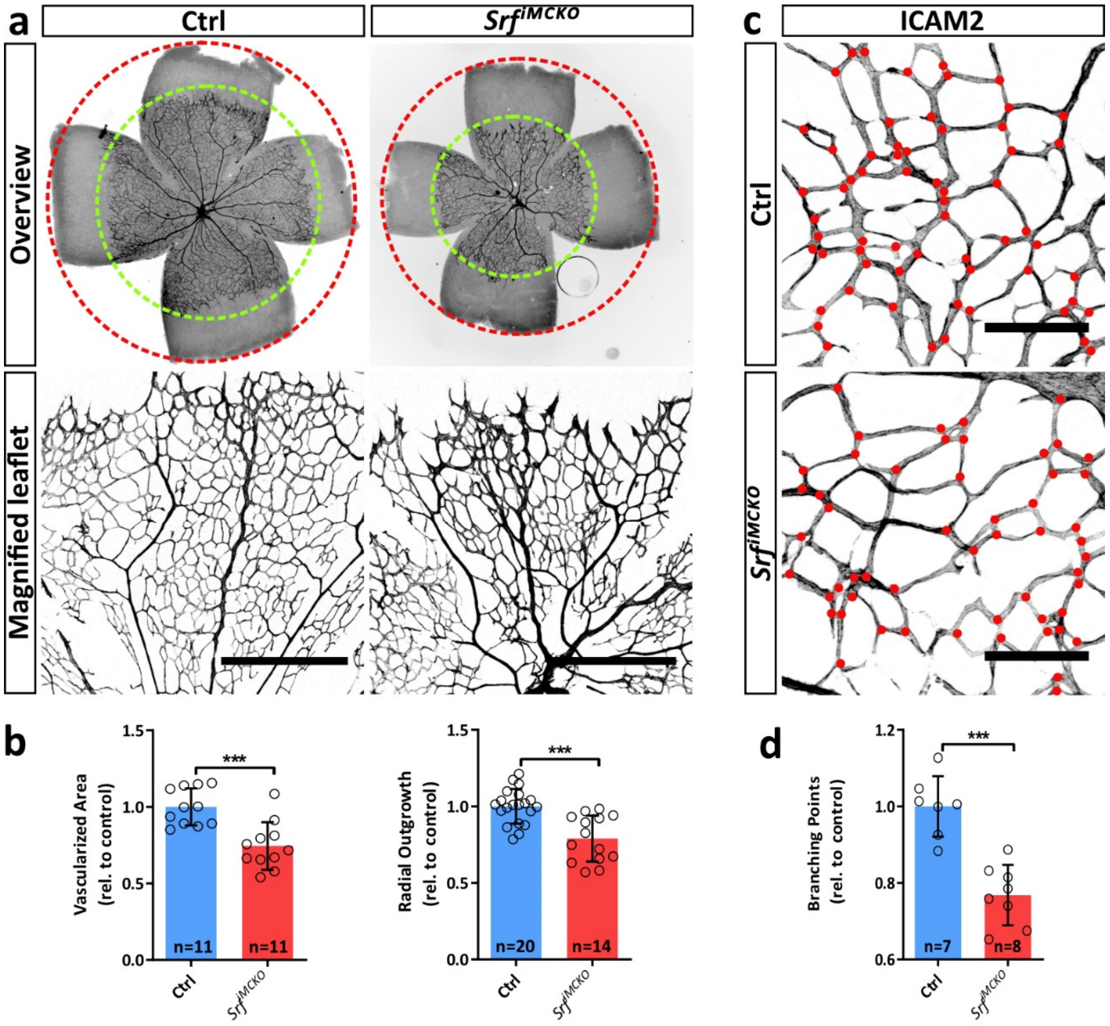

Figure 3.4| SRF-deficient PCs cause impairment of early vascular morphogenesis of the retina. (a) Epifluorescence overview images (upper panel) and confocal images (lower panel) of whole mount stainings of retina explants display delayed vascularization and outgrowth of the developing primary vascular plexus. Scale bar: 250 µm **(b)** Respective quantification of the vascular area (green) and the radial outgrowth (red) shown in (a). **(c)** Comparison of branching points between *Srf*^{iMCKO} retinas and respective controls. Red dots indicate branching points. **(d)** Quantification of branching points illustrated in (c). Error bars show s.d. of the mean. Statistical comparison by unpaired t-test with Welch's correction. Number of analyzed animals (n) is indicated. ns = not significant, *p≤0.05, **p≤0.01, ***p≤0.001.

Defective vascular morphogenesis is linked to deficient PC investment and correlated with increased leakage and breakdown of the blood retina barrier and thus to extravasation of red blood cells (RBC) [45,46,59]. ICAM2 and ColIV staining so far suggested a delayed vascular outgrowth and impaired remodeling. Therefore, Ter199-staining was performed to detect RBCs and possible extravasation. The retinal vasculature is not mature at P6, which means that the blood retina barrier (BRB) is not fully developed yet. RBC extravasation therefore occurs to a certain degree also in wild type vessels, especially on the sprouting front of the retinal vasculature. However, *Srf*^{iMCKO} retinas showed a dramatic increase of RBC extravasation

(5.38 times (±2.32; p=0.0298)) in comparison to control retinas (**Figure 3.5**). This emphasizes increased permeability and dysfunctional barrier capacities of the retinal vasculature in *Srf*^{iMCKO} mice.

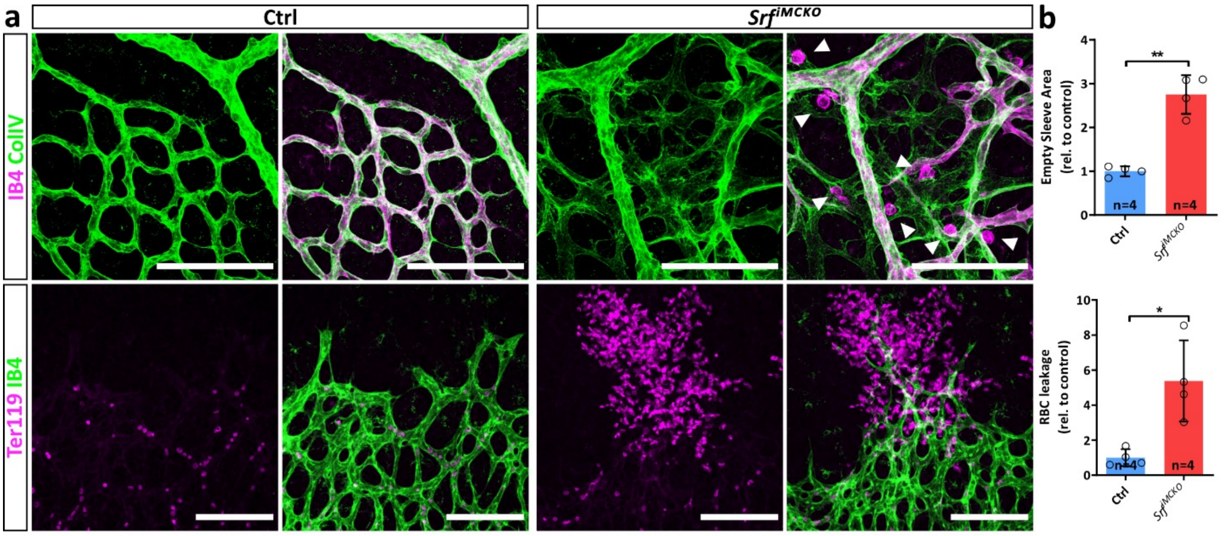

Figure 3.5| Increased vessel retraction and RBC extravasation in *Srf*^{iMCKO} retinas at P6. (a) Upper row showing confocal images of the endothelial vasculature (IB4, purple) and ColIV (green) highlighting present (IB4^{+}+ColIV^{+} area) and retracted vessels (ColV^{+}+IB4^{-} area). Note IB4^{+} microglia and/or macrophages (white arrowheads) in *Srf*^{iMCKO} retinas, suggesting inflammatory reactions. Lower row shows confocal images of RBC extravasation events at the angiogenic front. Note Ter119^{+} RBCs (magenta) without association to IB4^{+} (green) vessels. Scale bar 100 µm. **(b)** Respective quantifications of (a). Error bars show s.d. of the mean. Statistical comparison by unpaired t-test with Welch's correction. Number of analyzed animals (n) is indicated. ns = not significant, *p≤0.05, **p≤0.01, ***p≤0.001.

3.1.4 *Srf*-mutated PCs proliferate less and lag behind the sprouting front, resulting in dilated leading vessels

During vascular development, ECs at the angiogenic front recruit PCs via the paracrine PDGFB-PDGFRβ signaling axis [48]. A recent study showed - by application of an αPDGFB antibody (AB) - that disruption of PDGFB-PDGFRβ signaling inhibits PC migration towards the sprouting front [59]. This was confirmed by genetic studies, where conditional ablation of endothelial *Pdgfb* as well as the mural PDGFRβ adaptor proteins NCK1/2 resulted in nascent and PC deprived vessels at the sprouting front [45,46,59]. SRF is known to regulate genes needed for migration and proliferation in different cell types [113,169]. Therefore, *Srf*^{iMCKO} retinas and respective littermate controls were stained for NG2 to visualize PCs and to identify any potential differences in coverage of PCs. Control retinas displayed a uniform distribution of PCs throughout the capillary plexus (**Figure 3.6**). The angiogenic front was also evenly covered with PCs except for the endothelial tip cells, which is in line with previous reports [46,72]. In contrast, *Srf*^{iMCKO} retinas showed a 25.4 % (±7.3 %; p=0.0001) reduced coverage at the capillary plexus in comparison to control. Moreover, this effect was stronger at the angiogenic front, where the coverage was even reduced by 50.6 % (±9.3 %; $p<0.0001$). Here, PCs did not reach the nascent vessels at the front, thus leaving them uncovered. This suggests a defect in the migratory and/or proliferative behavior of PCs, which limits their ability to follow the endothelial angiogenic front. These results were reproduced by staining of the vasculature using the MC markers PDGFRβ and desmin (**Supplementary Figure 1**).

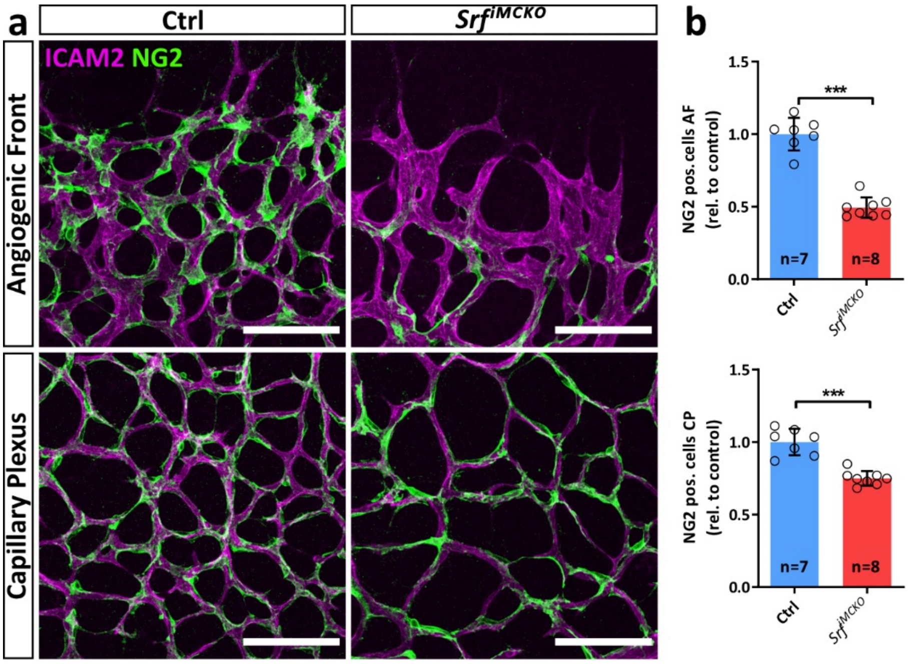

Figure 3.6| SRF-deficient PCs lag behind the sprouting front leaving leading vessels uncovered. (a) Confocal images showing PC coverage at the capillary plexus (CP) and the angiogenic front (AF). ECs were stained with ICAM2 (magenta) and PCs with NG2 (green). Note PC-uncovered and dilated vessels at the leading front of the AF in *Srf*^{iMCKO} retina (right). Scale bar: 100 µm. **(b)** Respective quantifications of the PC coverage. Error bars show s.d. of the mean. Statistical comparison by unpaired t-test with Welch's correction. Number of analyzed animals (n) is indicated. ns = not significant, *$p\leq0.05$, **$p\leq0.01$, ***$p\leq0.001$.

A previous study found that diphtheria toxin-mediated ablation of PCs leads to a dilation of capillaries and a reduction of filopodia at the sprouting front during early angiogenesis [72]. This phenotypic abnormality is triggered by dysregulated vascular endothelial growth factor (VEGF) signaling and causes increased EC proliferation and ultimately an enlargement of capillaries. Mechanistically, pericytic soluble VEGFR1, a potent binder of VEGFA, locally inhibits VEGF signaling and thus allows fine-tuning of EC proliferation and migration at the leading front. *Srf*^{iMCKO} retinas showed severe dilation of vessels at the angiogenic front (**Figure 3.6**). Moreover, and similar to the studies by Eilken et al. (2017) [72], filopodia formation on endothelial tip cells was also reduced in *Srf*^{iMCKO} retinas (33.7 ±6.8 %; $p=0.0002$, **Figure 3.7, a** and **b**). To investigate whether an increased proliferative behavior of ECs might be responsible for dilation of vessels, *Srf*^{iMCKO} animals at P6 and litter mate controls were injected with the thymidine analogue 5-Ethynyl-2´-deoxyuridine (EdU), which efficiently labels proliferative cells. EdU can be visualized by a following chemical click-it reaction. A co-staining with the EC specific nuclear marker ERG-1, allowed the identification of proliferative ECs. As shown in **Figure 3.7** (**c** and **d**), dilated capillaries showed increased numbers of ECs (40 ±14.3 %; p=0.0086) and a higher endothelial proliferation rate (50.5 ±18 %; p=0.0075), thus suggesting impaired PC investment in *Srf*^{iMCKO} mice, in line with previous observations by Eilken et al. (2017) [72].

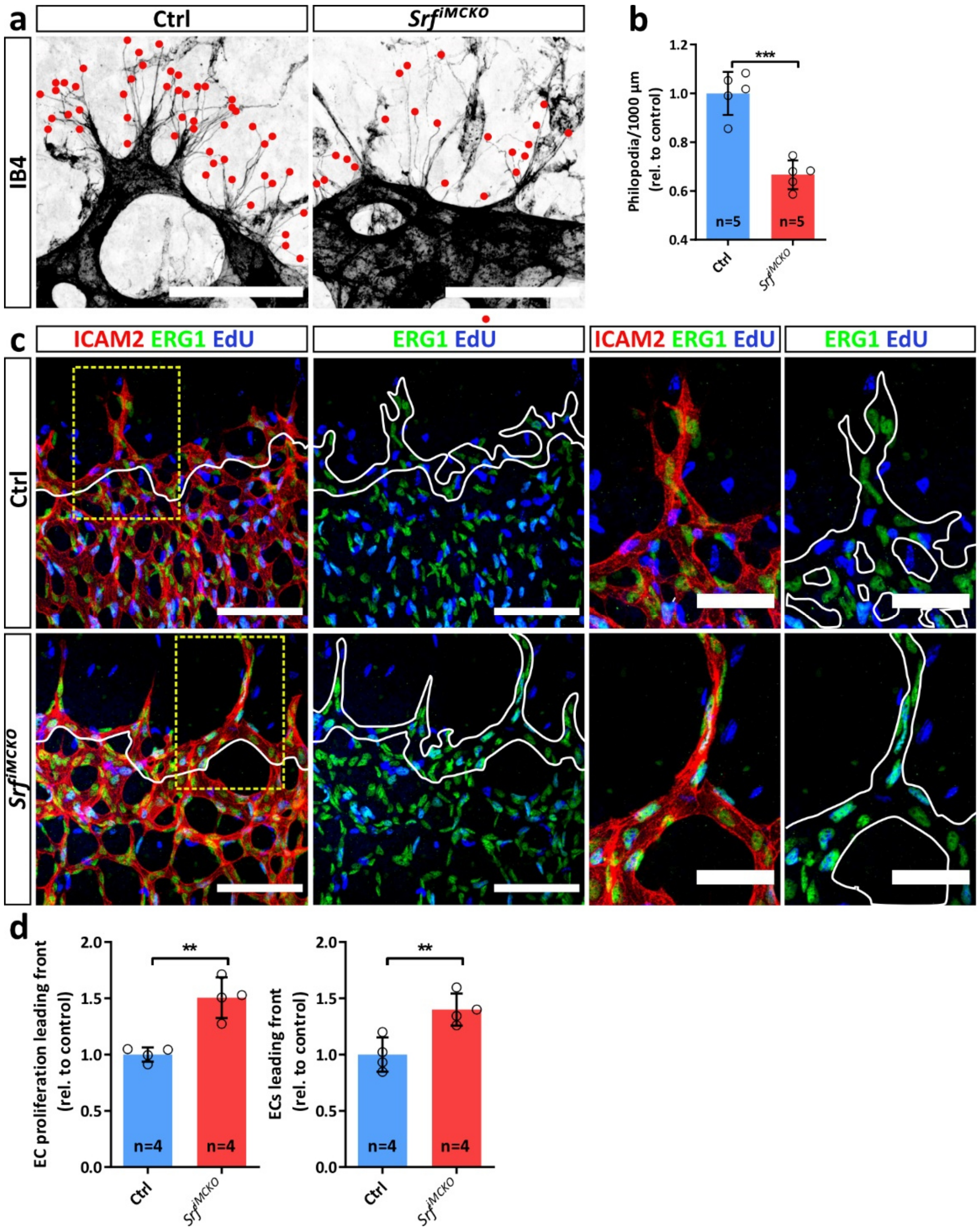

Figure 3.7| Impaired PC engagement leads to dilated capillaries with ECs forming fewer filopodia and displaying increased proliferation. (a) Confocal high-resolution images showing AF stained by IB4; filopodia of endothelial tip cells are highlighted by red dots. **(b)** Respective quantification of filopodia shown in (a). **(c)** Confocal images showing proliferating cells (EdU, blue), ICAM2 (red) and endothelial nuclei (ERG1, green). White lines indicate the border of the leading front (first column) or the vessel shape (second and forth column). Images on the right panels show magnification of the yellow dashed squares shown on the left panel. Scale bar, 100 µm (left) and 50 µm (right). **(d)** Quantification of EC proliferation density at the angiogenic leading front. Error bars show s.d. of the mean. Statistical comparison by unpaired t-test with Welch's correction. Number of analyzed animals (n) is indicated. ns = not significant, *p≤0.05, **p≤0.01, ***p≤0.001.

SRF is described as a master regulator of immediate early response, thus making it a crucial determinant in the process of migration and proliferation [113]. Several studies showed the ability of SRF to induce proliferation in different cell types [116,169]. To investigate whether proliferative defects of SRF-deficient pericytes could in part explain uncovered vessels at the angiogenic front, *Srf*^{iMCKO} and control pups at P6 were injected with EdU to quantify proliferating PCs at the angiogenic front and the capillary plexus. Proliferating PCs were identified by being simultaneously positive for EdU and the MC marker NG2. EdU analysis showed that PCs at the vascular front exhibit an increased proliferation in comparison to the PCs at the capillary plexus in control mice (**Figure 3.8**), which seems plausible as PDGFB is a strong mitogen and PDGF-B-PDGFRB signaling occurs mainly on active sites of angiogenesis [170]. Moreover, SRF-depleted PCs at the CP showed no change in proliferation compared to control, while at the AF a reduced proliferative behavior in comparison to control was observed (31.6 ±5.8 %; p=0.0029), suggesting proliferation deficiency of PCs.

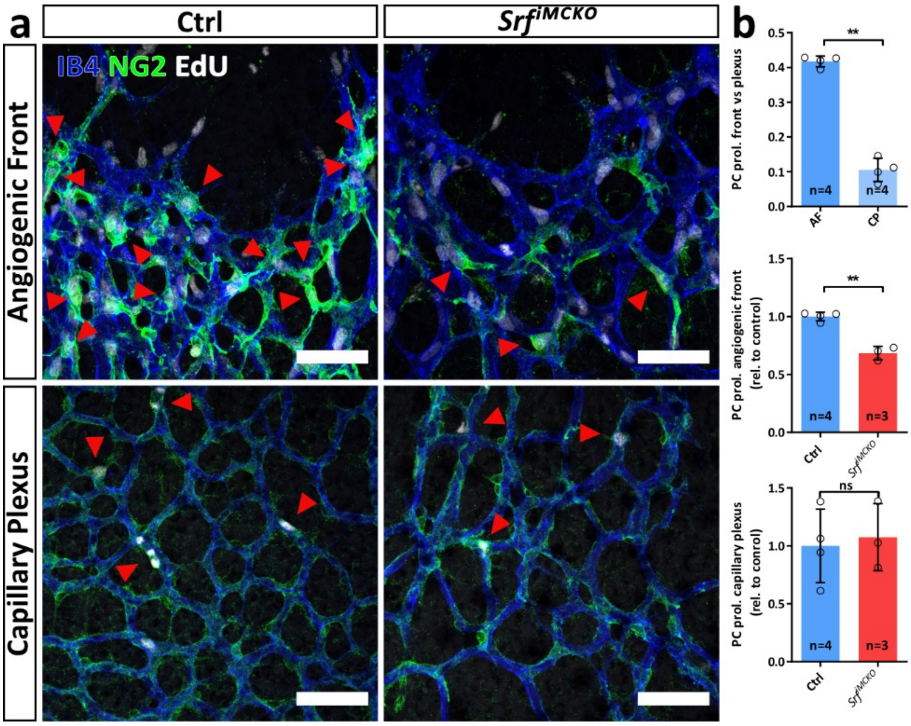

Figure 3.8| PCs with mutated *Srf* show reduced proliferation at the angiogenic front. (a) Confocal images showing proliferating cells (EdU, white), the vascular bed (CD31, blue) and PCs (NG2, green) at the AF and the CP. Red arrowheads point to proliferating PCs (NG2$^+$/EdU$^+$). Scale bar, 50 µm. **(b)** Quantification of PC proliferation at the angiogenic front (AF) in comparison to the capillary plexus (CP) in control retinas (upper graph). Intermediate and lower graph show quantifications of PC proliferation at the AF and the CP (Ctrl vs. *Srf*^{iMCKO}). Error bars show s.d. of the mean. Statistical comparison by unpaired t-test with Welch's correction. Number of analyzed animals (n) is indicated. ns = not significant, *p≤0.05, **p≤0.01, ***p≤0.001.

To further confirm proliferation defects of MCs upon *Srf* knockout, a proliferation assay using pBMCs was performed. To do so, pBMCs were cultured in the presence of the thymidine analogue bromodeoxyuridine (BrdU) for 6 h and treated with PDGFB to stimulate proliferation. Similar to EdU, BrdU incorporates into nuclei of proliferating cells. A staining for BrdU-positive cells confirmed previous *in vivo* observations (**Figure 3.8**) and revealed that proliferation of *Srf-KO* pBMCs was reduced by 47.6 % (±9.6 %, p=0.022) compared to control (**Figure 3.9**). It is thus likely that reduced PC proliferation partially explains uncovered nascent vessels in *Srf*^{iMCKO} retinas (**Figure 3.6**).

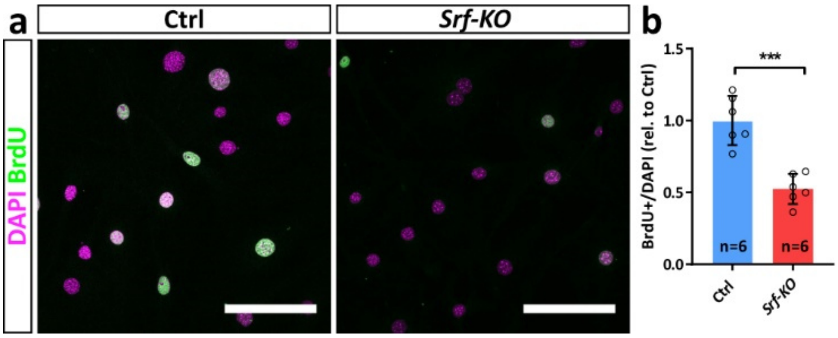

Figure 3.9| SRF deficiency reduces proliferative activity of pBMCs *in vitro*. (a) Confocal images of pBMC cultures stained for nuclei (DAPI, magenta) and proliferating cells (BrdU, green) Scale bar, 100 µm. **(b)** Quantification of pBMC proliferation (DAPI$^+$ + BrdU$^+$). Error bars show s.d. of the mean. Statistical comparison by Mann Whitney test. Number of independent repetitions (n) is indicated. ns = not significant *p≤0.05, **p≤0.01, ***p≤0.001.

3.1.5 Lack of SRF compromises MC migration *in vitro*

Previously shown results (**Figure 3.8** and **Figure 3.9**) demonstrated a significant reduction in PC proliferation upon SRF depletion, which can partially explain the reduced coverage of the vascular plexus. However, decreased PC migration could be a second important factor, which leaves nascent vessels largely uncovered towards the angiogenic front. SRF is known to be a critical determinant for migration in other cell types [113]. Moreover, the difference between the PC coverage of the CP and AF (25.4 % vs. 50.6 % reduction) suggests reduced migratory behavior besides decreased proliferation. To test whether PC migration is compromised upon SRF depletion, an *in vitro* transmigration assay using pBMCs (control vs. *Srf-KO*) was performed. During a transmigration assay, cells have to pass a membrane with defined pore size towards a chemotactic gradient, thus providing information about polarized migration ability. pBMCs were exposed to a PDGFB gradient to induce migration. The number of migrated cells passing the membrane was determined 6 h post stimulation. Notably, 61.1 % (±16.1 %) fewer *Srf-KO* cells passed the membrane in comparison to control (**Figure 3.10, a**), arguing for reduced migratory capacity of *Srf-KO* cells. To further strengthen this point, a scratch wound assay was performed. In this assay a scratch wound is created in a confluent cell monolayer and the closure of that wound by migrating cells is monitored in regular time intervals. Control pBMCs constantly migrated towards the wound, so that after 20 h of migration time approximately 65.9 % (±4.9 %) of the area was closed (**Figure 3.10, c; Supplementary Movie 1**). In contrast, *Srf-KO* cells migrated significant slower (**Figure 3.10, d** upper graph) and closed approximately 42.7 % (±3.8 %) of the scratched area (**Figure 3.10**, **d** lower graph). Moreover, the closure kinetic flattened earlier in comparison to control. Both assays showed a strong reduction in migratory behavior of *Srf-KO* pBMCs. It thus seems plausible that reduced PC migration could be a second crucial factor to explain a strong reduction in PC coverage at the angiogenic front besides reduced PC proliferation.

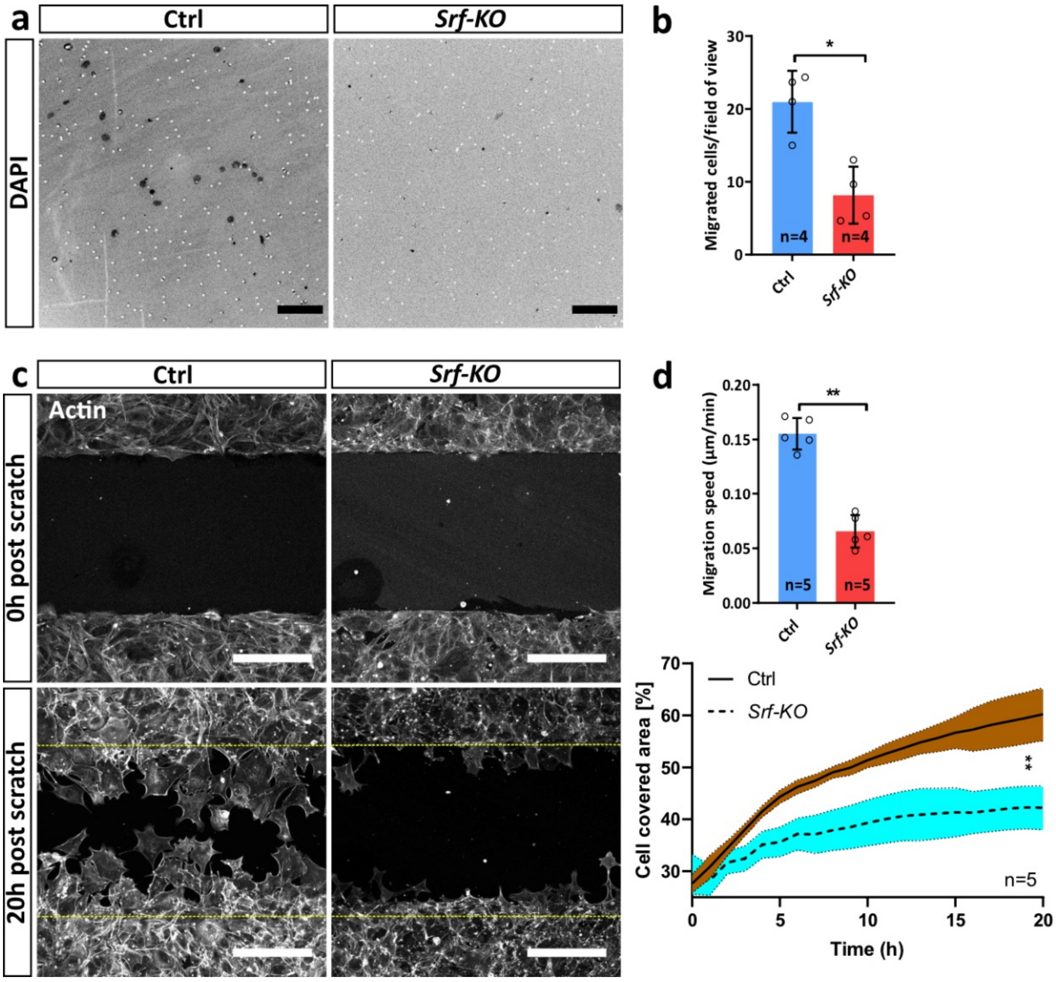

Figure 3.10| *Srf* deletion in pBMCs causes impaired cell migration. (a) Confocal images of a trans-well assay to determine polarized migration towards a PDGFB gradient trough a membrane with defined pore size. DAPI-positive structures (black dots) indicate migrated cells which passed the membrane. Scale bar, 100 µm **(b)** Respective quantification showing average migrated cells per field of view. **(c)** Confocal images of a scratch wound assay showing wound closure at the beginning and after 20 h. Scale bar, 250 µm **(d)** Upper graph, quantification of individual migration speed by cell tracking of 24 cells out of 5 independent experiments. Lower graph, quantification of wound closure over time. Error bars show s.d. of the mean. Statistical comparison by Mann Whitney test. Number of independent repetitions (n) is indicated. ns = not significant, *p≤0.05, **p≤0.01, ***p≤0.001.

3.1.6 SRF depleted PCs adopt an abnormal physiology and fail to form filopodia

MCs are highly plastic, which is apparent by their cell morphology. MC morphology strongly depends on the function of the vascular bed as well as on the position of MCs on the vascular bed [78]. Therefore, it can be assumed that cytoskeletal dynamics plays a crucial role in orchestrating morphologic adjustments of MCs. SRF is known as a master regulator of the actin network in ECs and fibroblasts [113,171]. During angiogenesis, SRF activates the expression of cytoskeletal proteins to enable filopodia formation in endothelial tip cells [30,147]. Furthermore, previously shown NG2 stainings at P6 retinas already suggested changes in PC morphology (**Figure 3.6**). It thus seems likely that observed changes in proliferative and migratory behavior could be associated with morphologic changes. To investigate this, P6 retinas of tamoxifen induced *Rosa-mTmG::Pdgfrb-CreERT2::Srf-flex1* and control mice were stained for GFP and IB4 to highlight the membrane of *Rosa26*^{mTmG}-recombined MCs and the vascular bed, respectively. Stainings were analyzed using high resolution confocal microscopy.

Confocal high-resolution imaging showed that PCs at the capillary plexus enveloped the capillaries in controls (**Figure 3.11, left panel**). The nuclei lay regularly on the edge of a branching point at the endothelial capillaries. Furthermore, PCs formed long and thin tube-like protrusions that contacted neighboring PCs. Contrary, *Srf*^{iMCKO} PCs did not show tube-like protrusions. Instead, protrusions were shortened and flattened.

Control PCs at the angiogenic front ubiquitously formed filopodia, which were oriented towards the sprouting front (**Figure 3.11, right panel**). Directional formation of filopodia towards the sprouting front suggests that PCs sense a PDGFB gradient created by endothelial tip cells. In comparison to PCs at the capillary plexus, PC nuclei were found on top of or under the capillaries. In addition, PCs were in close contact to neighboring PCs indicated by overlapping membranes. Strikingly, SRF-deficient PCs at the angiogenic front lost their ability to form filopodia. Instead, the cell edges were blunt ended, the PCs were prolonged and didn’t reach the leading front (as already shown in **Figure 3.6**). The membrane was strongly flattened and only partly covering the vascular bed. Taken together, *Srf*^{iMCKO} PCs were not seen to form proper filopodia, which was distinct from control PCs at the angiogenic front. This observation would be in agreement with impaired PDGFB signaling.

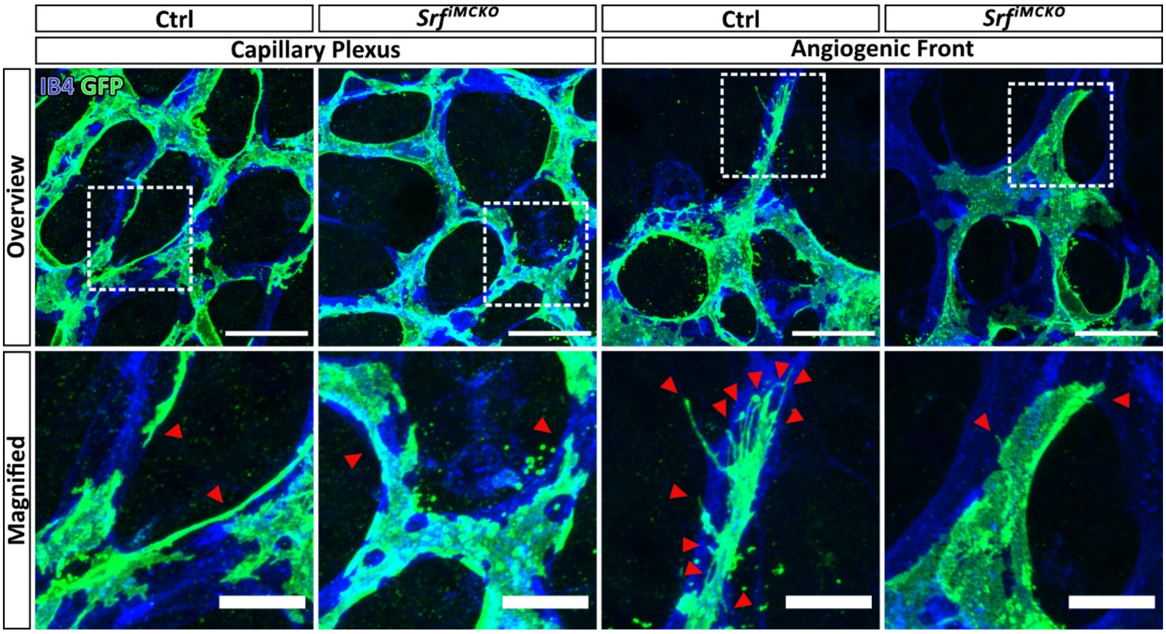

Figure 3.11| SRF-deficient PCs adopt abnormal morphology and fail to form filopodia. Confocal images showing the CP (left) and AF (right) stained by IB4 (ECs, blue) and GFP (PCs, green). Dashed, white boxes indicate magnified regions depicted in the lower row. Red arrowheads pointing to filopodia formations (in the angiogenic front) and tube like protrusions (in the capillary plexus). Note the absence of filopodia as well as the shortened and flattened protrusions at *Srf*^{iMCKO} PCs. Scale bars, 25 µm, 10 µm (magnified).

Filopodia are bundles of actin at the front of migratory cells which allow sensing of the environment [172]. The promoter region of beta actin (*Actb*) contains a CArG-box SRF binding element and previous studies have shown that SRF controls actin gene expression [115,114]. Hence, impairment in actin expression could partially explain the inability of *Srf*^{iMCKO} PCs to form filopodia. In order to study the cytoskeletal consequences of SRF absence, control and *Srf-KO* pBMC cultures were stained using SiR-Actin probes, which specifically mark filamentous (F-) actin. Movies using a confocal live-cell-imaging approach were acquired. The SiR-probes are cell permeable and fluorogenic molecules developed specifically for live imaging [173].

Interestingly, *Srf-KO* pBMCs showed a strong reduction of stress fibers in comparison to control cells (**Figure 3.12, a**). However, cortical actin seemed to be preserved. Measurement of actin signal of images revealed an approximate reduction by 67.4 % (±6 %; p=0.0079) in *Srf-KO* pBMCs compared to control (**Figure 3.12**, **b**). A complementary analysis of actin gene expression levels by qPCR in pBMC cultures verified microscopic observations and showed a reduction of *Actb* transcripts by 83 % (±2.1 %; p<0.001) (**Figure 3.12**, **b**). To test if compromised actin expression affects the ability of pBMCs to react to physiologically relevant stimuli, starved pBMCs were treated with PDGFB. As expected, control pBMCs reacted to PDGFB by strong changes in the actin skeleton, namely increased stress fiber formation and increased cell motility (**Figure *3.12*, c; Supplementary Movie 2**). In contrast, *Srf-KO* cells showed almost no reaction to the PDGFB stimulus. It is thus likely that the observed migration defects in *Srf*^{iMCKO} MCs are caused by the inability of the actin cytoskeleton to react to the natural PDGFB gradient during angiogenesis.

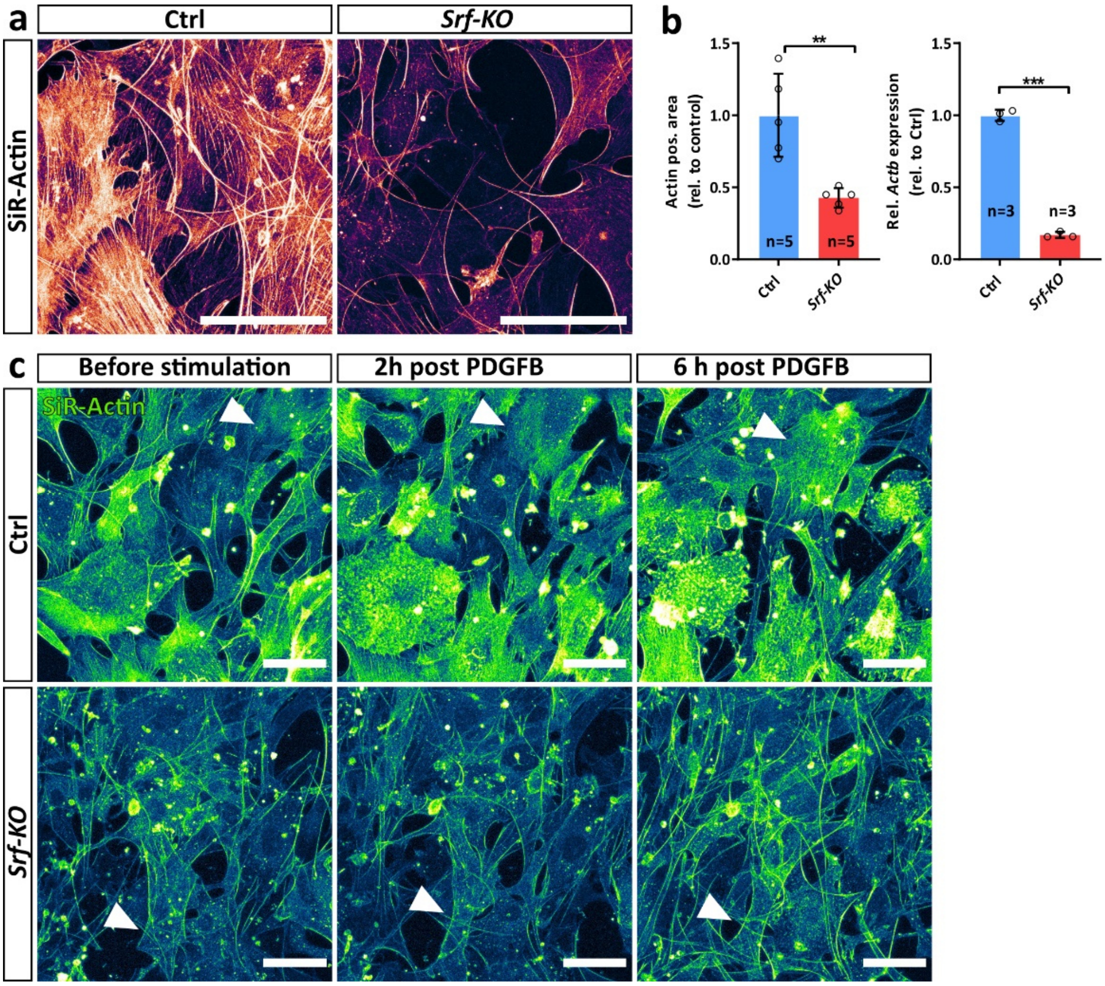

Figure 3.12| Deletion of *Srf* compromises actin gene expression and cytoskeleton dynamics *in vitro*. (a) *Srf-KO* and control pBMC cultures stained by SiR-Actin. Note the reduction of F-actin (highlighted by SiR-Actin) in *Srf-KO* cells. Scale 100 µm. **(b)** Respective quantification of actin positive area and relative transcript levels of *Actb* determined by qPCR. **(c)** Stimulation of Ctrl and *Srf-KO* pBMCs with 30 ng/ml of PDGFB. Note the accumulation of F-actin in Ctrl cells (white arrowheads, Ctrl row), whereas the *Srf-KO* cells show no detectable accumulation of F-actin (white arrowheads, *Srf-KO* row). Scale 50 µm. Error bars indicate s.d. of the mean. Statistical comparison by Mann Whitney test. Number of independent repetitions (n) is indicated. *p≤0.05, **p≤0.01, ***p≤0.001.

3.1.7 PDGFB activates SRF via MRTF

Seminal work suggested that SRF-mediated cell migration acts via a complex mechanism between Rho-GTPases, actin and MRTFs [113]. Receptor tyrosine kinases (RTKs) activate Rho-GTPases such as CDC42, leading to polymerization of monomeric globular-actin (G-actin), which is usually bound to MRTFs to hinder its nuclear translocation. Consequently, the reduced G-actin concentrations allow liberation of MRTF, followed by nuclear translocation of MRTF. Subsequently, activation of SRF Class II target gene expression can occur. This process is fast and occurs within a time frame of a few minutes [135]. In addition, PC co-migration following the leading edge of a vessel sprout in angiogenesis is thought to be dependent on PDGFB [170]. PDGFB is expressed by tip cells, which can be sensed by PCs and therefore migrate towards the sprout. However, so far it is not known how this migration is regulated. Previously shown *in vivo* results indicated reduced presence of PCs towards the sprouting front in Srf^{iMCKO} P6 retinas (**Figure 3.6**). In addition, the performed transmigration and scratch wound assays strongly suggest a defective migration in *Srf-KO* pBMCs (**Figure 3.10**). Therefore, an impaired PDGFB-MRTF-SRF signaling axis could explain the observed phenotype. In a first attempt to test this hypothesis, stably transfected MRTFA-GFP-3T3 cells were used as a model to investigate a potential PDGFB-triggered nuclear translocation of MRTFA. Cells were starved overnight in media containing low concentrations of FCS (0.2 %) which leads to a predominant cytosolic location of MRTFA-GFP (**Figure 3.13, a ; Supplementary Movie 3**). To observe potential MRTFA-GFP translocation, cells were imaged in a live cell imaging approach for 15 min prior to stimulation. Cells were then stimulated with 30 ng/ml PDGFB and imaged for further 45 min in order to observe the kinetics of potential MRTFA-GFP nuclear translocation. Strikingly, PDGFB stimulation increased MRTFA-GFP signal intensity in the nucleus by 3.5 fold in the first 5 min after stimulation. Interestingly, MRTFA-GFP localization shifted back from the nucleus to the cytoplasm after 10 min, reducing the nuclear signal from 3.5 fold to 1.5 fold compared to pre-stimulation conditions and subsequently remaining at this level for the remainder of the experiment (**Figure 3.13**, **b**).

To confirm that PDGFB stimulation does not only lead to MRTF-A translocation to the nucleus, but also induces SRF target gene expression, a luciferase assay was performed with 3T3 wild type cells, which were transfected with the vectors $(TSM)_2$, $(TMM)_2$ or $(MSM)_2$ (**Figure 3.13**, **c**) [29]. All constructs are based on the c-*Fos* promotor containing two times the TCF, SRF and an AP1 binding sites. The AP1 binding site is mutated to reduce initiation of transcription by other transcription factors besides TCF and SRF. The c-*Fos* regulatory elements are followed by the thymidine kinase minimal promotor TK120 to enable transcription of the luciferase gene. The $(TSM)_2$ vector has functional TCF and SRF binding sites, enabling SRF-driven luciferase expression to be subject to TCF or MRTF activity. The $(TMM)_2$ vector, in which the SRF binding site is mutated and thereby preventing any SRF driven response, served as control. The third reporter vector $(MSM)_2$, where the TCF binding site is mutated, monitors MRTF-SRF driven luciferase expression. As additional experimental control conditions besides the use of mutated reporter constructs, the Mek1/2 inhibitor PD-0325901 and the MRTF inhibitor CCG-203971 were used to inhibit the MAPK-activated TCF response and the actin-activated MRTF response, respectively.

Control conditions, using the $(TMM)_2$ reporter, resulted in a basal luciferase activity based on TK120 promotor activity (**Figure 3.13, d**). Addition of PDGFB did not lead to a considerable change in $(TMM)_2$-driven luciferase activity. Similar results were obtained using the $(MSM)_2$ plasmid without stimulation. The $(TSM)_2$ reporter showed without stimulation luciferase activity levels above of the control conditions. This, likely monitoring basal SRF-mediated luciferase expression. Interestingly, stimulation with PDGFB in combination with the $(TSM)_2$ plasmid showed significant and robust increase of luciferase activity by 52.4 % (±15.3 %; $p<0.0001$) in comparison to unstimulated $(TSM)_2$ conditions, suggesting PDGFB triggered activation of SRF. PDGFB stimulation in combination with the $(MSM)_2$ reporter still showed an increase of 20.9 % (±9.9 %; $p=0.1104$) in luciferase activity, which was however not significant. Treatment of PDGFB-stimulated cells with the MRTF inhibitor CCG-203971 in combination with the $(TSM)_2$ reporter led to reduction of luciferase activity, similar to that of the control conditions ($(TMM)_2$ + PDGFB). MEK1/2 inhibition of PDGFB stimulated cells using PD-0325901 also showed a decrease in $(TSM)_2$-luciferase activity, but this effect was less pronounced relative to the CCG-203971 effect. Taken together, the performed luciferase assays strongly argue for a PDGFB-driven SRF activity, which could be genetically and pharmacologically modulated. The assay also suggested an MRTF-dominated SRF activation by PDGFB, but additional experiments are needed to further investigate the effects of PDGFB signaling on MRTF-SRF activation.

Therefore, control and *Srf-KO* pBMCs were stimulated with PDGFB and gene expression of MRTF targets as well as TCF targets was evaluated. For this, pBMC cultures were starved overnight, in order to sensitize the cells for stimulation and to minimize the influence of other signaling pathways. After starvation, the cultures were stimulated with 20 ng/ml of PDGFB for 20 h. Cells were then harvested for RNA isolation and gene expression analysis by qPCR. Strikingly, gene expression analysis showed a strong upregulation of the MRTF-regulated SRF target genes *Acta2* (4.3 fold ±0.49; $p<0.0001$), *Tagln* (7.8 fold ±2.49; $p=0.0029$) and *Actb* (1.72 fold ±0.25; $p=0.0052$) upon PDGFB stimulation of control pBMCs, while *Acta2* and *Tagln* expression was almost abolished upon *Srf* deletion (**Figure 3.13, e**). Even though *Actb* expression was not abolished upon *Srf* deletion, nevertheless *Actb* expression was not further increased by PDGFB treatment of *Srf-KO* pBMCs. Interestingly, no significant increase of the TCF-SRF regulated immediate early genes *c-Fos* and *Egr-1* could be observed. Moreover, *c-Fos* expression was even decreased (4.3 fold ±0.13; p=0.0013), indicating a dominating MRTF-SRF signaling axis. Taken together, all three experiments suggest that PDGFB signaling drives SRF-activation, and most likely through actin-MRTF signaling.

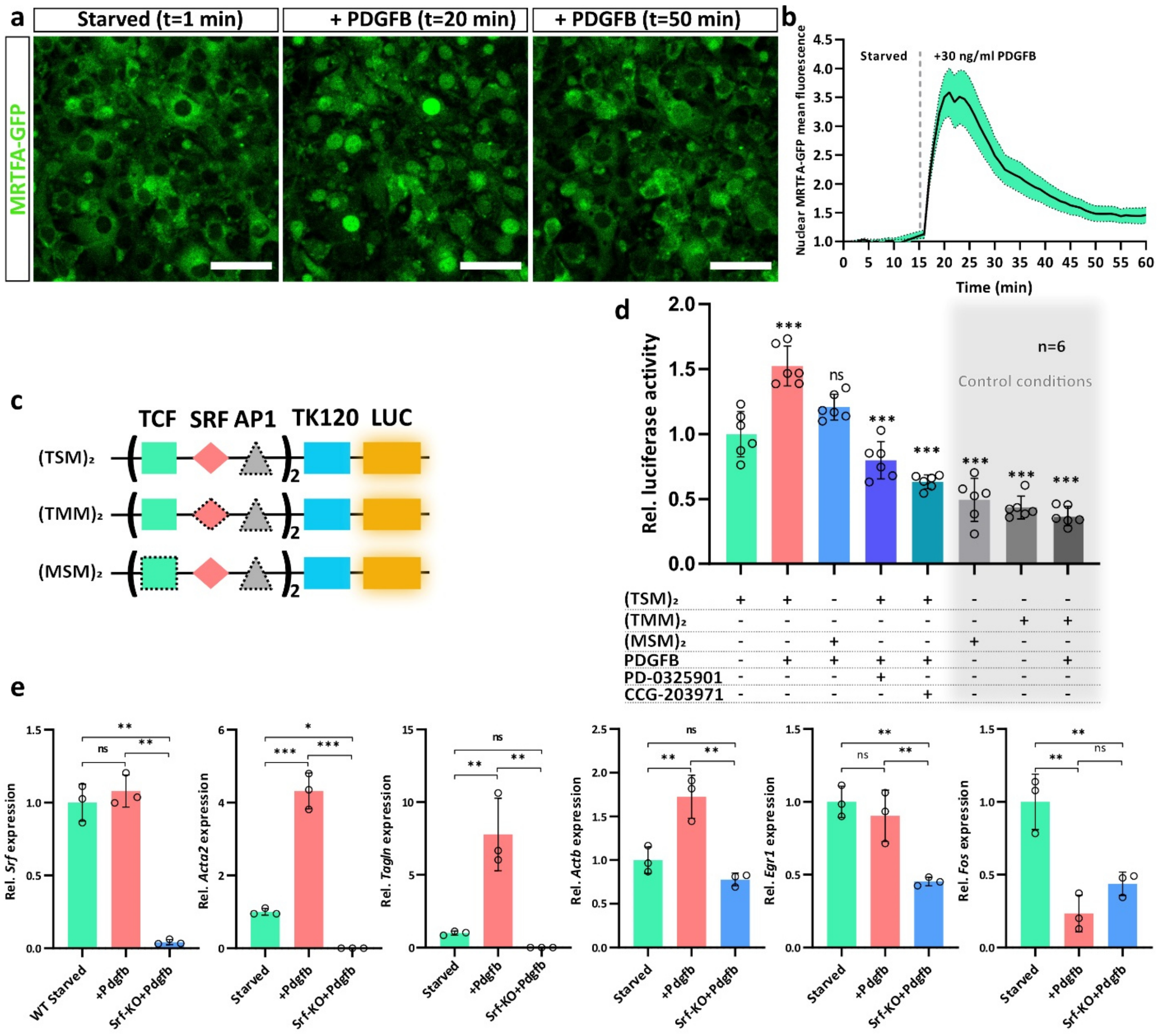

Figure 3.13| PDGFB drives nuclear translocation of MRTF-A and activates SRF target genes. (a) Confocal live imaging of 3T3 cells stably transfected with MRTFA-GFP. The cells are shown before and after PDGFB stimulation. Time points are indicated. Scale bar, 50 µm. **(b)** Quantification of nuclear mean intensity of MRTFA-GFP signal over the time course of the experiment. In total, 29 cells were quantified. The experiment was carried out three times (n=3). Standard error of the mean (s.e.m.) is indicated in green. **(c)** Vector constructs used for luciferase assay, containing TCF, SRF and AP1 binding sites of the c-*Fos* promoter. Thymidine kinase minimal promoter (TK120) drives basal luciferase (LUC) expression. Symbols with dashed borders indicate mutated binding sites for respective transcription (co-) factor. **(d)** Luciferase assay to verify SRF-driven luciferase activity upon PDGFB stimulation. Activity was modulated using vector constructs $(TMM)_2$ and $(MSM)_2$ as well as by using the Mek1/2 inhibitor PD-0325901 or the MRTF inhibitor CCG-203971. **(e)** Gene expression analysis using qPCR of MRTF-SRF target genes (*Acta2*, *Tagln* and *Actb*) as well as TCF-SRF target genes (*Egr1* and c-*Fos*) in starved and PDGFB stimulated *Srf*-wild type (green and red bars) and *Srf-KO* (blue bars) pBMCs. Error bars indicate s.d. of the mean. Statistical comparison by one-way ANOVA (Tukey's multiple comparison test). Number of independent repetitions is indicated. ns = not significant, *p≤0.05, **p≤0.01, ***p≤0.001.

3.1.8 *Srf*-ablated SMCs adopt an abnormal morphology and lose the ability of smooth muscle actin (αSMA) gene expression *in vivo* and *in vitro*

As previously discussed, *Srf*^{iMCKO} PCs exhibited morphologic changes (**Figure 3.11**). A similar comprehensive analysis was performed on SMCs covering arteries and veins of P6 tamoxifen-induced *Rosa-mTmG::Pdgfrb-CreERT2::Srf-flex1* animals and respective controls.

Images taken on aSMCs showed a circumferential structure ensheathing the artery and leaving almost no visible gaps (**Figure *3.14***). The structure of *Srf*^{iMCKO} aSMCs was largely conserved, but regular gaps showed their inability to fully cover the arteries. In addition, the GFP intensity on *Srf*^{iMCKO} membrane protrusions appeared lower, suggesting thinner membranes. vSMCs showed considerably lower coverage in comparison to aSMCs (**Figure 3.14**). vSMCs typically exhibited a stellate shaped morphology forming long and thin protrusions, which were tapered and wrapped around the vein. In contrast, protrusions in *Srf* ablated vSMCs were flattened, shorter and not tapered anymore, similar to previous observations on filopodia in *Srf*^{iMCKO} PCs (**Figure 3.11**). This could point again to defective cytoskeletal dynamics.

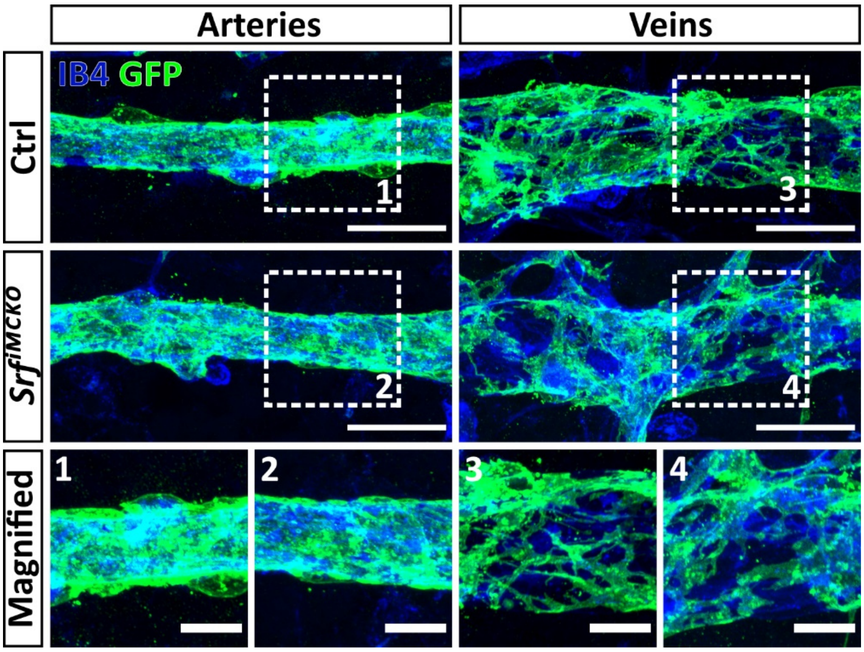

Figure 3.14| SRF-deficient SMCs adopt abnormal morphologies. Images by confocal microscopy showing arteries and veins stained by IB4 (blue) and SMCs by GFP (green). Dashed, white boxes showing magnified regions and are distinguished by numbering (1-4). Note that vSMCs in *Srf*^{iMCKO} animals display shortened and flattened protrusions. Scale bars, 25 µm, 10 µm (magnified).

Additionally, retinas were stained for NG2 and αSMA to visualize the SMC plasma membrane and parts of the contractile machinery. At P6, *Acta2* (αSMA gene name) is exclusively expressed by aSMC, therefore vSMC were not considered in this analysis. αSMA staining revealed solenoid and fibrous structures enveloping the artery (**Figure 3.15, a**). The nuclei were arranged on the side of the artery. Furthermore, the NG2 pattern co-localized largely with the αSMA pattern which was clearly visible on sites of the nucleus. Strikingly, αSMA signals on aSMC of *Srf*^{iMCKO} animals were almost 100 % abolished. A dramatic drop of αSMA gene expression was also observed by qPCR analysis of whole retina lysates (**Figure 3.15, b**). However, analysis of NG2 staining still showed a cell population at the artery, confirming previously shown GFP staining and presence of SMCs (**Figure 3.14**). Analysis of the arterial coverage by NG2-positive cells showed just a slight reduction of 10.1 % (±5.5 %, p=0.0368) but no depletion of cells in *Srf*^{iMCKO} retinas. These results clearly indicated that SRF-depleted aSMCs were not able to express αSMA.

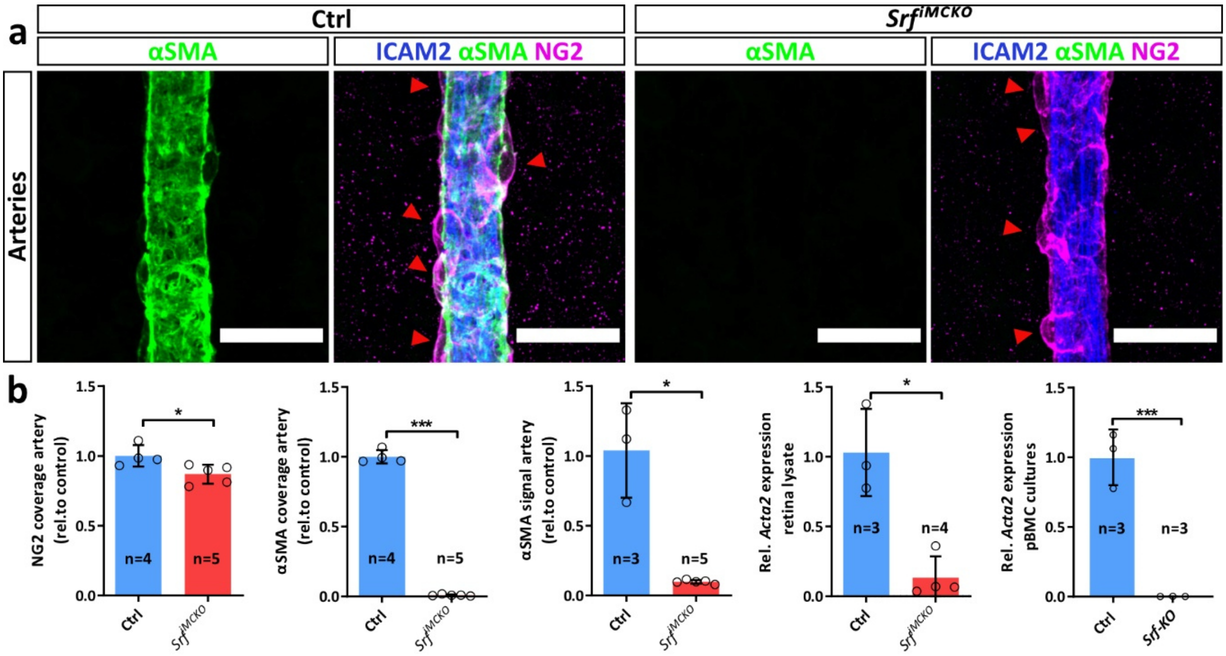

Figure 3.15| *Srf*^{iMCKO} SMCs do not express the contractile muscle protein αSMA. (a) Confocal high-resolution images of P6 arteries, showing ECs (ICAM2, blue), SMC marker αSMA (green) and MC marker NG2 (magenta). Red arrowheads indicate colocalization of αSMA and NG2 at the mural cell nuclei. Note the abolishment of αSMA in *Srf*^{iMCKO}. Scale bars, 25 µm. **(b)** Quantification of aSMC coverage determined by NG2 and αSMA coverage as well as by the measured intensity of αSMA staining. Relative transcript level of *Acta2* (αSMA gene name) determined by qPCR analysis of whole retina and pBMC culture lysates. Error bars indicate s.d. of the mean. Statistical comparison by unpaired t-test with Welch's correction. Number of analyzed animals or independent repetitions (n) is indicated. ns = not significant, *p≤0.05, **p≤0.01, ***p≤0.001.

3.2 Analyses of MC function during pathological angiogenesis

3.2.1 SRF is crucial for pathologic activation of PCs in the oxygen-induced retinopathy (OIR) murine disease model

A recent study showed for the first time that, apart from assuming physiological key functions, PCs can also obtain disease promoting properties under pathological conditions [46]. Using the oxygen induced retinopathy (OIR) mouse model, Dubrac et al. (2018) demonstrated that excessive PDGFB-PDGFRB signaling leads to pathological activation of PCs, which promotes the formation of neovascular tufts (NVT) [46]. NVTs are clustered capillary loops, which show excessive EC proliferation and extravasation of RBCs. During OIR, PCs undergo pathological activation accompanied by a phenotypic shift to a SMC like state, which is characterized by strong upregulation of αSMA. Conditional ablation of the PDGFRB adaptor proteins NCK1 and NCK2 reduced the migratory behavior of PCs and thereby partially rescued the OIR phenotype [46].

As described in chapter 3.1 , SRF-compromised MCs showed reduced migratory properties and a loss of *Acta2* gene expression. Deduced from these observations, I postulated that SRF might be needed during pathologic PC activation in ischemic proliferative events. To investigate any potential role of SRF in PCs during NVT formation, an OIR approach similar to Dubrac et al. was chosen [46].

Srf-flex1::Pdgfrb-CreER^{T2} pups were placed at P7 under hyperoxic conditions (75 % O_2) for 5 days (**Figure 3.16, a**). During this high oxygen phase, hypoxia-driven angiogenesis is suppressed, leading to vaso-obliteration. After the high oxygen phase, mice were returned to normal oxygen conditions (21 % O_2) to provoke a strong hypoxic answer, which forces dysregulated revascularization and NVT formation [174]. During the revascularization phase, tamoxifen was applied to *Srf-flex1::Pdgfrb-CreER*^{T2} mice (P12-P14) in order to induce ablation of *Srf* in MCs and observe any impact on NVT development. NVT formation reaches a peak at P17 , rendering this an optimal time point for analyses (**Figure 3.16, a**) [108].

As postulated, analyses of OIR retinas stained by CD31 indicated a significant reduction of NVT development by 38.5 % (±9.5 %; p=0.0025) in *Srf*^{iMCKO} retinas (**Figure 3.16, b and c**). Moreover, *Srf*^{iMCKO} retinas exhibited an improved revascularization, evident by a reduction of the avascular area by 35.2 % (±21.2 %; p=0.0005).

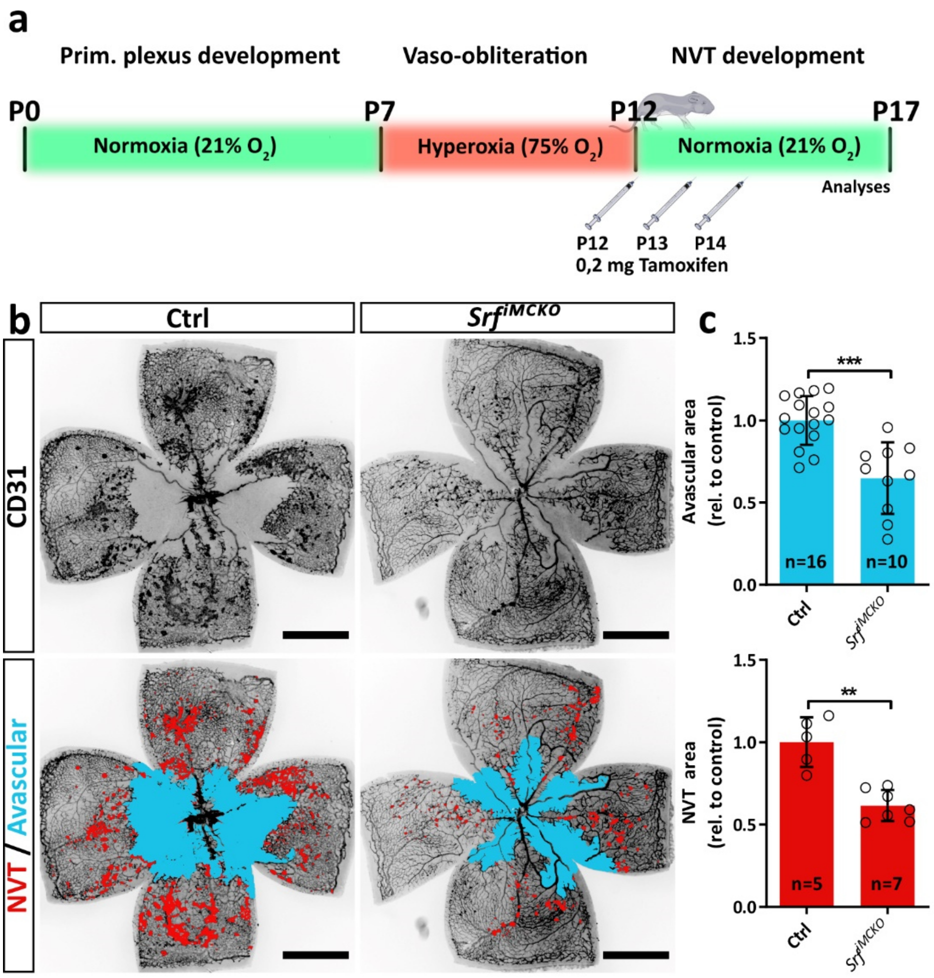

Figure 3.16| Lack of mural SRF leads to a partial rescue of the mouse OIR disease phenotype. (a) Schematic representation of performed OIR protocol. Pups (P7) were kept for five days at high oxygen condition (75 % O_2) leading to vascular obliteration of existing capillaries. At P12, these pups were transferred back to normoxic conditions (21 % O_2) to trigger NVT development. Tamoxifen was applied thrice between P12 and P14 to induce mural *Srf*-KO during the revascularization phase. **(b)** Epi-fluorescence overview images of *Srf*^{iMCKO} and control OIR retinas. The avascular (blue) and NVT area (red) are highlighted in the lower panel. Note the reduction of avascular and NVT area in *Srf*^{iMCKO} retinas. Scale bars, 1 mm. **(c)** Quantification of avascular (upper graph) and NVT area (lower graph). Error bars show s.d. of mean. Statistical analysis by unpaired t-test with Welch's correction. Number of analyzed animals (n) is indicated. ns = not significant, *p≤0.05, **p≤0.01, ***p≤0.001.

Additional high-resolution microscopy of OIR retinas confirmed reduced NVT sizes (**Figure 3.17**, **a**). Co-stainings of NG2 and desmin on OIR retinas verified the presence of PCs on NVTs. NG2 coverage was unchanged, whereas desmin coverage was slightly reduced in *Srf*^{iMCKO} retinas (**Figure 3.17**,**a** and **b**). This observation is in conflict with the previous publication by Dubrac et al. (2018), which reported a reduction of PCs upon genetic interfering with the PDGFBR pathway in PC [46].

Under control conditions, NVTs were strongly positive for αSMA, indicating pathologic PC activation, in line with the mentioned report [46]. Conversely, deletion of *Srf* resulted in almost full abolishment of αSMA coverage (92 ±6.2 %; $p<0.0001$), suggesting reduced pathologic activation (**Figure 3.17**, **a** and **b**).

Furthermore, qPCR analysis of whole *SRF*^{iMCKO} and littermate control OIR retina lysates was performed. *Srf* expression indicated a tendency of reduced transcript levels (49.2 ±4.5 %; $p=0.0679$) in *SRF*^{iMCKO} OIR retinas in comparison to control. However, in the measured small cohort ($n=3$) no significance could be determined (**Figure 3.17**, **c**). In line with the αSMA staining on OIR retinas (**Figure 3.17**, **a**), remarkably reduced *Acta2* expression levels were observed in *Srf*^{iMCKO} OIR retinas. Furthermore, expression levels of *Vegfa,* was measured. VEGFA is a primary marker of hypoxia, which is strongly upregulated under ischemic conditions [174]. Therefore, VEGFA is an ideal marker to estimate severity of hypoxia and provides indirect information on the tissue perfusion state. *Vegfa* expression levels were significantly reduced (40 ±3.39 %; $p=0.0202$) under SRF ablation conditions in OIR retinas. This argues for an improved perfusion of the retinal OIR tissue. Additionally, relative expression of *Pdgfb*, which regulates PC attraction, was suggested to be reduced as well in *Srf*^{iMCKO} OIR retinas, although this effect was not statistically significant.

Taken together, obtained results (**Figure 3.16** and **Figure 3.17**) suggested an activation of SRF in PCs during OIR neovascularization, leading to a pathologic PC activation, promoting OIR progression. MC specific deletion of *Srf* during this phase led to mitigation of the OIR disease phenotype.

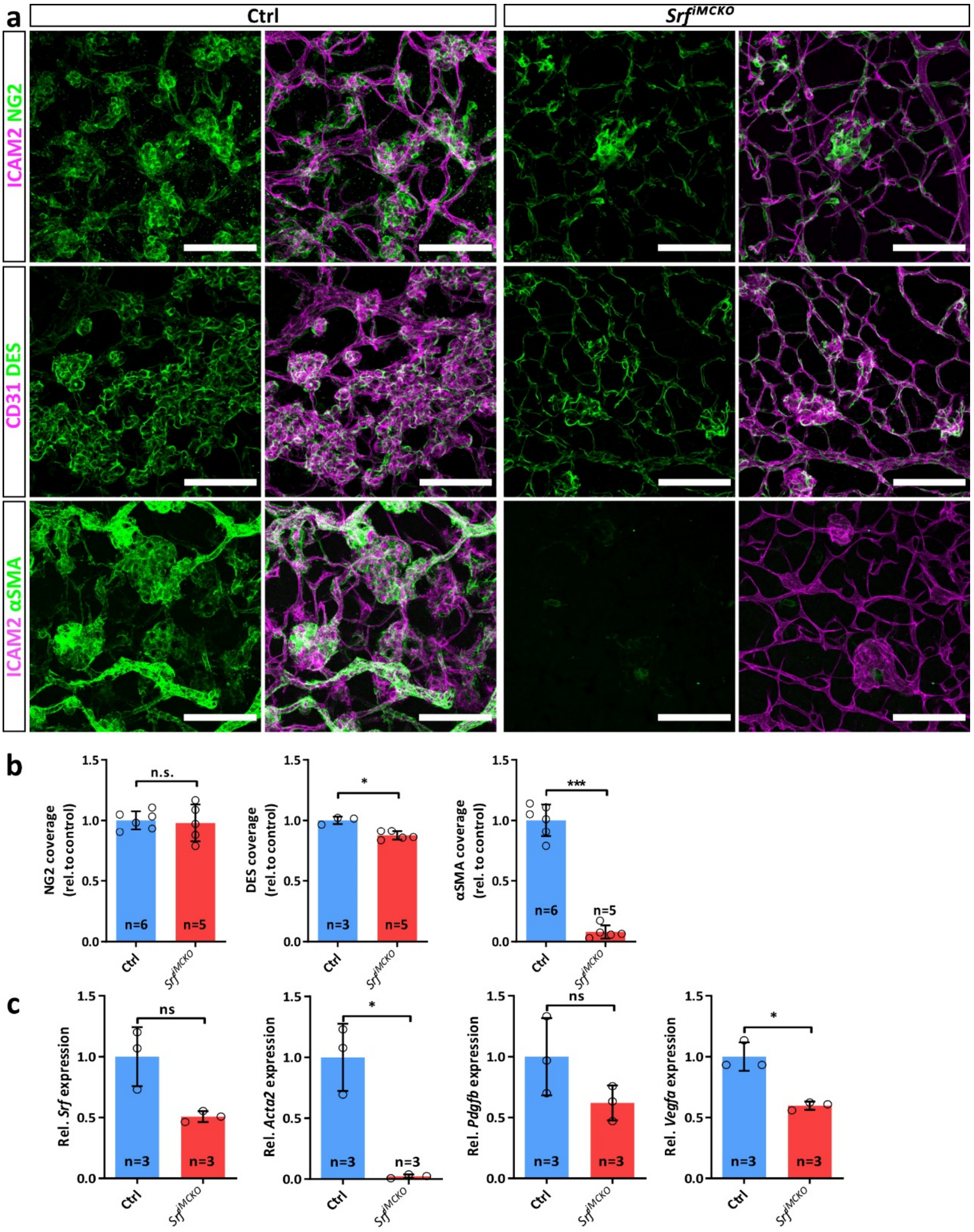

Figure 3.17| Deletion within the mural *Srf* locus reduces pathologic PC activation and mitigates the OIR phenotype. (a) Confocal images of control and *Srf*^{iMCKO} OIR retinas showing NVTs. Staining of NG2 (green, first row) or DES (green, second row) indicates PCs covering ICAM2 (magenta, first row) or CD31 (magenta, second row) stained vessels. Note the abolishment of αSMA signal (green, third row) as well as the reduction of amount and size of NVTs in *Srf*^{iMCKO} OIR retinas. Scale bar, 100 µm. **(b)** Quantification of PC coverage at NVTs, estimated by NG2 and DES coverage as well as pathologically activated PCs determined by αSMA coverage. **(c)** Quantification of relative transcript levels of *Srf*, *Acta2*, *Pdgfb* and *Vegfa* determined in whole OIR retina lysates by qPCR. Error bars indicate s.d. of the mean. Statistical comparison by unpaired t-test with Welch's correction. Number of analyzed animals (n) is indicated. ns = not significant, $^{*}p \leq 0.05$, $^{**}p \leq 0.01$, $^{***}p \leq 0.001$.

3.3 Analyses of MC functions during advanced retinal vascular development

3.3.1 *Srf* ablation in MCs triggers the development of arterio-venous shunts

The data described so far showed that *Srf*-mutated MCs negatively influence the development of the mouse retinal primary plexus (**Figure 3.4** and **Figure 3.5**). During further development (P7-P12), vessels start to sprout horizontally into the retinal tissue building the deep plexus [175]. During this phase of development, the vascular plexus undergoes extensive remodeling. Arteries and veins of the primary plexus become more established and matured and SMCs are increasingly important as the inner blood pressure on arteries and veins increases [63]. This renders P12 an attractive time point to observe potential SMC influence on retinal development. For clarity, MCs covering arteries and veins are referred to as SMCs whereas PCs can be found on capillaries [9]. Whenever both cell types are meant, or when it cannot be fully distinguished between SMCs and PCs, the collective term MC is used. In the following chapters, retinas of Srf^{iMCKO} and respective littermate controls were analyzed at P12 to determine any potential influences of SRF-depleted SMCs on advanced stages of retinal vascular development.

ICAM2 staining of retinas revealed an unexpected, strong impact of MC-specific SRF ablation on the developing vascular network (**Figure 3.18**). Both arteries and veins are found significantly dilated in Srf^{iMCKO} retinas (**Figure 3.18**, **b** and **c**). The arterial diameter increased by 38.6 % (±14.1 %; p=0.0003), while the diameter of veins increased by 27.2 % (s.d. ±13.1; p=0.0006). In control retinas, arteries started to branch out half-way toward the periphery of the retina, arteriolar branches merged gradually into the capillary network and the capillaries were connected to veins. In contrast, arteries in Srf^{iMCKO} retinas did not branch into the capillaries. Instead, arteries largely prevented the transition into capillaries and grew unimpaired toward the distal side of the retina, thereby forming a direct connection with the vein. Such connections are known as arteriovenous (AV)-shunts. Furthermore, the venous part of the shunt was severely dilated and appeared misshaped. Of note, all analyzed P12 retinas showed at least one AV-shunt, indicating a solid penetrance of the phenotype.

AV-shunts are one type of AV-malformations (AVMs), which is known to occur in several human vascular diseases such as hereditary hemorrhagic telangiectasia (HTT). HHT is linked to mutations in genes taking part in the TGFβ pathway of ECs. Interestingly, so far, MCs were not directly implied in the formation of AVMs. Therefore, further work was focused on characterization of AV-shunts in P12 Srf^{iMCKO} retinas.

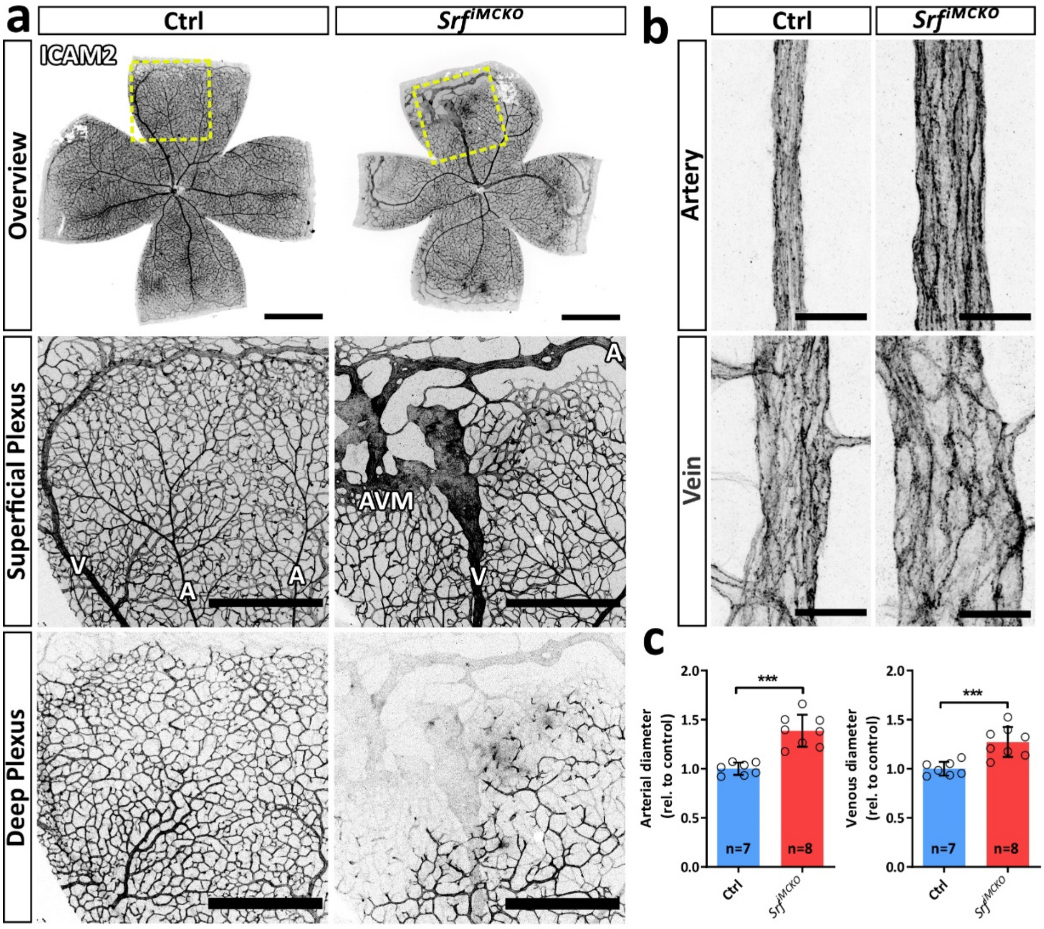

Figure 3.18| SRF-deficient MCs trigger the formation of AV-shunts. (a) Epi-fluorescence overview (upper row) and confocal images of P12 control and Srf^{iMCKO} retina whole mounts, stained using ICAM2. The yellow dashed squares indicate magnified regions of superficial and deep plexus (middle and lower row). Arteries (A), veins (V) and the arteriovenous malformation (AVM) are annotated in white letters. Scale bar: 1 mm (upper row), 500 µm (middle and lower row) **(b)** Confocal, representative images of arteries and veins indicating the dilation of Srf^{iMCKO} main vessels. **(c)** Quantification of artery and vein diameters. Error bars indicate s.d. of the mean. Statistical comparison by unpaired t-test with Welch's correction. Number of analyzed animals (n) is indicated. ns = not significant, *p≤0.05, **p≤0.01, ***p≤0.001.

In addition to displaying shunt formation, Srf^{iMCKO} retinas exhibited a partial loss of the deep plexus (**Figure 3.18** and **Figure 3.19**). In contrast to other studies, where PC depletion led to total disruption of the deep plexus [45,59], the deep plexus in Srf^{iMCKO} retinas was still formed, albeit only partially. The vascular density of the deep plexus was 30 % reduced (±9.2 %, p=0.0049) compared to control retinas (**Figure 3.19**, **a** and **b**). This was complemented by a reduced number of branching points (40.5 ±8.9 %; p=0.0012). On sites of AV-shunts, no deep plexus could be detected at all (**Figure 3.18**, **a**). During physiological retinal vascular development, endothelial sprouts mainly arise from venous origins. A local lack of the deep plexus on AV-shunts therefore indicates the inability of horizontal sprouting in Srf^{iMCKO} retinas.

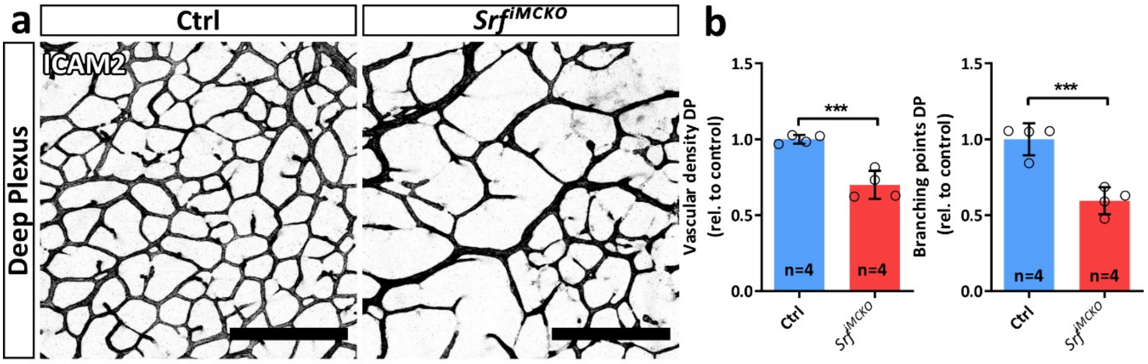

Figure 3.19| Disrupted development of the deep plexus in Srf^{iMCKO} retinas. (a) Confocal images stained with ICAM2 show the vasculature of the deep plexus. Note the reduction in vascular density and branching points. Scale bar, 150 µm **(b)** Respective quantification of vascular density and branching points. Error bars indicate s.d. of the mean. Statistical comparison by unpaired t-test with Welch's correction. Number of analyzed animals (n) is indicated. ns = not significant, *p≤0.05, **p≤0.01, ***p≤0.001.

3.3.2 AV-shunts exhibit increased EC density but reduced proliferation

Several conditional murine KO models provide evidence for formation of AVMs upon compromising the endothelial TGFβ pathway [94,176]. ECs of these malformations typically show increased proliferation and density. A similar behavior in Srf^{iMCKO} retinas might suggest dysregulated TGFβ signaling. Therefore, Srf^{iMCKO} animals and littermate controls were injected with EdU to highlight proliferating cells. Subsequent whole mount retina preparations were co-stained with ICAM2 and ERG1 to visualize the vessel network and endothelial nuclei, respectively. Interestingly, ERG1 staining revealed that EC density was locally increased at malformed areas (45.2 ±17.4 %, p=0.0019; **Figure 3.20**, **a** and **b**). However, malformed areas did not show increased proliferation (ERG1$^+$ counts/ERG1$^+$+EdU$^+$ counts). Instead, proliferation was reduced by remarkable 62.8 % (±3.5 %, p=0.0018) in Srf^{iMCKO} retinas compared to control. Possibly, the peak of EC proliferation upon *Srf*-KO occurred before the analyzed time point P12.

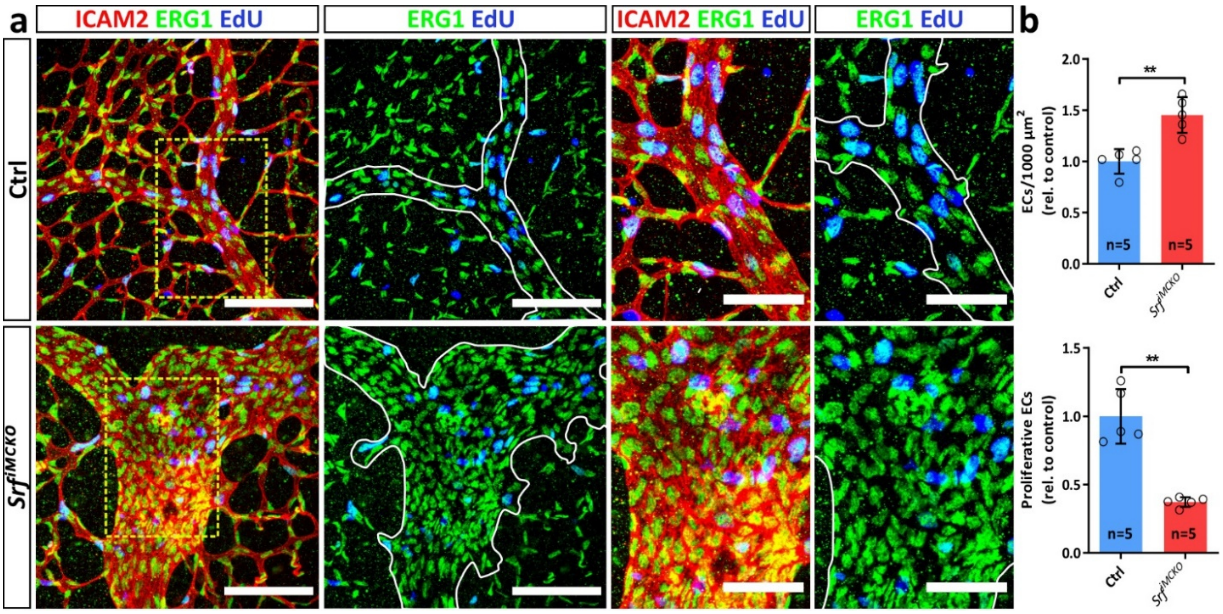

Figure 3.20| AV-shunts exhibit enriched EC density but reduced proliferation. (a) Confocal images of AV-shunts and control veins, showing proliferating cells (EdU, blue), malformed vessels (ICAM2, red) and endothelial nuclei (ERG1, green). White lines define the border of malformations or respective control positions, indicating the vessel shape (second and forth column). Images on the right panels show magnification of the yellow dashed squares shown on the left panel. Scale bar, 100 µm (left) and 50 µm (right). **(b)** Respective quantification of the EC density (ERG1$^+$ counts/ICAM2$^+$ area) and EC proliferation (ERG1$^+$ counts/ERG1$^+$+EdU$^+$ counts). Error bars indicate s.d. of the mean. Statistical comparison by unpaired t-test with Welch's correction. Number of analyzed animals (n) is indicated. ns = not significant, *p≤0.05, **p≤0.01, ***p≤0.001

Staining of VE-Cadherin, an EC specific junctional protein, which is an excellent marker to outline the ECs, was used to visualize the cell shape. VE-Cadherin staining revealed that ECs on malformed vessels display morphologic changes (**Figure 3.21, a**). ECs on veins in control retinas showed a spindle-like morphology, while ECs at AV-shunts appeared rounded and had a rounded structure. In addition, rounded ECs seemed to form protrusions, visualized by the partial zigzag pattern of VE-Cadherin staining. Complementary observations at the ultrastructural level, using transmission electron microscopy (TEM), identified these protrusion as endothelial invagination of the EC membrane (**Figure 3.21, b**). Hellström et al. (2001) previously observed similar invaginations in a mouse model of embryonic PDGFB depletion (global) leading to an MC-depleted embryonic brain vasculature [44]. In this study, depletion of MCs seemed to be responsible for metabolic EC stress and thus for the observed morphologic changes. Taking into account that the here observed AV-shunts display increased EC density (**Figure 3.20**), it could might be that these morphologic changes are provoked by "squeezing" of ECs, which could be accompanied by metabolic stress.

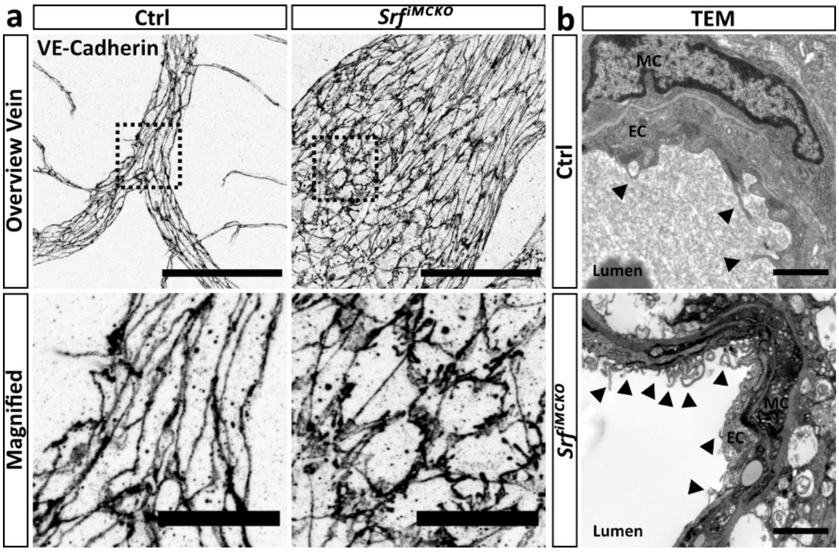

Figure 3.21| ECs at AV-shunts exhibit irregular morphology and invaginate into the vessel lumen. (a) Confocal images of *Srf*^{iMCKO} malformed vessel and respective control. VE-Cadherin staining highlights the outline of ECs. Lower panels show higher magnification of areas indicated in black (upper panels). Note the transition from a spindle-like to a rounded morphology of ECs in *Srf*^{iMCKO} condition. Scale bar, 100 µm (upper row) and 20 µm (lower row) **(b)** Ultrastructural depiction by electron microscopy of control and malformed vein. Black arrowheads pointing to invaginations of the endothelial plasma membrane into the lumen. Scale bar, 1 µm.

3.3.3 MCs in *Srf*^{iMCKO} retinas exhibit altered vessel coverage and a disorganized cytoskeleton

A next step in the phenotypic characterization of *Srf*^{iMCKO} retinas was the characterization of vascular MC coverage. For this, desmin, a type-3 intermediary filament protein specifically expressed in MCs, was stained in control and *Srf*^{iMCKO} retinas. Staining of retinas was performed in combination with ICAM2 to co-stain the vascular bed. Interestingly, the MC distribution on the vascular plexus was altered in *Srf*^{iMCKO} retinas. The MC coverage at malformed areas in *Srf*^{iMCKO} retinas appeared to be increased. A quantification of desmin coverage was performed to determine MC distribution on different areas of the vascular bed (**Figure 3.22, a and b**). In controls, highest MC coverage was observed on arteries (98.5 ±5 %), while the MC coverage on veins and the capillaries was 45.3 % (±6.6 %) and 37.7 % (±0.7 %), respectively. The distinctly higher coverage of arteries with MCs can possibly be explained by the fact that arteries are typically exposed to the highest blood pressure compared to vein and capillaries, which requires stronger support by MCs [177]. In contrast, *Srf*^{iMCKO} retinas showed slight reduction in MC coverage in comparison to controls in all three areas of the vascular bed. MC coverage on arteries was 88.2 % (±5.5 %), whereas veins and capillaries displayed a relative MC coverage of 44.8 % (±2.7 %) and 32 % (±2.2 %), respectively. Interestingly, the coverage on AVMs was 65.2 % (±3.5 %) and therefore remarkably higher than in veins and capillaries of the same group and the control group. A higher coverage may lead to the speculation, that AVMs are exposed to higher blood pressure than veins normally are. Strikingly, the arterial distal part of the artery, which partially forms the AVM, was almost uncovered of MCs (2.7 ±1.3 %). As the distal arterial part is in close proximity to the AVM, MCs might migrate from nearby areas to the AVM, leaving distal arteries uncovered and accumulating at the AVM site. Translocation of MCs could be caused by a local PDGFB gradient. This however, requires further in-depth analyses.

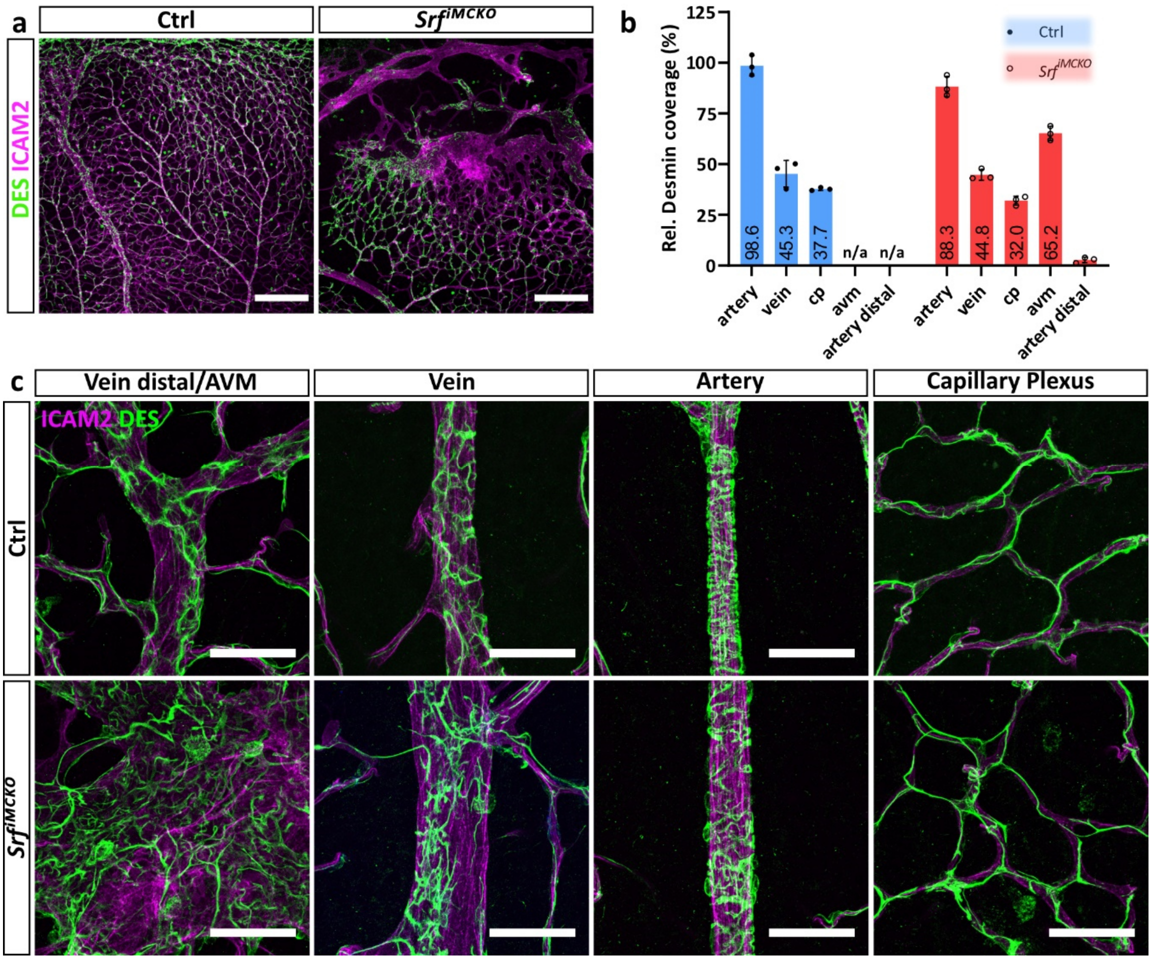

Figure 3.22| Altered MC distribution in *Srf*^{iMCKO} retinas at P12. (a) Confocal overview images showing ICAM2 (ECs, magenta) and DES (MCs, green). Note the accumulation of MCs on AVMs. Scale bar, 250 µm **(b)** Quantification of MC coverage (determined by desmin area/ICAM2 area). Error bars indicate s.d. of the mean. Number of analyzed animals (n) is indicated. **(c)** Confocal images of ICAM2/DES stain using high magnification on representative positions of the retinal vascular bed. Scale bar, 50 µm.

Besides changes in overall distribution, the stained desmin signals in mutant retinas also appeared altered in structure. Therefore, super-resolution airy scan imaging was performed to reveal structural changes. Desmin in control MCs usually showed a fibrous structure which was dramatically reduced in SRF-deficient MCs and seemed to cluster more tightly (**Figure 3.23**). Super-resolution imaging clearly showed that the fibrous structure of desmin was not preserved in SRF-deficient MCs anymore, possibly suggesting cytoskeletal rearrangements to result in deficiencies in contractile behavior.

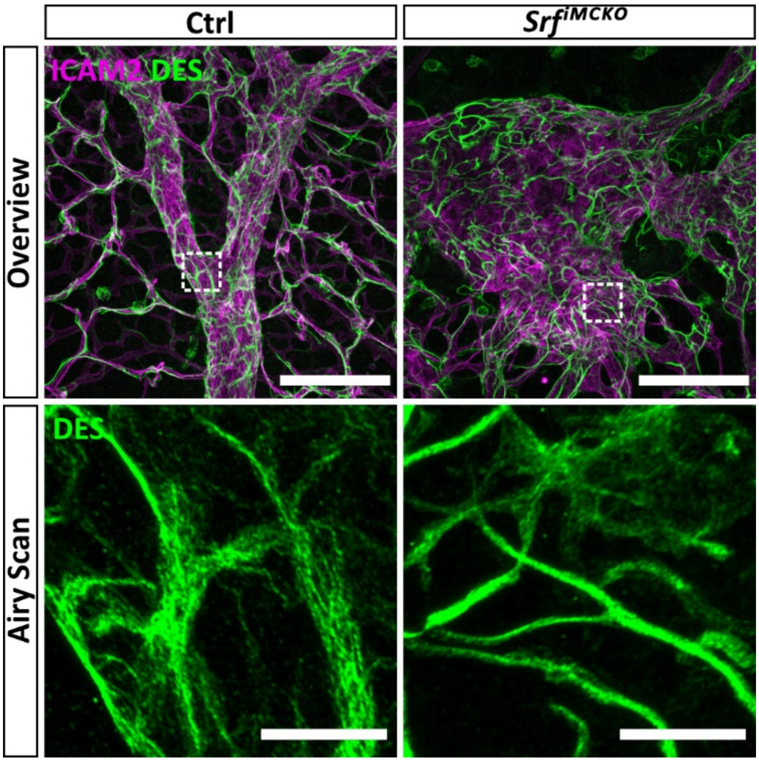

Figure 3.23| Cytoskeletal abnormalities in *Srf*^{iMCKO} MCs. Confocal images showing an overview image of AVM and control position (top panels) stained with ICAM2 (purple) and the cytoskeletal protein desmin (DES, green). White and dashed squares indicate positions of super resolution images by airy scan technology in the lower panels. Note the fibrous structure of DES under the control condition, which is strongly altered in *Srf*^{iMCKO} MCs. DES fibers appear bundled in *Srf*^{iMCKO} MCs. Scale bars, 100 µm (upper row) and 10 µm (lower row).

3.3.4 *Srf^{iMCKO}* MCs cluster on AV-shunts and exhibit strong morphologic changes

For further morphologic characterization of MCs, P12 retinas were analyzed using the fluorescently labeled Rosa26^{mTmG} reporter line. Genetic labeling of MCs enabled an in-depth analysis of the cell morphology. The endothelial marker CD31 served as co-staining to visualize blood vessels. The distribution of genetically labelled MCs was consistent with the previously illustrated desmin staining (**Figure 3.22**, **a** and **b**) and also demonstrated an altered MC distribution in *Srf^{iMCKO}* retinas (**Figure 3.24, a**). MCs clustered on AV-shunts, leaving the distal arterial part uncovered.

Upon comparing SMCs on veins and arteries it was noticeable that, similar to previous observations with P6 SMCs at arteries and veins (**Figure 3.14**), a lack of fine protrusions was apparent (**Figure 3.24, b**). In addition, aSMCs wrapped around the arteries, but partially failed to fully cover the vessels. Furthermore, aSMCs appeared to be stretched, likely by a partial inability to resist the arterial blood pressure, which may also explain the enlarged vessel diameter. A significant reduction of the SMC coverage of arteries and veins based on cell counts per area could not be determined, excluding the possibility of an enlarged arterial/venous diameter due to a lack of SMCs (**Figure 3.24**, **c**).

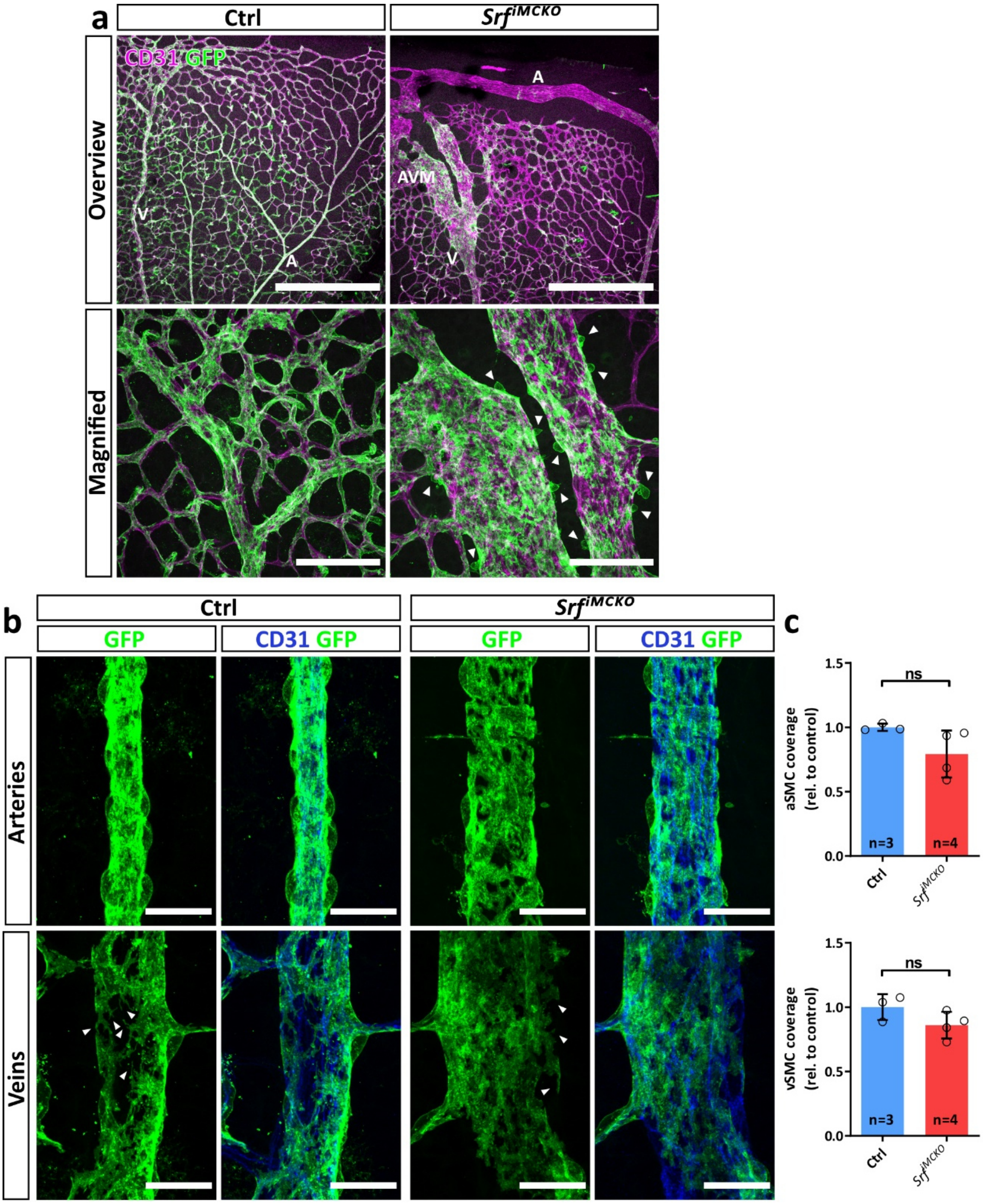

Figure 3.24| Altered SMC morphology at Srf^{iMCKO} arteries and veins at P12. (a) Confocal images of retinal vasculatures genetically labeled with the *$Rosa26^{mTmG}$* reporter for MCs (GFP, green) and co-stained for CD31 (ECs, blue). Arteries (A), veins (V) and AVM are highlighted with white letters. Note MC free area of arteries at the periphery in Srf^{iMCKO} retinas. White arrowheads point at MCs, which round up and appeared to be loosened in Srf^{iMCKO} animals. Scale bars, 500 µm (top panel) 100 µm (lower panel) **(b)** Confocal high resolution images of retinal arteries and veins. Note the size difference of Srf^{iMCKO} vessels as well as the reduction of thin protrusions of vSMCs (indicated by white arrowheads). aSMCs display a stretched morphology. Scale bars, 25 µm **(c)** Quantification of arterial and venous SMC coverage, determined by cell counts per vascular area. Error bars indicate s.d. of the mean. Statistical comparison by unpaired t-test with Welch's correction. Number of analyzed animals (n) is indicated. ns = not significant, *p≤0.05, **p≤0.01, ***p≤0.001.

Strikingly, Srf^{iMCKO} MCs found on AVMs, either appeared regularly rounded or, a subgroup, displayed a detached cell body up from the vessels (**Figure 3.24, a white arrowheads**). The cell morphology of the latter seemed to be strongly altered, but this was difficult to be analyzed by classical 2D projections. Therefore, a 3D surface representation was chosen to segment single cells and enable a visualization of the MC morphology. The 3D representation displayed the formation of long protrusions, which were tortuous and uncoordinatedly overlapping other MCs on top of the vessels (**Figure 3.25, a**). Schratt et al. (2002) observed similar rounding of cells in cultured *Srf*-null embryonic stem cells [114]. This phenotype was linked to a disrupted actin cytoskeleton. A similar mechanism seems likely to contribute to the here observed morphology of MCs.

A complementary TEM analysis of AVMs confirmed the overlapping pattern of MCs (**Figure 3.25, b**). Remarkably, the basal lamina, which is formed by both ECs and MCs, was strongly thickened in Srf^{iMCKO} animals. This observation suggests increased deposition of extracellular matrix proteins. As the malformed vessels are dramatically enlarged, an increased mechanical exposure by stretching is likely. Thickening of the basal lamina could be a response of the vessel toward increasing the resistance of the vessel to blood pressure.

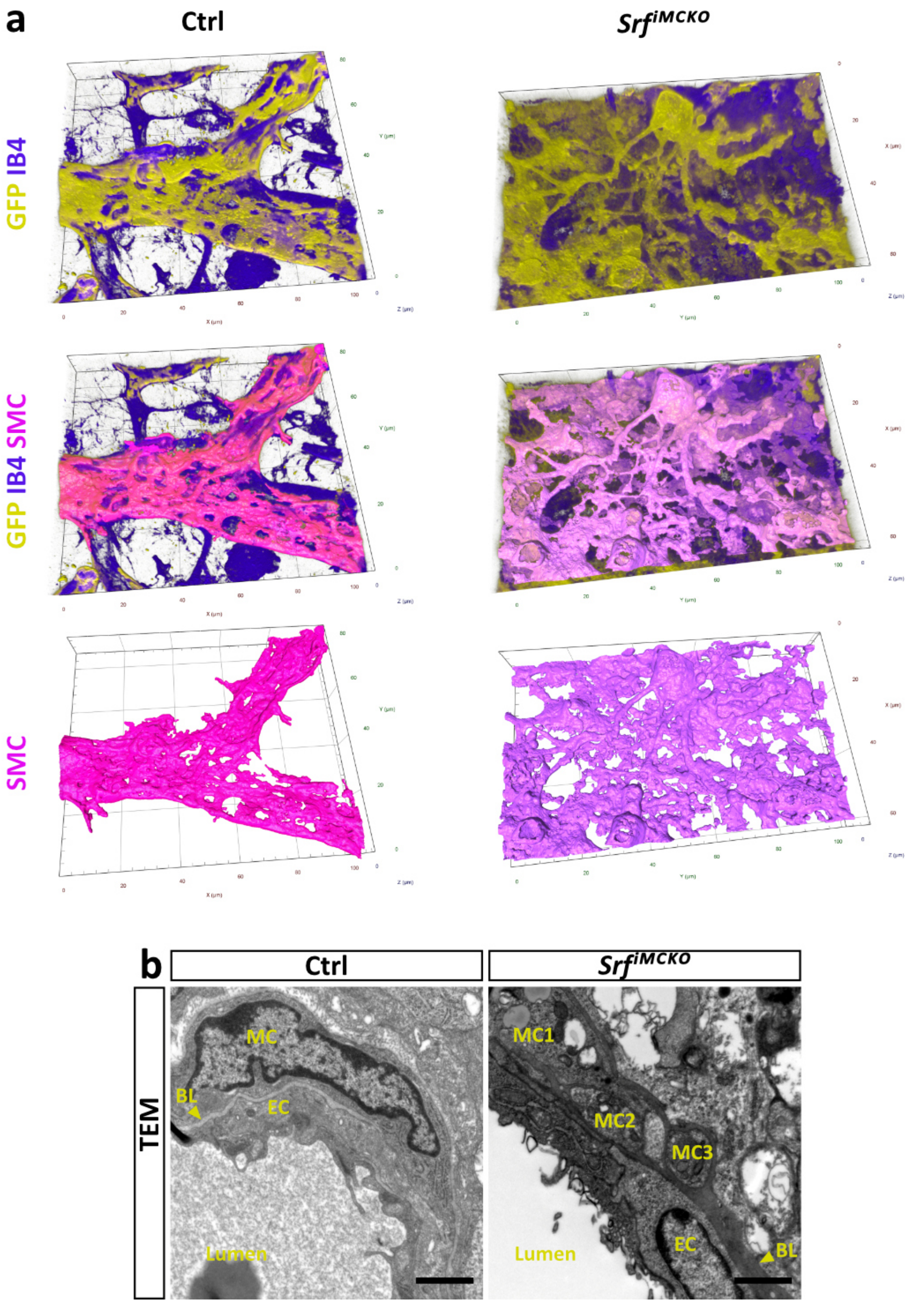

Figure 3.25| *Srf*^{iMCKO} MCs undergo strong morphologic changes and overlap with each other. (a) Structure of 3D-rendered MCs of control and AV-shunt SMCs of *Srf*^{iMCKO}. Third row shows 3D-segmented MC surface (magenta). Note the rounded and partially detached cell body of *Srf*^{iMCKO} MCs which possess long and thin protrusions. **(b)** TEM images of an AV-shunt in *Srf*^{iMCKO} animals and respective control. Yellow arrowheads point to the basal lamina (BL). Note the overlapping parts of SMCs outside the AV-shunts and the thickened BL inside the AV-shunts. Scale bars, 1 µm.

3.3.5 SRF-deficient MCs fail to express typical SMC markers

Previous analyses of *Srf*^{iMCKO} retinas at P6 revealed the absence of αSMA expression compared to control retinas, which suggested the loss of SMC identity (**Figure 3.15**). To investigate the degree of impairment of SMC development, *Srf*^{iMCKO} and control retinas were next analyzed at P12. Typically, SMC development at P12 is largely advanced, and can be measured by high αSMA expression on arteries as well as by the first occurrence of low αSMA expression on veins [178]. Therefore, P12 *Srf*^{iMCKO} and control retinas were stained for αSMA. Additionally, relative transcript levels of *Acta2* as well as *Tagln* and *Myh11* were measured in whole retina lysates, which are also markers typically expressed in normal SMCs.

Image analysis confirmed the previous observations (**Figure 3.15**) on P6 *Srf*^{iMCKO} retinas (**Figure 3.26, a and b**). While almost no αSMA signal was detectable, the NG2 co-staining verified the presence of SMCs on arteries and veins. In addition, mRNA expression levels of *Acta2*, *Tagln* and *Myh11* were remarkably decreased, as measured in total retina lysates of *Srf*^{iMCKO} animals (**Figure *3.26*, c**). Together, these data suggest that SMC development is not delayed, but rather, SMC identity is – to a large extent - lost in *Srf*^{iMCKO} MCs.

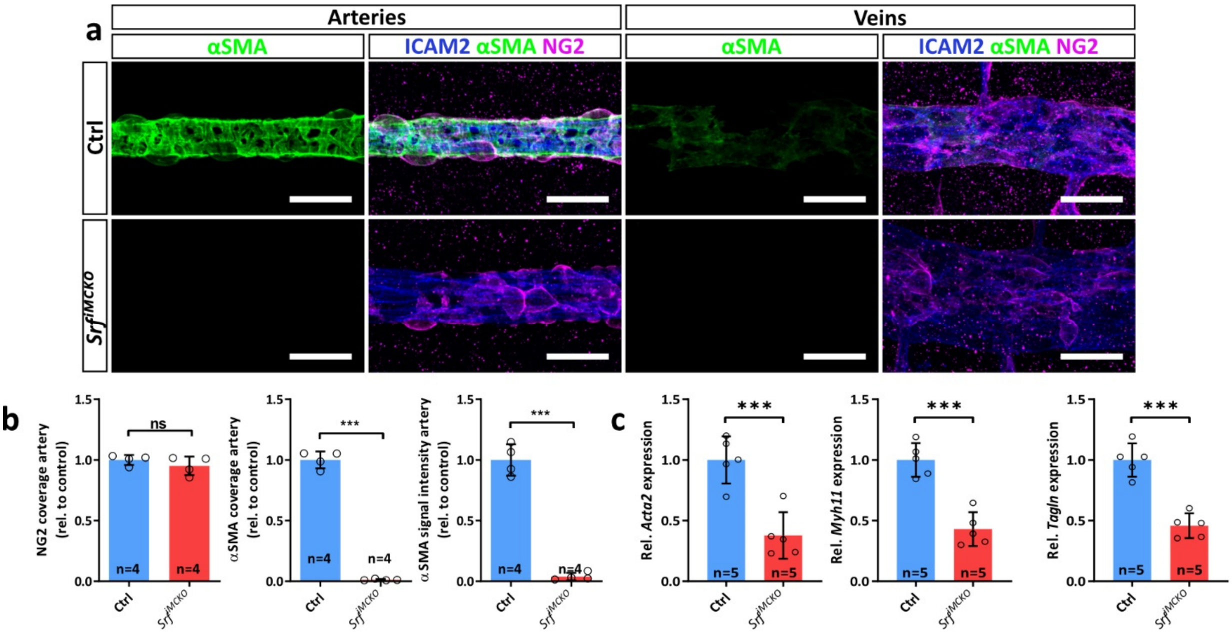

Figure 3.26| Expression of SMC marker genes is remarkably reduced in *Srf*^{iMCKO}. (a) Confocal images of arteries and veins of *Srf*^{iMCKO} and respective control retinas stained for αSMA (green), ICAM2 (blue) and NG2 (magenta). Note the abolishment of αSMA signal despite the presence of NG2 positive cells. Scale bar, 25 µm **(b)** Quantification of aSMC coverage determined by NG2-/ICAM2 area, αSMA-/ICAM2 area and αSMA signal intensity on arteries. **(c)** Gene expression of the SMC markers *Acta2*, *Myh11* and *Tagln* in whole retina lysates. Error bars indicate s.d. of the mean. Statistical comparison by unpaired t-test with Welch's correction. Number of analyzed animals (n) is indicated. ns = not significant, *p≤0.05, **p≤0.01, ***p≤0.001.

In order to examine the dependence of SMC genes on SRF, gene expression was measured on serum-stimulated pBMCs. Serum stimulation is a well-known trigger of SRF activation, which is in part - activated through Rho-actin signaling and hence mainly mediated by MRTF cofactors [115]. A further study showed that pBMCs strongly upregulate αSMA in response to serum [167]. Therefore, *Srf* (as control), *Acta2*, *Tagln* as and *Myh11* expression levels in *Srf-KO* and respective control pBMCs were determined by qPCR, either in culture medium containing 2 % serum or under stimulated conditions using 10 % serum.

Control samples showed a slight upregulation of *Srf* gene expression upon serum stimulation (1.5-fold), while the SMC marker genes were moderately to strongly upregulated (**Figure *3.27***). *Myh11* expression was 2-fold upregulated, whereas *Acta2* and *Tagln* expression was 20-fold and 15-fold upregulated, respectively. This profound increase of the MRTF targets *Acta2* and *Tagln* as well as the non MRTF target *Myh11* upon serum stimulation indicates the differentiation of pBMCs towards a SMC-like phenotype [115].

However, *Srf-KO* pBMCs showed barely detectable levels of *Srf* transcripts, evidencing successful *Srf* deletion. Furthermore, *Srf-KO* showed a strong downregulation of *Myh11* and almost no detectable levels for *Acta2* and *Tagln*. Stimulation treatments had almost no effect on expression levels of all measured genes. This in vitro stimulation experiment correlates well with the observed phenotype in *Srf*^{iMCKO} retinas at P6 (**Figure 3.15**) and P12 (**Figure 3.26**) and further emphasizes that ablation of SRF causes a loss of SMC characteristics in MCs.

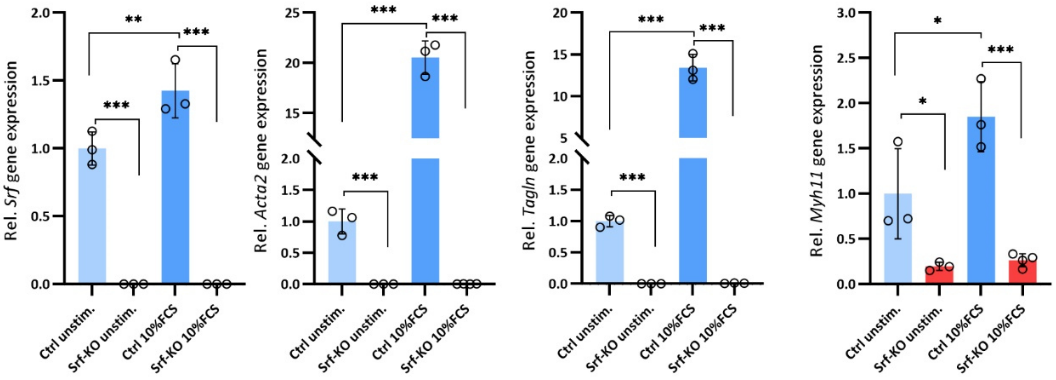

Figure 3.27| SRF is crucial for expression of SMC-specific genes in pBMCs. Transcription levels of SMC genes *Acta2*, *Tagln* and *Myh11* measured by qPCR. *Srf* expression was determined to confirm gene deletion in *Srf-KO* pBMCs. Control and *Srf-KO* pBMCs were maintained in 2 % serum or stimulated with 10 % serum for 24 h. Error bars indicate s.d. of the mean. Statistical comparison by one-way ANOVA (Tukey's multiple comparison test). Number of independent repetitions (n) = 3. ns = not significant, $*p \leq 0.05$, $**p \leq 0.01$, $***p \leq 0.001$.

3.3.6 Isolation of pure EC and MC populations from *Srf*^{iMCKO} and control retinas using FACS methodology

In order to gain molecular insights into dysregulated pathways in SRF-deficient MCs and non-autonomously influenced ECs, the RNA sequencing (RNA-Seq) methodology was employed. For the isolation of purified MC and EC populations from whole retina lysates, a FACS approach was chosen. *Srf*^{iMCKO} retinas and respective controls were enzymatically digested and labeled with fluorophore-coupled antibodies to selectively enrich EC and MC populations while depleting non-endothelial and non-mural fractions. The gating strategy included exclusion of dead (DAPI$^+$) cells, red blood cells (Ter119$^+$) as well as hematopoietic (CD45$^+$) and mesenchymal (CD140a$^+$) cell lineages. Final enrichment was carried out for endothelial (CD31$^+$) and mural (CD140b$^+$) cell populations. For the sorting strategy see **Figure 3.28** below. A first analysis of whole retina single cell suspensions detected approximately 0.2-0.4 % CD31$^+$ and 0.1-0.2 % of CD140b$^+$ cells.

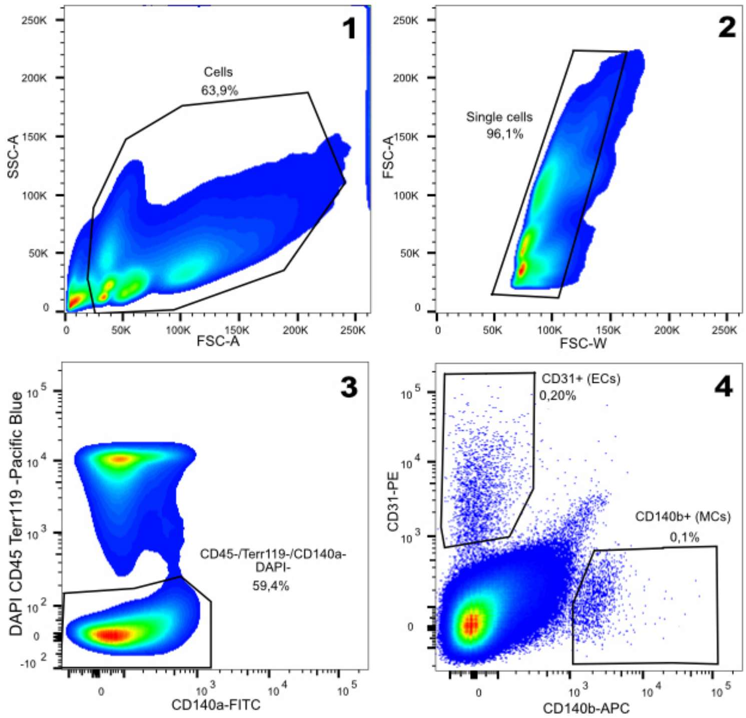

Figure 3.28| FACS gating strategy to isolate ECs and MCs from murine P12 *Srf*^{iMCKO} and control retinas. After initial forward (FSC-A) and sideward scatter (SSC-A) to distinguish cells from debris **(1)**, doublets were excluded **(2)**. Living cells (DAPI$^-$) as well as CD45$^+$ (hematopoietic cells), Ter119$^+$ (erythrocytes) and CD140a$^+$ (fibroblasts) cells were excluded **(3)**. The resulting population was subdivided into CD31$^+$ (ECs) and CD140b$^+$ (MCs) cells and collected for follow up applications **(4)**.

Total RNAs of purified EC and MC populations were isolated and reverse transcribed to cDNA for qPCR analysis. Gene expression of the EC marker *Pecam1* (CD31) and the MC marker *Pdgfrb* (CD140b) was measured by qPCR to interrogate the purity of EC and MC populations and exclude cross contaminations

(**Figure 3.29**, **a**). Finally, 11 MC samples (4x *Srf*^{iMCKO} and 7x control) and 9 EC samples (4x *Srf*^{iMCKO} and 5x control) were analyzed by RNA-Seq and confirmed the FACS and qPCR measurements (**Figure 3.29**, **b**). Furthermore, the prominent EC markers *Emcn*, *Pdgfb*, *Cdh5* and *Pecam1* were enriched in sorted fractions of EC preparations, while absent in PC fractions. In contrast, sorted MC populations expressed the MC markers *Pdgfrb*, *Notch3*, *Rgs5* and *Acta2,* which are absent in EC fractions. Taken together, the performed qPCR and RNA-Seq measurements confirmed the isolation of purified EC and MC fractions.

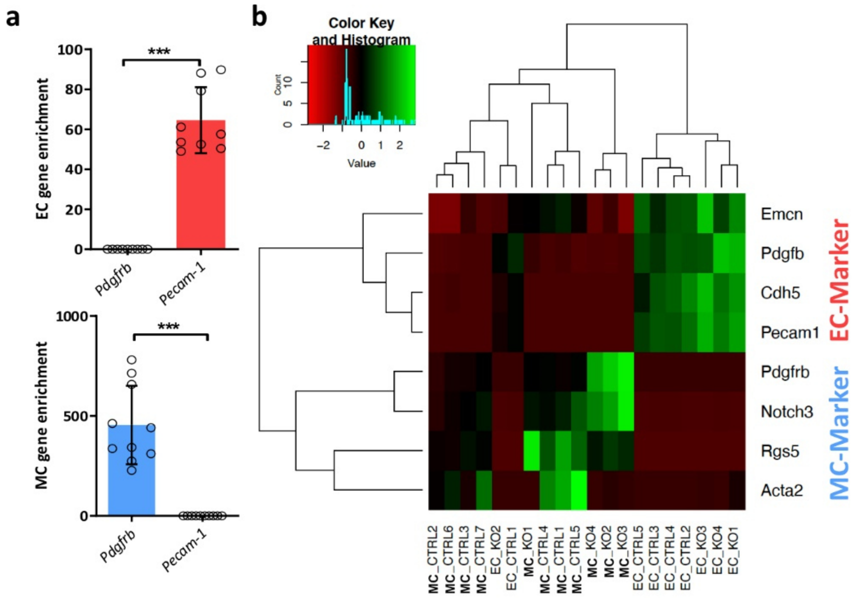

Figure 3.29| EC and MC populations sorted by FACS do not show cross contaminations. (a) qPCR of the EC marker *Pecam-1* and the MC marker *Pdgfrβ* in FACS-sorted EC and MC populations. Error bars indicate s.d. of the mean. Statistical comparison by unpaired t-test with Welch's correction. Number of analyzed animals (n) is indicated. ns = not significant, $*p\leq0.05$, $**p\leq0.01$, $***p\leq0.001$. **(b)** Heatmap of selected EC and MC marker expression across all EC and MC samples measured by RNA-Seq.

3.3.7 Transcriptome analysis revealed disruption of the contractile apparatus in *Srf*^{iMCKO} MCs

After verification of the purity of sorted MCs and ECs, further bioinformatic processing of the RNA-Seq data was performed. Out of 7 control and *4 Srf*^{iMCKO} samples, 3 per group were selected for differential gene expression analysis. Samples were selected based on highest similarity within the group, judged by a principal component analysis, in order to exclude outliers (**Supplementary Figure 2**). Differential gene expression analysis of isolated MC fractions identified 2,265 upregulated and 2,537 downregulated genes ($p<0.05$, **Figure 3.30, a**). First, the list of differentially expressed genes was compared to SRF target genes according to Esnault et al. (2014) and Gualdrini et al. (2016) [115,171]. Interestingly, out of 1, 585 published SRF target genes, 167 were downregulated within the *Srf*^{iMCKO} dataset (**Figure 3.30, b**). Of these 167 SRF target genes, 110 genes are classified as regulated by MRTF-SRF, while 63 genes are classified to be regulated by TCF-SRF. An overlapping MRTF/TCF signature of 6 genes was also noticed. Among the downregulated SRF target genes were especially structural components of smooth muscle contraction machinery such as various actin and actin-binding proteins (**Supplementary Figure 4**). Surprisingly, 350 SRF target genes in the dataset were upregulated in *Srf* ablated MCs. With 229 genes, the majority of this subset are MRTF targets, whereas 162 genes are regulated by TCFs. The overlap between both cofactors was 41 genes. Among the upregulated SRF-target genes were Rho-GTPases, transcription factors and structural proteins which are also involved in the contraction apparatus (**Supplementary Figure 3**). Therefore, a gene set enrichment analysis (GSEA) of MC RNA-Seq dataset was performed, in order to get an overview of dysregulated pathways in *Srf*^{iMCKO} MCs.

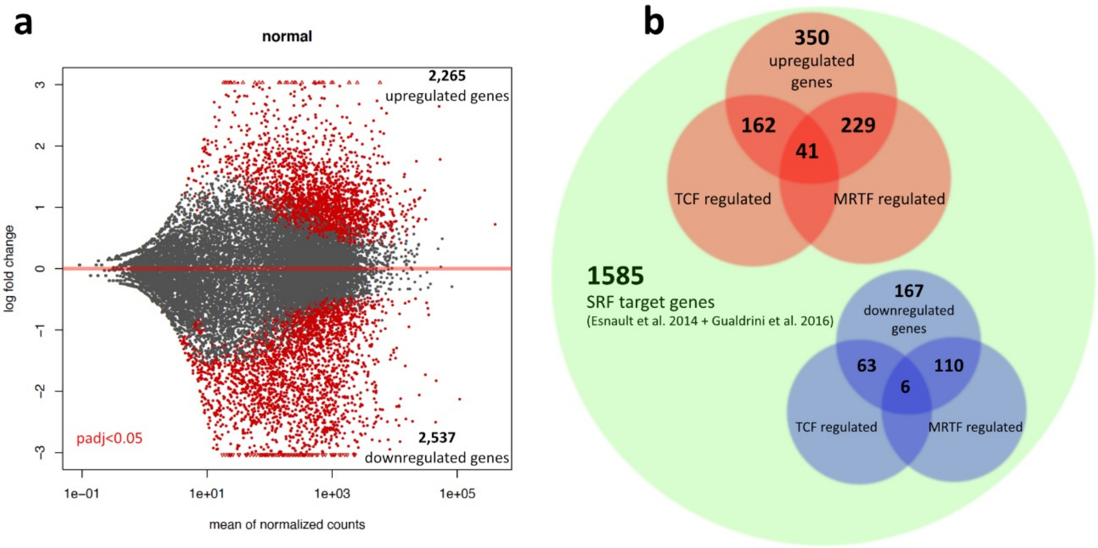

Figure 3.30| RNA-Seq methodology showed numerous dysregulated genes in *Srf*^{iMCKO} cells. (a) Vulcano plot displaying RNA-Seq detected genes according to the degree of dysregulation (log_2 fold change). Red dots indicate significantly ($p<0.05$) dysregulated genes. **(b)** Venn diagram summarizing upregulated and downregulated SRF target genes detected by RNA-Seq of sorted *Srf*^{iMCKO} and respective control MCs from retina single cell suspensions. Green circle indicates the amount of validated SRF target genes according to Esnault et al. (2014) and Gualdrini et al. (2016). Red and blue diagrams depict significant up/downregulated SRF target genes.

Gene set enrichment analysis (GSEA) using the Kyoto Encyclopedia of Genes and Genomes (KEGG) dataset resulted in numerus upregulated and downregulated pathways ranked by a normalized enrichment score (NES) [179]. Positive values indicate an enrichment of downregulated genes within a gene set, whereas negative values indicate upregulated genes within a gene set. Interestingly, the pathways “KEGG cardiac muscle contraction” (NES: 1.39) and “KEGG calcium signaling” (NES: 1.38) were among the top downregulated pathways and revealed downregulation of numerous genes which are important in regulation of SMC contraction (e.g. *Myl9* and *Cacna1d*). In contrast, the pathways “KEGG focal adhesion” (NES: -2.04) and “regulation of actin cytoskeleton” (NES: -1.81) were upregulated in *Srf*^{iMCKO} MCs. As multiple contraction pathways seemed to be dysregulated in *Srf*^{iMCKO} MCs using KEGG-based GSEA, these findings were further investigated by GSEA for pathways within the Gene Ontology (GO), Reactome and Biocarta databases specifically for contraction- related gene sets [180–182]. Out of 50 tested gene sets, 20 sets showed a significant positive NES (gene sets including downregulated genes) and 28 gene sets with a negative NES (gene sets with upregulated genes). A representative selection of gene sets is shown in **Figure 3.31**.

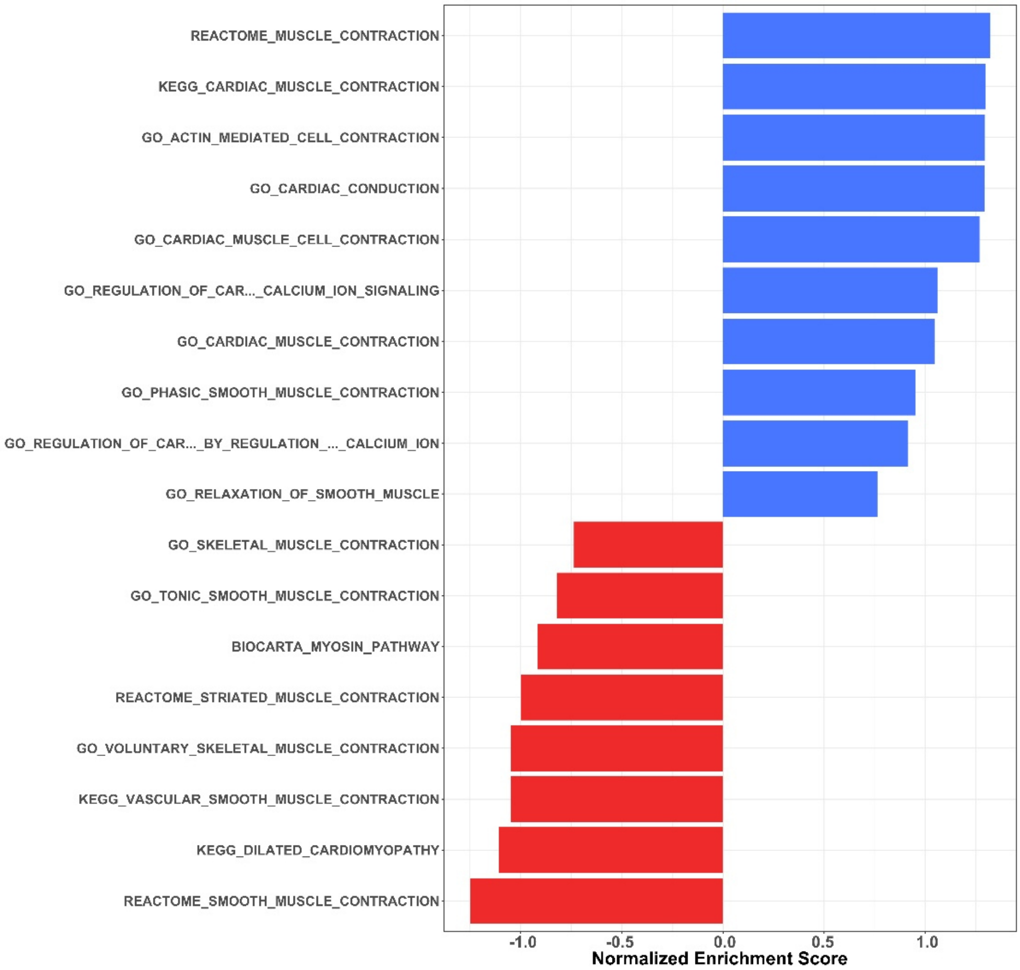

Figure 3.31| SRF-deficient MCs show dysregulated pathways connected to cellular contractile functions. GSEA of RNA-Seq dataset of *Srf*^{iMCKO} and control MCs. Positive normalized enrichment scores (NES) indicate pathways containing downregulated genes whereas negative NES indicate pathways containing genes which are upregulated. Representative summary of tested contraction-related gene sets within the GO, Reactome and Biocarta databases.

Interestingly, GSEA identified numerous genes which are crucial for the process of smooth muscle contraction (**Figure 3.32**) and which are dysregulated in *Srf*^{iMCKO} MCs. Importantly, the SMC marker genes *Acta2* and *Tagln*, which were previously shown to be downregulated in *Srf*^{iMCKO} MCs, could be verified by RNA-Seq methodology (**Figure 3.26** and **Figure 3.32**). In addition to the strong downregulation of *Acta2* ($\log_2$ fold change (fc): -3.85 ±0.61) as an important structural factor within the contraction machinery, several other actin family members such as *Acta1* ($\log_2$fc: -3.68 ±1.14), *Actc1* ($\log_2$fc: -2.69 ±1.03) and *Actg1* ($\log_2$fc: -0.97 ±0.31) were found to be less expressed in *Srf*^{iMCKO} MCs. Of note, a strong downregulation of the myosin light chain 9 (*Myl9*; $\log_2$fc: -2.59 ±0.36) was noticed. This SRF target gene was recently described as a critical factor for SMC contraction in a mouse model of hypertension [115,183]. Moreover, the important actin binding components *Cnn2* and *Synpo2* were downregulated in addition to *Tagln.* Of note, multiple ion channel proteins important for Ca^{2+} release into the cytoplasm to enable initiation of SMC contraction were remarkably downregulated (*Cacna1d*, $\log_2$fc: -1.91 ±0.64; *Cacna1f*, $\log_2$fc: -2.46 ±0.34; *Kcnma1*, $\log_2$fc: -2.92 ±0.42 and *Kcnmb1*, $\log_2$fc: -5.27 ±0.7). Surprisingly, the type III intermediate filaments *Vim* and *Des*, parts of the contractile machinery, were upregulated ($\log_2$fc: 1.70 ±0.34 and 1.81 ±0.27), likely as part of a compensatory mechanism to maintain partially contractile functions.

In addition to components which are directly involved in the process of SMC contraction, cellular proteins with regulatory functions were also found to be dysregulated. Ca^{2+}/Calmodulin protein kinases (CAMK) are known to regulate calcium ion concentration by activation via phosphorylation of ryanodine receptors (RYR) and L-type Ca^{2+} channels, which increases intracellular Ca^{2+} concentration and finally initiates contraction [87]. The transcriptomic analysis identified the CAMKs *Camk2b* and *Camk2d* to be strongly downregulated ($\log_2$fc: -2.61 ±0.39 and 1.09 ±0.26). Interestingly, the p21 protein kinase 1 (PAK1) is known to attenuate contraction whereas the janus kinase 2 (JAK2) induces angiotensin mediated contraction [184]. Expression of *Pak1* was found to be reduced ($\log_2$fc: -3.0 ±0.34), whereas *Jak2* levels were found to be elevated ($\log_2$fc: 1.14 ±0.37) in *Srf*^{iMCKO} MCs. Increased expression levels were also found for several contraction promoting integrins (*Itga5*, $\log_2$fc: 2.24 ±0.50; *Itgav*, $\log_2$fc: -1.23 ±0.26; and *Itgb,* $\log_2$fc: -1.55 ±0.24;). These integrins were previously shown to be essential for assembly of ECM within the vascular vessel wall [185]. Furthermore, numerous Rho-GTPases such as *Rhoa* ($\log_2$fc: 0.90 ±0.21), *Rhoc* ($\log_2$fc: 1.74 ±0.25) and *Rhoj* ($\log_2$fc: 1.41 ±0.23) were upregulated in *Srf*^{iMCKO} MCs, which are known to positively regulate contraction [89]. Finally, the transcriptional co-activator of SRF, myocardin (*myocd*), which is critical in inducing muscle-specific gene expression upon binding to SRF and thus activation of SRF, was strongly upregulated ($\log_2$fc: 3.08 ±0.43) [129]. Increased expression levels of the transcription factors *Mef2a* ($\log_2$fc: 0.81 ±0.26), *Mef2c* ($\log_2$fc: 0.91 ±0.23), *Prrx1* (*mhox1*; $\log_2$fc: 1.55 ±0.39) and *Tead1* ($\log_2$fc: 0.67 ±0.23), which are important for SMC differentiation, were also observed in *Srf*^{iMCKO} MCs [186,187]. Upregulation of transcription factors which induce a SMC phenotype may support the speculation that *Srf*^{iMCKO} MCs are impaired to differentiate into functional SCMs.

Taken together, the transcriptomic analyses of MCs isolated from P12 *Srf*^{iMCKO} and respective control retinas revealed downregulation of critical genes within the contractile force generating machinery including cytoskeletal proteins, ion channels and regulating kinases. In turn, other regulating kinases, GTPases and transcription factors which support regulation of contraction and SMC differentiation were found to be upregulated, most likely as part of a compensatory mechanism.

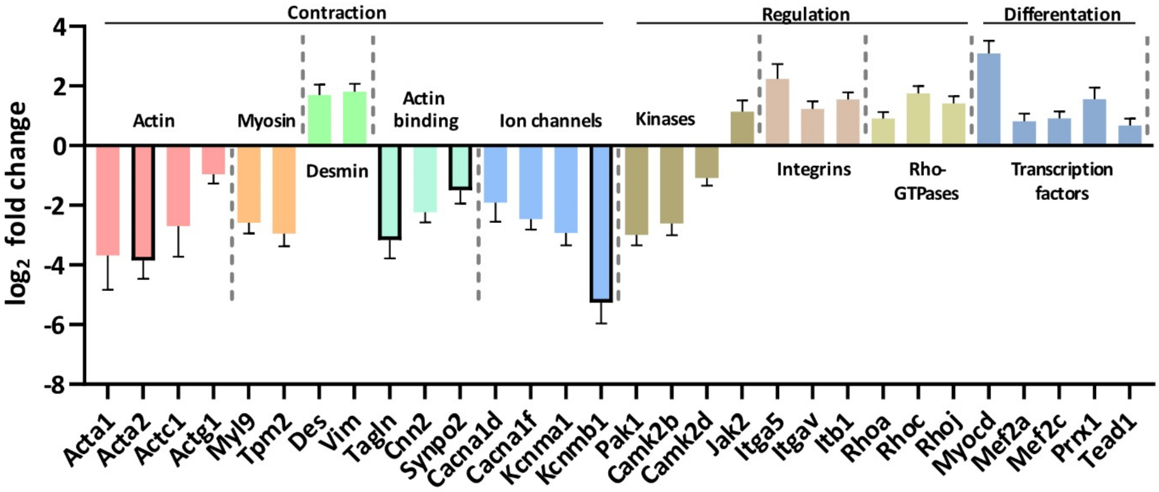

Figure 3.32| *Srf*^{iMCKO} MCs exhibit dysregulated expression patterns of essential components of the contractile machinery. Gene expression $\log_2$ fold changes of selected genes identified by the RNA-Seq methodology and subsequent GSEA. Listed genes are essential contributors to SMC contraction and were functionally grouped (headings). Framed bars indicate frequent used SMC markers. Error bars indicate the standard error of the mean (s.e.m.). All presented genes were significantly dysregulated ($p<0.05$).

Transcriptomic analyses were also performed on sorted EC fractions isolated from *Srf*^{iMCKO} and control retinas. The PCA plot revealed a greater separation between samples, likely due to the non-cell autonomous effect on ECs originating from MCs, which lead to a variation in phenotype and thus to variances in gene expression patterns. However, differential gene expression analysis identified 114 upregulated and 203 downregulated genes ($p<0.05$;**Supplementary Figure 5**). Subsequently, GSEA was performed (**Supplementary Figure 6**). Genes involved in metabolism-related pathways such as “KEGG glycolysis gluconeogenesis” (NES: 1.77) were found to be downregulated in *Srf*^{iMCKO} ECs, while genes of “KEGG focal adhesion” pathways were found to be upregulated (NES: -1.97). Moreover, gene expression of angiopoietin 2 (*Angpt2;* $\log_2$fc: 1.86 ±0.40) and the vascular endothelial growth factor receptor 2 (*Kdr;* $\log_2$fc: 1.02 ±0.23) was found to be upregulated (**Figure 3.33**). In support, both proteins were recently described to be upregulated in destabilized ECs, triggered by a loss of PC coverage [45,59]. The bone morphogenic protein 4 (*Bmp4*) was also found to be upregulated (log_2fc: 2.67 ±0.57). BMP4 was shown to induce contraction of ECs and vasoconstriction via *Bmpr1a* in diabetic mice [188,189]. *Gja5,* also known as connexin 40 (CX40), is also involved in the TGFβ pathway together with Bmp4 [190]. Recent reports suggested a role of endothelial CX40 in induction of arterial specification and arterial MC investment [190]. Interestingly, loss of endothelial CX40 favored the development of AVMs in a murine HHT model [191]. Gja5 was found to be upregulated in *Srf*^{iMCKO} ECs (log_2fc: 3.0 ±0.56), this may again indicate a compensatory mechanism. Of note, expression levels of the vasoconstrictor endothelin-1 (*Edn1*) was remarkably increased (log_2fc: 2.29 ±0.28). *Edn1* is a well-known and powerful vasoconstrictor which is found to be upregulated in hypertension [192]. Edn1 is acting through its receptor *Edn1ra,* which is expressed on SMCs and activates intracellular Ca^{2+} influx via RYR mediated contraction. Furthermore it can activate proliferative and migratory behavior of SMCs through MAPK signaling [88,193]. *Edn1* upregulation in ECs could be a reaction to strong dilated vessels and is therefore in line with transcriptomic data of MCs.

Overall, ECs isolated from *Srf*^{iMCKO} retinas showed less pronounced transcriptomic dysregulation in comparison to isolated MCs. Dysregulated genes in ECs included markers for destabilized ECs and upregulation of a potent vasoconstrictor which could be a reaction to strong dilation of vessels.

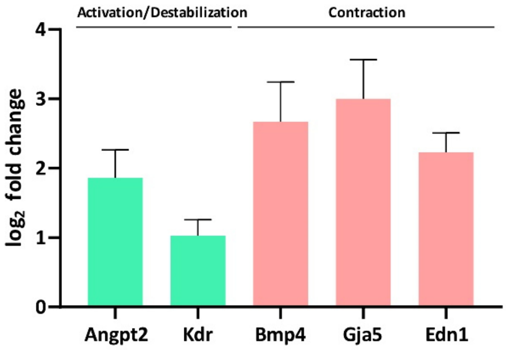

Figure 3.33| *Srf*^{iMCKO} ECs upregulate activating and contractile pathways. Gene expression log_2 fold changes of chosen genes identified by RNA-Seq methodology of *Srf*^{iMCKO} and control ECs isolated from P12 retinas. Listed genes are important players in activation/destabilization of endothelial quiescence as well as paracrine (Bmp4 and Edn1) and juxtacrine (Gja5) induction of contraction.

3.4 Analyses of MC function during vascular quiescence in adult retinas

3.4.1 *Srf*^{iMCKO}-associated vascular abnormalities influence retinal function but vary in severity

The so far obtained results collectively suggest dysfunctional contractility of SMCs in *Srf*^{iMCKO} retinas. Analyses were mainly based on whole mount retina stainings, which provides valuable and high-resolution information at the moment of fixation. However, spatiotemporal information gets lost due to tissue fixation. Scanning laser ophthalmoscopy (SLO) is a powerful tool to image retinal tissue *in vivo*. It is an important tool in medicine, where it is used for recognition of human ophthalmic disorders [163]. SLO is based on confocal microscopy. Using lasers of varying wavelength enables the observation of different tissues due to their unique light reflecting capabilities. In addition, fluorescent dyes such as indocyanine green (ICG) can be used as contrast agent to enable visualization of perfused capillaries and detection of leakages [164]. Moreover, SLO can be combined with optical coherence tomography (OCT) in one instrument. OCT utilizes week infrared laser light and analyses reflectance properties of the tissue to enable vertical optical sectioning of retinal layers [163]. As OCT is based on reflectance of tissues, highly reflecting objects appear bright, while tissues with higher transmitting abilities, e.g. vessels, appear dark in the OCT.

Srf^{iMCKO} animals were analyzed using both SLO and OCT in order to observe vascular function *in vivo*. Animals were analyzed at an age of approximately 4 weeks. SLO confirmed that arteries and veins are enlarged in *Srf*^{iMCKO} animals (**Figure 3.34**). In addition, some vessels appeared bulged. Interestingly, the severity of vascular alterations varied across measured *Srf*^{iMCKO} animals. Moreover, differences could also be observed between the left and right eye of one animal (**Figure 3.34, D-F vs. K-M**). The severity of vascular alterations could be classified in mild, intermediate and strong alterations. Mild alterations were characterized by enlarged and bulged arteries and veins (**Figure 3.34, A-C**). Intermediate alterations showed stronger enlargement and bulging of vessels (**Figure 3.34, D-E**). Furthermore, OCT revealed sights of vitreous detachment at intermediate and strong staged retinas, indicating leakage of fluid at the retinal surface (**Figure 3.34, M**). Retinas with strong alterations showed extreme bulging of arteries and veins combined with signs of vitreous detachment (**Figure 3.34, K-M**). In retinas with strong alterations, diameters of individual veins were increased as much as 2-3 fold, compared to controls, and, in consequence, the veins were severely inflated. Live imaging of these inflated vessels revealed strong movements of the vessels wall as a result of vascular blood flow through these vessels (**Supplementary Movie 4**). As SMCs are responsible for maintenance of the vascular tonus, the degree of pulsation observed in *Srf*^{iMCKO} retinas must be considered non-physiological or pathological. Comparable vessels of control retinas do not show any visible pulsation. This obviously shows a loss of the vascular tonus provoked by mural deletion of *Srf.*

Blood pressure is typically highest in arteries, which causes the blood to drain into the capillaries, where blood pressure drops. The deoxygenated, low-pressure blood then drains into the veins. The blood pressure is here at a minimum [177]. SLO in combination with ICG contrast agent (angiography) revealed disturbed perfusion of capillaries in Srf^{iMCKO} retinas with strong alterations, suggesting that the blood flow is mainly distributed through vessels of bigger diameter. This illustrates the pathologic redirection of blood flow by AVM-shunts and likely negatively affects the blood and oxygen supply of the surrounding retinal tissue (**Figure 3.34, L**).

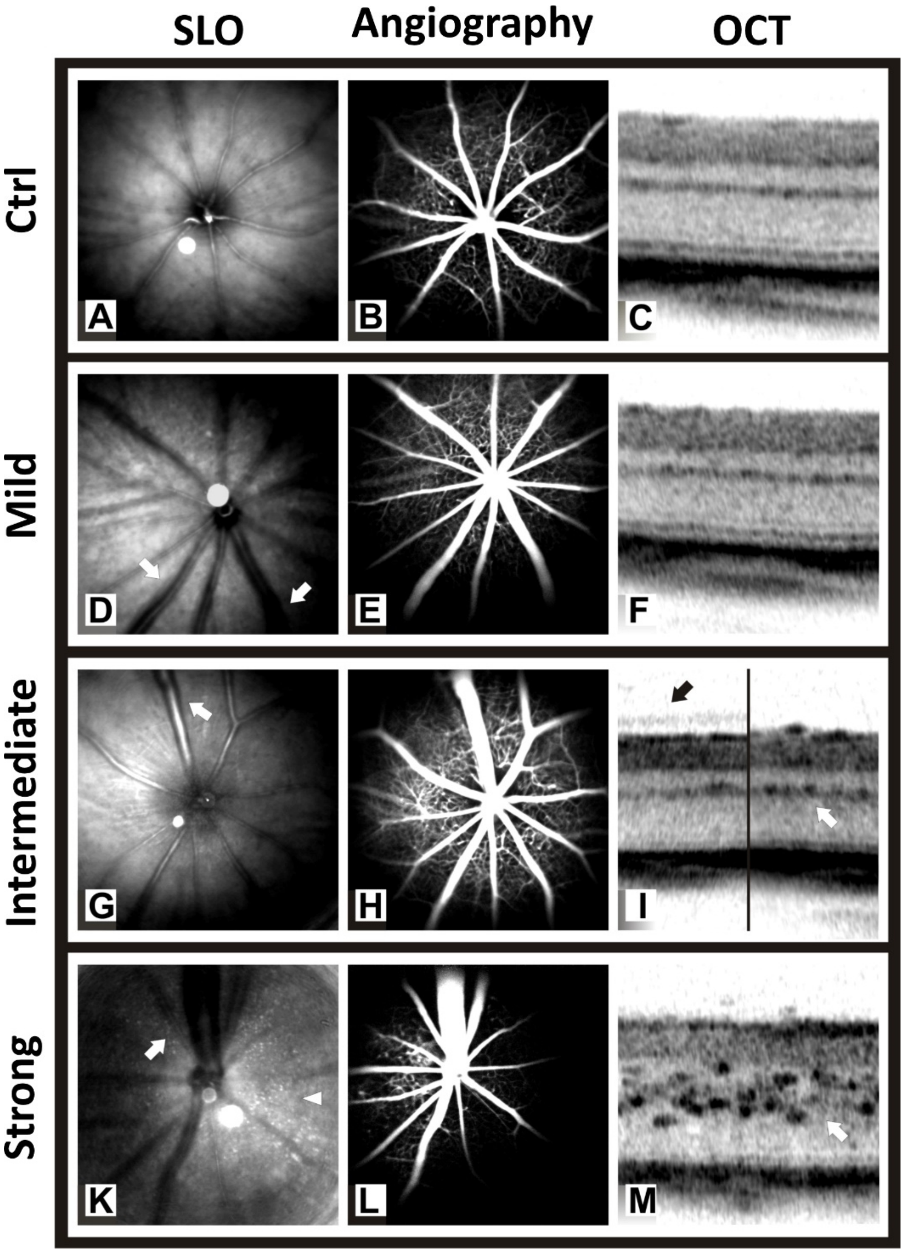

Figure 3.34| SLO and OCT imaging of control and *Srf*^{iMCKO} retinas. *In vivo* imaging of the retinal vasculature including the capillary network and retinal layer morphology at three to four weeks of age. Native SLO imaging (**D,G,K**) and ICG angiography (**E,H,L**) indicates different degrees of vascular bulging in the large surface vessels of *Srf*^{iMCKO} mutant animals (arrows) compared to age matched controls (**A)** and **(B**). The vascular alterations vary in strength from mild (**D** and **E**) and intermediate (**G** and **H**) to strong (**K** and **L**). OCT optical sections were obtained to assess the status of the retinal capillaries. Representative details of WT mice (**C**) and *Srf*^{iMCKO} mutant animals (**F**, **I**, **M**) illustrate the corresponding microvascular alterations in the mid-periphery of the retina. In comparison to the regular retinal layering in control animals (**C**), alterations in retinal capillary morphology were found in *Srf*^{iMCKO} mutant mice that again varied in strength from a mild enhancement particularly in the OPL (**F**) and a strong enhancement (**I**, white arrow) to a massive extension of the entire layer with extremely bulged capillaries (**M**). In the latter situation, the microvascular alterations become already visible in the native SLO image (arrowhead in **K**). In cases of intermediate to strong vascular bulging, there were signs of vitreous detachment (**I**, black arrow).

Electroretinography (ERG) is a method to quantify action potentials generated by the retina in reaction to flashlight exposure. ERG was performed on *Srf*^{iMCKO} and littermate controls before or subsequent to SLO/OCT in order to measure retinal function. Animals were measured under dark (scotopic) and light (photopic) adaptation conditions. Scotopic measurements mainly measure the response of the rod system whereas photopic measurements force response of the cone system [166]. Immediately after exposing the eye to a single flash series, photoreceptors polarize and initiate a negative deflection, termed a-wave, which is followed by a positive deflection, called b-wave, typically initiated by bipolar cells [166].

ERG measurements revealed a variable functional deficit in *Srf*^{iMCKO} mutants under both scotopic and photopic conditions. A representative measurement of one mutant and one control animal is shown in **Figure 3.35**. Measurements of the *oculus dexter* (OD; right eye) and the *oculus sinister* (OS; left eye) also showed alterations within one animal. Interestingly, the observed differences correlated well with the degree of morphological alterations found in SLO/OCT measurements. Mutants with mild vascular alterations (**Figure 3.34, D-F**) showed also slight or almost no change in a-wave and b-wave response in comparison to wild type controls (**Figure 3.35, Srf OS**), depicting intact retinal functionality. However, strong vascular alterations almost lead to the abolishment of a-wave and b-wave, suggesting a loss of retinal function in these *Srf*-mutants (**Figure 3.35, Srf OD**). The major difference between OD and OS in the same mutant individual indicates that the reduced eye functionality in *Srf*^{iMCKO} animals is more likely caused by a local retinal effect than by a systemic vascular effect.

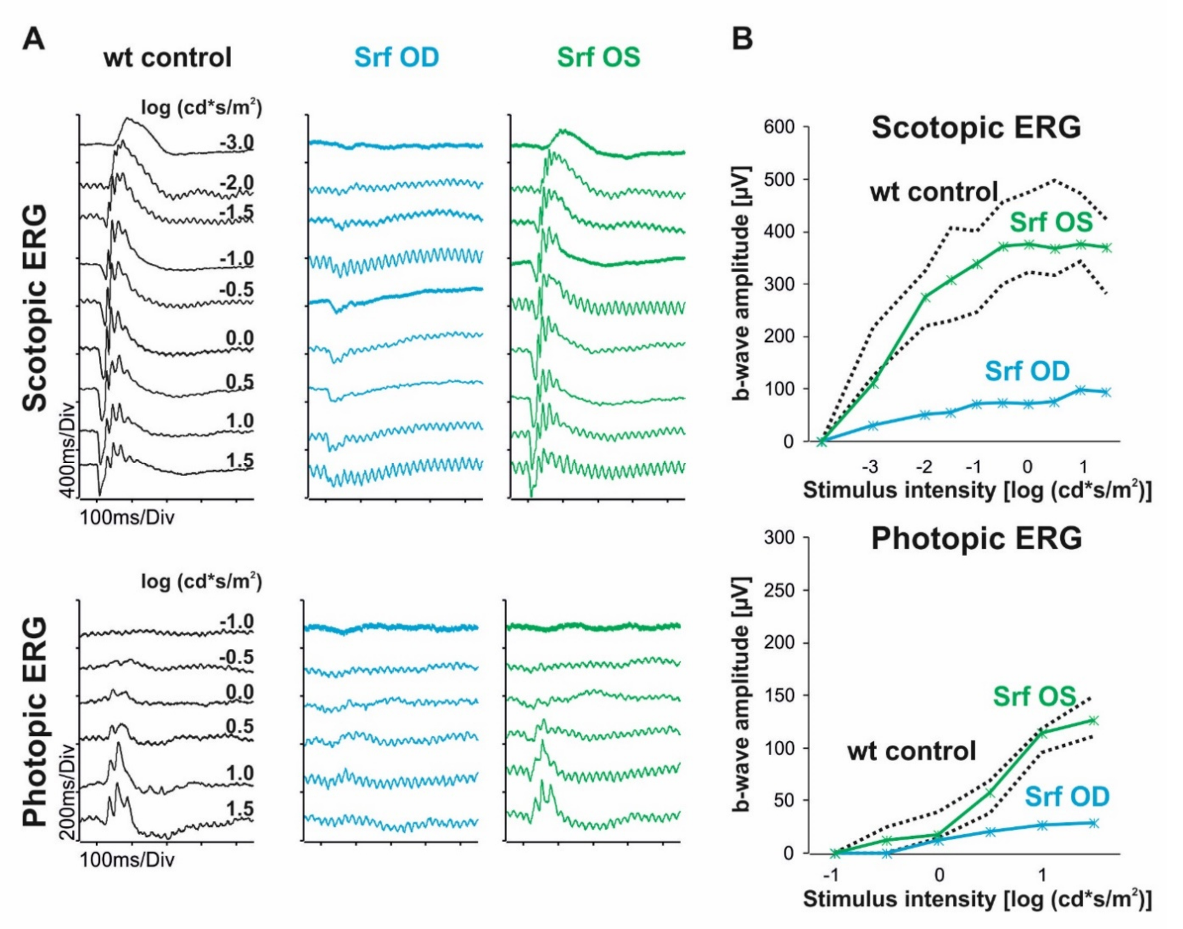

Figure 3.35| Retinal function in control and *Srf*^{iMCKO} retinas. Selected *in vivo* electroretinography (ERG) data obtained from the two eyes of the same mutant animal at the age of 4 weeks, corresponding to the imaging data in **Figure 3.34** (OD: K-M, OS: D-F). **(A)** Scotopic (dark-adapted, top row) and photopic (light-adapted, bottom row) single flash ERG intensity series. **(B)** Quantification of the scotopic (top) and photopic (bottom) ERG b-wave amplitudes of the traces shown in (A) as a function of the logarithm of the flash intensity (VlogI function). Green color indicates the data of the left and blue of the right eye of a *Srf*^{iMCKO} mutant, respectively. For comparison, amplitude data of wt control mice (n=4) are shown as black dotted lines that mark the 5 % (lower black trace) and 95 % (upper black trace) quantiles.

3.4.2 Mural cell SRF is necessary to sustain contractile capability of quiescent SMCs

Transcriptomic analysis suggested a loss of contraction capabilities of MCs in *Srf^{iMCKO}* retinas (P12), which could lead to increased arterial and venous tube diameter. However, it is unclear if a loss of *Srf* in fully developed and quiescent MCs could lead to a loss of contraction and thus to a similar phenotype as previously observed at P12 (**Figure 3.18**). Park et al. (2017) used diphtheria toxin-mediated ablation to delete MCs in adult mice and found only mild vascular phenotypic changes in retina [45]. MC-depleted retinas were still resistant to vascular leakage and showed no obvious vessel dilation. However, the mentioned study characterized MC depleted retinas only after a relatively short time period after depletion (2 and 8 weeks). In order to verify any potential effect on quiescent MCs upon *Srf* deletion, adult 8-week old *Srf-flex1::Pdgfrb-CreER^{T2}* mice and littermate controls (without CreER^{T2} transgene) were injected with tamoxifen on 5 consecutive days to induce mural cell *Srf* ablation. A first examination of retinas after 8 weeks showed no obvious vascular phenotype (data not shown). However, after 1 year, phenotypic changes in the retinas were observed (**Figure 3.36**). Arteries and veins were significantly dilated (arteries: 50 ±6.9 %, p=0.0026; veins: 48 ±24.97 %; p=0.0213). Moreover, αSMA as well as desmin staining showed no reduction of SMC coverage on arteries (**Figure 3.36**, **d** and **e**). On veins however, αSMA was almost fully depleted. Despite the seeming loss of vSMCs, a simultaneous desmin co-staining verified the presence of vSMC and aSMCs (**Figure 3.36**, **d)**. This rather suggests a reduction in contractile protein expression than a loss of SCMs. Therefore, the signal intensity of αSMA staining was determined (**Figure 3.36**, **e**). The aSMA signal intensity on arteries was significantly reduced on arteries (61.69 ±12 %; p=0.0490) and almost entirely lost on veins (96.6 ±3.6 %, p=0.0049) of *Srf^{iMCKO}* retinas compared to control. To complement data extracted from retina stainings, further qPCR analysis of whole brain lysates of the same animals was performed. The brain is, similar to the retina, a part of the CNS and is therefore a useful model for further measurements. qPCR analysis of whole brain lysates verified the reduced expression levels of *Acta2* and *Tagln*.

Phenotypic changes in the capillary plexus network of retinas could not be observed. These results suggest that SRF is needed to sustain the contractile capabilities of SMCs over long time periods. Likely, a loss of SRF leads to reduced availability of parts of the contractile machinery and thus to dilated arteries and veins. It remains to be investigated if reduction of αSMA is caused in the context of cell division (new cells lack SRF and therefore *Acta2* cannot be expressed) or whether protein turnover inside individual cells contributes. The latter would suggest an extremely long half-life of αSMA.

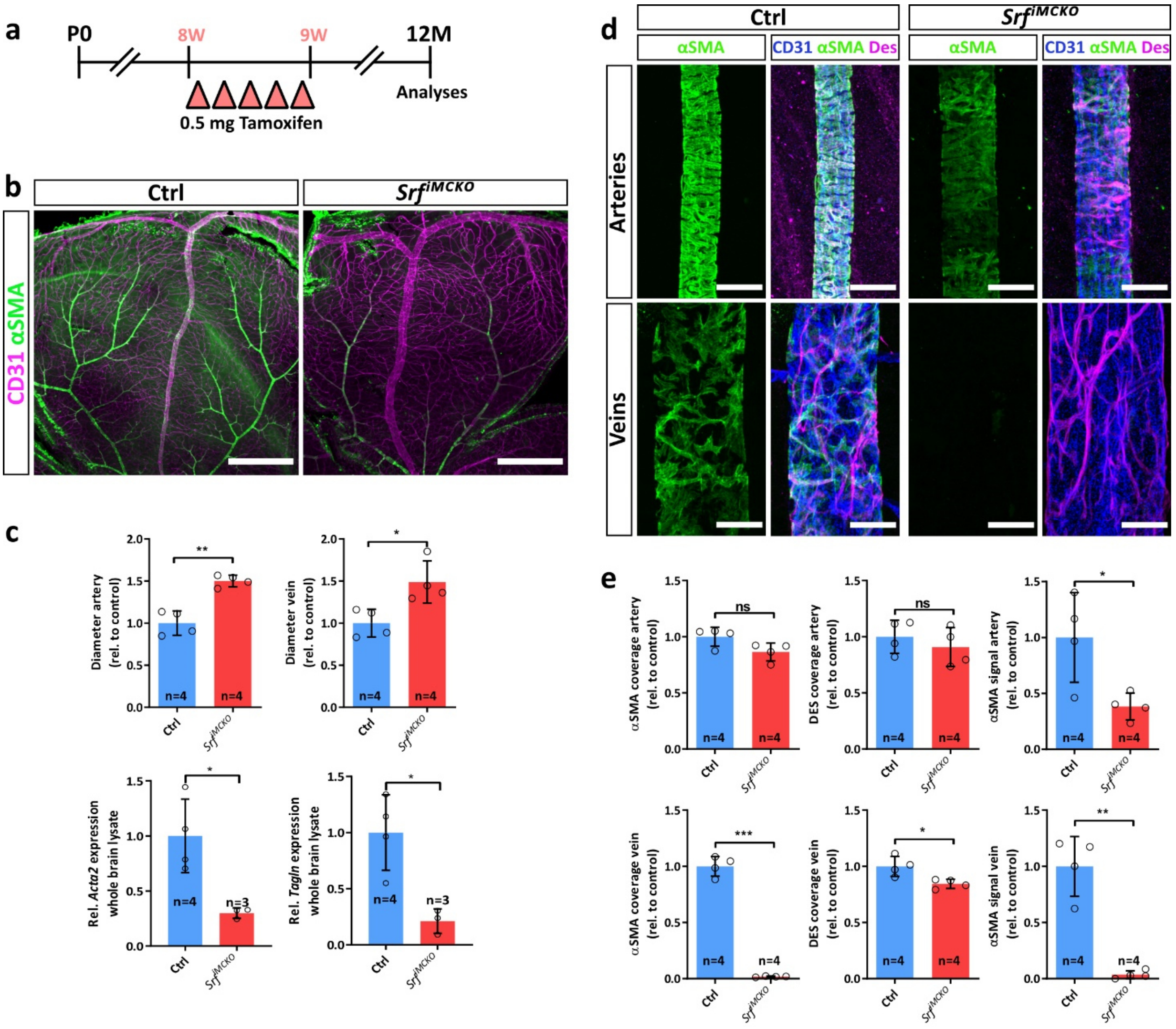

Figure 3.36| SRF is necessary for sustained contractile properties of SMCs. (a) Illustration of experimental protocol for deletion of the mural cell *Srf* gene in adult mice. 8-weeks old mice were injected with 5 consecutive injections of tamoxifen to activate Cre-mediated *Srf* deletion. Analysis was at the age of 12 months. **(b)** Overview images of retinal vascular bed stained for CD31 and αSMA. Note the enlarged vessel diameter of arteries and veins as well as the reduced signal intensity of αSMA staining in *Srf*^{iMCKO} retinas. **(c)** Quantification of diameters of arteries and veins (upper graphs) as well as the quantification of the expression of SMC marker genes *Acta2* and *Tagln* determined in whole brain lysates. **(d)** Confocal high-resolution images of arteries and veins stained for CD31, αSMA and DES. Note the strong reduction of αSMA signal in *Srf*^{iMCKO}. DES positive structures confirm the presence of SMCs. **(e)** Quantification of αSMA and DES coverage as well as the αSMA signal intensity on arteries and veins. Error bars indicate s.d. of the mean. Statistical comparison by unpaired t-test with Welch's correction. Number of analyzed animals (n) is indicated. ns = not significant, *p≤0.05, **p≤0.01, ***p≤0.001.

Chapter 4

4 Discussion

PCs and SMCs, collectively known as MCs, are a vital part of the vascular system. Due to the high organotypic heterogeneity and the absence of cell specific markers which distinguish PCs from SMCs, a comprehensive study of these cell types is difficult. Studies which aim to unravel MC functions rely on the utilization of multiple cell marker combinations and microscopy technologies. For these reasons, we lack deep knowledge about how MCs regulate developmental and pathological angiogenesis.

This study aimed to understand murine MC functions during early, advanced, and pathological angiogenesis, while distinguishing between PC- and SMC-related functions. PCs are thought to co-migrate with ECs during angiogenesis. These cellular motile functions require extensive remodeling of the cytoskeleton. A master regulator of cytoskeletal function is the transcription factor SRF, which drives *inter alia* the expression of cytoskeletal proteins. SRF is also needed for the differentiation of SMCs by expression of genes conferring contractile properties [117,194]. Initially, this study showed via immune-histological staining that SRF is expressed in retinal SMCs, confirming previous observations of Franco et al. (2013) [30]. Furthermore, I could show that SRF is also expressed in PCs, however to a lower degree compared to SMCs. The fact that both cell types express *Srf* but that PCs express very low levels of contractile SRF target genes while SMCs express high levels makes mural SRF activity especially intriguing to study.

4.1 SRF regulates PC proliferation and migration during early postnatal angiogenesis

Using a novel MC-specific *Srf-flex1::Pdgfrb-CreER*^{T2} mouse line, the functions of SRF in MCs were studied in postnatal retinas [81,157]. Mural *Srf*-ablated retinas (*Srf*^{iMCKO}) were compared to littermate controls. Initially, it was shown that tamoxifen application to *Srf-flex1::Pdgfrb-CreER*^{T2} mice efficiently induced mutation of the *Srf-flex1* allele (**Figure 3.3**). This was shown by a generic PCR which specifically amplified the mutated exon 1 of *Srf* (**Figure 3.3**, **d**). Furthermore, mRNA levels of retinal MCs sorted by FACS methodology showed significant reduced levels of *Srf* (**Figure 3.3**, **e**), proving successful and efficient ablation of the *Srf* allele. However, it needs to be mentioned that the Cre-ER^{T2} mediated recombination of the *Srf-flex1* allele could in principle lead to a shortened gene product of approximately 36 kDa. Angstenberger et al. (2007) performed a study in which the *Srf-flex1* allele was mutated by using a SM22α driven Cre-ER^{T2} mouse line, which specifically targets SMCs. In their study, a gene product of 36 kDa was observed in the KO [117].

Nevertheless, this new gene product was interpreted as not contributing in a major way to the *Srf*-KO phenotype as a similar and independent study confirmed the *Srf*-KO phenotype [194].

After conformation of the MC specific deletion of *Srf*, the resulting retinal phenotype was analyzed at P6. During early angiogenesis at P6, SMCs are immature and most MC coverage of the retinal vasculature is comprised of PCs [195]. Therefore, this developmental stage was optimal to study the effect of SRF on PC functions during angiogenesis.

The data showed remarkable effects of SRF ablation on retinal angiogenesis already at P6, as was apparent by reduced vascular outgrowth and lower complexity of the capillary plexus (**Figure 3.4**). Further stainings revealed increased vessel instability, leakage of RBCs, as well as macrophage infiltration indicating inflammation (**Figure 3.5**). These observations are in line with other studies where retinal MC ablation led to similar, but more severe phenotypic changes [45,60]. In these studies, a lack of PC coverage increased VEGFA signaling and thus lead to upregulation of ANG2, which acts pro-angiogenic and destabilizes ECs. This is followed by disruption of the endothelial ANG1-TIE2 signaling axis crucial for vascular stabilization and therefore lead to disintegration of the BRB. I also observed a reduction in PC coverage in P6 Srf^{iMCKO} retinas, which can explain the observed phenotypic changes (**Figure 3.6**). Furthermore, RNA-Seq analysis of Srf^{iMCKO} ECs at P12 also revealed upregulation of VEGFR2 and ANG2 (**Figure 3.33**).

Moreover, Eilken et al. (2017) showed that PCs fine-tune angiogenesis by sequestration of VEGFR1 at the angiogenic front [72]. In their report, vascular tip structures devoid of PCs were blunted and accompanied by a reduced number of filopodia and increased EC proliferation. Interestingly, similar blunt-ended vascular tips and lower number of filopodia were also observed in Srf^{iMCKO} P6 retinas (**Figure 3.7**). Increased EC proliferation was also evident in blunt-ended vascular tips , which were devoid of PCs (**Figure 3.7**), and thus my observations are in line with Eilken et al. (2017) [72].

A detailed analysis of vessel coverage by PCs revealed a remarkable difference between the capillary plexus and the vascular front (**Figure 3.6**). PC coverage was more reduced at the angiogenic front than at the vascular plexus of P6 Srf^{iMCKO} retinas. As PCs co-migrate with ECs towards the angiogenic front, a difference in PC coverage could be explained by defective migration and/or proliferation of PCs, provoked by the SRF deficiency. SRF is a known regulator of both, proliferation and migration [113,196]. SRF-driven proliferation is usually regulated by MAPK signaling, ultimately activating immediate early gene response (e.g. c-*Fos* expression) to induce proliferation [121]. Regulation of motile functions, however, is regulated by Rho/actin signaling via MRTFs/SRF [197]. Analysis of proliferative behavior of PCs revealed impaired proliferation of PCs at the angiogenic front in Srf^{iMCKO} retinas (**Figure 3.8**). At the capillary plexus, however, no difference in proliferation of PCs could be observed between control and Srf^{iMCKO} retinas. This could be explained by the fact that PCs at the angiogenic front in general show high proliferation rates, whereas PCs at the capillary plexus are more quiescent and therefore proliferate less [195]. Accordingly, a similar difference in proliferation behavior of PCs at the angiogenic front and the capillary plexus was also observed in P6 control retinas and may explain that a difference in PC proliferation between Srf^{iMCKO} and controls could only be noticed at the angiogenic front (**Figure 3.8**). Furthermore, reduced proliferation was also observed in *Srf-KO* pBMCs in comparison to control pBMCs, which harbor the functional *Srf* allele (**Figure 3.9**). This proliferation study suggests that PCs primarily utilize the MAPK-TCF-SRF signaling axis during angiogenesis and this could explain the observed reduction in vessel coverage.

Nevertheless, further experiments on PDGFB-stimulated *Srf-KO* and control pBMCs also showed deficiencies in migration besides proliferation and, importantly, a strong reduction in stress fiber density (**Figure 3.10** and **Figure 3.12**). Moreover, *Srf-KO* pBMCs did not show changes in cytoskeletal arrangement in response to PDGFB stimulation (**Figure 3.12**). These data indicate that PCs favor Rho-Actin-MRTF-SRF-regulated migration and this could also explain the reduction of vessel coverage by PCs in Srf^{iMCKO} retinas. Additional high-resolution microscopy of PCs revealed morphological abnormalities (**Figure 3.11**). Interestingly, PCs at the angiogenic front of control retinas in proximity to endothelial tip cells formed long filopodia, likely to sense a PDGFB gradient originating from endothelial tip cells [9]. Conversely, filopodia of PCs in Srf^{iMCKO} retinas were shortened, indicating disrupted cytoskeletal remodeling and impaired sensing of the PDGFB gradient. A comparable phenotype was observed by Weinl et al. (2013) upon endothelial *Srf* ablation in postnatal retinas, where tip cells also showed shortened filopodia [29]. Importantly, these observations were phenocopied by simultaneous ablation of endothelial *Mkl1* (MRTFA) and *Mkl2* (MRTFB), but not by endothelial ablation of TCFs, suggesting a preferred Rho-Actin-MRTF-SRF axis [29,141]. The analogy between shortened EC filopodia observed by Weinl et al. (2013) and similarly affected PC filopodia in this study also favors MRTF-mediated SRF activation to regulate migration. This is furthermore supported by Alvarez et al. (2020; unpublished work), who ablated the GTPase *Cdc42* in MCs during postnatal angiogenesis ($Cdc42^{iMCKO}$). CDC42 is a known factor upstream of MRTF and also a mediator of SRF function [124]. Strikingly, the Srf^{iMCKO} and $Cdc42^{iMCKO}$ retinal phenotypes at P6/P7 shared significant similarities which further argue for MRTF-directed SRF activation in PCs (personal communication with Konstantin Gaengel, University of Uppsala).

Additional *in vitro* assays were performed to gain molecular insights into PDGFB signaling. For this, the established 3T3 cell line was used as a model system for pBMCs as they are also of mesenchymal origin [9,198]. In comparison to pBMCs, transfection of 3T3 cells is more efficient, which constituted a requirement for conducting the experiment. 3T3 cells stably transfected with a GFP-tagged MRTFA expression plasmid revealed nuclear translocation of MRTF-GFP upon PDGFB stimulation (**Figure 3.13, a and b**). Additionally, luciferase assays scoring for SRF activation showed a significant increase of luciferase activity upon stimulation with PDGFB (**Figure 3.13, c and d**). Importantly, pharmacological inhibition of either MRTF or MAPK signaling reduced luciferase activity, whereby MRTF inhibition had a stronger effect on luciferase activity than MAPK inhibition. These findings suggest that PDGFB shows a higher prevalence for MRTF-mediated SRF signaling, but could also be explained by a higher effectivity of the MRTF inhibitor. Finally, stimulation of pBMCs with PDGFB resulted in upregulation of MRTF/SRF but not of TCF/SRF target genes, thus further supporting the domination of MRTF-mediated SRF signaling upon PDGFB stimulation (**Figure 3.13, e**). In support, Vasudevan et al. (2014) reported MRTF-driven activation of SRF in response to PDGFRα signaling in mesenchymal cells during craniofacial development [169]. Both PDGFRα and PDGFRβ belong to the PDGFR family and therefore share a lot of similarities in signaling [199]. This further supports MRTF-driven activation of SRF in PCs to regulate migration.

Collectively, it can be stated that pericytic SRF is essential for proper morphogenesis in early angiogenesis. EC-derived PDGFB binds to its receptor PDGFRβ on PCs, thereby activating Rho-GTPases such as CDC42 in order to induce actin polymerization (i.e. F-actin formation). The resulting reduction of intracellular G-actin concentration subsequently liberates MRTFs from G-actin, which translocate into the cell nucleus and activate class II SRF target gene expression to regulate PC migration. Alternatively, but likely to a lesser extent, PDGFB induces MAPK signaling to activate SRF class I target gene expression via TCFs to regulate PC proliferation.

Despite the abundant indications arguing for defective PC migration *in vivo*, it needs to be emphasized that final evidence is missing due to technical limitations. A complementary and useful experiment to validate defective PC migration would be the aortic ring assay. In this assay, aortic rings are isolated from mice and subsequently cultured for up to one week [200]. VEGFA stimulation of aortic rings activates an angiogenic response which can be monitored over time. This *ex vivo* assay supports live imaging techniques and would enable observation of PC migration in *Srf*^{iMCKO} and control aortic rings. Furthermore, linage tracing experiments would be useful to indirectly verify deficiencies in migration. This would require crossing an additional reporter mouse line into the existing *Srf-flex1::Pdgfrb-CreER*^{T2} mouse line. An attractive reporter model would be the *Brainbow* line which allows monitoring clonal expansion of cell lineages over time [201].

4.2 SRF drives pathologic activation of PCs under ischemic conditions

Besides the observed changes in PCs, also aSMCs were affected by SRF ablation. *Srf*^{iMCKO} aSMCs at P6 lost their ability to express αSMA (**Figure 3.15**). This observation was further supported by experiments performed on pBMCs. According to Esnault et al. (2014) and others, the *Acta2* gene (encoding αSMA) contains a CArG element and is therefore transcriptionally activated by SRF [115,202,203]. Nevertheless, it is impressive that the loss of αSMA levels upon ablation of *Srf* in the retina and in pBMCs was almost 100 %. This indicates the total dependency of its regulation on SRF. Furthermore, it also suggests a high penetrance of CreER^{T2}-driven *Srf* ablation.

Dubrac et al. (2018) reported that PCs are able to acquire pathological functions by shifting their phenotype towards a more SMC-like phenotype characterized by high αSMA expression [46]. This was shown by using the OIR mouse model of pathologic angiogenesis. In OIR, postnatal mice are kept under high oxygen concentrations for several days, leading to an underdeveloped retinal primary plexus. A transfer of the animals back to normoxic conditions triggers excessive hypoxia and thus the development of pathologic NVTs. Using a lineage tracing approach, it was shown that NVTs are inordinately covered by pathologically activated PCs [46]. Impaired PDGFRB signaling reduced PC migration towards NVTs and therefore mitigated its development [46].

Based on the suggested model of SRF-regulated PC migration in early angiogenesis and on the fact that aSMCs of P6 *Srf*^{iMCKO} retinas were not able to express αSMA, it is likely that ischemic pathological activation of PCs requires SRF function. Indeed, OIR experiments on *Srf*^{iMCKO} animals showed reduced NVT development and improved revascularization and therefore proofed the pathologic function of SRF in PCs under ischemic conditions (**Figure 3.16**). Despite the fact that NVTs were significantly smaller in *Srf*^{iMCKO} OIR retinas, PC coverage was unchanged in comparison to littermate controls. This suggests that pathologic PC activation is a more important driver of NVT formation than PC migration itself. As *Acta2* belongs to SRF class II genes, pathologic PC activation is most likely regulated by the MRTF-SRF axis.

Interesting in this context is the fact that PDGFB appears to trigger MRTF-driven SMC gene expression in OIR PCs [46]. This was further supported by *in vitro* PDGFB stimulation studies on pBMCs (**Figure 3.13**, **e**). PDGFB stimulation of pBMCs led to upregulation of MRTF/SRF target genes instead of TCF/SRF target genes. PDGFB is well known to act as mitogen via the MAPK signaling pathway and should therefore upregulate TCF/SRF target genes [204]. Moreover, according to Wang et al. (2004), PDGFB stimulates the activation of TCFs, which reduces SMC gene expression [129]. This seeming contradiction could be attributed to the fact that gene expression in SMCs is mainly regulated by myocardin and not by MRTFs [197]. In contrast to MRTFs, myocardin is constitutively localized in the cell nucleus [125]. Conversely, the subcellular localization of MRTFs depends on Rho-GTPase activity. Vanlandewijck et al. (2018) showed that in the adult murine brain, myocardin expression is limited to SMCs and not PCs [74]. This further suggests that PCs utilize MRTFs to upregulate SMC specific genes under ischemic conditions. As PCs are also thought to play an important role in diabetic retinopathy, it would be interesting to study pericytic MRTF function in more detail. In this context, MRTF inhibitors could be useful for potential therapeutic approaches. Recently, MRTF inhibitors were published which seem to be promising candidates to modify MRTF function [205]. These inhibitors were already shown to attenuate hyper-activation of fibroblasts and stellate cells in pathological fibrotic mouse models [206,207].

4.3 SRF sustains the expression of SMC-specific genes

Besides of the phenotype of SRF ablation in P6 retinas, *Srf*^{iMCKO} also showed a striking impact on the vascular development of P12 retinas. Arteries and veins were significantly dilated and formed AV-shunts (**Figure 3.18**). The EC density at AV-shunts was increased, but no increased proliferation was observed. In fact, EC proliferation was even decreased (**Figure 3.20**). Additional VE-Cadherin staining suggested that ECs are pressed tightly together (**Figure 3.21**), which likely causes contact inhibition and thus reduction of proliferation [208–210]. Furthermore, ultrastructural analysis of malformed endothelium displayed membrane invaginations into the vessel lumen which may indicate metabolic stress [211]. Despite of the mentioned changes, ECs appear to remain functional, as they showed no aberrant proliferation and only minor changes in RNA-Seq expression patterns (**Figure 3.33**).

In contrast to ECs, the effects of *Srf*-depletion were more pronounced in MCs. The comparison of MC coverage on *Srf*^{iMCKO} retinas at P12 and respective controls revealed altered MC distribution (**Figure 3.22**). Whereas the overall MC coverage was slightly reduced in *Srf*^{iMCKO} retinas, MC coverage on AVMs was found to be increased compared to other parts of arteries and veins. This observation may be explained by differences in blood pressure distribution. Normally, veins are exposed to the lowest blood pressure and therefore coverage and SMC gene expression of vSMCs is typically lower than that of aSMC, which are typically exposed to high arterial blood pressure [1,177]. An AV-shunt however circumvents the capillaries and the blood pressure is directly transmitted to the vein, which could result in the inflation of the AVM. The observed increase in MC coverage on AVMs is possibly a compensatory mechanism of ECs to attract MCs in order to increase vascular integrity. Ultrastructural analysis of AVMs further supports the hypothesis of pressure-triggered AVM inflation, as the basal lamina at AVMs was found to be thickened (**Figure 3.25**, **b**), indicating a possible attempt to increase vessel resistance.

It is conceivable that, in reaction to AVM inflation, ECs start to express PDGFB to attract further MCs to stabilize the vasculature. This could be tested by a PDGFB staining of *Srf*^{iMCKO} retinas. AV-shunts should be strongly positive for PDGFB and this could explain the increased MC coverage on AVMs.

3D-segmentation of high-resolution images taken on AV-shunts revealed that MCs undergo significant morphological changes, recognizable by the formation of long protrusions, which were tortuous and overlapping with other MCs on top of the vessels (**Figure 3.25**, **a**). In addition, the cell body was rounded up and appeared detached. A similar rounded phenotype was previously observed by Schratt et al. (2002) in cultured *Srf*-null embryonic stem cells [114]. Schratt et al. linked this observation to a disrupted actin cytoskeleton. Cytoskeletal abnormalities were also observed in P12 *Srf*^{iMCKO} MCs by utilization of super-resolution microscopy (**Figure 3.23**) as well as in *Srf-KO* pBMCs (**Figure 3.12**).

Several observations made on *Srf*^{iMCKO} retinas at P12 support the hypothesis that these AVMs are caused by a reduction or loss of contractile ability of SMCs. First of all, the diameter of arteries and veins was found to be significantly enlarged and aSMCs showed a stretched (**Figure 3.24**) morphology. More importantly, immune-histological stainings revealed the inability of *Srf*^{iMCKO} SMCs to express αSMA, while mRNA expression levels of SM22α and Myh11 were drastically reduced in whole retinal lysates (**Figure 3.26**). Surprisingly, previous reports showed that αSMA and SM22α null mutants were viable, demonstrating only a mild contraction deficiency, and therefore not sharing obvious similarities to the *Srf*^{iMCKO} mouse model [86,212,213]. It is possible that deletion of a single component of the contractile machinery can be compensated. For example, αSMA null mutants upregulate *Acta1*, which can at least partially compensate for αSMA function [86]. RNA-Seq of sorted MCs of *Srf*^{iMCKO} and control retinas, however, revealed downregulation of numerous transcripts encoding proteins that take part in contraction (**Figure 3.32**). Among them were genes encoding various structural proteins such as different actin isoforms, actin binding proteins and myosins. Here especially to highlight is the myosin light chain 9 (MYL9), which was previously shown to play an essential role in contraction in the DOCA-Salt hypertension mouse model [183]. Mice with reduced MYL9 levels in this model showed an enlarged diameter of arteries and veins. Of note, mRNA levels of numerous ion channel proteins, which regulate the intracellular Ca^{2+} influx to induce contraction of the SMC, were also strongly downregulated in *Srf*^{iMCKO} MCs (**Figure 3.32**). Most likely, the combined downregulation of these critical parts of the contractile machinery could not be compensated anymore. In addition, the strong upregulation of myocardin indicates complications in *Srf*^{iMCKO} SMC differentiation and is possibly a part of a compensatory mechanism. Nevertheless, myocardin function is dependent on association with SRF in order to induce SMC gene expression and hence myocardin is unlikely to induce SMC gene expression in Srf^{iMCKO} SMCs [128,214].

In addition, the RNA-Seq dataset of ECs isolated from Srf^{iMCKO} and control retinas revealed a significant upregulation of the vasoconstrictor endothelin (ET1; *Edn1;* **Figure 3.33**). ET1 is one of the most potent vasoconstrictors in mammals and crucial for the regulation of the vascular tone [88]. Elevated *Edn1* expression levels indicate induction vasoconstriction of malformed vessels. Ultimately, retinal live imaging by SLO methodology revealed strong movements of the vessel walls as a result of vascular blood flow through these vessels (**Supplementary Movie 4**). These movements are not physiologic and should normally be compensated by the tone of the vessel walls. The observed strong movements therefore strongly suggest a disruption of the vascular tone in Srf^{iMCKO} retinas.

The mentioned observations strongly support the hypothesis of a contractile loss of SMCs. The loss of contractility could lead to the formation of AV-shunts. Under physiological conditions, SMCs ensure vessel resistance against the blood pressure to enable drainage of blood into the capillaries [82]. SRF-ablated SMCs lose SMC specific gene expression (**Figure 3.26** and **Figure 3.32**) and thus possibly also their contractile ability and are expected to not be able to sustain vascular resistance. This is further supported by studies of Angstenberger et al. (2007) and Mericskay et al. (2007), in which the specific deletion of *Srf* in SMCs led to impaired contraction of intestinal smooth muscle [117,194]. These animals developed a severe dilation of the intestinal tract. Therefore, one possible way to reduce the increasing blood pressure during vascular development is the formation of a direct shunt to a vein, which allows acute pressure removal. However, venous vessels possess a much higher vascular compliance than arteries, meaning that veins easily enlarge with increasing pressure [215]. It is thus possible that the formation of an AV-shunt causes vessel inflation at the shunt itself and also dilation of venous vessels.

Of note, the mentioned data obtained from P12 Srf^{iMCKO} and control retinas suggest that the observed AVM phenotype is attributed to the dysfunctionality of SMCs and not PCs. Therefore, it would be valuable to test this hypothesis by deletion of *Srf* exclusively in SMCs. This could be achieved with CreER^{T2} lines which specifically target SMCs. Appropriate lines would be the *αSMA-CreEr*^{T2} or *Myh11-CreER*^{T2} lines, which were already shown to reliable target SMCs linages [216,217].

Another consequence of AV-shunt formation is a reduction of adequate perfusion of capillaries. This was shown by applying angiography to Srf^{iMCKO} mice (**Figure 3.34**). Depending on the severity of the vascular abnormalities, the retinal function was compromised, which was shown by ERG measurements on Srf^{iMCKO}

mice (**Figure 3.35**). Bypassing of blood flow through AVMs could therefore lead to insufficient blood supply of the retinal tissue and in consequence to the disruption of retinal function.

In comparison to its postnatal deletion, adult deletion of mural *Srf* resulted in a mild vascular phenotype (**Figure 3.36**). AVMs were not observed and development of any vascular changes appeared late. Nevertheless, analyses of retinas one-year post deletion revealed significant enlarged arterial and venous diameters. Moreover, aSMCs displayed reduced αSMA levels, whereas vSMCs lost αSMA expression entirely. This confirms that SMCs engage SRF to maintain basic levels of contractile proteins during quiescence. Deletion of *Srf* reduced the expression levels of these contractile proteins, which might explain the increased diameter of arteries and veins. The fact that mice do not form AVMs-shunts upon induction of *Srf* deletion in adulthood could be attributed to the reduced plasticity of blood vessels in adults compared to earlier stages of development. During retinal development, venous vessels take part in the generation of arterial vessels as well as in the formation of the deep and intermediate plexi which also requires extensive vessel remodeling [70,218,219]. In contrast, adult retinal vessels are already fully developed and just undergo minor changes. Therefore, AVM formation was more pronounced in early development and not observed in adult *Srf*^{iMCKO} mice. In addition, the decline of mRNAs encoding contractile proteins progressed slowly upon *Srf* deletion in SMCs, which probably allowed them to at least partially sustain the vascular tone. Notably, no obvious morphologic changes were determined in the capillary plexus of adult *Srf*^{iMCKO} retinas (**Figure 3.36**), suggesting that SRF is dispensable in PCs during quiescence.

Important to mention is that AV-shunts observed in *Srf*^{iMCKO} retinas partially resemble the human genetic disease HHT (hereditary hemorrhagic telangiectasia) which is characterized by development of AV-shunts throughout the body. This disorder is in most cases triggered by mutations in the human ENG or ACVRL1 genes, which both take part in the TGFβ pathway [220]. Affected patients frequently suffer from nasal and gastrointestinal bleedings. In particular, AVMs in the CNS can be live threatening [221]. MCs were so far not described to trigger HTT-like malformations, although they were thought to be immature on AVMs contributing to the instability of vessels [222].

A recent report showed the disruption of the ANG1-TIE2 signaling axis in the endothelial *Smad4*-KO mouse model, which develops HHT-like AVMs [223]. Pharmacological inhibition of ANG2 partially rescued the development of AVMs, because ANG2 is an inhibitor of TIE2 signaling and competes with ANG1 for TIE2 binding. Interestingly, MCs are thought to be the primary source of ANG1 [9,223]. This further indicates the potential importance of MCs in HHT. Interestingly, *Srf*^{iMCKO} ECs showed increased ANG2 expression levels (**Figure 3.33**), displaying similarities to the endothelial *Smad4*-KO model.

Another study used the pharmacologically active substance thalidomide for HHT treatment in mice and humans [95]. Surprisingly, thalidomide stimulated endothelial PDGFB secretion, which resulted in increased vessel MC coverage of AV-shunts and vessel stability. A consequence of thalidomide treatment was a reduction in bleedings. This study further supports the importance of MCs for treatment of HHT. Despite these recent achievements, which identified MCs as potential target in HHT development, their relevance in this context is largely unknown and needs to be addressed in more detail in the future. The Srf^{iMCKO} model will be a useful tool to study the impact of SMC dysfunction on HHT formation.

Chapter 5

5 Conclusion and Outlook

Over the last decades, vascular research was mainly focused on ECs and thus explains why the relevance of other cell types such as MCs remains poorly understood. Especially a precise distinction between SMCs and PCs is frequently ignored, leading to contradictory reports in literature [76,77]. This study utilized an MC-specific CreER^{T2} mouse line to investigate the function of the transcription factor SRF in MCs. In order to distinguish between the two types of MCs, SMCs and PCs, retinas with MC-specific *Srf* deletion were evaluated morphologically during various stages of vascular development.

The findings of this study identified SRF as a critical factor of MC function during vascular development and quiescence. By phenotypic characterization of *Srf*^{iMCKO} and control retinas, as well as by the *in vitro* utilization of pBMCs, this study identified SRF as regulator of cytoskeletal dynamics in MCs. Complementing *in vitro* experiments on 3T3 cell lines allowed the development of a mechanistic model of endothelial PDGFB-regulated PC migration via the MRTF-SRF axis.

It was shown that PCs become pathologically activated under ischemic conditions. This study suggests that SRF takes a pivotal role in this activation, as its deletion mitigated the pathologic activation. As ischemic eye pathologies such as ROP are a frequent pathology in infants, MRTFs pose attractive targets for ROP therapy. Inhibition of MRTF-directed SRF activation could represent a promising therapy for prevention of excessive NVT development in ROP.

Furthermore, this study offers a novel mechanism of AVM formation triggered by the inability of SMC contraction. In this concept, *Srf*^{iMCKO} SMCs are not able to provide arterial vessel resistance, which could lead to impaired drainage of the circulating blood into capillaries. In response, formation of a direct AV-shunt may bypass the arterial blood pressure towards the vein, leading to venous vessel inflation.

The *Srf*^{iMCKO} model therefore provides a great opportunity to investigate how blood flow directs arterial-venous development and potentially drives vascular malformations over time. Moreover, the identified AVMs share physiologic similarities with other mouse models of HHT but develop substantially later and could therefore be used as a model for late developing shunts in HHT disease. So far, HHT has been attributed to EC malfunction but is however a multicellular process. The *Srf*^{iMCKO} mouse model provides a new perspective on MC function in AVM development, in order to gain a better understanding of HHT.

6 Bibliography

1. Adams, R. H. & Alitalo, K. Molecular regulation of angiogenesis and lymphangiogenesis. *Nat. Rev. Mol. Cell Biol.* **8**, 464–478 (2007).

2. Tammela, T. & Alitalo, K. Lymphangiogenesis: Molecular Mechanisms and Future Promise. *Cell* **140**, 460–476 (2010).

3. Schulte-Merker, S., Sabine, A. & Petrova, T. V. Lymphatic vascular morphogenesis in development, physiology, and disease. *J. Cell Biol.* **193**, 607–618 (2011).

4. Carmeliet, P. Angiogenesis in health and disease. *Int. J. Biochem.* **25**, 1344 (1993).

5. Folkman, J. Angiogenesis: An organizing principle for drug discovery? *Nat. Rev. Drug Discov.* **6**, 273–286 (2007).

6. Pozzi, A., Yurchenco, P. D. & Iozzo, R. V. The nature and biology of basement membranes. *Matrix Biol.* **57**–**58**, 1–11 (2017).

7. Potente, M. & Mäkinen, T. Vascular heterogeneity and specialization in development and disease. *Nat. Rev. Mol. Cell Biol.* **18**, 477–494 (2017).

8. Yousif, L. F., Di Russo, J. & Sorokin, L. Laminin isoforms in endothelial and perivascular basement membranes. *Cell Adhes. Migr.* **7**, 101–110 (2013).

9. Armulik, A., Genové, G. & Betsholtz, C. Pericytes: Developmental, Physiological, and Pathological Perspectives, Problems, and Promises. *Dev. Cell* **21**, 193–215 (2011).

10. Sweeney, M. D., Sagare, A. P. & Zlokovic, B. V. Blood-brain barrier breakdown in Alzheimer disease and other neurodegenerative disorders. *Nat. Rev. Neurol.* **14**, 133–150 (2018).

11. Risau, W. & Flamme, I. Vasculogenesis. *Annu. Rev. Cell Dev. Biol.* **11**, 73–91 (1995).

12. Risau, W. Mechanisms of angiogenesis. *Nature* **386**, 671–674 (1997).

13. Strilić, B. *et al.* The Molecular Basis of Vascular Lumen Formation in the Developing Mouse Aorta. *Dev. Cell* **17**, 505–515 (2009).

14. Groppa, E. *et al.* EphrinB2/EphB4 signaling regulates non-sprouting angiogenesis by VEGF. *EMBO Rep.* **19**, (2018).

15. Gianni-Barrera, R. *et al.* VEGF over-expression in skeletal muscle induces angiogenesis by intussusception rather than sprouting. *Angiogenesis* **16**, 123–136 (2013).

16. Fraisl, P., Mazzone, M., Schmidt, T. & Carmeliet, P. Regulation of Angiogenesis by Oxygen and Metabolism. *Dev. Cell* **16**, 167–179 (2009).

17. Ho, V. C., Duan, L. J., Cronin, C., Liang, B. T. & Fong, G. H. Elevated vascular endothelial growth factor receptor-2 abundance contributes to increased angiogenesis in vascular endothelial growth factor receptor-1-deficient mice. *Circulation* **126**, 741–752 (2012).

18. Mustonen, T. & Alitalo, K. Endothelial receptor tyrosine kinases involved in angiogenesis. *J. Cell Biol.* **129**, 895–898 (1995).

19. Eilken, H. M. & Adams, R. H. Dynamics of endothelial cell behavior in sprouting angiogenesis. *Curr. Opin. Cell Biol.* **22**, 617–625 (2010).

20. Gerhardt, H. *et al.* VEGF guides angiogenic sprouting utilizing endothelial tip cell filopodia. *J. Cell Biol.* **161**, 1163–1177 (2003).

21. Hellström, M. *et al.* Dll4 signalling through Notch1 regulates formation of tip cells during angiogenesis. *Nature* **445**, 776–780 (2007).

22. Noguera-Troise, I. *et al.* Blockade of Dll4 inhibits tumour growth by promoting non-productive angiogenesis. *Nature* **444**, 1032–1037 (2006).

23. Ridgway, J. *et al.* Inhibition of Dll4 signalling inhibits tumour growth by deregulating angiogenesis. *Nature* **444**, 1083–1087 (2006).

24. Jakobsson, L. *et al.* Endothelial cells dynamically compete for the tip cell position during angiogenic sprouting. *Nat. Cell Biol.* **12**, 943–953 (2010).

25. Blanco, R. & Gerhardt, H. VEGF and Notch in tip and stalk cell selection. *Cold Spring Harb. Perspect. Med.* **3**, 1–19 (2013).

26. Potente, M., Gerhardt, H. & Carmeliet, P. Basic and therapeutic aspects of angiogenesis. *Cell* **146**, 873–887 (2011).

27. Franco, C. A. *et al.* Dynamic Endothelial Cell Rearrangements Drive Developmental Vessel Regression. *PLoS Biol.* **13**, e1002125 (2015).

28. Ferrara, N. *et al.* Heterozygous embryonic lethality induced by targeted inactivation of the VEGF gene. *Nature* **380**, 439–442 (1996).

29. Weinl, C. *et al.* Endothelial SRF/MRTF ablation causes vascular disease phenotypes in murine retinae. *J. Clin. Invest.* **123**, 2193–2206 (2013).

30. Franco, C. A. *et al.* SRF selectively controls tip cell invasive behavior in angiogenesis. *Dev.* **140**, 2321–2333 (2012).

31. Laviña, B. *et al.* Defective endothelial cell migration in the absence of Cdc42 leads to capillary-venous malformations. *Dev.* **145**, 1–20 (2018).

32. Fong, G. H., Rossant, J., Gertsenstein, M. & Breitman, M. L. Role of the Flt-1 receptor tyrosine kinase in regulating the assembly of vascular endothelium. *Nature* **376**, 66–70 (1995).

33. Hiratsuka, S., Minowa, O., Kuno, J., Noda, T. & Shibuya, M. Flt-1 lacking the tyrosine kinase domain is sufficient for normal development and angiogenesis in mice. *Proc. Natl. Acad. Sci. U. S. A.* **95**, 9349–9354 (1998).

34. Koch, S., Tugues, S., Li, X., Gualandi, L. & Claesson-Welsh, L. Signal transduction by vascular endothelial growth factor receptors. *Biochem. J.* **437**, 169–183 (2011).

35. Olsson, A. K., Dimberg, A., Kreuger, J. & Claesson-Welsh, L. VEGF receptor signalling - In control of vascular function. *Nat. Rev. Mol. Cell Biol.* **7**, 359–371 (2006).

36. Gerhardt, H. *et al.* Neuropilin-1 is required for endothelial tip cell guidance in the developing central nervous system. *Dev. Dyn.* **231**, 503–509 (2004).

37. Mukouyama, Y. S., Gerber, H. P., Ferrara, N., Gu, C. & Anderson, D. J. Peripheral nerve-derived VEGF

promotes arterial differentiation via neuropilin 1-mediated positive feedback. *Development* **132**, 941–952 (2005).

38. Gaengel, K. *et al.* The Sphingosine-1-Phosphate Receptor S1PR1 Restricts Sprouting Angiogenesis by Regulating the Interplay between VE-Cadherin and VEGFR2. *Dev. Cell* **23**, 587–599 (2012).

39. Benedito, R. *et al.* The Notch Ligands Dll4 and Jagged1 Have Opposing Effects on Angiogenesis. *Cell* **137**, 1124–1135 (2009).

40. Ubezio, B. *et al.* Synchronization of endothelial Dll4-Notch dynamics switch blood vessels from branching to expansion. *Elife* **5**, (2016).

41. Hasan, S. S. *et al.* Endothelial Notch signalling limits angiogenesis via control of artery formation. *Nat. Cell Biol.* **19**, 928–940 (2017).

42. Pitulescu, M. E. *et al.* Dll4 and Notch signalling couples sprouting angiogenesis and artery formation. *Nat. Cell Biol.* **19**, 915–927 (2017).

43. Lindahl, P., Johansson, B. R., Levéen, P. & Betsholtz, C. Pericyte loss and microaneurysm formation in PDGF-B-deficient mice. *Science (80-.).* **277**, 242–245 (1997).

44. Hellström, M. *et al.* Lack of pericytes leads to endothelial hyperplasia and abnormal vascular morphogenesis. *J. Cell Biol.* **152**, 543–553 (2001).

45. Park, D. Y. *et al.* Plastic roles of pericytes in the blood-retinal barrier. *Nat. Commun.* **8**, 1–16 (2017).

46. Dubrac, A. *et al.* NCK-dependent pericyte migration promotes pathological neovascularization in ischemic retinopathy. *Nat. Commun.* **9**, 1–15 (2018).

47. Andrae, J., Gallini, R. & Betsholtz, C. Role of platelet-derived growth factors in physiology and medicine. *Genes Dev.* **22**, 1276–1312 (2008).

48. Lindblom, P. *et al.* Endothelial PDGF-B retention is required for proper investment of pericytes in the microvessel wall. *Genes Dev.* **17**, 1835–1840 (2003).

49. Ando, K. *et al.* Peri-arterial specification of vascular mural cells from naïve mesenchyme requires notch signaling. *Dev.* **146**, (2019).

50. Joutel, A. *et al.* Notch3 mutations in CADASIL, a hereditary adult-onset condition causing stroke and dementia. *Nature* **383**, 707–710 (1996).

51. Davis, S. *et al.* Isolation of angiopoietin-1, a ligand for the TIE2 receptor, by secretion-trap expression cloning. *Cell* **87**, 1161–1169 (1996).

52. Puri, M. C., Rossant, J., Alitalo, K., Bernstein, A. & Partanen, J. The receptor tyrosine kinase TIE is required for integrity and survival of vascular endothelial cells. *EMBO J.* **14**, 5884–5891 (1995).

53. Suri, C. *et al.* Requisite role of angiopoietin-1, a ligand for the TIE2 receptor, during embryonic angiogenesis. *Cell* **87**, 1171–1180 (1996).

54. Jeansson, M. *et al.* Angiopoietin-1 is essential in mouse vasculature during development and in response to injury. *J. Clin. Invest.* **121**, 2278–2289 (2011).

55. Thurston, G. *et al.* Leakage-resistant blood vessels in mice transgenically overexpressing angiopoietin-1. *Science (80-.).* **286**, 2511–2514 (1999).

56. Huang, H., Bhat, A., Woodnutt, G. & Lappe, R. Targeting the ANGPT-TIE2 pathway in malignancy. *Nat. Rev. Cancer* **10**, 575–585 (2010).

57. Vajkoczy, P. *et al.* Microtumor growth initiates angiogenic sprouting with simultaneous expression of VEGF, VEGF receptor-2, and angiopoietin-2. *J. Clin. Invest.* **109**, 777–785 (2002).

58. Del Toro, R. *et al.* Identification and functional analysis of endothelial tip cell-enriched genes. *Blood* **116**, 4025–4033 (2010).

59. Ogura, S. *et al.* Sustained inflammation after pericyte depletion induces irreversible blood-retina barrier breakdown. *JCI Insight* **2**, 1–22 (2017).

60. Uemura, A. *et al.* Recombinant angiopoietin-1 restores higher-order architecture of growing blood vessels in mice in the absence of mural cells. *J. Clin. Invest.* **110**, 1619–1628 (2002).

61. Wilhelm, K. *et al.* FOXO1 couples metabolic activity and growth state in the vascular endothelium. *Nature* **529**, 216–220 (2016).

62. Betsholtz, C. Cell–cell signaling in blood vessel development and function. *Embo Mol. Med.* **10**, 1–4 (2018).

63. Franco, C. A. *et al.* Dynamic Endothelial Cell Rearrangements Drive Developmental Vessel Regression. *PLoS Biol.* **13**, 1–19 (2015).

64. Lobov, I. B. *et al.* The Dll4 / Notch pathway controls postangiogenic blood vessel remodeling and regression by modulating vasoconstriction and blood flow. *Blood* **117**, 6728–6737 (2011).

65. Lobov, I. B. *et al.* WNT7b mediates macrophage-induced programmed cell death in patterning of the vasculature. *Nature* **437**, 417–421 (2005).

66. Hughes, S. & Chan-Ling, T. Roles of endothelial cell migration and apoptosis in vascular remodeling during development of the central nervous system. *Microcirculation* **7**, 317–333 (2000).

67. Crist, A. M., Young, C. & Meadows, S. M. Characterization of arteriovenous identity in the developing neonate mouse retina. *Gene Expr. Patterns* **23**–**24**, 22–31 (2017).

68. Fischer, A., Schumacher, N., Maier, M., Sendtner, M. & Gessler, M. The Notch target genes Hey1 and Hey2 are required for embryonic vascular development. *Genes Dev.* **18**, 901–911 (2004).

69. Krebs, L. T. *et al.* Haploinsufficient lethality and formation of arteriovenous malformations in Notch pathway mutants. *Genes Dev.* **18**, 2469–2473 (2004).

70. Xu, C. *et al.* Arteries are formed by vein-derived endothelial tip cells. *Nat. Commun.* **5**, 1–11 (2014).

71. You, L. R. *et al.* Suppression of Notch signalling by the COUP-TFII transcription factor regulates vein identity. *Nature* **435**, 98–104 (2005).

72. Eilken, H. M. *et al.* Pericytes regulate VEGF-induced endothelial sprouting through VEGFR1. *Nat. Commun.* **8**, (2017).

73. Armulik, A. *et al.* Pericytes regulate the blood-brain barrier. *Nature* **468**, 557–561 (2010).

74. Vanlandewijck, M. *et al.* A molecular atlas of cell types and zonation in the brain vasculature. *Nature* **554**, 475–480 (2018).

75. Bergan, J. J. *et al.* Chronic venous disease. *Minerva Cardioangiol.* **55**, 459–476 (2007).

76. Hall, C. N. *et al.* Capillary pericytes regulate cerebral blood flow in health and disease. *Nature* **508**, 55–60 (2014).

77. Hill, R. A. *et al.* Regional Blood Flow in the Normal and Ischemic Brain Is Controlled by Arteriolar Smooth Muscle Cell Contractility and Not by Capillary Pericytes. *Neuron* **87**, 95–110 (2015).

78. Holm, A., Heumann, T. & Augustin, H. G. Microvascular Mural Cell Organotypic Heterogeneity and Functional Plasticity. *Trends Cell Biol.* **28**, 302–316 (2018).

79. Tsuchida, T. & Friedman, S. L. Mechanisms of hepatic stellate cell activation. *Nat. Rev. Gastroenterol. Hepatol.* **14**, 397–411 (2017).

80. Dore-Duffy, P., Katychev, A., Wang, X. & Van Buren, E. CNS microvascular pericytes exhibit multipotential stem cell activity. *J. Cereb. Blood Flow Metab.* **26**, 613–624 (2006).

81. Chen, Q. *et al.* Endothelial cells are progenitors of cardiac pericytes and vascular smooth muscle cells. *Nat. Commun.* **7**, 1–13 (2016).

82. Touyz, R. M. *et al.* Vascular smooth muscle contraction in hypertension. *Cardiovasc. Res.* **114**, 529–539 (2018).

83. Webb, R. C. Smooth muscle contraction and relaxation. *Am. J. Physiol. - Adv. Physiol. Educ.* **27**, 201–206 (2003).

84. Fatigati, V. & Murphy, R. A. Actin and Tropomyosin Variants in Smooth Muscles. *J. Biol. Chem.* **259**, 14383–14388 (1984).

85. Hafen, B. B. & Burns, B. *Physiology, Smooth Muscle*. *StatPearls* (StatPearls Publishing, 2019).

86. Zeidan, A. *et al.* Ablation of SM22α decreases contractility and actin contents of mouse vascular smooth muscle. *FEBS Lett.* **562**, 141–146 (2004).

87. Maier, L. S. & Bers, D. M. Role of Ca 2 + / calmodulin-dependent protein kinase (CaMK) in excitation – contraction coupling in the heart. *Cardiovasc. Res.* **73**, 631–640 (2007).

88. Vignon-Zellweger, N., Heiden, S., Miyauchi, T. & Emoto, N. Endothelin and endothelin receptors in the renal and cardiovascular systems. *Life Sci.* **91**, 490–500 (2012).

89. Guilluy, C. *et al.* The Rho exchange factor Arhgef1 mediates the effects of angiotensin II on vascular tone and blood pressure. *Nat. Med.* **16**, 183–190 (2010).

90. Khalil, R. A. Regulation of Vascular Smooth Muscle Function. *Colloq. Ser. Integr. Syst. Physiol. From Mol. to Funct.* **2**, 1–62 (2010).

91. Murphy, R. A. & Rembold, C. M. The latch-bridge hypothesis of smooth muscle contraction. *Can. J. Physiol. Pharmacol.* **83**, 857–864 (2005).

92. Fernández-L., A., Sanz-Rodriguez, F., Blanco, F. J., Bernabéu, C. & Botella, L. M. Hereditary hemorrhagic telangiectasia, a vascular dysplasia affecting the TGF-β signaling pathway. *Clin. Med. Res.* **4**, 66–78 (2006).

93. Goumans, M. J., Liu, Z. & Ten Dijke, P. TGF-β signaling in vascular biology and dysfunction. *Cell Res.* **19**, 116–127 (2009).

94. Jin, Y. *et al.* Endoglin prevents vascular malformation by regulating flow-induced cell migration and specification through VEGFR2 signalling. *Nat. Cell Biol.* **19**, 639–652 (2017).

95. Lebrin, F. *et al.* Thalidomide stimulates vessel maturation and reduces epistaxis in individuals with hereditary hemorrhagic telangiectasia. *Nat. Med.* **16**, 420–429 (2010).

96. Haasdijk, R. A., Cheng, C., Maat-Kievit, A. J. & Duckers, H. J. Cerebral cavernous malformations: From molecular pathogenesis to genetic counselling and clinical management. *Eur. J. Hum. Genet.* **20**, 134–140 (2012).

97. Castro, M. *et al.* CDC42 Deletion Elicits Cerebral Vascular Malformations via Increased MEKK3-Dependent KLF4 Expression. *Circ. Res.* **124**, 1240–1252 (2019).

98. Diéguez-Hurtado, R. *et al.* Loss of the transcription factor RBPJ induces disease-promoting properties in brain pericytes. *Nat. Commun.* **10**, (2019).

99. Kofler, N. M., Cuervo, H., Uh, M. K., Murtomäki, A. & Kitajewski, J. Combined deficiency of Notch1 and Notch3 causes pericyte dysfunction, models CADASIL, and results in arteriovenous malformations. *Sci. Rep.* **5**, 1–13 (2015).

100. Sapieha, P. *et al.* Retinopathy of prematurity: Understanding ischemic retinal vasculopathies at an extreme of life. *J. Clin. Invest.* **120**, 3022–3032 (2010).

101. Hanahan, D. & Weinberg, R. A. Review Hallmarks of Cancer : The Next Generation. *Cell* **144**, 646–674 (2011).

102. Goel, S. *et al.* Normalization of the Vasculature for Treatment of Cancer and other Diseases. *Physiol. Rev.* **91**, 1071–1121 (2012).

103. Chiu, K., Chang, R. C. C. & So, K. F. Intravitreous injection for establishing ocular diseases model. *J. Vis. Exp.* e313 (2007).

104. Mitchell, C. A., Werner Risau & Drexler, H. C. A. Regression of vessels in the tunica vasculosa lentis is initiated by coordinated endothelial apoptosis: A role for vascular endothelial growth factor as a survival factor for endothelium. *Dev. Dyn.* **213**, 322–333 (1998).

105. Dorrell, M. I., Aguilar, E. & Friedlander, M. Retinal vascular development is mediated by endothelial filopodia, a preexisting astrocytic template and specific R-cadherin adhesion. *Investig. Ophthalmol. Vis. Sci.* **43**, 3500–3510 (2002).

106. Selvam, S., Kumar, T. & Fruttiger, M. Retinal vasculature development in health and disease. *Prog. Retin. Eye Res.* **63**, 1–19 (2018).

107. Ruhrberg, C. & Bautch, V. L. Neurovascular development and links to disease. *Cell. Mol. Life Sci.* **70**, 1675–1684 (2013).

108. Connor, K. M. *et al.* Quantification of oxygen-induced retinopathy in the mouse: A model of vessel loss, vessel regrowth and pathological angiogenesis. *Nat. Protoc.* **4**, 1565–1573 (2009).

109. Stahl, A. *et al.* The mouse retina as an angiogenesis model. *Investig. Ophthalmol. Vis. Sci.* **51**, 2813–2826 (2010).

110. Treisman, R. Identification of a protein-binding site that mediates transcriptional response of the c-fos gene to serum factors. *Cell* **46**, 567–574 (1986).

111. Treisman, R. Regulation of transcription by MAP kinase cascades. *Curr. Opin. Cell Biol.* **8**, 205–215 (1996).

112. Arsenian, S., Weinhold, B., Oelgeschla, M. & Ru, U. Serum response factor is essential for mesoderm formation during mouse embryogenesis. **17**, 6289–6299 (1998).

113. Olson, E. N. & Nordheim, A. Linking actin dynamics and gene transcription to drive cellular motile functions. *Nat. Rev. Mol. Cell Biol.* **11**, 353–365 (2010).

114. Schratt, G. *et al.* Serum response factor is crucial for actin cytoskeletal organization and focal adhesion assembly in embryonic stem cells. *J. Cell Biol.* **156**, 737–750 (2002).

115. Esnault, C. *et al.* Rho-actin signaling to the MRTF coactivators dominates the immediate transcriptional response to serum in fibroblasts. *Genes Dev.* **28**, 943–958 (2014).

116. Gualdrini, F. *et al.* SRF Co-factors Control the Balance between Cell Proliferation and Contractility. *Mol. Cell* **64**, 1048–1061 (2016).

117. Angstenberger, M. *et al.* Severe Intestinal Obstruction on Induced Smooth Muscle-Specific Ablation of the Transcription Factor SRF in Adult Mice. *Gastroenterology* **133**, 1948–1959 (2007).

118. Parlakian, A. *et al.* Targeted Inactivation of Serum Response Factor in the Developing Heart Results in Myocardial Defects and Embryonic Lethality. *Mol. Cell. Biol.* **24**, 5281–5289 (2004).

119. Parlakian, A. *et al.* Temporally controlled onset of dilated cardiomyopathy through disruption of the srf gene in adult heart. *Circulation* **112**, 2930–2939 (2005).

120. Li, S. *et al.* Requirement for serum response factor for skeletal muscle growth and maturation revealed by tissue-specific gene deletion in mice. *Proc. Natl. Acad. Sci. U. S. A.* **102**, 1082–1087 (2005).

121. Shaw, P. E., Schröter, H. & Nordheim, A. The ability of a ternary complex to form over the serum response element correlates with serum inducibility of the human c-fos promoter. *Cell* **56**, 563–572 (1989).

122. Wei, G. H. *et al.* Genome-wide analysis of ETS-family DNA-binding in vitro and in vivo. *EMBO J.* **29**, 2147–2160 (2010).

123. Treisman, R. Ternary complex factors: growth factor regulated transcriptional activators. *Curr. Opin. Genet. Dev.* **4**, 96–101 (1994).

124. Hill, C. S., Wynne, J. & Treisman, R. The Rho family GTPases RhoA, Racl, and CDC42Hs regulate transcriptional activation by SRF. *Cell* **81**, 1159–1170 (1995).

125. Wang, D. Z. *et al.* Activation of cardiac gene expression by myocardin, a transcriptional cofactor for serum response factor. *Cell* **105**, 851–862 (2001).

126. Small, E. M. *et al.* Myocardin is sufficient and necessary for cardiac gene expression in Xenopus. *Development* **132**, 987–997 (2005).

127. Li, S., Wang, D. Z., Wang, Z., Richardson, J. A. & Olson, E. N. The serum response factor coactivator myocardin is required for vascular smooth muscle development. *Proc. Natl. Acad. Sci. U. S. A.* **100**, 9366–9370 (2003).

128. Wang, D. Z. *et al.* Potentiation of serum response factor activity by a family of myocardin-related transcription factors. *Proc. Natl. Acad. Sci. U. S. A.* **99**, 14855–14860 (2002).

129. Wang, Z. *et al.* Myocardin and ternary complex factors compete for SRF to control smooth muscle

gene expression. *Nature* **428**, 185–189 (2004).

130. Parmacek, M. S. Myocardin-related transcription factors: Critical coactivators regulating cardiovascular development and adaptation. *Circ. Res.* **100**, 633–644 (2007).

131. Li, S., Chang, S., Qi, X., Richardson, J. A. & Olson, E. N. Requirement of a Myocardin-Related Transcription Factor for Development of Mammary Myoepithelial Cells. *Mol. Cell. Biol.* **26**, 5797–5808 (2006).

132. Li, J. *et al.* Myocardin-related transcription factor B is required in cardiac neural crest for smooth muscle differentiation and cardiovascular development. *Proc. Natl. Acad. Sci. U. S. A.* **102**, 8916–8921 (2005).

133. Oh, J., Richardson, J. A. & Olson, E. N. Requirement of myocardin-related transcription factor-B for remodeling of branchial arch arteries and smooth muscle differentiation. *Proc. Natl. Acad. Sci. U. S. A.* **102**, 15122–15127 (2005).

134. Miralles, F., Posern, G., Zaromytidou, A. I. & Treisman, R. Actin dynamics control SRF activity by regulation of its coactivator MAL. *Cell* **113**, 329–342 (2003).

135. Vartiainen, M. K., Guettler, S., Larijani, B. & Treisman, R. Nuclear Actin Regulates Dynamic Subcellular Localization and Activity of the SRF Cofactor MAL. *Science (80-.).* **316**, 1749–1752 (2007).

136. Baarlink, C., Wang, H. & Grosse, R. Nuclear actin network assembly by formins regulates the SRF coactivator MAL. *Science (80-.).* **340**, 864–867 (2013).

137. Ho, C. Y., Jaalouk, D. E., Vartiainen, M. K. & Lammerding, J. Lamin A/C and emerin regulate MKL1-SRF activity by modulating actin dynamics. *Nature* **497**, 507–513 (2013).

138. Lundquist, M. R. *et al.* Redox modification of nuclear actin by MICAL-2 regulates SRF signaling. *Cell* **156**, 563–576 (2014).

139. Chai, J., Jones, M. K. & Tarnawski, A. S. Serum response factor is a critical requirement for VEGF signaling in endothelial cells and VEGF-induced angiogenesis. *FASEB J.* **18**, 1264–1266 (2004).

140. Franco, C. A. *et al.* Serum Response Factor Is Required for Sprouting Angiogenesis and Vascular Integrity. *Dev. Cell* **15**, 448–461 (2008).

141. Weinl, C. *et al.* Elk3 deficiency causes transient impairment in post-natal retinal vascular development and formation of tortuous arteries in adult murine retinae. *PLoS One* **9**, (2014).

142. Hinkel, R. *et al.* MRTF-A controls vessel growth and maturation by increasing the expression of CCN1 and CCN2. *Nat. Commun.* **5**, (2014).

143. Torrado, M. *et al.* Myocardin mRNA is augmented in the failing myocardium: Expression profiling in the porcine model and human dilated cardiomyopathy. *J. Mol. Med.* **81**, 566–577 (2003).

144. Xing, W. *et al.* Myocardin induces cardiomyocyte hypertrophy. *Circ. Res.* **98**, 1089–1097 (2006).

145. Chang, J. *et al.* Inhibitory cardiac transcription factor, SRF-N, is generated by caspase 3 cleavage in human heart failure and attenuated by ventricular unloading. *Circulation* **108**, 407–413 (2003).

146. Zhou, N. *et al.* Inhibition of SRF/myocardin reduces aortic stiffness by targeting vascular smooth muscle cell stiffening in hypertension. *Cardiovasc. Res.* **113**, 171–182 (2017).

147. Weinl, C. *et al.* Endothelial depletion of murine SRF/MRTF provokes intracerebral hemorrhagic stroke. *Proc. Natl. Acad. Sci. U. S. A.* **112**, 9914–9919 (2015).

148. Camacho, E. *et al.* The role of age in intracerebral hemorrhages. *J. Clin. Neurosci.* **22**, 1867–1870 (2015).

149. Descot, A. *et al.* OTT-MAL Is a Deregulated Activator of Serum Response Factor-Dependent Gene Expression. *Mol. Cell. Biol.* **28**, 6171–6181 (2008).

150. Sawada, T. *et al.* Fusion of OTT to BSAC results in aberrant up-regulation of transcriptional activity. *J. Biol. Chem.* **283**, 26820–26828 (2008).

151. Muehlich, S. *et al.* The transcriptional coactivators megakaryoblastic leukemia 1/2 mediate the effects of loss of the tumor suppressor deleted in liver cancer 1. *Oncogene* **31**, 3913–3923 (2012).

152. Ohrnberger, S. *et al.* Dysregulated serum response factor triggers formation of hepatocellular carcinoma. *Hepatology* **61**, 979–989 (2015).

153. Sternberg, N. & Hamilton, D. Bacteriophage P1 site-specific recombination. I. Recombination between loxP sites. *J. Mol. Biol.* **150**, 467–486 (1981).

154. Ghosh, K. & Van Duyne, G. D. Cre-loxp biochemistry. *Methods* **28**, 374–383 (2002).

155. Kim, H., Kim, M., Im, S. & Fang, S. Mouse Cre-LoxP system: general principles to determine tissue-specific roles of target genes. *Lab. Anim. Res.* **34**, 147 (2018).

156. Sheikh, A. Q., Misra, A., Rosas, I. O., Adams, R. H. & Greif, D. M. Smooth muscle cell progenitors are primed to muscularize in pulmonary hypertension. *Sci. Transl. Med.* **7**, 1–12 (2015).

157. Wiebel, F. F., Rennekampff, V., Vintersten, K. & Nordheim, A. Generation of mice carrying conditional knockout alleles for the transcription factor SRF. *Genesis* **32**, 124–126 (2002).

158. Muzumdar, M. D., Tasic, B., Miyamichi, K., Li, L. & Luo, L. A Global Double-Fluorescent Cre Reporter Mouse. *Genesis* **605**, 593–605 (2007).

159. Wadia, J. S., Stan, R. V. & Dowdy, S. F. Transducible TAT-HA fusogenic peptide enhances escape of TAT-fusion proteins after lipid raft macropinocytosis. *Nat. Med.* **10**, 310–315 (2004).

160. Schindelin, J. *et al.* Fiji: An open-source platform for biological-image analysis. *Nat. Methods* **9**, 676–682 (2012).

161. Pitulescu, M. E., Schmidt, I., Benedito, R. & Adams, R. H. Inducible gene targeting in the neonatal vasculature and analysis of retinal angiogenesis in mice. *Nat. Protoc.* **5**, 1518–1534 (2010).

162. Huber, G. *et al.* Spectral domain optical coherence tomography in mouse models of retinal degeneration. *Investig. Ophthalmol. Vis. Sci.* **50**, 5888–5895 (2009).

163. Fischer, M. D. *et al.* Noninvasive, in vivo assessment of mouse retinal structure using optical coherence tomography. *PLoS One* **4**, (2009).

164. Seeliger, M. W. *et al.* In vivo confocal imaging of the retina in animal models using scanning laser ophthalmoscopy. *Vision Res.* **45**, 3512–3519 (2005).

165. Tanimoto, N. *et al.* Vision tests in the mouse: Functional phenotyping with electroretinography. *Front. Biosci.* **14**, 2730–2737 (2009).

166. Tanimoto, N., Sothilingam, V. & Seeliger, M. W. Functional Phenotyping of Mouse Models with ERG. in *Methods in molecular biology (Clifton, N.J.)* vol. 935 69–78 (Methods Mol Biol, 2012).

167. Tigges, U., Welser-Alves, J. V., Boroujerdi, A. & Milner, R. A novel and simple method for culturing pericytes from mouse brain. *Microvasc. Res.* **84**, 74–80 (2012).

168. Peitz, M., Pfannkuche, K., Rajewsky, K. & Edenhofer, F. Ability of the hydrophobic FGF and basic TAT peptides to promote cellular uptake of recombinant Cre recombinase: A tool for efficient genetic engineering of mammalian genomes. *Proc. Natl. Acad. Sci. U. S. A.* **99**, 4489–4494 (2002).

169. Vasudevan, H. N. & Soriano, P. SRF Regulates Craniofacial Development through Selective Recruitment of MRTF cofactors by PDGF signaling. *Dev. Cell* **31**, 332 (2014).

170. Gaengel, K., Genové, G., Armulik, A. & Betsholtz, C. Endothelial-mural cell signaling in vascular development and angiogenesis. *Arterioscler. Thromb. Vasc. Biol.* **29**, 630–638 (2009).

171. Gualdrini, F. *et al.* Article SRF Co-factors Control the Balance between Cell Proliferation and Contractility Article SRF Co-factors Control the Balance between Cell Proliferation and Contractility. *Mol. Cell* **64**, 1048–1061 (2016).

172. Le Clainche, C. & Carlier, M. F. Regulation of actin assembly associated with protrusion and adhesion in cell migration. *Physiol. Rev.* **88**, 489–513 (2008).

173. Lukinavičius, G. *et al.* Fluorogenic probes for live-cell imaging of the cytoskeleton. *Nat. Methods* **11**, 731–733 (2014).

174. Kim, C. B., D'Amore, P. A. & Connor, K. M. Revisiting the mouse model of oxygen-induced retinopathy. *Eye Brain* **8**, 67–79 (2016).

175. Fruttiger, M. Development of the retinal vasculature. *Angiogenesis* **10**, 77–88 (2007).

176. Ola, R. *et al.* SMAD4 Prevents Flow Induced Arteriovenous Malformations by Inhibiting Casein Kinase 2. *Circulation* **138**, 2379–2394 (2018).

177. Lubashevsky, W., Lubashevsky, I. & Mahnke, R. Distributed self-regulation of living tissue. Effects of nonideality. *arXiv* 1–15 (2008).

178. Poissonnier, L., Villain, G., Soncin, F. & Mattot, V. Egfl7 is differentially expressed in arteries and veins during retinal vascular development. *PLoS One* **9**, (2014).

179. Minoru Kanehisa, S. G. KEGG: Kyoto Encyclopedia of Genes and Genomes. *Nucleic Acids Res.* **28**, 27–30 (2000).

180. Ashburner, M. *et al.* Gene ontology: Tool for the unification of biology. *Nat. Genet.* **25**, 25–29 (2000).

181. Fabregat, A. *et al.* Reactome graph database: Efficient access to complex pathway data. *PLoS Comput. Biol.* **14**, (2018).

182. Nishimura, D. BioCarta. *Biotech Softw. Internet Rep.* **2**, 117–120 (2001).

183. Licht, A. H. *et al.* Junb regulates arterial contraction capacity , cellular contractility , and motility via its target Myl9 in mice. *J. Clin. Invest.* **120**, 2307–2318 (2010).

184. Bernstein, K. E. & Fuchs, S. Angiotensin II and JAK2 put on the pressure. *Nat. Med.* **16**, 165–166 (2010).

185. Turner, C. J., Badu-nkansah, K., Crowley, D., Flier, A. Van Der & Hynes, R. O. α 5 and α v integrins cooperate to regulate vascular smooth muscle and neural crest functions in vivo. *Development* **142**, 797–808 (2015).

186. Solway, J. *et al.* Transcriptional regulation of smooth muscle contractile apparatus expression. *Am. J. Respir. Crit. Care Med.* **158**, 100–108 (1998).

187. Wen, T. *et al.* Transcription factor TEAD1 is essential for vascular development by promoting vascular smooth muscle differentiation. *Cell Death Differ.* **26**, 2790–2806 (2019).

188. Wong, W. T. *et al.* Bone morphogenic protein-4 impairs endothelial function through oxidative stress-dependent cyclooxygenase-2 upregulation: Implications on hypertension. *Circ. Res.* **107**, 984–991 (2010).

189. Zhang, Y. *et al.* Inhibition of bone morphogenic protein 4 restores endothelial function in db/db diabetic mice. *Arterioscler. Thromb. Vasc. Biol.* **34**, 152–159 (2014).

190. Fang, J. S. & Hirschi, K. K. Molecular regulation of arteriovenous endothelial cell specification. *F1000Research* **8**, 1208 (2019).

191. Gkatzis, K. *et al.* Interaction between ALK1 Signaling and Connexin40 in the Development of Arteriovenous Malformations. *Arterioscler. Thromb. Vasc. Biol.* **36**, 707–717 (2016).

192. Watts, S. W., Fink, G. D., Northcott, C. A. & Galligan, J. J. Endothelin-1-induced venous contraction is maintained in DOCA-salt hypertension ; studies with receptor agonists. *Br. J. Pharmacol.* **137**, 69–79 (2002).

193. Randa Hilal-Dandan and Laurence L. Brunton. *Encyclopedia of Signaling Molecules*. *Encyclopedia of Signaling Molecules* vol. 6 (2012).

194. Mericskay, M. *et al.* Inducible Mouse Model of Chronic Intestinal Pseudo-Obstruction by Smooth Muscle-Specific Inactivation of the SRF Gene. *Gastroenterology* **133**, 1960–1970 (2007).

195. Figueiredo, A. M. *et al.* Phosphoinositide 3-kinase-regulated pericyte maturation governs vascular remodeling. *Circulation* **142**, 688–704 (2020).

196. Posern, G. & Treisman, R. Actin' together: serum response factor, its cofactors and the link to signal transduction. *Trends Cell Biol.* **16**, 588–596 (2006).

197. Pipes, G. C. T., Creemers, E. E. & Olson, E. N. The myocardin family of transcriptional coactivators: Versatile regulators of cell growth, migration, and myogenesis. *Genes Dev.* **20**, 1545–1556 (2006).

198. Dastagir, K. *et al.* Murine embryonic fibroblast cell lines differentiate into three mesenchymal lineages to different extents: New models to investigate differentiation processes. *Cell. Reprogram.* **16**, 241–252 (2014).

199. Heldin, C. H. & Lennartsson, J. Structural and functional properties of platelet-derived growth factor and stem cell factor receptors. *Cold Spring Harb. Perspect. Biol.* **5**, 1–19 (2013).

200. Baker, M. *et al.* Use of the mouse aortic ring assay to study angiogenesis. *Nat. Protoc.* **7**, 89–104 (2012).

201. Livet, J. *et al.* Transgenic strategies for combinatorial expression of fluorescent proteins in the nervous system. *Nature* **450**, 56–62 (2007).

202. Sun, Q. *et al.* Defining the mammalian CArGome. *Genome Res.* **16**, 197–207 (2006).

203. Xiong, Y. *et al.* Targeting MRTF/SRF in CAP2-dependent dilated cardiomyopathy delays disease onset. *JCI Insight* **4**, 1–16 (2019).

204. Tallquist, M. & Kazlauskas, A. PDGF signaling in cells and mice. *Cytokine Growth Factor Rev.* **15**, 205–213 (2004).

205. Lisabeth, E. M. *et al.* Identification of Pirin as a Molecular Target of the CCG-1423/CCG-203971 Series of Antifibrotic and Antimetastatic Compounds. *ACS Pharmacol. Transl. Sci.* **2**, 92–100 (2019).

206. Yu-Wai-Man, C. *et al.* Local delivery of novel MRTF/SRF inhibitors prevents scar tissue formation in a preclinical model of fibrosis. *Sci. Rep.* **7**, 1–13 (2017).

207. Leal, A. S., Misek, S. A., Lisabeth, E. M., Neubig, R. R. & Liby, K. T. The Rho/MRTF pathway inhibitor CCG-222740 reduces stellate cell activation and modulates immune cell populations in Kras G12D ; Pdx1-Cre (KC) mice. *Sci. Rep.* **9**, 1–12 (2019).

208. Sweeney, M. & Foldes, G. It Takes Two: Endothelial-Perivascular Cell Cross-Talk in Vascular Development and Disease. *Front. Cardiovasc. Med.* **5**, 154 (2018).

209. Choi, H. J. *et al.* Yes-associated protein regulates endothelial cell contact-mediated expression of angiopoietin-2. *Nat. Commun.* **6**, 1–14 (2015).

210. Viñals, F. & Pouysségur, J. Confluence of Vascular Endothelial Cells Induces Cell Cycle Exit by Inhibiting p42/p44 Mitogen-Activated Protein Kinase Activity. *Mol. Cell. Biol.* **19**, 2763–2772 (1999).

211. Lindahl, P., Johansson, B. R., Levéen, P. & Betsholtz, C. Pericyte loss and microaneurysm formation in PDGF-B-deficient mice. *Science (80-.).* **277**, 242–245 (1997).

212. Schildmeyer, L. A. *et al.* Impaired vascular contractility and blood pressure homeostasis in the smooth muscle α-actin null mouse. *FASEB J.* **14**, 2213–2220 (2000).

213. Tomasek, J. J. *et al.* Deletion of smooth muscle α-actin alters blood-retina barrier permeability and retinal function. *Investig. Ophthalmol. Vis. Sci.* **47**, 2693–2700 (2006).

214. Wang, Z., Wang, D. Z., Pipes, G. C. T. & Olson, E. N. Myocardin is a master regulator of smooth muscle gene expression. *Proc. Natl. Acad. Sci. U. S. A.* **100**, 7129–7134 (2003).

215. Tansey, E. A., Montgomery, L. E. A., Quinn, J. G., Roe, S. M. & Johnson, C. D. Understanding basic vein physiology and venous blood pressure through simple physical assessments. *Adv. Physiol. Educ.* **43**, 423–429 (2019).

216. Wirth, A. *et al.* G12-G13-LARG-mediated signaling in vascular smooth muscle is required for salt-induced hypertension. *Nat. Med.* **14**, 64–68 (2008).

217. Wendling, O., Bornert, J. M., Chambon, P. & Metzger, D. Efficient temporally-controlled targeted mutagenesis in smooth muscle cells of the adult mouse. *Genesis* **47**, 14–18 (2009).

218. Pitulescu, M. E. *et al.* Dll4 and Notch signalling couples sprouting angiogenesis and artery formation. *Nat. Cell Biol.* **19**, 915–927 (2017).

219. Selvam, S., Kumar, T. & Fruttiger, M. Retinal vasculature development in health and disease. *Prog. Retin. Eye Res.* **63**, 1–19 (2018).

220. Tual-Chalot, S., Oh, S. P. & Arthur, H. M. Mouse models of hereditary hemorrhagic telangiectasia:

Recent advances and future challenges. *Front. Genet.* **5**, 1–12 (2015).

221. Peacock, H. M., Caolo, V. & Jones, E. A. V. Arteriovenous malformations in hereditary haemorrhagic telangiectasia: Looking beyond ALK1-NOTCH interactions. *Cardiovasc. Res.* **109**, 196–203 (2016).

222. Thalgott, J., Dos-Santos-Luis, D. & Lebrin, F. Pericytes as targets in hereditary hemorrhagic telangiectasia. *Front. Genet.* **5**, 1–16 (2015).

223. Crist, A. M. *et al.* Angiopoietin-2 Inhibition Rescues Arteriovenous Malformation in a Smad4 Hereditary Hemorrhagic Telangiectasia Mouse Model. *Circulation* **139**, 2049–2063 (2019).

Appendix A

Abbreviations

aaSMCs	Arteriolar SMCs
AB	Antibody
ABC	ATP-binding cassette
AF	Angiogenic front
afPCs	Angiogenic front pericytes
AMKL	Acute megakaryoblastic leukemia
ANG1	Angiopoietin-1
aSMC	Arterial SMCs
AT2	Angiotensin-2
AV	Arteriovenous
AVMs	Arteriovenous malformations
AVN	Arteriovenous-nicking
BBB	Blood-brain barrier
BM	Basement membrane
BRB	Blood-retina barrier
BrdU	Bromodeoxyuridine
BSA	Bovine serum albumin
CADASIL	Cerebral autosomal dominant arteriopathy with subcortical infarcts and leukoencephalopathy
CAMK	Ca^{2+}/calmodulin-dependent protein kinase
CCMs	Cerebral cavernous malformations
CNS	Central nervous system
ColI	Collagen I
ColIV	Collagen IV
qPCR	Quantitative polymerase chain reaction
cpPCs	Capillary pericytes
CX40	Connexin 40
DES	Desmin
DLL4	Delta-like-4
EB	Evans blue
EBSS	Earl's Balanced Salt Solution
ECM	Extracellular matrix
ECs	Endothelial cells
Edn1	Endothelin-1
EdU	5-Ethynyl-2´-deoxyuridine

EM	Electron microscopy
Eph	Ephrin
ES cells	Embryonic stem cells
FACS	Fluorescence-activated cell sorting
F-actin	Filamentous actin
FCS	Fetal calf serum
flex1	Floxed exon 1
G-actin	Globular actin
GO	Gene Ontology
GSEA	Gene set enrichment analysis
HCC	Hepatocellular carcinoma
HHT	Hereditary hemorrhagic telangiectasia
HIF1α	Hypoxia inducible factor 1α
HRP	Horseradish peroxidase
i.p.	Intraperitoneally
IB4	Isolectin-B4
ICG	indocyanine green
InsP3R	IP receptor Ca^{2+} channel
ISI	Inter-stimulus interval
JAG1	Jagged 1
JAK2	Janus kinase 2
kbp	Kilo base pair
KEGG	Kyoto Encyclopedia of Genes and Genomes
KO	Knockout
MAPK	Mitogen activated protein kinase
MCs	Mural cells
MEFs	Mouse embryonic fibroblasts
MLCK	Myosin light chain kinase
MLCP	Myosin light chain phosphatase
MMPs	Metalloproteinases
MRTFA	Myocardin-related transcription factor A
MRTFB	Myocardin related transcription factor B
MYL9	Myosin light chain 9
myocd	Myocardin
NES	Normalized enrichment score
NRP	Neuropilin
NVTs	Neovascular tufts

OD	Oculus dexter
OIR	Oxygen-induced retinopathy
OS	Oculus sinister
P	Postnatal day
PAK1	p21-activated protein kinase 1
PB	Phosphate buffer
pBMCs	Primary brain mural cells
PBS	Phospate-buffered saline buffer
PCR	Polymerase chain reaction
PCs	Pericytes
PDGFB	Platelet derived growth factor B
PDGFRβ	Platelet derived growth factor receptor β
PLGF	Placental growth factor
qPCR	Quantitative polymerase chain reaction
RBCs	Red blood cells
RIPA	Radio-immuno precipitation assay
RNA-Seq	RNA-sequencing
ROP	Retinopathy of prematurity
RTKs	Receptor tyrosine kinases
RYR	Ryanodine receptors
S1P	Sphingosine-1 phosphate
SDS	Sodium dodecyl sulfate
SDS-PAGE	Sodium dodecyl sulfate - polyacrylamide gel electrophoresis
SLO	Scanning-Laser Ophthalmoscopy
SMCs	Smooth muscle cells
SMGs	Smooth muscle cell-specific genes
SRF	Serum response factor
TB	Terrific broth
TCFs	Ternary complex factors
TEM	Transmission electron microscopy
TGFβ	Transforming growth factor beta
VEGFA	Vascular endothelial growth factor A
VEGFR1	Vascular endothelial growth factor receptor 1
VEGFR2	Vascular endothelial growth factor receptor 2
vSMCs	Venous SMCs
WT	Wild type
αSMA	Alpha smooth muscle

Appendix B

Contributions

The following colleagues and collaboration partners contributed to the work presented in this thesis:

1. Prof. Dr. Ralf Adams, provided *Pdgfrb(BAC)-CreER*^{T2} mouse line.
2. Dr. Rodrigo Diéguez-Hurtado, isolated RNA from sorted MCs and ECs and performed the RNA-Seq analysis.
3. Dr. Hyun-Woo Jeong, performed initial bioinformatical analysis of RNA-Seq results obtained from sorted MCs and ECs.
4. Dr. Regine Muehlfriedel, performed live imaging SLO and OCT and interpreted results.
5. Dr. Vithiyanjali Sothilingam, performed ERG experiments and interpreted results.
6. Prof. Dr. Mathias Seeliger, interpreted SLO, OCT and ERG results.
7. Dr. Kristin Bieber, performed FAC sorted MCs and ECs out of retinal single cell suspensions.
8. Gabi Frommer-Kaestle, performed EM sample preparation out of fixed retina tissue.
9. Dr. Hartwig Wolburg, imaged and interpreted EM retinal samples.
10. Cansu Ebru Oender, established isolation and culture method of pBMCs, as well as the Tat-Cre isolation and purification procedure.
11. Pascal Woelffing, performed luciferase and MRTFA translocation live cell experiments.

All remaining work presented in this thesis was performed by myself.

Appendix C

Publications and manuscripts by Michael Orlich

Orlich M, Hurtado RD, Oender CE, Wolburg H, Muehlfriedel R, Sothilingam V, Seeliger M, Gaengel K, Adams RH and Nordheim A. SRF controls mural cell migration, proliferation and triggers the development of vascular malformations. *Manuscript in preparation*

Winkler I*, Thavamani A*, Ducker G, Matic K, Weichenhan D, Graeve M, **Orlich M**, ... & Nordheim A. Metabolic reprogramming of Serine Synthesis, Mitochondrial One-Carbon Metabolism, and Methionine Cycle Activity in Hepatocellular Carcinoma. *Manuscript in preparation*

Mohan K, Gasparoni G, Salhab A, **Orlich M**, Geffers R, Hoffmann S, Adams RH, Walter J and Nordheim A. Age-linked changes in murine endothelial gene expression and chromatin accessibility associate with blood-brain barrier disruption and increased risk of intracerebral hemorrhage. *Manuscript in preparation*

Orlich M^{+} & Kiefer F (2018) A qualitative comparison of ten tissue clearing techniques. *Histol. Histopathol. 33: 181–199*

Chen X, Venkatachalapathy M, Kamps D, Weigel S, Kumar R, **Orlich M**, Garrecht R, Hirtz M, Niemeyer CM, Wu YW and Dehmelt L. (2017) “Molecular Activity Painting”: Switch-like, Light- Controlled Perturbations inside Living Cells. *Angew Chem Int Ed Engl. 15;56(21):5916-5920 12/2010*

Lehmann ML, Selinski S, Blaszkewicz M, **Orlich M**, …, Golka K. (2010) Rs710521[A] on chromosome 3q28 close to TP63 is associated with increased urinary bladder cancer risk. *Arch Toxicol. 84(12):967-78*

Appendix D

List of figures

Appendix E

Supplementary figures

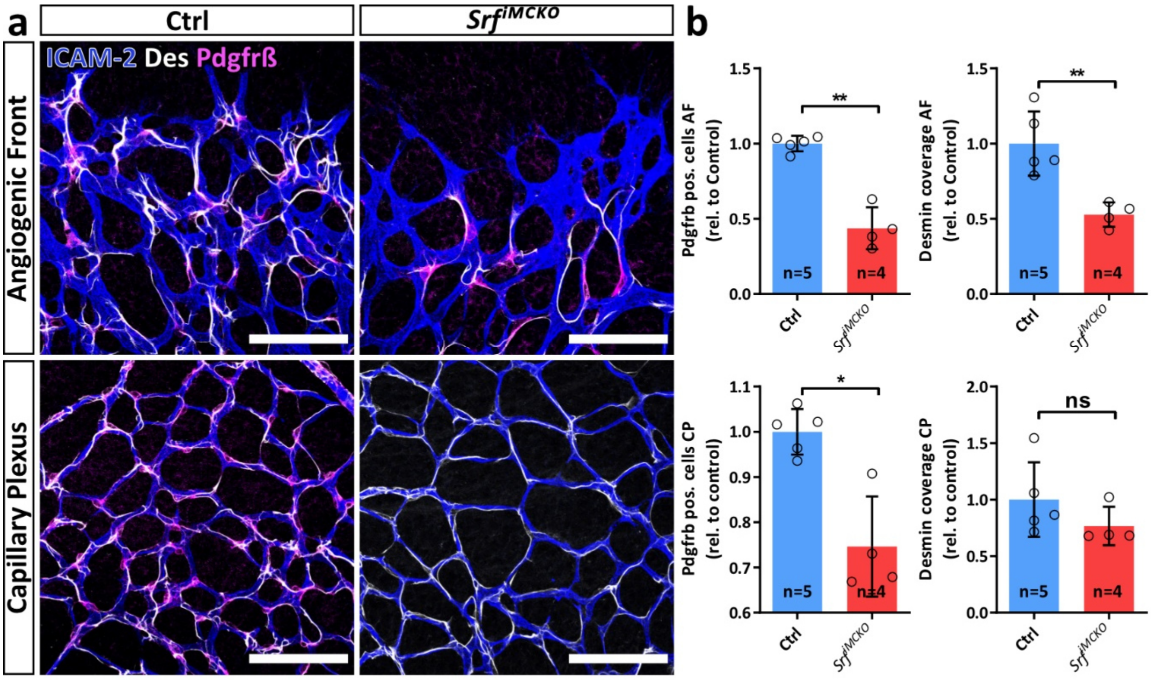

Supplementary Figure 1 | SRF-deficient PCs lag behind the sprouting front leaving leading vessels uncovered (extension to Figure 3.6) . (a) Confocal images showing PC coverage at the capillary plexus (CP) and the angiogenic front (AF). ECs were stained with ICAM2 (blue) and PCs with desmin (white) and PDGFRB (magenta). Note PC-uncovered and dilated vessels at the leading front of the AF in Srf^{iMCKO} retina (right). Scale bar: 100 µm. **(b)** Respective quantifications of the PC coverage. Error bars show s.d. of the mean. Statistical comparison by unpaired t-test with Welch's correction. Number of analyzed animals (n) is indicated. ns = not significant, *p≤0.05, **p≤0.01, ***p≤0.001.

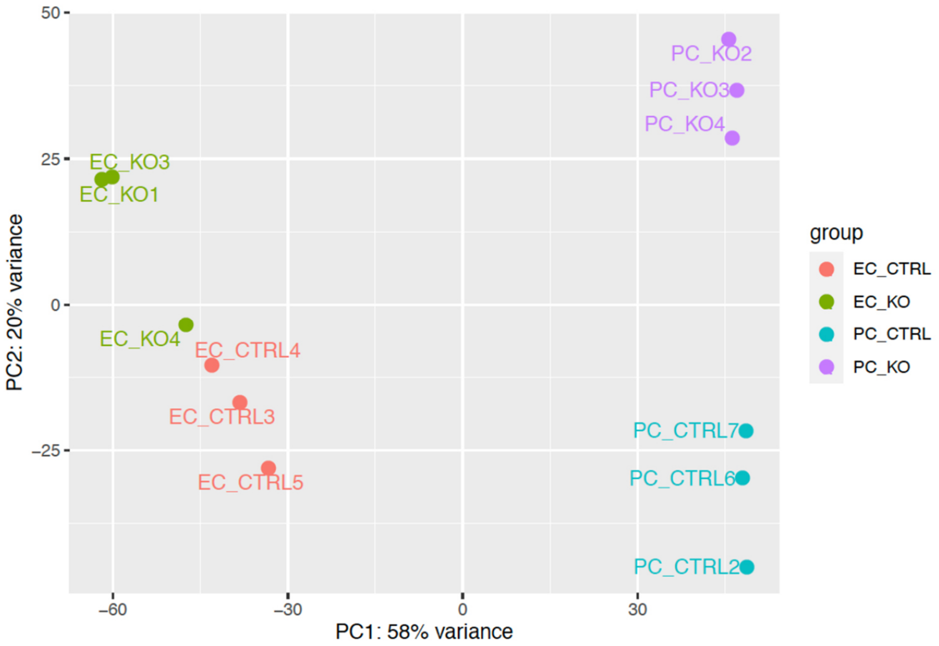

Supplementary Figure 2 | Principal component analysis (PCA) plot of RNA-Seq data sets of control and *Srf*^{iMCKO} MCs and ECs.

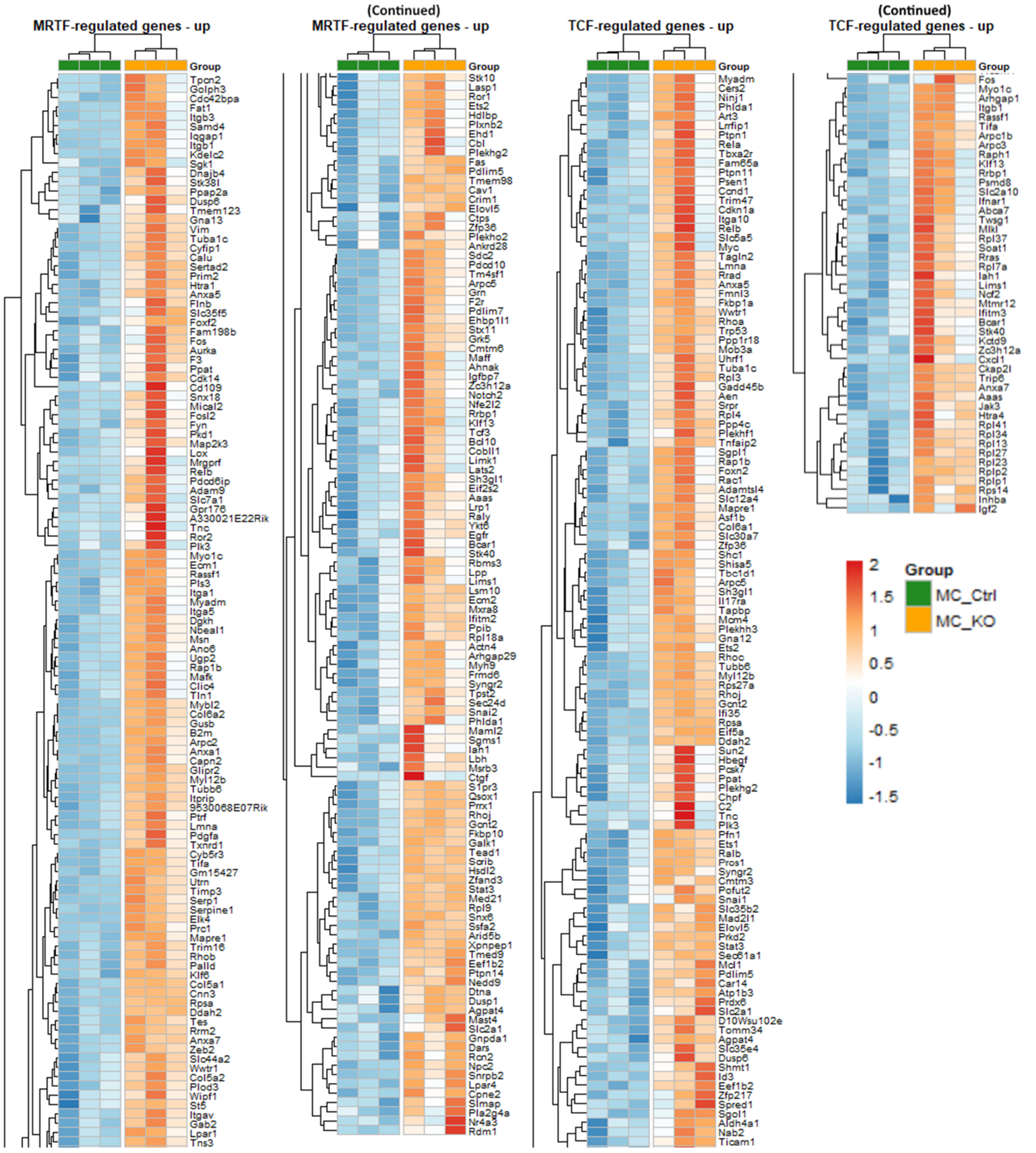

Supplementary Figure 3 | Heatmap of upregulated SRF target genes identified in MC RNA-Seq dataset. Identified genes are subdivided into MRTF-SRF and TCF-SRF regulated targets, according to Esnault et al. (2014) and Gualdrini et al. (2016) [115,116].

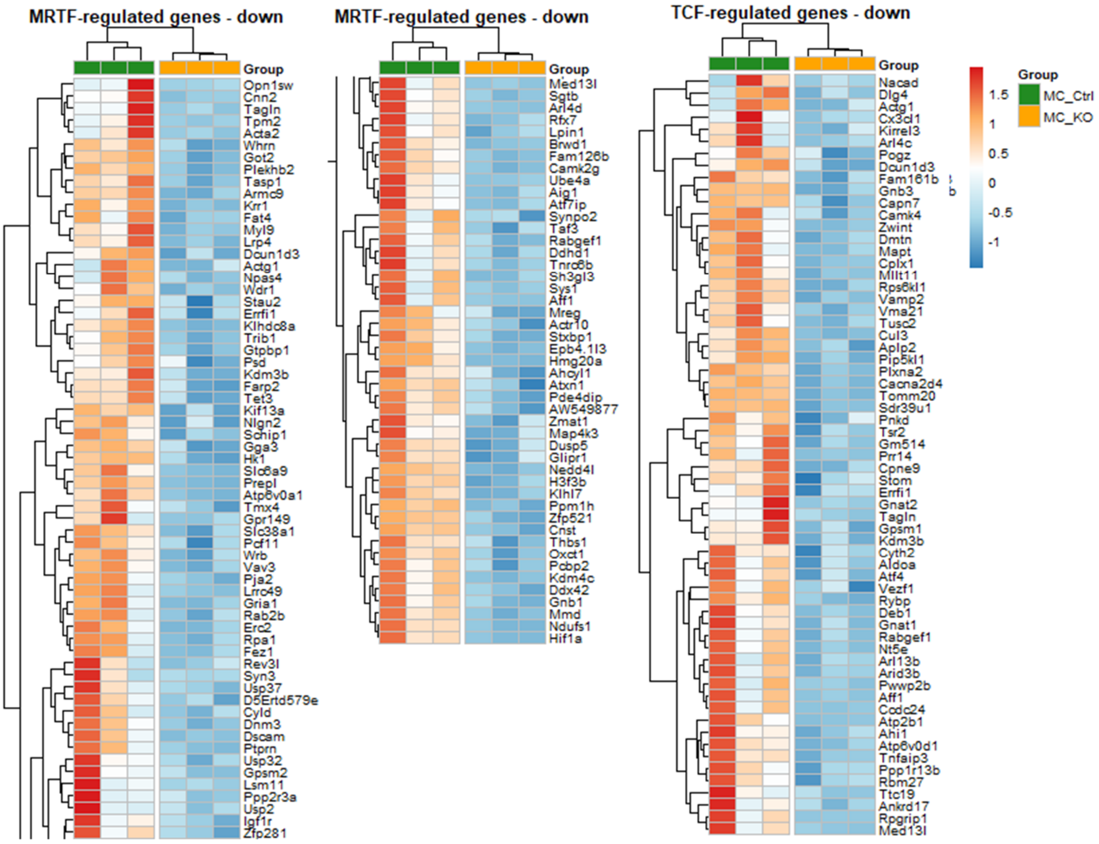

Supplementary Figure 4 | Heatmap of downregulated SRF target genes identified in MC RNA-Seq dataset. Identified genes are subdivided into MRTF-SRF and TCF-SRF regulated targets, according to Esnault et al. (2014) and Gualdrini et al. (2016) [115,116].

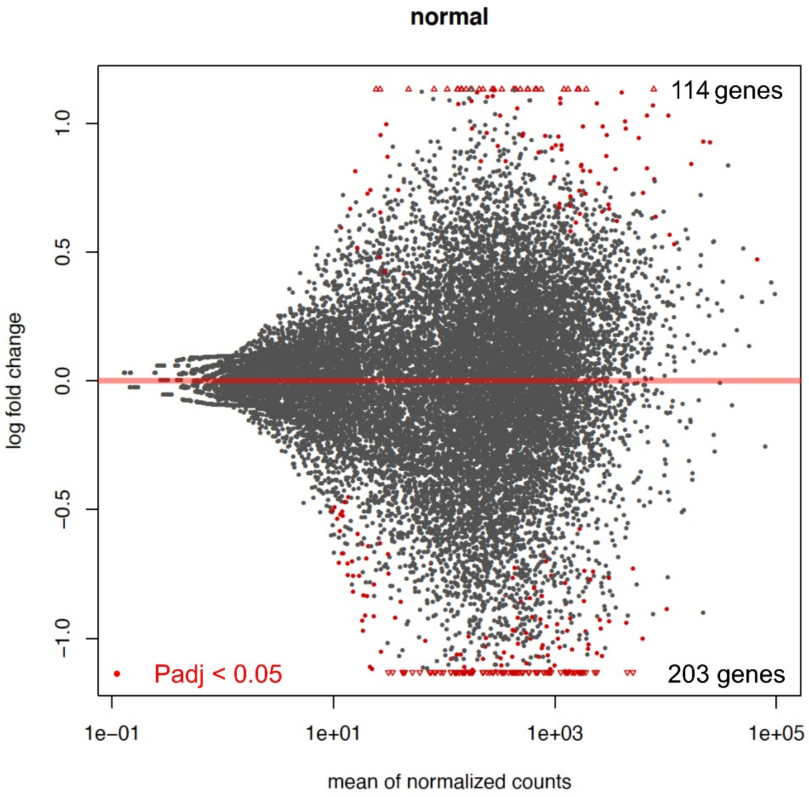

Supplementary Figure 5 | Vulcano plot displaying RNA-Seq detected EC genes according to the degree of dysregulation ($\log_2$ fold change). Red dots indicate significantly ($p<0.05$) dysregulated genes.

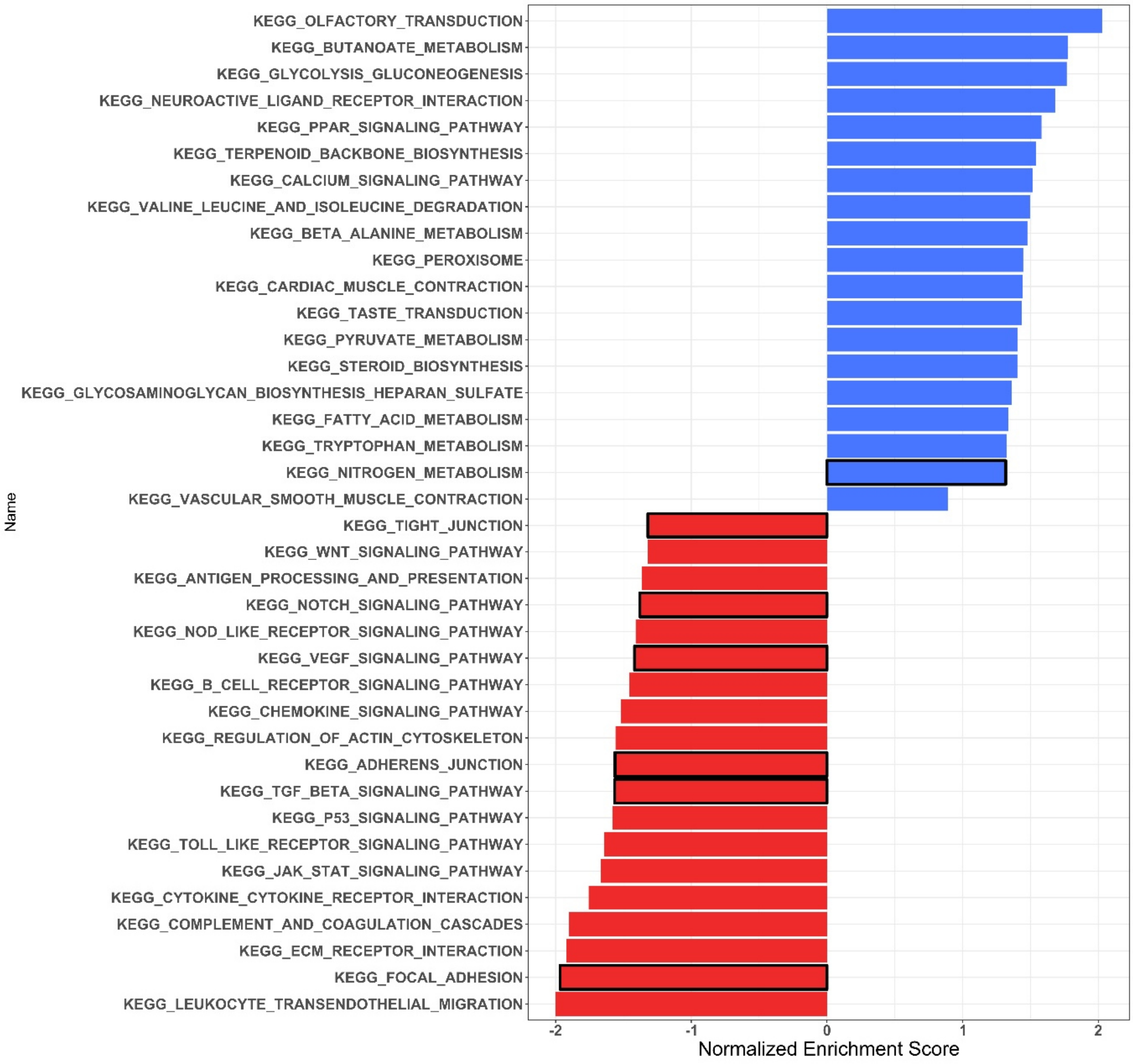

Supplementary Figure 6 | GSEA of RNA-Seq dataset of *Srf*^{iMCKO} and control ECs. Positive normalized enrichment scores (NES) indicate pathways containing downregulated genes whereas negative NES indicate pathways containing genes which are upregulated. Representative summary of tested gene set from the KEGG database.

Appendix F

Supplementary movies

Supplementary Movie 1 |Representative migration assay of *Srf-KO* and control pBMC cultures stained by SiR-Actin. Cells were stimulated with PDGFB to stimulate migration. Note the difference in migration speed. This movie is supportive to **Figure 3.10**.

Supplementary Movie 2 |Representative PDGFB stimulation of *Srf-KO* and control pBMC cultures stained by SiR-Actin. Cells were stimulated with PDGFB to observe cytoskeletal modulation. Note the absence of reaction of *Srf-KO* pBMCs. This movie is supportive to **Figure 3.12**.

Supplementary Movie 3 |Representative PDGFB stimulation of 3T3 cells expressing MRTFA-GFP. 3T3 cells were stimulated with PDGFB to observe MRTFA-GFP nuclear translocation. This movie is supportive to **Figure 3.13**.

Supplementary Movie 4 |Representative SLO *in vivo* imaging of *Srf*^{iMCKO} and respective control retinas. Note the strong vessel movements of dilated vessels indicating a loss of vascular tone in *Srf*^{iMCKO} animals. This movie is supportive to **Figure 3.34**.